UNIVERSITAT DE BARCELONA

Anomalous transport and diffusion of Brownian particles on disordered landscapes

Marc Suñé Simon

ADVERTIMENT. La consulta d'aquesta tesi queda condicionada a l'acceptació de les següents condicions d'ús: La difusió d'aquesta tesi per mitjà del servei TDX (**www.tdx.cat**) i a través del Dipòsit Digital de la UB (**diposit.ub.edu**) ha estat autoritzada pels titulars dels drets de propietat intel·lectual únicament per a usos privats emmarcats en activitats d'investigació i docència. No s'autoritza la seva reproducció amb finalitats de lucre ni la seva difusió i posada a disposició des d'un lloc aliè al servei TDX ni al Dipòsit Digital de la UB. No s'autoritza la presentació del seu contingut en una finestra o marc aliè a TDX o al Dipòsit Digital de la UB (framing). Aquesta reserva de drets afecta tant al resum de presentació de la tesi com als seus continguts. En la utilització o cita de parts de la tesi és obligat indicar el nom de la persona autora.

ADVERTENCIA. La consulta de esta tesis queda condicionada a la aceptación de las siguientes condiciones de uso: La difusión de esta tesis por medio del servicio TDR (**www.tdx.cat**) y a través del Repositorio Digital de la UB (**diposit.ub.edu**) ha sido autorizada por los titulares de los derechos de propiedad intelectual únicamente para usos privados enmarcados en actividades de investigación y docencia. No se autoriza su reproducción con finalidades de lucro ni su difusión y puesta a disposición desde un sitio ajeno al servicio TDR o al Repositorio Digital de la UB. No se autoriza la presentación de su contenido en una ventana o marco ajeno a TDR o al Repositorio Digital de la UB (framing). Esta reserva de derechos afecta tanto al resumen de presentación de la tesis como a sus contenidos. En la utilización o cita de partes de la tesis es obligado indicar el nombre de la persona autora.

WARNING. On having consulted this thesis you're accepting the following use conditions: Spreading this thesis by the TDX (**www.tdx.cat**) service and by the UB Digital Repository (**diposit.ub.edu**) has been authorized by the titular of the intellectual property rights only for private uses placed in investigation and teaching activities. Reproduction with lucrative aims is not authorized nor its spreading and availability from a site foreign to the TDX service or to the UB Digital Repository. Introducing its content in a window or frame foreign to the TDX service or to the UB Digital Repository is not authorized (framing). Those rights affect to the presentation summary of the thesis as well as to its contents. In the using or citation of parts of the thesis it's obliged to indicate the name of the author.

Anomalous transport and diffusion of Brownian particles on disordered landscapes

– Ph.D. Thesis –

Marc Suñé Simon

Dr. José María Sancho Herrero
– Ph.D. Advisor and Tutor–

June, 2016

Universitat de Barcelona

Facultat de Física
Departament de Física de la Matèria Condensada
Programa de Doctorat en Física

Anomalous transport and diffusion of Brownian particles on disordered landscapes

Ph.D. Thesis
Programa de Doctorat en Física
Línia de Recerca en Física de la Matèria Condensada
Memòria presentada per optar al títol de Doctor per la UB
Període 2011-2016
Barcelona, Juny de 2016

Typeset by the author, adapted from the *fncychap* LaTeX package distributed under the conditions of the LaTeX Project Public License (© 2007 Ulf Lindgren). It has been also followed the article "Writing a thesis with LaTeX", *The PracTeX Journal*, No.1, 2008, Lapo F. Mori (© 2007 Lapo F. Mori).

Marc Suñé Simon
sune@ecm.ub.edu
Departament de Física de la Matèria Condensada
Facultat de Física
Universitat de Barcelona
Barcelona, E-08028
Spain

The work covered in this thesis was funded by the *Universitat de Barcelona*, under the *APIF2014-2015* program (*Ajuts de Personal Investigador Predoctoral en Formació*).

The work submitted had also financial support from the *Ministerio de Economía y Competitividad* under projects FIS2009-13360-C03-01, FIS2012-37655-C02-02, and FIS2015-66503-C3-3-P, and from the *Generalitat de Catalunya* under projects 2009SGR14 and 2014SGR878.

Als meus pares

Acknowledgements

A thesis is a corpus of skills, knowledge, experience, erudition and information in the hands of someone, yet emanated from the wisdom, kindness, benevolence, encouragement and friendship of many other people. Hence, it is not only a matter of gratitude but also of honesty to express a brief, albeit warm and heartfelt, appreciation to them. Since it's all about an emotional affair rather than an ordinary procedure, I feel like speaking out in my mother tongue.

La primera vegada que vaig enraonar amb el que esdevindria el meu director de tesi, el professor José María Sancho, va ser acabat el període d'exàmens del primer semestre de la llicenciatura de Física. Devia ser el febrer de 2006. Les coses no m'havien anat bé, eren temps convulsos per mi; ignoro si la conversa, d'escassos minuts de durada, va servir per ajudar-me a sortir del sot amb el que m'havia entrebancat. En qualsevol cas, guardo encara ara a la memòria el missatge d'aquell encontre; alguna cosa així com "*los profesores preparamos los exámenes para que aprobéis, tienes que aprender a encontrar las cuestiones sencillas antes que enredarte con las preguntas difíciles. Las primeras deberías saberlas responder y con esto te bastará para aprobar.*" Uns quants anys més tard, vaig retrobar-me amb el professor Sancho en el màster de Biofísica, i el projecte de neurociència que vam endegar va conduir a la posterior recerca sobre el moviment Brownià que presenta aquesta tesi; el canvi de la línia de recerca s'explica per una altra reflexió seva que recordo vivament "*podemos seguir con los modelos*

de las neuronas, pero nos lanzamos a la piscina sin saber, ni tan siquiera, si hay piscina".

Serveixin aquest parell de fets anecdòtics, però alhora indicatius del seu tarannà i la seva lucidesa, per expressar la meva gratitud envers en José María, per tota la seva saviesa que m'ha ajudat a resoldre les qüestions que han sorgit durant la tesi; senzilles en algunes ocasions, complicades com mai m'hauria imaginat aquell febrer gris del 2006 en d'altres.

En el període de temps que he estat duent a terme les investigacions incloses en la tesi, ha estat un goig poder comptar amb la col·laboració, l'aportació i els coneixements de la Dra. Katja Lindenberg, de la *University of California San Diego*, així com de la Dra. Ana María Lacasta, de la *Universitat Politècnica de Catalunya*. Per altra banda, també voldria destacar l'ajuda i els bons consells que el Dr. Rubén Pérez, actualment al *University College London*, m'ha donat sempre que li ho he requerit. De forma genèrica, manifesto un agraïment sincer a tots els membres de l'extint Departament d'Estructura i Constituents de la Matèria, des del personal docent fins als col·legues doctorands, passant pel personal d'administració i servis i els tècnics. També a la Marina Bertran per ajudar-me en el disseny de la portada.

De petit, l'avi Ramon em portava a jugar amb excavadores i camions. Absort com estava de comparar l'exigüitat de les meves joguines amb les grans màquines que aquells dies treballaven a ritme frenètic en la construcció de la variant de Puig-reig, li deia "*avi, de gran portaré una excavadora giratòria*"; "*el que has de fer quan et facis gran, és estudiar per ser l'enginyer que dibuixa la carretera*", ell em contestava. L'avi fa temps que se'n va anar, si fa no fa al mateix temps que ho va fer aquella ocurrència pueril; mentrestant, vaig seguir aprenent com ell hauria volgut, i de les *senyoretes*, als professors d'institut, i d'aquí a la facultat. A tots els docents que he tingut els dec un respecte, admiració i agraïment enormes.

Aquell episodi particular d'infantesa, anecdòtic, entre jo i el meu avi, il·lustra prou bé l'empara familiar que he tingut sempre per fer allò que m'he proposat. Sempre han estat al meu costat, estimant-me, ensenyant-me, educant-me; reprenent-me quan ha calgut; en definitiva, guiant-me, però deixant-me prendre les meves decisions amb llibertat, els meus pares. També l'avi Pep i la iaia Angelina, la iaia Carme i l'avi Ramon, els tiets i els cosins. Últimament, l'Esteve i la Concep, el Jaume, la Teresina, el Josep i la Montserrat, m'han fet sentir com un més a casa seva.

No puc deixar de tenir un record per l'Arnau, l'Anna, la Judit i el Martí, quatre barbamecs amb pretensions d'adults que l'any 2005 ens vam presentar a Barcelona amb una il·lusió immensa per descobrir un nou món, per iniciar una nova vida. Més tard també s'hi va afegir en Roger. Ben aviat però, vam donar-nos compte que en aquella nova realitat no hi podien faltar el Lluís, ni l'Àngel, l'Agustí, el Ramon, el Toti o l'Oriol, però tampoc la Mireia; de fet, no ens van mancar mai, afortunadament. I per això els estic profundament agraït.

Els lligams atàvics amb Puig-reig s'han enfortit cada dia que he passat fora de casa. La melangia que sovint la llunyania m'ha suscitat ha estat més lleu gràcies a l'amistat de la Núria, la Isabel i la Queralt, i a les fantasies que hem gosat somiar. Tanmateix, no només a l'univers purreixtenc dec un agraïment per no haver-me sentit mai sol; la bicicleta ha estat una companya tossuda durant tot aquest temps. El mal de cames d'un empit sobtat, l'olor del paisatge, l'espatec de la cadena caient a un pinyó més petit, i la fatiga d'una jornada interminable, han estat la forja de grans amistats, d'entre elles, el Joan Claret i el Pep Cabanas.

Reconec que la informàtica no ha estat mai ni la meva passió ni el meu fort, fins i tot em concitava dubtes a l'hora d'escollir la llicenciatura de Física. Després d'haver-me passat davant d'una computadora gairebé tota la jornada laboral durant els últims cinc anys, la informàtica continua sense apassionar-me; nogensmenys, hem après a conviure. Àdhuc li dec alguns

dels moments més plaents que he viscut en el procés d'investigar la dinàmica del moviment Brownià; la superació de cada trava que ha aparegut en la simulació d'un problema nou ha constituït un estímul per seguir endavant. I no només això, sinó que m'ha permès conèixer la gent—directora, tècnics i becaris—de la *Unitat Informàtica Diagonal Nord Sud*, als quals estic molt agraït pel tracte que en vaig rebre i els coneixements que em van transmetre. El Josep Maria Planell i la LuzMa Rojo són amistats que aprecio molt i que he conegut a través de la informàtica.

Finalment, dono les gràcies a la Mariona per totes les abraçades que m'ha fet cada vespre en arribar a casa, per comprendre'm, per fer que tot plegat sigui menys costerut, per estimar-me com sóc.

Puig-reig, June 2016 *Marc Suñé Simon*

Preface

This thesis is arranged in two parts and eight chapters.

The first part comprises an introduction to the phenomenon of Brownian motion and the description of the theoretical framework employed throughout the scientific investigations (Chap. 1), as well as a summary of the thesis, the main results, and the subsequent conclusions that have been attained (Chap. 2).

The second part is made up of five chapters (Chapters 3 to 8) that conduct a thorough discussion of each particular case that has been inquired.

Finally, a catalan résumé of the thesis, the list of publications, a glossary of the nomenclature, and the bibliography are included at the rear end of the book.

Contents

Part I

Introduction, summary, main results, and leading conclusions

CHAPTER 1

Introduction

1.1. About Brownian motion

Brownian motion refers to the random movement that undergo meso-sized particles suspended in a simple solvent. It has become the keystone of a fully probabilistic formulation of statistical mechanics and a prevailing subject of physical investigation. The history of stochastic motion may be traced back to 1784, when a Dutch scientist called Jan Ingen-Housz reported the erratic motion that coal dust particles exhibited when observing powdered charcoal on an alcohol surface under light microscope [Ingen-Housz, 1784, 1789]. Notwithstanding that this observation might be claimed as the discovery of the jiggling movement at the mesoscale between the atomic and the macroscopic realms, this phenomenon was named for the Scottish botanist Robert Brown, who published in 1828 an investigation of the agitated movements of minute particles ejected from certain pollen grains in the liquid he was looking at in the microscope [Brown, 1828], (Fig. 1.1). Further, Brown repeated his experiments with pollen kept in alcohol for several months—presumably dead—and with non–organic particles. He noticed the same unceasing motion [Ford, 1992], and so he concluded that this movement had nothing to do with life.

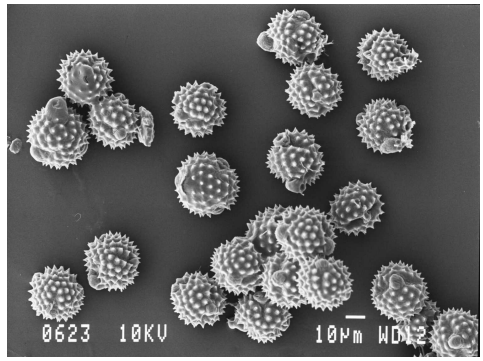

Figure 1.1 – Pollen grains suspended in water. From the Image Library of the Bioimaging Laboratory of IBERS, University of Wales.

The qualitative explanation of Brownian motion was put forward by several authors by the end of the *XIX*th century. In 1889, the French physicist Louis George Gouy reported detailed qualitative studies of the phenomenon [Gouy, 1889]. He found that Brownian motion is not due to random external influences, such as vibrations, and electric or magnetic fields, and that its magnitude depends mainly on two factors: the particles' size and the temperature.

In the first decade of the *XX*th century, the theoretical description of Brownian motion was carried out independently by Albert Einstein [Einstein, 1905]—in 1905—and Marian von Smoluchowski [Von Smoluchowski, 1906]—in 1906—employing probability arguments. In particular, Einstein's probabilistic approach to the Brownian motion is founded on the principal that the random movement is on account of the molecular motions of heat [Einstein, 1905]. He argued that Brownian particles obey the well-known differential equation for diffusion of chemical species in aqueous solutions [Fick, 1855] that Adolf Eugen Fick, a German physician and physiologist, had developed empirically by direct analogy with the heat and electricity transfer equations. From this equation, Einstein predicted that the root mean square displacement of suspended particles is proportional to the square root of time. Further, employing thermodynamics arguments and

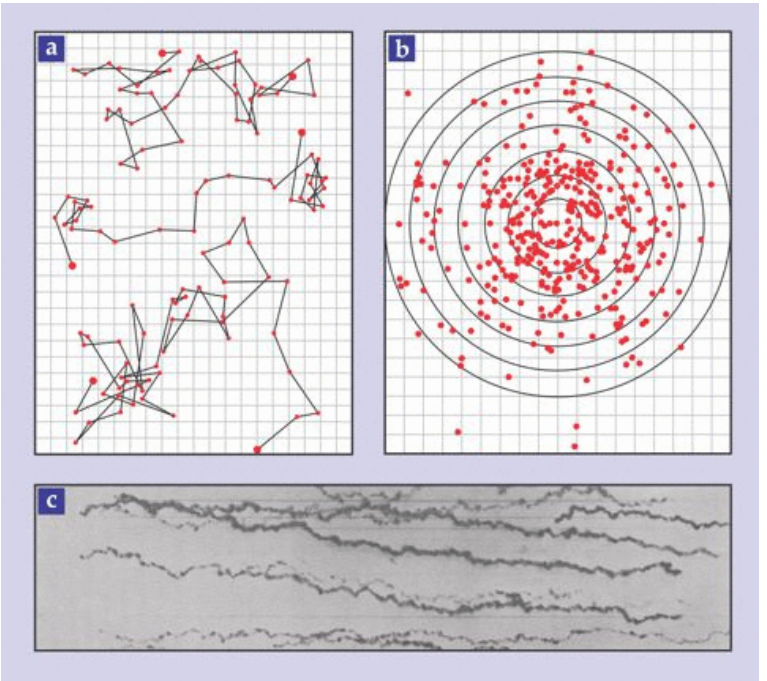

Figure 1.2 – Obtained from [Barkai et al., 2012]. (a) In 1908 Jean Perrin traced individual trajectories of microscopically putty particles in water at 30–second intervals [Perrin, 1908] (red dots). (b) By fitting a Gaussian to the distribution of all the 30–second displacements, shifted to a common origin, he obtained an ensemble diffusion constant [Perrin, 1908]. (c) Six years later, Ivar Nordlund recorded individual trajectories of mercury particles in water as they settled to the bottom, and obtained the time averaged mean squared displacements [Nordlund, 1914]. The waviness of the trajectories is a sign of Brownian motion and their advance is a trace of transport.

the concept of osmotic pressure of suspended particles, Einstein obtained a relation between the particle diffusion constant, the fluid viscosity—or friction—, the absolute temperature, and the Avogadro–Loschmidt number. This relation provided an emphatic and categorical evidence for the atomistic conception of matter. Summarizing, Einstein's theory on Brownian motion follows from three postulates. First, particles are assumed not to interact with each other. Second, the motion is memoryless at long times. Third, the distribution of particle displacements possesses at least two lower moments, for they are independent.

Between 1908 and 1911, Jean Perrin and his students performed a series of experiments comprising meticulous analyses of single trajectories of colloidal particles observed under a microscope [Perrin, 1909] (Fig. 1.2) that not only verified the Einstein's predictions but they also brought about an improved estimation of the Avogadro–Loschmidt number. Perrin was awarded with the Nobel prize in 1926 for this contribution that bolstered the atomistic hypothesis of matter.

The ideas of Einstein and von Smoluchowski were rephrased by Paul Langevin [Langevin, 1908; Lemons and Gythiel, 1997]—in 1908—so as to account for the Brownian trajectories, leading to a new type of differential equations, namely the so–called stochastic differential equations. Such equations separate the force balance into a deterministic and a random part; they can be regarded as generalizations of Newtonian mechanical equations. The characterization of the random forces was mainly ascribed to the work of Leonard Ornstein [Ornstein, 1919], who settled the basis of the so–called random Gaussian white noise—Gaussian distributed with δ correlation function—. The modern calculus of Langevin equations is still nowadays founded on the random forces conceived by the Dutch physicist.

Back to the initial approach of Einstein, in which the Brownian movement was based on the discussion of deterministic equations for the probability densities, its generalization leads to the Fokker–Planck or the diffusion equation method. The diffusion–like equation for the Brownian motion with drift was first proposed be Adriaan Fokker [Fokker, 1914] in 1914 and discussed later by Max Planck [Planck, 1917] in 1917; it consists of a linear second–order partial differential equation—a forward Kolmogorov equation [Schuss, 1980]—. The approach states that for an ensemble of particles or systems, macroscopic fluctuations—e.g. the distribution function of the fluctuating macroscopic velocity—are like a diffusion process. The distribution function of the random variables will, therefore, fulfill a partial differential equation of the diffusion type. A detailed discussion on the Fokker–Planck equations can be found in the books of Hannes Risken [Risken, 1989], and Werner Ebeling and Igor M. Sokolov [Ebeling

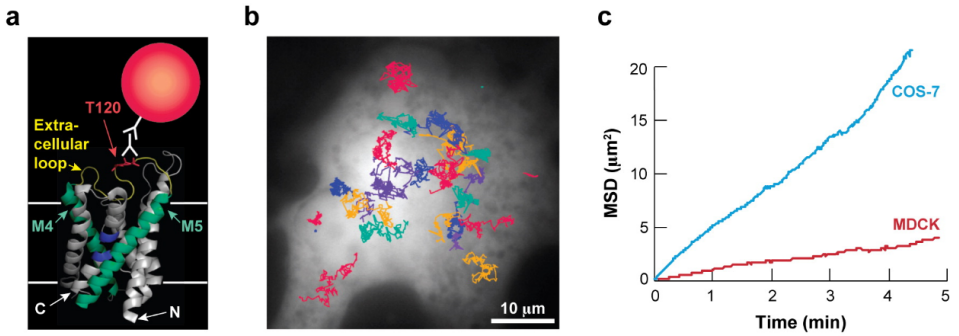

Figure 1.3 – Obtained from [Dix and Verkman, 2008; Crane and Verkman, 2008]. Membrane protein diffusion. Long–range diffusion of aquaporin–1 (AQP1) water channels in cell plasma membranes. (a) Schematic of a quantum dot (Qdot)–labeled AQP1 monomer. (b) AQP1 trajectories from time-lapse of single particle tracking acquired at 1 Hz (total time $\approx$ 6 min) overlaid onto fluorescence images of green fluorescent proteins in the cytoplasm of a COS–7 cell. Each trajectory is shown in a different color. (c) MSD versus time curves for AQP1 diffusion in COS–7—a nonpolarized fibroblast—and MDCK cells—Madine–Darby canine kidney cells, an epithelial cell type—($\approx$ 300 individual trajectories averaged for each cell type). Nearly linear MSD plots are obtained in agreement with the theory of Brownian motion developed by Einstein.

and Sokolov, 2005].

Subsequent theoretical artifacts, such as the well–known fluctuation–dissipation theorem [Callen and Welton, 1951] developed by Herbert Callen and Theodore A. Welton—in 1951—, and the linear response theory of Ryogo Kubo [Kubo, 1957]—in 1957—entailed generalizations of the Einstein relation.

The Einstein's theory of Brownian motion based on the molecular-kinetic theory of heat constitutes one of the milestones in physics. It provides the link between the elementary underlying microscopic dynamics and macroscopic observables, such as the ubiquitous underlying fluctuations in plenty of processes in natural and social sciences, for example in membrane protein diffusion [Crane and Verkman, 2008], see Figure 1.3. Many areas of physics, still subject to active research, have been prompted by theories of

Brownian motion indeed [Hänggi and Marchesoni, 2005]. However, extrapolating mesoscopic type of behavior to microscopic scales, as the Langevin or Fokker–Planck approaches assume, is not always advantageous. It might otherwise be appropriate to build up the theory from a simple microscopic kinematic model, as for example the so–called random walk approaches do. The term "random walk" is ascribed to Karl Pearson, who was engaged in biostatistical problems in 1905 [Pearson, 1905]. The first random walk model was nonetheless put forward in 1900 by Louis Bachelier in his doctoral thesis on the stock market prices [Bachelier, 1900a,b; Courtault et al., 2000]. Random walk models are versatile, for they adapt to non–Markovian situations. General information about the random walk approaches to different physical milieus can be found in the review articles by Joseph W. Haus and Klaus W. Kehr [Haus and Kehr, 1987], by Jean–Philippe Bouchaud and Antoine Georges [Bouchaud and Georges, 1990], and by M. B. Isichenko [Isichenko, 1992]. Random walk models are often employed to shed light into a myriad of processes exhibiting anomalous dynamics, for example, the diffusion of potassium channels in plasma membranes of living cells [Weigel et al., 2011].

Random walk approaches consider the motion of a particle as a sequence of independent steps. In each of these steps the particle travels some distance away from its initial position within a particular time. The step's duration and length are obtained from some probability distribution. Depending on the properties of the probability distribution, a wealth of different approaches arise. Among them, the lattice random walk allows the particle to jump only to the next–neighboring lattice sites; it was put into practice by Elliott W. Montroll and George Weiss in the sixties of the XXth century to account for luminiscent reactions in molecular crystals [Montroll and Weiss, 1965; Montroll, 1969]. Concerning the time behavior, random walks split between the so–called simple random walks, in which the time step is fixed, and the continuous–time random walks (CTRW), in which the time is itself a random variable. In the latter, the random walk may result from a series of scattering events, in which case the time and the displacement are strongly correlated. May the particle remain trapped in

some bounded state until it is released from time to time and makes a random motion until it gets trapped again, the displacement and time random variables are otherwise independent. Transport in disordered semiconductors may be described by this class of CTRW [Scher and Montroll, 1975]. CTRW with power–law waiting time distributions do have a corresponding formulation through deterministic equations, leading to the so–called fractional Fokker–Planck equations [Metzler and Klafter, 2000; Sokolov et al., 2002]—a Fokker–Planck approach to non Fickian processes [Balakrishnan, 1985; Schneider and Wyss, 1987, 1989] which brings about non–Markovian outcome—. Finally, may the third Einstein's postulate of normal diffusion be abandoned—the mean square displacement is not finite—leads to several different models. For example, the CTRW with step lengths distributed according to a power–law results in the so–called Lévy flights, which is a Markovian process of indefinitely large jumps—hence the model does not exhibit a limiting velocity—. Another important model is the Lévy walk built up by Michael F. Shlesinger, Bruce J. West and Joseph Klafter in 1987 [Shlesinger et al., 1987]. In such a process the particle moves at a constant velocity during a certain period of time—given by a probability density—, after which the direction of the velocity is chosen anew. Lévy walks can also be described within the framework of fractional kinetic equations as Igor M. Sokolov and Ralf Metzler demonstrated in 2003 [Sokolov and Metzler, 2003].

Posterior to the historical overview of the Brownian motion phenomenon, this opening chapter goes on with the discussion of the theoretical formalism employed throughout the investigations that account for the present thesis.

1.2. Transport and diffusion

The basic concepts that will make up the subject matter of this thesis, that are contained in Einstein's paper [Einstein, 1905], are reviewed in this section. Further, an extended excerpt of Einstein's reasoning can be found

in the book by Crispin W. Gardiner [Gardiner, 1985].

1.2.1. Free particles: Einstein's diffusion and the Fokker-Planck approach

A suspended particle in a solvent is subjected to rapid collisions with the solvent molecules; these kicks occur at the time scale of the liquid dynamics—picosecond regime—and lead to a tiny exchange of momentum. Concomitantly, they also give rise to the macroscopic friction force. May $\hat{\boldsymbol{r}}(\hat{t})$ be the vector that points the position of a suspended particle at time $\hat{t}$, increments concerning a time scale where the particle moves significantly— i.e. these time intervals are not chosen too small—$\Delta\hat{\boldsymbol{r}}(\hat{t}) = \hat{\boldsymbol{r}}(\hat{t}+\hat{t}') - \hat{\boldsymbol{r}}(\hat{t}')$ are considered as random variables that are identically and independently distributed. This assumption mans that the process is memoryless—Markovian—[Wang and Uhlenbeck, 1945]. Besides, hydrodynamic effects are not taken into account for it would violate the Markovian assumption. Considering an ensemble of n identical particles performing Brownian movements, and assuming the former conjectures, there will be a certain frequency law for the increments $\Delta\hat{\boldsymbol{r}}(\hat{t})$; Einstein demonstrated by a microscopic interpretation that the differential equation to approach the dynamics of the distribution of particles is—up to second order in $1-d$—

$$\frac{\partial P(\hat{r},\hat{t})}{\partial \hat{t}} = \hat{D}\,\frac{\partial^2 P(\hat{r},\hat{t})}{\partial \hat{r}^2} + \dots \,, \tag{1.1}$$

where $\hat{r}$ is the position, that in $1-d$ is a scalar. This is already known as the differential equation of diffusion—second law of Fick, and so $P(\hat{r},\hat{t})$ displays the same space–time dynamics as the macroscopic concentration—in which $\hat{D}$ is the diffusion coefficient, and its solution is

$$P(\hat{r},\hat{t}) = \frac{n}{\sqrt{4\pi\hat{D}\hat{t}}}\,\exp\left(-\frac{\hat{r}^2}{4\hat{D}\hat{t}}\right) \,. \tag{1.2}$$

This is the well–known normal distribution, whose cumulants beyond the first two—other than the mean and the variance—are zero; the variance exhibits a linear time behavior indeed

$$\langle \Delta\hat{r}^2(\hat{t})\rangle = 2\hat{D}\hat{t} \,, \tag{1.3}$$

where the brackets $\langle \ldots \rangle$ indicate the average over the displacements at a fixed time $\hat{t}$ along the trajectory of a particle, as well as over the ensemble of identical non–interacting particles. The generalization of Equation (1.3) to d–dimensional space reads

$$\langle \Delta \hat{r}^2_{\hat{\boldsymbol{u}}}(\hat{t}) \rangle = 2d\, \hat{D}_{\hat{\boldsymbol{u}}}\, \hat{t}\ , \tag{1.4}$$

where subindex $\hat{\boldsymbol{u}}$—the hat indicates that $\hat{\boldsymbol{u}}$ is a unit vector—labels any direction in the Euclidean d–space, $\hat{D}_{\hat{\boldsymbol{u}}}$ is the component along $\hat{\boldsymbol{u}}$ of the Cartesian diffusion tensor $\hat{\boldsymbol{D}} = \{\hat{D}_{i_1,\ldots,i_d}\}$—$i_1, \ldots, i_d$ label the components in a d–space—that is computed by the product

$$\hat{D}_{\hat{\boldsymbol{u}}} = \hat{\boldsymbol{u}} \cdot \hat{\boldsymbol{D}} \cdot \hat{\boldsymbol{u}}\ . \tag{1.5}$$

Einstein's work goes beyond and evaluates the particle diffusion constant. Balancing a diffusion current—to be obtained from the osmotic pressure deduced from the molecular–kinetic theory of heat—with a drift current—inferred from the Stokes' law—leads to the so–called Stokes–Einstein relation—assuming $1 - d$ space so that diffusion is a constant—,

$$\hat{D} = \frac{k_B \hat{T}}{\eta}\ , \tag{1.6}$$

where k_B is the Boltzmann's constant, $\hat{T}$ is the absolute temperature, and η is the phenomenological friction coefficient. For a sphere of hydrodynamic radius r_h immersed in a solvent of kinematic viscosity ν and density ρ

$$\eta = 6\pi\, \nu\, \rho\, r_h\ . \tag{1.7}$$

Equation (1.7) corresponds to stick boundary conditions between the solute and solvent. May no stickiness be applied between the solvent and the solute—slip boundary conditions—the factor 6π in equation (1.7) would be replaced by 4π. For nonspherical shapes, the friction coefficient is multiplied by a shape factor greater than 1.

Briefly, the displacements of free Brownian particles ought to exhibit a Gaussian distribution whose variance is proportional to time with a coefficient that involves the temperature and the friction coefficient. This

statement (1.4) is the standard fundamental point when inquiring into the diffusion of Brownian particles. Free Brownian particles thus spread isotropically over space without a privileged direction at a constant time rate.

It ought to be noted that the diffusion equation (1.1) is a special case of the Fokker–Planck equation, which describes stochastic processes in which the system has a continuous sample path. In this case, it means that the particles' trajectories can be described by continuous time random functions. This corollary leads to consider the possibility of describing the dynamics of the system in some direct probabilistic way, so that the path of a particle would be described by a stochastic differential equation [Chandrasekhar, 1949]. This procedure was initiated by Paul Langevin [Langevin, 1908], bringing on the so–called Langevin equation, that is advantageous in many respects as it is argued in the following section.

1.2.2. Linear potentials: transport and the Langevin equation

Single–particle experiments [Greenleaf et al., 2007] have given rise to a novel paradigm in the study of Brownian particles for the trajectories of individual particles can be accessed. These techniques have a broad application, for example in investigations of genetic trafficking [Babcock et al., 2004] in and out of the cell nucleus; indeed, Figure 1.4 includes a series of images of the mRNA motion within a living cell [Golding and Cox, 2006]. Einstein's theory on Brownian motion brings about a probability density function, from which seeking single particle trajectories might be a demanding job. Nevertheless, Langevin equations implement Newtonian dynamics to describe Brownian motion by assuming that the influence of the surrounding medium can be split up in two parts [Chandrasekhar, 1949]: a systematic part $-\eta\hat{\boldsymbol{v}}$, the dynamic friction; and a fluctuating part $\hat{\xi}(\hat{t})$ that comes from thermal motion—both contributions are considered isotropic—. Hence, the dynamic equation [Langevin, 1908] for the velocity of a Brownian

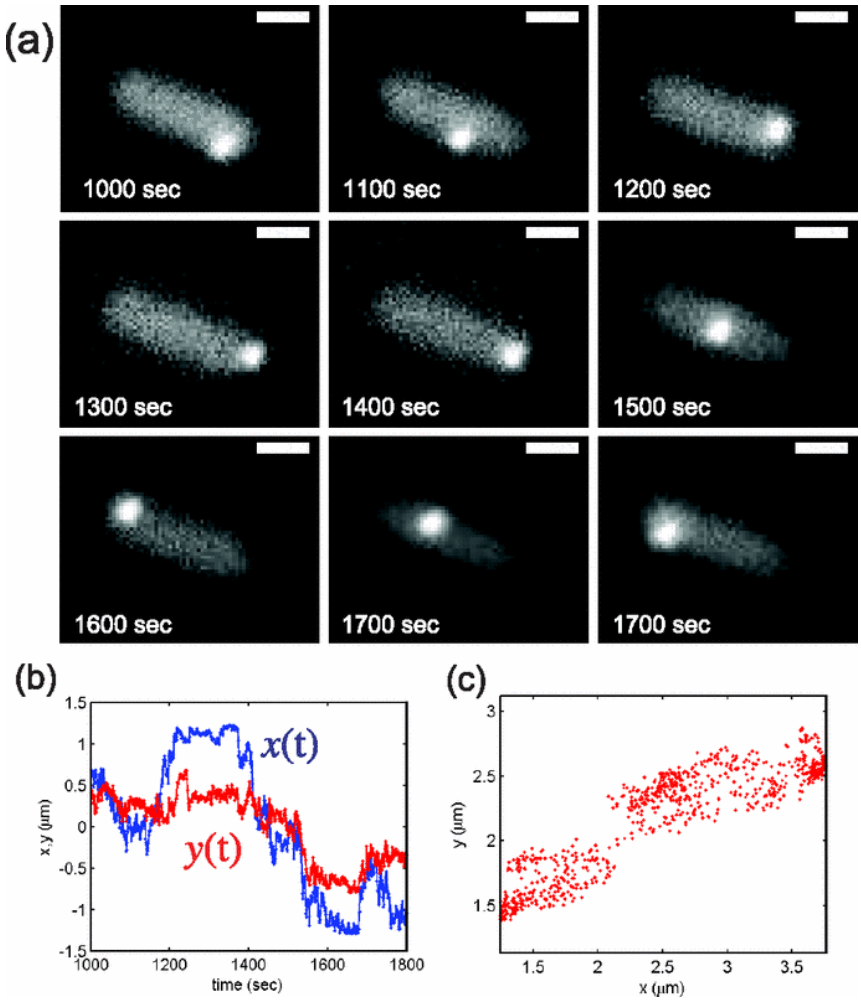

Figure 1.4 – Obtained from [Golding and Cox, 2006]. Single particle tracking. Motion of a tagged RNA molecule inside an *E. coli* cell. (a) Series of epifluorescent images of the mRNA—bright spot—within the cell—grey oval—. Scale bar = 100 μm. (b) x and y particle position during the time covered in (a) for axis chosen arbitrarily. (c) Cloud of particle location corresponding to the data in (a) and (b).

particle of mass m is

$$m\frac{d\hat{\boldsymbol{v}}}{d\hat{t}} = -\eta\hat{\boldsymbol{v}} + \hat{\xi}(\hat{t}) \ , \tag{1.8}$$

and so every individual trajectory of any Brownian particle can be readily obtained by its integration. The fluctuating force $\hat{\xi}(\hat{t})$ is characterized completely by the only non–vanishing cumulant—it has zero mean $\langle\hat{\xi}(\hat{t})\rangle = 0$ indeed—[Ornstein, 1919],

$$\langle\hat{\xi}_i(\hat{t})\,\hat{\xi}_j(\hat{t}')\rangle = 2k_B\hat{T}\,\eta\,\delta_{ij}\,\delta(\hat{t}-\hat{t}') \ , \tag{1.9}$$

where $\hat{\xi}_i(\hat{t})$ are the Cartesian components of the random force, that are hence Gaussian distributed and independent for different times. It ought to be noted that the correlation (1.9) at equal times is dictated by the fluctuation–dissipation theorem [Callen and Welton, 1951; Kubo, 1957; Kubo et al., 1991]. The delta–correlation in the temporal domain translates to white noise for the corresponding power spectral density is independent of the frequency. In terms of physical implications, the fluctuation dissipation theorem is a consequence of causality, microscopic reversibility and thermodynamics close to equilibrium.

The stationary velocity distribution function may be obtained from the Fourier transform of the characteristic function, that is built up by the moments $\langle\hat{v}^{2n}\rangle$. The corresponding stationary velocity distribution of the free Brownian motion described by Equations (1.8) and (1.9) is

$$W(\hat{v}) = \sqrt{\frac{m}{2\pi k_B\hat{T}}}\,\exp\left(-\frac{m\hat{v}^2}{2k_B\hat{T}}\right) \ , \tag{1.10}$$

hence it is the Maxwell distribution.

Langevin equations point to a second advantage compared with the Fokker–Planck approach; incorporating any supplementary force to Equation (1.8) is effortless indeed. Restricting by now to those forces that derive from a linear potential—i.e. constant forces, $\hat{\boldsymbol{F}} = -\nabla\hat{V}(\hat{\boldsymbol{r}})$, $\hat{V}(\hat{\boldsymbol{r}}) \propto \hat{\boldsymbol{r}}$—, the corresponding Langevin equation is

$$m\frac{d\hat{\boldsymbol{v}}}{d\hat{t}} = -\eta\hat{\boldsymbol{v}} + \hat{\boldsymbol{F}} + \hat{\xi}(\hat{t}) \ , \tag{1.11}$$

that for the one dimensional case leads to the following solution

$$\hat{v}(\hat{t}) = v_0\, e^{-\eta\hat{t}/m} + \frac{\hat{F}}{\eta}\,(1 - e^{-\eta\hat{t}/m}) + \frac{1}{m}\int_0^{\hat{t}} e^{-\eta(\hat{t}-\hat{t}')/m}\,\hat{\xi}(\hat{t}')\,\mathrm{d}\hat{t}' \ . \qquad (1.12)$$

The mean velocity in the stationary limit is thus a constant $\langle\hat{v}(\hat{t})\rangle = \hat{F}/\eta$, and so the mean displacement is to scale linearly with time $\langle\Delta\hat{r}(\hat{t})\rangle \propto \hat{t}$; this relation accounts for the normal transport. Back to the general Euclidean d–space, the velocity along any direction $\hat{\boldsymbol{u}}$ reads

$$\langle\hat{v}_{\hat{\boldsymbol{u}}}\rangle = \langle\hat{\boldsymbol{v}}\rangle \cdot \hat{\boldsymbol{u}} \ , \qquad (1.13)$$

and so the mean displacement along $\hat{\boldsymbol{u}}$ is

$$\langle\Delta\hat{r}_{\hat{\boldsymbol{u}}}(\hat{t})\rangle \propto \hat{t} \ . \qquad (1.14)$$

The trajectory to be obtained would display a bias towards the force's direction. Together with Equation (1.4), Equation (1.14) makes up the primary framework of transport and diffusion of Brownian particles. Transport is lead by deterministic Newtonian dynamics, whereas diffusion is a trace of the random motion caused by thermal fluctuations as a primer source of disorder; Figure 1.5 illustrates both effects.

The average energy of a Brownian particle in $1 - d$ is

$$\langle E\rangle = \frac{1}{2}\,m\,\langle[\hat{v}(\hat{t})]^2\rangle = \frac{1}{2}\,k_B\hat{T} \ , \qquad (1.15)$$

where $\langle[\hat{v}(\hat{t})]^2\rangle$ is computed from the average steady correlation function of the velocity, and brackets $\langle\ldots\rangle$ denote time averages. Equation (1.15) is indeed the equipartition law of classical statistical mechanics that motivates the choice for the white noise's intensity (1.9).

1.2.3. Anomalous regimes

The phenomena of anomalous or complex transport refers to the dynamics where the diffusive regime—characterized by Equations (1.4) and (1.14)—is not visible even on time scales that exceed by many orders of magnitude

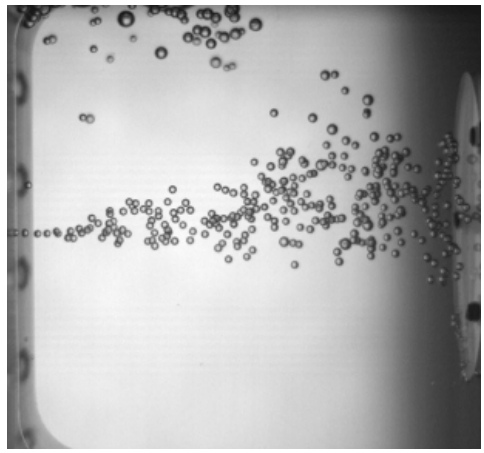

Figure 1.5 – Obtained from [Bitlloch et al., 2015]. Transport and diffusion. Snapshot of an experiment of slug bubble injection after 2.5 seconds of microgravity. Bubbles are injected from the left side and move towards the right, yet they also disperse around the jet direction.

the picosecond regime—the time scale of the liquid dynamics, and so of the random kicks that give rise to Brownian movement—. Transport and diffusion anomalous regimes [Bouchaud and Georges, 1990] are conventionally traced by a non–linear growth of either the mean position or the mean square displacement. Typically, the mean position exhibits a power–law

$$\langle \Delta \hat{r}_{\hat{\boldsymbol{u}}}(\hat{t}) \rangle \propto \hat{t}^{\alpha} \ ; \tag{1.16}$$

may it be sub–linear, $0 < \alpha < 1$, this behavior is referred to as subtransport. When exponent $\alpha = 1$ it renders normal transport—Equation (1.14) is retrieved indeed—, and $\alpha > 1$ gives rise to supertransport. Concerning the mean square displacement, it may exhibit a power–law as well

$$\langle \Delta \hat{r}^2_{\hat{\boldsymbol{u}}}(\hat{t}) \rangle \propto \hat{t}^{\beta}, \tag{1.17}$$

leading to subdiffusion for $\beta < 1$ and to superdiffusion for $\beta > 1$, yet it may as well display particle transport that is nondispersive ($\beta = 0$) or coherent over long time intervals [Lindenberg et al., 2007].

In order to dig into the transport and diffusion anomalies, it is often employed the mean velocity and diffusion coefficients, which are calculated

with the trajectories driven by an ensemble of independent particles,

$$\langle \hat{v}_{\hat{\boldsymbol{u}}}(\hat{t}) \rangle = \frac{\langle \Delta \hat{r}_{\hat{\boldsymbol{u}}}(\hat{t}) \rangle}{\hat{t}}\,, \quad \hat{D}_{\hat{\boldsymbol{u}}}(\hat{t}) = \frac{\langle \Delta \hat{r}^2_{\hat{\boldsymbol{u}}}(\hat{t}) \rangle}{2\hat{t}}\,, \tag{1.18}$$

the brackets indicate an ensemble average, and subindex $\hat{\boldsymbol{u}}$ labels any direction.

Anomalous diffusion means that the central–limit theorem does not apply at the time scales of interest; the increments along the particle's trajectory $\Delta\hat{\boldsymbol{r}}(\hat{t}) = \hat{\boldsymbol{r}}(\hat{t}+\hat{t}') - \hat{\boldsymbol{r}}(\hat{t}')$ are not distributed independently, they manifest persistent correlations that are hidden in the dynamics of meso- or macroscopic time scales. A simple violation of the central–limit theorem in some intermediate time window ought to be discerned from the mechanisms leading to steady anomalous diffusion. The first scenario may be due to slow dynamic processes that are likely to spoil the central–limit theorem on these scales, yet ultimately Fickian diffusion resumes. This situation is usually engendered by media with constituents of different sizes or by soft interactions, e. g., polymers. Hence the mean square displacement displays a crossover from some short–time motion to long–time diffusion. Since the crossover can span over several decades due to a series of slow processes occurring in the medium, fits by power–laws are often a satisfactory description. The effect of different time scale processes in diffusion is carefully discussed in [Katsumi et al., 2005] supported with experimental evidences. Transient anomalous diffusion has been reported for the movement of telomeres in the nucleus of mammalian cells [Bronstein et al., 2009], (Fig. 1.6). In the second case—steady anomalous diffusion—, the correlations in the increments decay slowly and the anomalous regime's extent can last arbitrarily by tuning suitable control parameters. Steady subdiffusive motion has been observed for intracellular transport processes in living cells [Caspi et al., 2000; Wachsmuth et al., 2000; Tolić-Nørrelykke et al., 2004; Golding and Cox, 2006; Weber et al., 2010; Jeon et al., 2011; Tabei et al., 2013], see Figure 1.4, in cell membranes [Horton et al., 2010], and in hair–bundle—a mechanosensitive organelle in the ear's apparatus—motion [Kozlov et al., 2012], among others; superdiffusion is displayed by *in vitro* [Köhler et al., 2011; Douglass et al., 2012] and *in vivo* [Lau et al.,

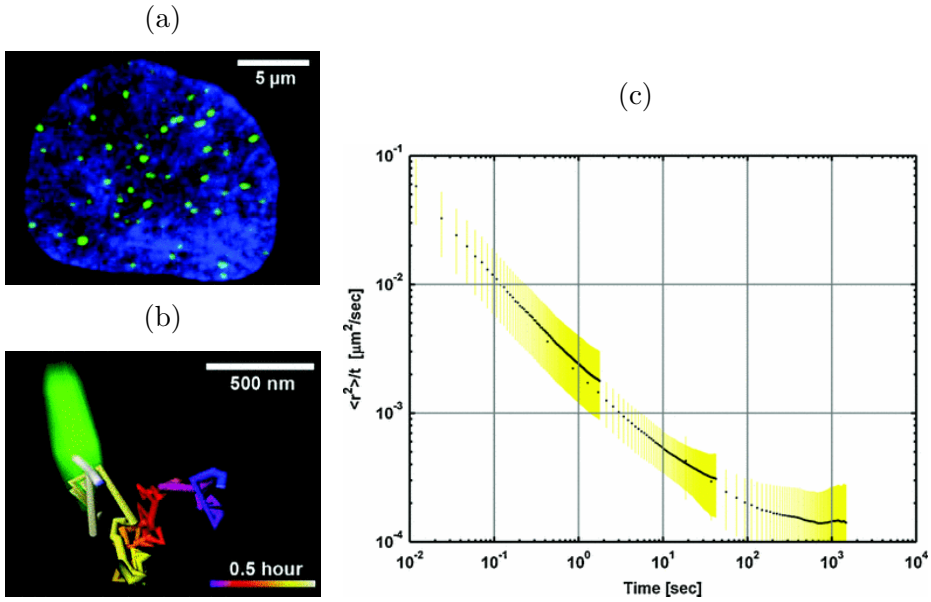

Figure 1.6 – Adapted from [Bronstein et al., 2009]. Transient anomalous diffusion. The measure of individual trajectories of telomeres in the nucleus of eukaryotic cells brings about subdiffusion at short times and long time normal diffusion. (a) Projection image of a $3-d$ data. Typical distribution of telomeres—bright spots, labelled by green fluorescent protein—in the stained nucleus of living human cells—U2OS osteosarcoma cell line—. (b) $3-d$ motion of a telomere—bright object—as measured over $2 \cdot 10^3$ s. (c) Log-log plot of $\langle \hat{r}^2 \rangle / \hat{t}$ *vs* $\hat{t}$ of the recorded trajectories. The diffusion is anomalous up to ≈ 100 s where it changes to normal diffusion.

2003; Bursac et al., 2005; Bruno et al., 2009] experiments involving active media. Anomalous transport is often prompted by embedding a non–linear potential to the Langevin equation and hence they are thoroughly discussed in the following section.

1.3. Non-linear potentials

The motion of non–interacting Brownian particles under a linear potential ($\hat{\boldsymbol{F}}$ is constant) brings about a well established outcome that is in agreement with the theory of Einstein on the Brownian movement [Einstein, 1905]. However, may a Brownian particle undergo a non–linear potential, then not only the Stokes–Einstein relation (1.6) might not be

fulfilled [Blickle et al., 2007; Sancho and Lacasta, 2010], but neither the transport (1.14) nor the diffusion (1.4) regular definitions might hold [Sancho et al., 2004; Lindenberg et al., 2007; Sancho and Lacasta, 2010]. The origin of all these deviations from Einstein's results might be ascribed to a very fundamental process that underlies the phenomena of Brownian movement undergoing any non–linear potential: the barrier crossing by thermal activation. A non–linear potential accounts for a landscape in which there are some space locations—barriers—that are energetically unfavorable to the particles, so they have to deplete a great deal of kinematic energy—provided partially or entirely by thermal fluctuations—in case they attempt to move into these positions. Therefore, the presence of energetic barriers ought to affect the probability density function $P(\hat{\boldsymbol{r}}, \hat{t})$ [Condamin et al., 2008]. The spatial arrangement, the length scale, the energy height, and the time behavior of the barriers might be critical for the transport and diffusion regimes to emerge as it will be remarked later on. By now, the elementary process of crossing a barrier for a particle driven by thermal energy is considered, (Fig. 1.7).

1.3.1. Diffusion over a barrier

The problem of thermal noise–assisted escape of a particle bound in a potential well was addressed by Hans Kramers [Kramers, 1940; Tucker, 2000] in 1940. Using a diffusion–equation approach, devising a specific Fokker–Planck equation—now called Kramers–Klein equation—, and assuming that the barrier height is much larger than the thermal energy $k_B\hat{T}$, the inverse of the escape rate k is—details of the derivation can be found in [Risken, 1989]—

$$\frac{1}{k} = \frac{1}{k_B\hat{T}} \int_{x_1}^{x_2} e^{-\hat{V}(\hat{x})/k_B\hat{T}}\, \mathrm{d}\hat{x} \int_{x_{min}}^{x_3} e^{\hat{V}(\hat{x})/k_B\hat{T}}\, \mathrm{d}\hat{x}\ . \tag{1.19}$$

By expanding the potential around x_{min} and x_{max} and extending the integration boundaries in both integrals to $\pm\infty$, it is obtained the well–

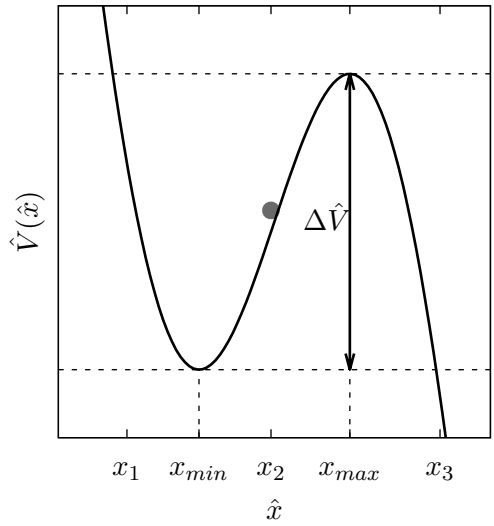

Figure 1.7 – Sketch of the potential well for calculating the escape rate of a Brownian particle.

known Kramers' escape rate

$$k_K = \frac{\sqrt{\hat{V}''(x_{min})\,|\hat{V}''(x_{max})|}}{2\pi}\,\exp\left(\frac{-\Delta\hat{V}}{k_B\hat{T}}\right)\,, \tag{1.20}$$

where $\hat{V}''$ is the second derivative of the potential evaluated at x_{min} and x_{max}, and $\Delta\hat{V} \equiv \hat{V}(x_{max}) - \hat{V}(x_{min})$. The Kramers' escape rate (1.20) leads to a characteristic time scale for the particles to surmount a barrier by thermal fluctuations $\hat{t}_K = k_K^{-1}$.

1.3.2. Periodic landscape

The simplest construction for a landscape of barriers would be to consider a periodic arrangement of equally sized barriers of the same height. A possible formulation of such a potential might be through trigonometric

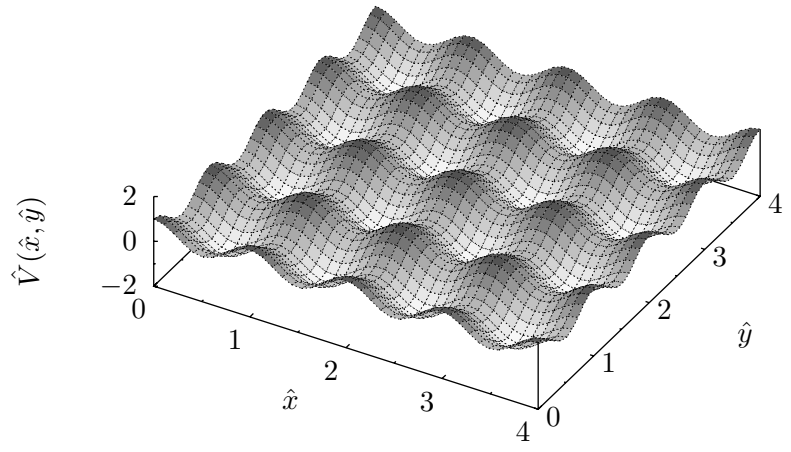

Figure 1.8 – $2-d$ periodic potential $\hat{V}(\hat{x},\hat{y})$ obtained by Eq. (1.21) with $V_0 = 1$ and $\lambda_p = 1$.

functions,

$$\hat{V}(\hat{x}) = \frac{V_0}{2}\cos\left(\frac{2\pi\hat{x}}{\lambda_p}\right), \quad \hat{V}(\hat{x},\hat{y}) = \frac{V_0}{2}\left[\cos\left(\frac{2\pi\hat{x}}{\lambda_p}\right) + \cos\left(\frac{2\pi\hat{y}}{\lambda_p}\right)\right], \tag{1.21}$$

for one or two dimensions (Fig. 1.8).

May a constant force be applied supplementary, the potential will tilt slightly towards the force's direction. When this tilting force is as strong as $\hat{F}_c = \pi V_0/\lambda_p$—called critical force—, then the periodic landscape will exhibit saddle points instead of the minima. Hence, transport regimes are expected to arrange according to $\hat{F}/\hat{F}_c$. To one hand, for $\hat{F}/\hat{F}_c \ll 1$ particles would remain at the minima for large sojourn times until they may escape by thermal fluctuations exhibiting a characteristic escape time $\hat{t}_K$, according to the Kramers' theory. In this scenario, particles are said to be in the "locked" state. To the other, when $\hat{F}/\hat{F}_c \gg 1$ potential wells disappear, and so particles move freely in a flat landscape; the mean velocity saturates to the free particle value $\langle\hat{v}(\hat{t})\rangle = \hat{F}/\eta$ (1.12)—already discussed

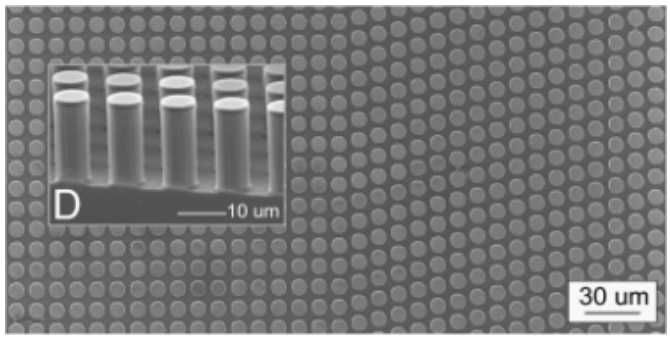

Figure 1.9 – Obtained from [Morton et al., 2008]. Periodic potentials. Top view scanning electron micrograph (SEM) of a microfabricated post array. Inset: Cross–sectional SEM image showing individual posts made of Polydimethylsiloxane.

in Section 1.2.1—leading to the so–called "running" state. There is nevertheless an intermediate regime of forces slightly beneath the critical value in which the "locked" and "running" states combine, as it has been noticed for a single colloidal sphere under a periodically modulated optical vortex trap [Lee and Grier, 2006]. In this conditions, different phenomena, such as giant diffusion [Colet et al., 1989; Lindner et al., 2001; Reimann et al., 2001; Lindenberg et al., 2005; Lee and Grier, 2006] and dispersionless transport [Lindenberg et al., 2007], come to light.

Finally, it ought to be enlightened that periodic potentials do have practical applications. Particularly, they are often implemented in sorting [Sancho et al., 2005] experiments of mesoscopic objects—such as colloids and cells—through arrays of optical traps [Korda et al., 2002; MacDonald et al., 2003; Grier, 2003], and DNA molecules [Huang et al., 2004] and blood cells [Morton et al., 2008] in microfabricated arrays, (Fig. 1.9).

1.3.3. Disorder

After the simple construction of a periodic field has been discussed, in which potential barriers were aligned periodically along space, the more complex scenario of disordered media is considered. A disordered landscape is a potential whose attributes—at least one of them—are not periodic. The

present section is devoted to the particular case in which neither the space location nor the barriers' height follow a regular behavior; potential's arrangement exhibits instead some degree of randomness which is controlled through a statistical approach. The generation of disorders is profoundly reviewed in the book of J. García-Ojalvo and J. M. Sancho [García-Ojalvo and Sancho, 1999].

Disorder generation is most often carried out by a random variate with a Gaussian distribution, and so it is assumed all along this thesis. May the disorder be static—dynamic disorders are considered in the following section—, every random variable has a precise space location and exhibits some dependency on the surrounding disorder values that is controlled by the correlation function

$$\langle \hat{V}(\hat{\boldsymbol{r}})\, \hat{V}(\hat{\boldsymbol{r}}') \rangle = g\left(\frac{\hat{\boldsymbol{r}} - \hat{\boldsymbol{r}}'}{\lambda_r} \right) , \tag{1.22}$$

λ_r is the disorder's correlation length. Figure 1.10 depicts an example of a Gaussian disorder with a prescribed correlation function. When a disordered potential $\hat{V}(\hat{\boldsymbol{r}})$ is incorporated to the Langevin equation

$$m\frac{d\hat{\boldsymbol{v}}}{d\hat{t}} = -\eta\hat{\boldsymbol{v}} + \hat{\boldsymbol{F}} - \nabla\hat{V}(\hat{\boldsymbol{r}}) + \hat{\xi}(\hat{t}) , \tag{1.23}$$

numerical integration ought to be carried out by specific algorithms that are detailed in Chapter 7.

The interest in studying Brownian motion in disordered milieus goes back to the last decades of the XXth century, when emerging experimental techniques in single–molecule measurements [Greenleaf et al., 2007] and increasing computer facilities brought about new insights into the mechanisms that drive molecular movements in disordered media. At the time when those techniques emerged, the main focus was on the effects of the disorder on the diffusion [De Gennes, 1975; Bässler, 1987; Zwanzig, 1988]; afterward, on the mobility [Dunlap et al., 1996] as well as on both [Parris et al., 1997]. The mentioned examples lay within the framework of the Einstein's theory of Brownian motion—the mean square displacement scales as the square root of time—. However, a more recent upsurge of

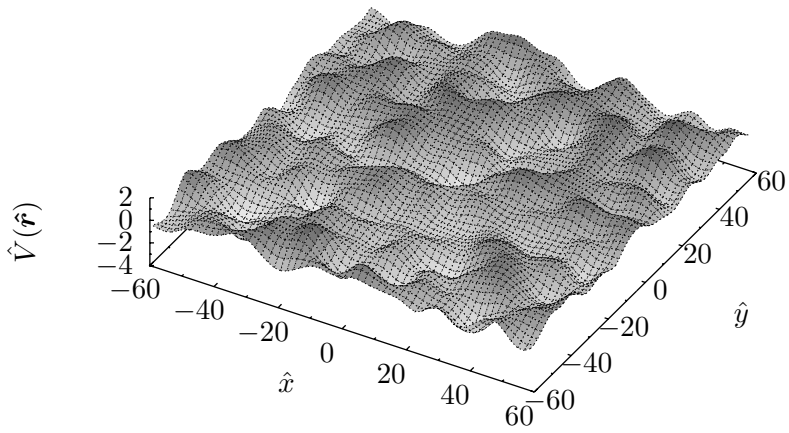

Figure 1.10 – $2-d$ Gaussian random potential $\hat{V}(\hat{\boldsymbol{r}})$ with spatial correlation $g(|\hat{\boldsymbol{r}} - \hat{\boldsymbol{r}}'|/\lambda_r) = V_0^2 \ \frac{1}{2} \ e^{-(\hat{\boldsymbol{r}}-\hat{\boldsymbol{r}}')^2/2\lambda_r^2}$; $V_0 = 1$ and $\lambda_r = 5$. All the physical quantities are in arbitrary units.

interest in the Brownian movement in random landscapes came about due to the observation of a variety of qualitative anomalies—outcome deviating from Einstein's predictions—such as non–diffusive regimes [Bouchaud and Georges, 1990] and other "abnormal" behaviors [Sancho and Lacasta, 2010]. Several theoretical [Reimann and Eichhorn, 2008; Khoury et al., 2009; Denisov et al., 2010], numerical [Romero and Sancho, 1998; Khoury et al., 2009, 2011; Lindenberg et al., 2012; Hanes and Egelhaaf, 2012; Evers et al., 2013] and experimental studies [Evers et al., 2013; Hanes et al., 2013] have lately shed light on the foundations of anomalous Brownian movement in disordered milieus.

From the experimental point of view, spatial random potentials may be a reliable approach for describing diffusion of adsorbing particles at solid surfaces [Schunack et al., 2002; Xu et al., 2011; De Wijn, 2011; Skaug et al., 2013], of proteins along DNA molecules [Slutsky et al., 2004; Goychuk and Kharchenko, 2014], and trafficking in porous media [Dickson et al., 1996;

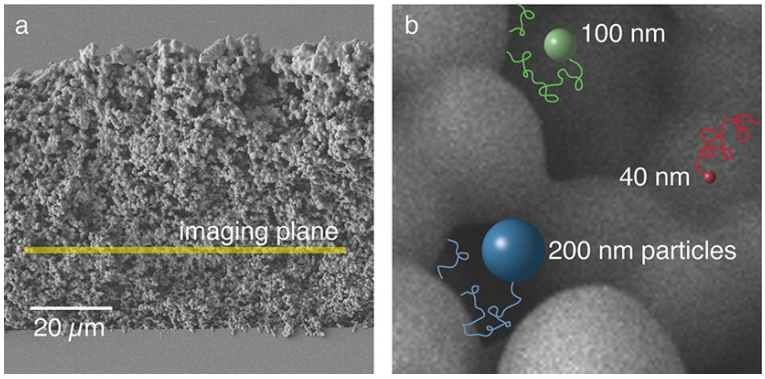

Figure 1.11 – Obtained from [Skaug et al., 2015]. Disordered solid medium. (a) Scanning electron microscopy (SEM) image of a porous media. (b) Zoom image of the porous sample including the illustration of possible fluorescent tracer particles.

Skaug et al., 2015] (Fig. 1.11), among others.

1.3.4. Spatiotemporal disorder

Likewise the values of a spatial disorder change from one point to another, disorder's components may as well evolve non deterministically in time. In such case, the process will exhibit a spatiotemporal correlation function,

$$\langle \hat{V}(\hat{\boldsymbol{r}}, \hat{t})\, \hat{V}(\hat{\boldsymbol{r}}', \hat{t}') \rangle = g(\hat{\boldsymbol{r}} - \hat{\boldsymbol{r}}', \hat{t} - \hat{t}')\,. \tag{1.24}$$

Gaussian spatiotemporal disorders, or also called colored noises, can be generated by a linear reaction–diffusion Langevin equation with Gaussian white noise [García-Ojalvo et al., 1992]. Details on the algorithm are detailed in Chapter 7.

There is a wealth of physical and biological systems and processes that involve inherent spatiotemporal disorders. In particular, soft matter systems comprising objects that exhibit non–thermally driven motion can be accounted spatiotemporal disorders; among others, the cell cytoplasm [Dix and Verkman, 2008; Trovato and Tozzini, 2014], the cell membrane [Dix and Verkman, 2008], and monolayers of colonies of gliding bacteria [Baskaran and Marchetti, 2009; Peruani et al., 2012] (Fig. 1.12). These systems are

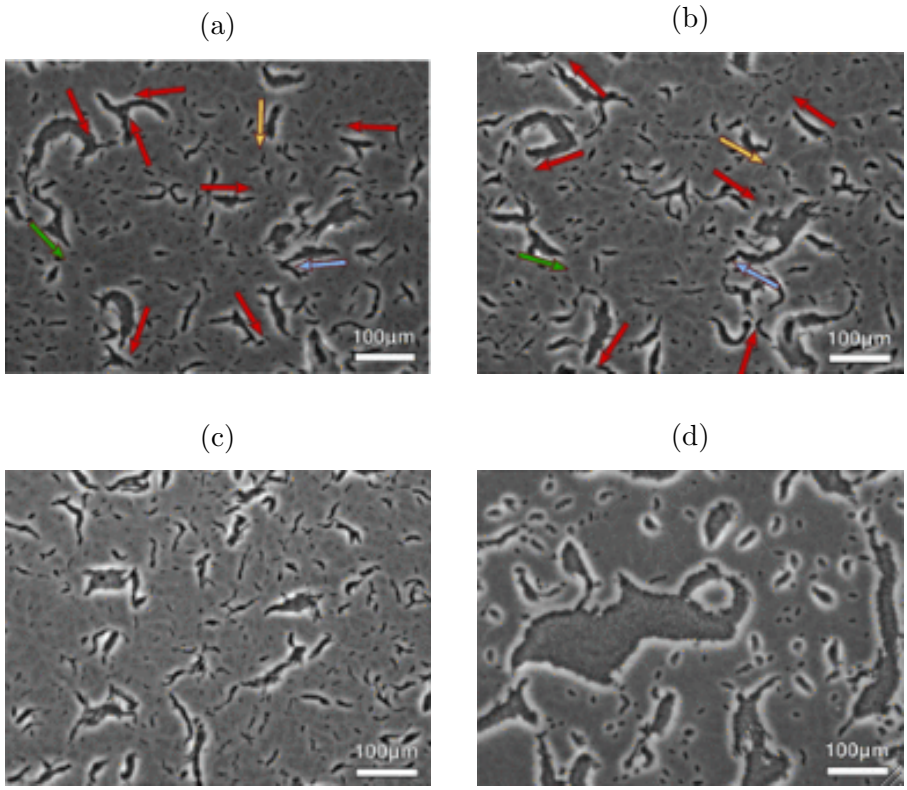

Figure 1.12 – Adapted from [Peruani et al., 2012]. Spatiotemporal disorder. Clustering of SA2407 cells. (a),(b) Myxobacterial cells form moving clusters. Arrows indicate the direction of motion of the moving clusters; the time interval between snapshots is 15 min. (c),(d) The dynamical clustering process reaches a steady state that strongly depends on cell density. Typical snapshots corresponding to packing fractions of 0.1 in (c), and 0.24 in (d).

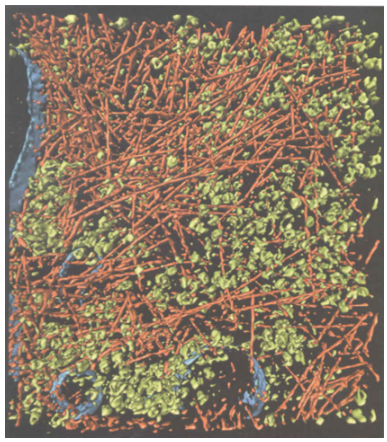

Figure 1.13 – Obtained from [Medalia et al., 2002]. Macromolecular crowding. Three–dimensional reconstruction from a peripherial region of a vitrified *Dictyostelium* cell imaged by conventional transmission electron micrograph. It concerns a volume of 815 nm by 870 nm by 97 nm. Actin filaments are displayed in reddish; other macromolecular complexes, mostly ribosomes, in green; and membranes in blue.

examples of active matter media, whose dynamics may as well be described by hydrodynamic equations for a macroscopic field [Basu et al., 2008; Sarkar and Basu, 2011; Marchetti et al., 2013]. There must be a continuous supply of energy in order to perpetuate a spatiotemporal disorder; equilibrium systems do not consume energy continuously, their dynamics is characterized by the fluctuation–dissipation theorem and describe time evolution of fluctuations around the minimum free energy or maximum entropy states instead. For example, cells and the actin cytoskeleton are driven out of equilibrium by the ATP field.

Soft–matter media are often subjected to macromolecular crowding, that is, the exclusion of solvent volume resulting from the presence of a large number of solute particles, such as macromolecules, organelles, polymeric networks, colloids and polymers [Höfling and Franosch, 2013]. The cell cytoplasm is a ubiquitous example of macromolecular crowding: the total concentration of macromolecules inside the cell—up to 400 g/l—means that between the 5% and 40% of the total volume is physically occupied by these molecules [Ellis and Minton, 2003], (Fig. 1.13). The effects of

crowded environments on Brownian motion have been explored by means of fluorescent correlation spectroscopy of inert tracer particles in the cytoplasm of living cells [Weiss et al., 2004], and by single particle tracking experiments of nanometer–sized beads in artificial—dextran and sucrose solutions—crowded fluids [Weiss, 2013].

1.4. Infradamped and overdamped: dimensionless approaches

A very primary classification of the problem regarding particles undergoing thermal fluctuations and a supplementary random force concerns the concomitant viscosity to which they are subjected. A low Reynolds number means that viscosity overwhelms the particles' inertia [Purcell, 1977], and so the acceleration can be disregarded because the velocity equilibrates quickly [Risken, 1989; Parris et al., 1997; Reimann et al., 2001; Reimann and Eichhorn, 2008]. This scenario mostly applies to biological [Bickel, 2006] and colloidal [Tierno et al., 2010; Démery et al., 2014] systems. In the opposite—i.e. low friction—inertial forces ought to be taken into account [Risken, 1989; Sancho et al., 2004; Lindenberg et al., 2007; Marchenko and Marchenko, 2012; Marchenko et al., 2014] and thus the velocity can exhibit a non–Maxwellian distribution; examples of this domain are found in solid state systems [Adelman and Doll, 1977; Poirier and Plyant, 1996; Yokoyama et al., 2001; Ho, 2002; Goohpattader et al., 2009; De Wijn, 2011]. Chapters 4 and 5 are devoted respectively to the study of Brownian motion in each of the damping scenarios. The following sections inquire into the Langevin equations to rule in every approach when a non–linear random potential is considered, and how they can be scaled.

1.4.1. Underdamped approach

The scenario of low friction is accounted by the Langevin equation (1.23), including inertial terms. May the length scale λ_0 and the energy scale V_0 be employed, a proper choice for the characteristic time scale would be

$\tau_0 = \lambda_0 (m/V_0)^{1/2}$. Accordingly, the scaled dimensionless space $\boldsymbol{r}$ and time t are

$$\boldsymbol{r} = \frac{\hat{\boldsymbol{r}}}{\lambda_0} \ , \quad t = \frac{\hat{t}}{\tau_0} \ ; \tag{1.25}$$

for the rest of scaled dimensionless physical quantities,

$$\begin{aligned} V(\boldsymbol{r},t) = \frac{\hat{V}(\boldsymbol{r},t)}{V_0} \ , \quad \boldsymbol{F} = \frac{\lambda_0}{V_0}\, \hat{\boldsymbol{F}} \ , \quad T = \frac{k_B \hat{T}}{V_0} \ , \\ \xi(t) = \frac{\lambda_0}{V_0}\, \hat{\xi}(t) \ , \quad \gamma = \frac{\lambda_0}{(mV_0)^{1/2}}\, \eta \ . \end{aligned} \tag{1.26}$$

The resulting scaled underdamped Langevin equation is therefore

$$\frac{d\boldsymbol{v}}{dt} = -\gamma \boldsymbol{v} + \boldsymbol{F} - \nabla V(\boldsymbol{r},t) + \xi(t) \ , \tag{1.27}$$

and the noise's correlation reads

$$\langle \xi_i(t)\, \xi_j(t') \rangle = 2T\, \gamma\, \delta_{ij}\, \delta(t-t') \ . \tag{1.28}$$

1.4.2. Overdamped approach

The overdamped version of the Langevin equation (1.23) stems from the consideration that the inertial term can be vanished ($d\hat{\boldsymbol{v}}/d\hat{t} = 0$), and so the stochastic differential equation to govern the trajectory of the Brownian particle is—may a multiplicative noise be considered, in which the temperature could depend upon space, this assumption would fail—

$$\eta \hat{\boldsymbol{v}} = \hat{\boldsymbol{F}} - \nabla \hat{V}(\hat{\boldsymbol{r}},\hat{t}) + \hat{\xi}(\hat{t}) \ . \tag{1.29}$$

The former scaled dimensionless physical quantities (1.25) and (1.26) hold, yet the friction parameter η is not defined. May the time scale be $\tau_0 = \eta \lambda_0^2 / V_0$, the scaled overdamped Langevin equation is

$$\boldsymbol{v} = \boldsymbol{F} - \nabla V(\boldsymbol{r},t) + \xi(t) \ . \tag{1.30}$$

The fluctuation–dissipation theorem then reads

$$\langle \xi_i(t)\, \xi_j(t) \rangle = 2T\, \delta_{ij}\, \delta(t-t') \ . \tag{1.31}$$

It ought to be enlightened that the main difference between the overdamped and the underdamped approach resides in the scaling times, $\tau_0 = \eta\lambda_0^2/V_0$ for the overdamped, $\tau_0 = \lambda_0(m/V_0)^{1/2}$ for the underdamped. Hence, in order to compare the outcome of both approaches, time ought to be adjusted. The relationship between the scaled time in the underdamped and the overdamped approaches is thus mandatory. May the underdamped time scale $\tau_0 = \lambda_0(m/V_0)^{1/2}$ be employed to scale Eq. (1.29), the resulting scaled Langevin equation would be—subindexes are employed for the scaled quantities that differ from the ones in Eq. (1.30)—

$$\boldsymbol{v}_u = \frac{1}{\gamma}\left[\boldsymbol{F} - \nabla V(\boldsymbol{r}, t_u) + \xi(t_u)\right] \ , \tag{1.32}$$

and the white noise correlation would be equivalent to (1.28). Therefore, bearing in mind that the scaled space is the same for both approaches,

$$\frac{t_u}{t} = \gamma \ , \quad \boldsymbol{v} = \gamma\, \boldsymbol{v}_u \ , \quad D = \gamma\, D_u \ , \tag{1.33}$$

where the diffusion coefficients are computed according to (1.18). Briefly, time ought to be adjusted by a factor γ—the scaled friction parameter—in order to compare the results to be obtained with the proposed scaled Langevin equations (1.27) and (1.30).

Up to now, the key theoretical concepts related to the subject of the present thesis have been discussed. To end this first part, the following Chapter (Chap. 2) states the line of argument of the thesis, and summarizes the leading results and conclusions of each case of study considered within the framework here detailed.

CHAPTER 2

The thesis

The present thesis aims at exploring the emerging phenomena regarding transport and diffusion to exhibit non–interacting Brownian particles being pulled by an external constant force in a disordered medium. The method of choice are numerical simulations of the classical Langevin equation in the overdamped and in the underdamped limit. In order to carry out a robust study, the scaled stochastic differential equations are considered, so as to attain widespread results that may accommodate to a myriad of specific circumstances. It is of particular interest to find out a reduced set of those leading parameters to rule the physical behavior of the system. May the chief parameters be identified, they are tuned so as to survey their impact on the transport and diffusion features.

To grasp the influence of the disorder's attributes—either spatial or temporal—on Brownian motion is the main focus of the thesis. Further, the outcome sheds light into the physical foundations of the anomalous transport and diffusion of non–interacting thermally driven particles on disordered biased landscapes. Complementarily, some refinements are made on the models and algorithms employed to numerically simulate the stochastic differential equations concerning each scenario.

2.1. Summary, results and conclusions

The scheme of the second part of this thesis is arranged in different chapters, each devoted to a particular case of study. The main results obtained and the leading conclusions are also summarized in the following guide to the thesis.

2.1.1. Brownian Motion in a periodic potential: from underdamping to overdamping

The succeeding Chapter (Chap. 3) comprises a brief study of Brownian motion in a periodic potential concerning different external constant pulling forces and friction coefficients. It constitutes a preliminary stage to the forthcoming chapters (Chapters 4 to 6). The mean velocity and the diffusion coefficients are computed so as to interpret the leading transport features under changing conditions, either concerning the damping—overdamped/underdamped—or the external force—compared to the critical force—. According to the attained outcome, some hypothesis are conjectured for the subsequent explorations in disordered media: transport anomalies—if any—would be only of subtransport type (Sec. 1.2.3) when the disorder is static, enhanced diffusion and superdiffusion are likely to be reached, and anomalous transport and diffusion regimes might be transient in dynamic landscapes.

2.1.2. Transport and diffusion of overdamped Brownian particles in random static potentials

Chapter 4 is devoted to the description of the motion of overdamped Brownian particles in a totally disordered static potential and subject to a constant external force. It presents a numerical study of the anomalies in transport and diffusion in one and in two dimensions. The anomalous

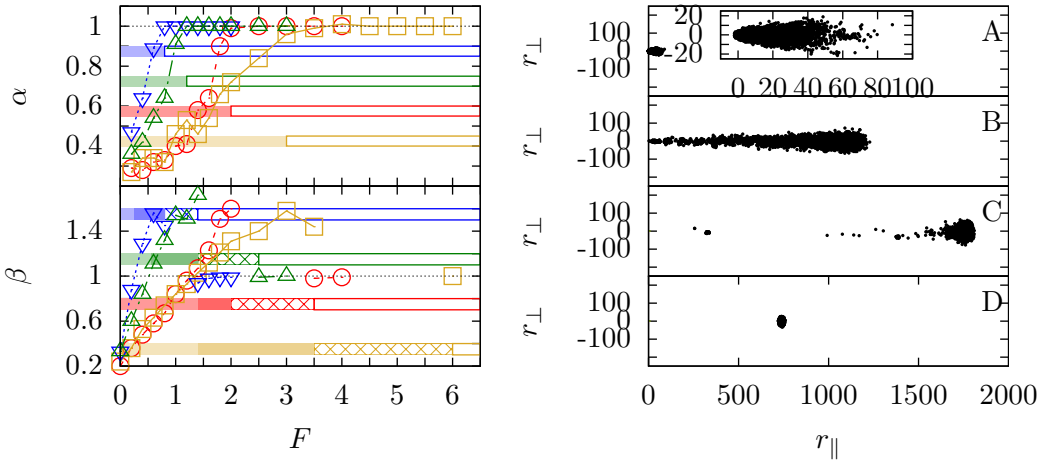

Figure 2.1 – Left panel: Transport—top—and diffusion—bottom—exponents for different distributions of disorder; a Gaussian correlation in red, an exponential in gold, and two power–laws of different exponents in green and blue. Wide horizontal colored bars indicate each dynamical regime, subtransport and subdiffusion in pale colors, superdiffusion in bright colors, uncertain diffusion in patterned bars, and normal transport and diffusion in empty bars. Right panel: Particle positions with respect to their initial conditions at time $t = 1000$ (except for panel (D) that $t = 250$) for different forces $F = 0.6$ (A), 1.5 (B), 2.0 (C), 3.0 (D). Inset: Zoom-in of the cloud of particle positions for the case (A).

regimes are characterized by the time exponents that exhibit the statistical moments of the ensemble of particle trajectories, (Fig. 2.1)–left panel; they are also reviewed through the particle displacement distributions and the clouds of particles—the ensemble's particle positions at different times—, (Fig. 2.1)–right panel.

On the one hand, simulations in $1-d$ static random potentials of different spatial correlations give rise to anomalous transport and diffusion regimes. These anomalies span a range of forces that depends upon the potential's roughness, that can be further associated with an effective correlation length. A larger effective correlation length corresponds to smoother portraits—i.e. with shallower wells—leading to a recovery of regular transport and diffusion at lower force strengths. Indeed, a power–law correlation function brings about a smooth potential in which regular Brownian motion is resumed at weak forces, see Figure 2.1–left panel. On the other, simula-

tions in $2-d$ spaces give rise to a novel representation of the results that is useful to dig into the physical causes of each anomalous regime. Figure 2.1—to the right—shows the cloud of particles for different pulling forces so that each panel stands for a particular type of anomaly: subtransport and subdiffusion (A), normal transport and superdiffusion (B), normal transport and undefined diffusion (C), and normal transport and diffusion (D). This case of study, with the mentioned results and supplementary material, leads to a published paper entitled "*Transport and diffusion of overdamped Brownian particles in random potentials*" [Suñé et al., 2013].

This case of study bears out that the length scale of the roughness of the potentials is an essential parameter in the understanding of the effect of disorder in anomalous regimes. Besides, the shape of the particle density histograms and the particle clouds—the latter only in $2-d$—have been proved to be related to the transport and diffusion anomalies.

2.1.3. Transport and diffusion of underdamped Brownian particles in random static potentials

The analogous scenario for Brownian movement in Chapter 4, yet in the underdamped limit, is handled in Chapter 5. The outcome compares to the overdamped regime and to the results for a periodic potential. Numerical results for the transport and diffusion in one–dimensional landscapes exhibit anomalous regimes—subtransport, subdiffusion, superdiffusion, etc.—(Fig. 2.2)–left panel.

The observed anomalous transport and diffusion are related to the time dependent probability distributions for the displacements—as for the overdamped—and for the velocities of the particles, that are useless in the overdamped regime because particle's velocities tend to thermalize instantaneously. The instantaneous velocity distributions of underdamped Brownian particles disclose appealing properties of the system. For example, the velocity distribution (Fig. 2.2)–right panel corresponding to a superdiffusive regime exhibits two Mawxell distributions centered respectively at

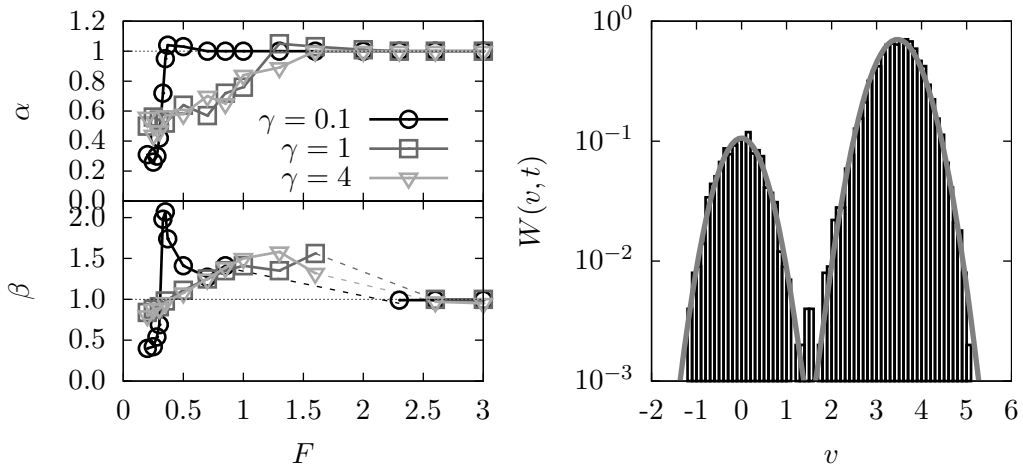

Figure 2.2 – Left panel: Transport—top—and diffusion—bottom—exponents for different friction coefficients. Broken lines correspond to the uncertain diffusion regime. Right panel: Velocity histogram at a fixed time for underdamped Brownian particles ($\gamma = 0.1$) subject to an external force $F = 0.35$ in a random potential. A double Gaussian distribution is also included, with the requirement that the left Gaussian in each case should correspond to the Maxwellian distribution centered at 0, and with dispersion equal to the temperature ($T = 0.2$).

the deterministic velocities corresponding to the particles at rest—locked state—and to the particles being propelled at the velocity of the stationary limit driven by the pulling and the drag forces—running state—. More detailed results and discussion regarding the underdamped approach is carried out in the publication "*Transport and diffusion of underdamped Brownian particles in random potentials*" [Suñé et al., 2014].

The main outcome of this study is that anomalous transport an diffusion regimes occur no matter the damping, yet they come about at higher forces for high friction conditions—overdamped—than when low friction is instead considered—underdamped case—. The latter scenario is much more sensitive to the external applied force's strength, and the leading anomalous regimes are more vigorous, since exponents exhibit a greater deviation from one. In addition, the study of the distribution of instantaneous velocities renders a novel insight into the physical basis of anomalous

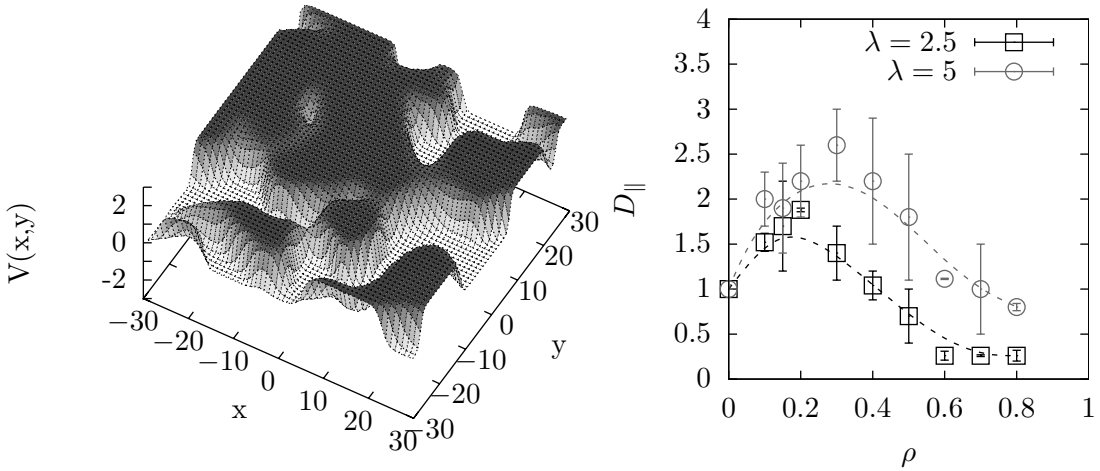

Figure 2.3 – Left panel: Portion of a random landscape made up by obstacles of characteristic size 5 and density 0.6. Right panel: Steady diffusion coefficients in the parallel direction to the external force against the density of obstacles in the medium. Smoothed curves are best fits to clarify the trends.

behavior.

2.1.4. Brownian motion on random dynamical landscapes

The goal of Chapter 6 is to model overdamped Brownian motion of tracer particles in densely packed random landscapes of moving deformable obstacles—spatiotemporal disorder—. Tracer particles cannot surmount the landscape's obstacles, which move randomly, assemble, and dissociate with slower dynamics compared to Brownian motion, (Fig. 2.3)–left panel. A variety of simulation results for the velocity and diffusion are submitted.

Diffusion coefficients above that of free diffusion are attained, (Fig. 2.3)–right panel. It is a trace of transient superdiffusion that comes about at short time scales. Indeed, it has been noticed that anomalous transport and diffusion regimes last as long as the observation—simulation—time reaches the disorder's characteristic time. This outcome belongs to the published work entitled "*Brownian motion on random dynamical landscapes*" [Suñé

et al., 2016].

The leading attainment of this review is the settlement of an effective set of quantities—the characteristic time scale, the width, and the concentration of obstacles—to portray the transport and diffusion of Brownian particles in a landscape made up by unsurmountable obstacles. Each of them has a well established effect on the system. The characteristic time scale constrains the time span of transient anomalies, and thus the subsequent steady transport and diffusion coefficients, (Fig. 2.3)–right panel. For a given density of obstacles, both trafficking and diffusion are favored by wider and therefore fewer obstacles, (Fig. 2.3)–right panel. To end, a high density of obstacles hinders both transport and dispersion.

2.1.5. Methodology

Numerical techniques and algorithms to carry out the numerical simulations referred throughout the thesis are detailed in Chapter 7. It reports a novel straightforward method to build Gaussian potential landscapes with arbitrary spatial correlation functions and the only requirement of isotropy. The method has the particularity that, although it uses the Fourier space, all its constraints and information are in real space. Figure 2.4 depicts the generation of random potentials with different correlation functions employing the numerical recipe detailed in the review "*On generating random potentials*" [Suñé et al., 2012]. Furthermore, a refreshing architecture for simulating random dynamic obstacles is also covered [Suñé et al., 2016].

The novelty of the numerical procedure developed to generate disorder potentials [Suñé et al., 2012] is that any statistical correlation—isotropic and periodic in the finite simulation domain—can be employed. All constraints can be inferred to real space, and thus Fourier space is left as a mere stage in the process. With regard to the method to construct a dynamic disordered landscape of obstacles of equal height [Suñé et al., 2016], the average obstacle width and time scales are well controlled quantities, and the density of obstacles is constant in time. This landscape may ac-

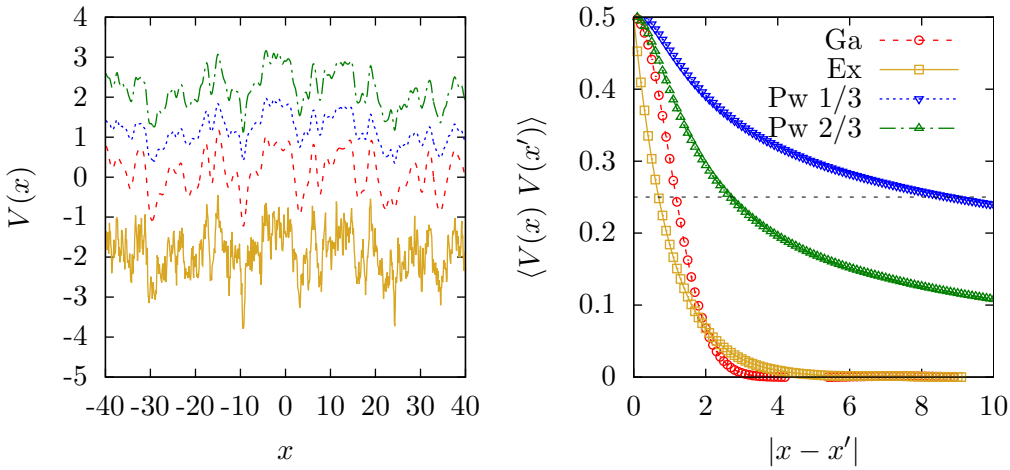

Figure 2.4 – Left panel: Potential landscapes for three correlation types: Gaussian (Ga), double–sided exponential (Ex), and power–law with exponent 1/3 (Pw 1/3) and 2/3 (Pw 2/3). A vertical shift is implemented for better visualization. Right panel: Numerical correlation of the left–hand side portraits. The same color legend than in the left panel applies and matches to the one employed in Figure 2.1.

count for a soft matter or liquid environment in which large obstacles move slowly leading to crowding effects; it also constitutes a novel approach to the macroscopic dynamics exhibited by active matter media.

2.1.6. Spare investigations

Skills and proceedings carried out throughout the former chapters may be useful to attain a description of specific cases of study. Chapter 8 reports two examples of physical systems to be faced within the framework of the thesis. The first one surveys the physics of particles undergoing thermal fluctuations, changing viscosities, and confinement to quasi $2 - d$ layers—also called interfaces—. The second is a study of Brownian motors; a two–dimensional ratchet model for the kinesin motor KIF1A is employed to assess the transport properties of the motor when it travels along microtubules that comprise defects.

Part II

Dissertation on the investigations

CHAPTER 3

Brownian motion in a periodic potential: from underdamping to overdamping

The second part of the thesis begins with a short review on the dynamics of Brownian particles in a tilted periodic potential, a system that accounts for several physical problems; superionic conductors [Fulde et al., 1975], the damped pendulum with torque [Risken, 1989], Josephson junctions [Longobardi et al., 2011], among others. This framework constitutes a basic nonequilibrium model of statistical physics that entails a rich miscellany of transport and diffusion phenomena, such as enhanced and giant diffusion [Lindner et al., 2001; Reimann et al., 2001, 2002; Lindenberg et al., 2005; Lee and Grier, 2006; Khoury et al., 2009; Lindner and Sokolov, 2016], orthogonal velocity emergence with respect the driving force [MacDonald et al., 2003; Lacasta et al., 2005, 2006], and dispersionless anomalous transport [Lindenberg et al., 2007]. Further, such scenario is worthy of consideration still nowadays [Lindner and Sokolov, 2016].

The purpose of this Chapter is to briefly discuss the transport and diffusion features within this simple milieu, so that it brings some clues about the plausible hypothesis and the parameter choices to consider when ex-

tending the problem to the disordered scenario. The very initial hypothesis is that, may some deviations from the free Brownian motion occur due to the interference with periodic arranged barriers of equal size, then, a disordered display of this barriers—whose height can be random—is expected to increase these deviations, as well as it would bring about novel phenomena of anomalous transport and diffusion.

3.1. Setting

A conceivable formulation of a periodic landscape of equally sized barriers of the same height might be through trigonometric functions (Sec. 1.3.2). May the potential's length scale be employed to carry out the scaling transformation ($\lambda_0 = \lambda_p$, hence $\lambda = 1$), the periodic potential in two dimensions reads

$$V(x, y) = \cos(x) + \cos(y)\,, \tag{3.1}$$

where space isotropy has been assumed. Compared to (1.21), it should be noticed that constants $1/2$ and 2π are included into the energy V_0 and length λ_p scales respectively.

Langevin dynamics for Brownian motion under a periodic potential (3.1) and a constant tilting force $\boldsymbol{F}$ are embodied in the following expression—quantities are scaled according to the transformations in Section 1.4.1—,

$$\frac{dv_w}{dt} = -\gamma v_w - \frac{\partial V(\boldsymbol{r})}{\partial r_w} + \xi(t)\ ,\ w = x, y\ , \tag{3.2}$$

where the potential reads

$$V(r_w) = \cos(r_w) - F_w \cdot r_w\ ,\ w = x, y\ . \tag{3.3}$$

In one dimension, it looks like an inclined oscillatory function whose barriers tend to decrease as it is being tilted by a stronger constant external force (Fig. 3.1). Hence, there is a critical force at which the potential

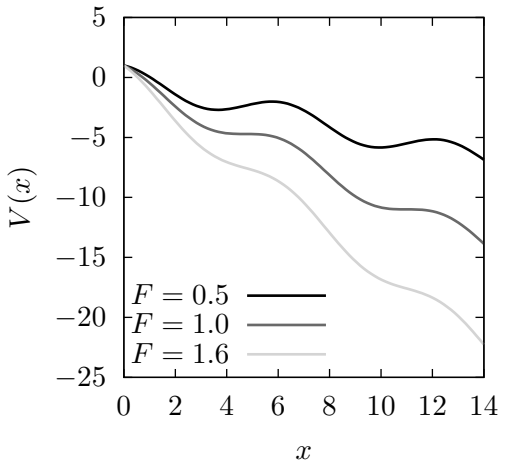

Figure 3.1 – One dimension inclined periodic potential by different force strengths (3.3).

minima transform into inflection points—or saddle points when a $2-d$ potential is considered—

$$F_c = 1\,. \tag{3.4}$$

Forces beyond the critical $F > F_c$ lead to a monotonically decreasing potential ($F = 1.6$ in Figure 3.1).

3.2. Overview of transport and diffusion

May the $1-d$ space be considered, the mean position and the dispersion trajectories usually display a long–term linear behavior (Fig. 3.2)—there is but one exception further analyzed—. Within this scenario of normal transport and diffusion, it makes sense to determine the steady mean velocity and the diffusion coefficient (1.18). Thus, Figure 3.3 succeeds to display most of the transport and diffusive features.

Extension to higher dimensions might lead to a richer phenomenology. The following sections are devoted to the analysis of the most meaningful transport and diffusion features based on the $1-d$ outcome (Fig. 3.3), yet some phenomena inherent to the bidimensional scenario are also discussed.

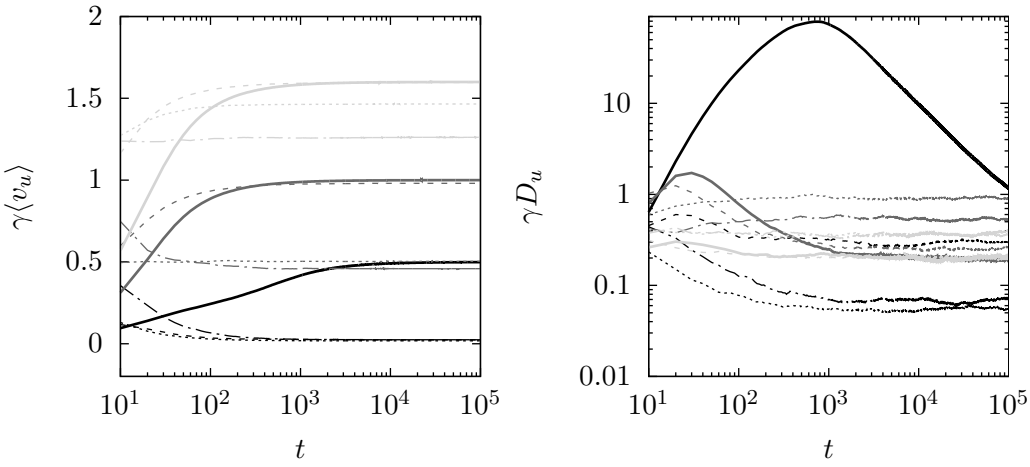

Figure 3.2 – Mean velocity—left—and diffusion—right—of Brownian movement in a $1-d$ periodic potential computed from numerical simulations of Langevin dynamics (3.2) for 1000 particles distributed uniformly over 20000λ ($\lambda = \lambda_p/\lambda_0 = 1$). Initial velocities are distributed according to the Maxwell distribution (Sec. 1.2.2), with temperature $T = 0.2$. $F = 0.5$ (black), 1.0 (gray), and 1.6 (light gray); $\gamma = 0.1$ (solid), 0.4 (dashed), 1.0 (dotted), and 4.0 (dotted–dashed).

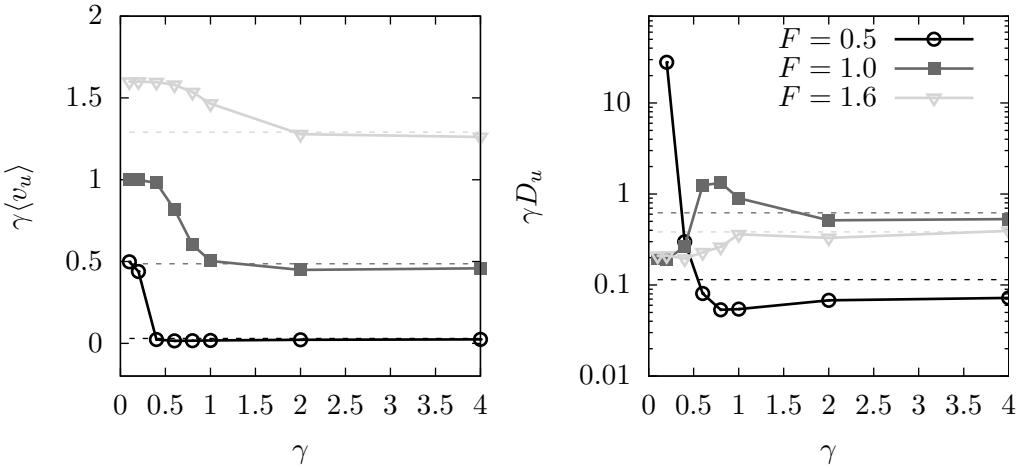

Figure 3.3 – Mean velocity—left—and diffusion—right—of Brownian movement in a $1-d$ periodic potential averaged over the last 1000 units of time for the mean position and the dispersion trajectories (Fig. 3.2). Dashed lines account for the analytical predictions for the particle current (3.6) and the diffusion coefficient (3.11) of Brownian particles in the overdamped regime under a tilted periodic potential.

3.2.1. Transport and symmetry breaking

Transport's features displayed in Figure 3.3 are unremarkable. The free Brownian motion limit is attained at very low friction conditions,

$$\gamma\langle v_u\rangle = F\,. \tag{3.5}$$

The asymptotic mean velocity decreases when dissipation increases—and so more kinematic energy is dissipated—until it eventually reaches the limit of overdamped Brownian particles under a non–linear potential [Reimann et al., 2001, 2002]. There is an exact analytical expression for the particle current within this limit, that can then be derived by computing the moments of the first passage times [Reimann et al., 2001, 2002], and coincides with the Stratonovich's expression [Stratonovich, 1958; Kuznetsov et al., 1965],

$$\langle v\rangle \equiv \langle \dot{x}\rangle = \lim_{t\to\infty}\frac{\langle x(t)\rangle}{t} = \frac{1-e^{-LF/T}}{\int_{x_0}^{x_0+L}\frac{dx}{L}\,I_{\pm}(x)}\,, \tag{3.6}$$

where L is the period of the periodic potential ($L = 2\pi$ for the potential considered in (3.1)),

$$I_{\pm}(x) \equiv \int_0^L \frac{dz}{D_0}\exp\{\pm[V(x)-V(x\mp z)]/T\}\,, \tag{3.7}$$

z is an auxiliary scaled space variable. D_0 is the scaled diffusion coefficient for free Brownian particles—in absence of any external field—(1.6), that, since it is assumed the overdamped scaling approach—see Section 1.4.2—,

$$\hat{D}_0 = \frac{k_B T}{\eta} = T\,\frac{\lambda_0^2}{\tau_0} = D_0\,\frac{\lambda_0^2}{\tau_0}\,, \tag{3.8}$$

and so it is

$$D_0 = T\,. \tag{3.9}$$

It ought to be noted that $\langle v_u\rangle$—and D_u for the diffusion—to which the vertical axis of Figure 3.3 refer, involve the underdamped time scale (Sec. 1.4.1), hence the outcome of the simulations compare to the analytical expressions (3.6)—(3.11) for the diffusion—through a factor γ (Sec. 1.4.2).

Transport in two dimensions

Recently developed experimental techniques, such as optical tweezers and micro–assembling techniques, have promoted the implementation of microfluidic devices capable to separate mixtures of micro–sized particles—and thus subject to thermal fluctuations—according to their size. These devices consist of periodic arrays of obstacles, either optical traps [Korda et al., 2002; MacDonald et al., 2003; Grier, 2003] or microfabricated posts [Huang et al., 2004; Morton et al., 2008], the dynamics within which it can be numerically simulated by Langevin equations comprising $2-d$ periodic potential energy landscapes [Lacasta et al., 2005, 2006; Sancho and Lacasta, 2010]. Besides, analytical predictions for the dependence of the angle between the direction of motion, and the driving force, on a number of model parameters, have also been provided [Gleeson et al., 2006]. The underlying mechanism for sorting micro–sized particles is concomitant to the geometry of the system and the laminar flow induced by a drifting force. Indeed, a perpendicular component of the mean velocity emerges respect to the driving force, leading to a symmetry break. Nonetheless, it ought to be stressed that the potential and thermal fluctuations are completely symmetric, so that the phenomenon is not associated with any kind of ratchet effect.

3.2.2. Enhanced and giant diffusion

Diffusion attains the well–known limit of free particles, in the regime of a very low friction, and of overdamped Brownian motion submitted to a non–linear field, at a high dissipation, (Fig. 3.3). For the free–particle limit, the Stokes–Einstein relation (1.6) holds

$$\gamma D_u = T\,. \tag{3.10}$$

On the other hand, the analytical prediction for the effective diffusion coefficient for the overdamped Brownian motion in a tilted periodic potential is [Reimann et al., 2001, 2002]

$$D = D_0\,\frac{\int_{x_0}^{x_0+L}\frac{dx}{L}\,I_{\pm}(x)\,I_{+}(x)\,I_{-}(x)}{\left[\int_{x_0}^{x_0+L}\frac{dx}{L}\,I_{\pm}(x)\right]^3}\,, \tag{3.11}$$

where

$$I_+(x) \equiv \frac{1}{D_0}\, e^{V(x)/T} \int_{x-L}^{x} dy\, e^{-V(y)/T}\,, \tag{3.12}$$

$$I_-(x) \equiv \frac{1}{D_0}\, e^{-V(x)/T} \int_{x}^{x+L} dy\, e^{V(y)/T}\,, \tag{3.13}$$

y is an auxiliary scaled space variable.

In the overdamped regime, the diffusion coefficient exhibits a maximum around the critical force. This maximum diffusion is well above the Stokes–Einstein relation for free Brownian motion (3.10), yet it is far from being giant [Reimann et al., 2001; Lee and Grier, 2006]. Results in Figure 3.3 reveal a pretty good agreement between numerical simulations and the analytical prediction (3.11). The diffusion coefficient in the underdamped regime does nonetheless greatly exceeds the Stokes–Einstein relation, leading to the giant diffusion phenomenon, that has been analytically demonstrated [Reimann et al., 2001], experimentally observed [Lee and Grier, 2006], and numerically tested [Sancho and Lacasta, 2010]. Obtaining a greater diffusion coefficient than the free–particles' outcome is a remarkable feature, since no other source of randomness is introduced apart from thermal fluctuations.

The underlying physical motivation for the diffusion coefficient to exceed the thermal fluctuations' dispersion without considering any supplementary source of randomness is the bimodal distribution of the particles in the locked state, in which particles oscillate stochastically around the potential minima, and in the running state, in which the gain from potential energy balances the dissipative losses. This behavior has been observed experimentally for atoms and molecules diffusing on surfaces [Senft and Ehrlich, 1995; Schunack et al., 2002]. The literature on this subject often invokes Lévy walks or flights [Luedtke and Landman, 1999; Oh et al., 2002; Shlesinger et al., 1993].

The maximum dispersion in the overdamped regime is located at the critical force because it leads to the most favorable scenario for the ensemble of particles to split into the former two states. For lower forces, particles hardly scape from potential minima—particle current is nearly zero (Fig. 3.3)—; whereas particles tend to glide uninterruptedly over the landscape when the tilting force transforms the potential's barriers into inclined sections. The maximum's height respect to the free–particle diffusion scales with a negative power of the temperature [Colet et al., 1989; Lindner et al., 2001; Reimann et al., 2001; Lindenberg et al., 2005], and so it grows when T decreases. However, the behavior in the underdamped scenario is slightly different. The peak's coordinates and its height depend on the temperature, friction and external force. It should be gathered (Fig. 3.3) that dispersion is favored by a low energy dissipation and a landscape of considerably big barriers ($F < F_c$), rather than by an otherwise flatter landscape ($F \approx F_c$) in which particles travel under a higher friction.

3.2.3. Dispersionless

A force below that of critical ($F = 0.5$) (Fig. 3.2)–right, in the low friction scenario ($\gamma = 0.1$), brings about an anomalous regime of diffusion decreasing linearly with time, yet with finite velocity of about that of free particles. This is the so–called dispersionless regime [Lindenberg et al., 2007], in which particle transport is essentially *nondispersive* or *coherent* over long time intervals at an average velocity that approaches $v = F/\gamma$. The associated distribution of the particle positions (1.1) is far from Gaussian–like (1.2); it exhibits an exponential distribution instead [Lindenberg et al., 2007],

$$P(l_e, t) = \frac{1}{l_K} \exp\left(\frac{l_e - l_t}{l_K}\right) , \tag{3.14}$$

due to the well–known exponential distribution of first exit times to escape from potential wells (Sec. 1.3.1), and assuming that particles emerge with velocities narrowly distributed about $v \approx F/\gamma$. $l_K \equiv (F/\gamma)t_K$, where t_K is the mean exit time—given by the Kramers' escape rate (1.20)–; $l_e \equiv (F/\gamma)t_e$, where t_e is the actual exit time from a potential well; and

$l_t \equiv (F/\gamma)t$ is the distance the distribution will have travelled at time t undistorted. The spatial distribution of particles (3.14) ought to resume asymptotically to the Gaussian (1.2), and so the dispersionless regime would be transient. However, it may take a long time to do so, so long that it would not be reached in some experiments and numerical simulations.

3.2.4. About the simulations

A comment on the time integration step is worthy of consideration, for its choice is critical for the numerical simulation of (3.2). When dissipation is low, there likely are particles in the distribution that move at high speeds, so that they may travel over a distance greater than the potential's length scale λ during the time integration step. These particles would artificially explore the potential landscape. In order to avoid this spurious behavior, the integration time step must be chosen small—yet, how much?—. An extremely tinny time step might prevent this bug, yet it would involve a great computational effort. In order to set up a reasonable and reasoned time step, it ought to be taken into account the limiting scenario of a large external force in which the features of the potential are essentially unseen by the particle. The velocity is hence $v = F/\gamma$, and the characteristic time to explore a distance λ with this velocity is λ times $(F/\gamma)^{-1}$. Assuming that in the presence of the potential the velocity of a particle will hardly exceed $v = F/\gamma$, it should be required the integration time step to be shorter than $\lambda \cdot (F/\gamma)^{-1}$, for example, 100 times

$$\Delta t \leq 0.01\, \lambda\, \frac{\gamma}{F}\,. \tag{3.15}$$

This condition for the integration time step is employed throughout all the simulations within the underdamped approach (Chap. 5).

3.3. Conjectures

According to the phenomenology that have been reviewed for Brownian particles in a tilted periodic potential at a rather low temperature,

the following hypotheses might be guessed at when Brownian motion goes through disordered media:

- There may be no mechanisms to enhance the mean velocity in an isotropic static disorder. Hence, transport anomalies—if any—would be of sublinear type (Sec. 1.2.3); the maximum particle drift ought to be that of free Brownian motion.
- The diffusion peak may be further boosted—a phenomenon already described and observed for a weak disorder [Reimann and Eichhorn, 2008]—; besides, anomalous superdiffusion is likely to happen.
- Anomalous transport and diffusion regimes ought to resume to the normal behavior at the time scale of a putative dynamic disorder because every particle is to be promoted to the running state, at least once, as soon as the potential configuration is completely changed.

The former conjectures prompt the investigations submitted in the following chapters. The next one deals with overdamped Brownian particles in a totally random static potential.

CHAPTER 4

Transport and diffusion of overdamped Brownian particles in random potentials

The scope of this Chapter is the study of motion of overdamped Brownian particles in a totally disordered potential landscape (Sec. 1.3.3) and subject to a constant external force [Denisov et al., 2010; Suñé et al., 2013]. Overdamped Brownian motion is ubiquitous in biophysics [Weiss et al., 2004; Tolić-Nørrelykke et al., 2004; Bickel, 2006], where the Reynolds number is low, and as a result acceleration plays no role because the velocity equilibrates quickly. However, due to the landscape being static, the present description applies to the transport and diffusion of particles in disordered solids [Schunack et al., 2002; Xu et al., 2011; De Wijn, 2011]. "Totally disordered" means that there is no systematic part in the potential other than the constant force—responsible for the transport—, that contrasts with potentials with some periodic component [Khoury et al., 2009, 2011; Lindenberg et al., 2012], (Chap. 3).

Concerning $1-d$ systems, anomalous regimes are observed: subtransport, subdiffusion and superdiffusion. Not only they might be characterized by the time exponents, as in Section 1.2.3 it is already described, but they

are also likely to match to specific particle density portraits. Besides, the transport and diffusion attributes are revealed to rely on the disordered potential's statistical settings. For what it concerns the $2-d$ space, it allows the discussion along different directions separately. Mixed anomalies are then feasible, for example, subdiffusion in the direction perpendicular to the force and superdiffusion in the parallel direction may coexist. The $2-d$ exploration enables the outcome arrangement in clouds of particle positions at different times, that constitutes a novel and complementary description of the transport and diffusion attributes, together with the already employed time exponents and the particle displacement histograms.

4.1. Anomalous exponents in one dimension: impact of the potential correlation function

Recent studies [Khoury et al., 2011] prove that the potential's spatial length scale λ, a putative constant force F, and the temperature T influence the transport and diffusion anomalies of Brownian particles in various pronounced ways. It ought to be remarked that all the physical quantities to be employed throughout this Chapter are dimensionless (Sec. 1.4.2).

4.1.1. Correlation functions

Considering the overdamped Brownian movement in the $1-d$ scaled space undergoing a disordered field, the first goal to be attained hereinafter is to inquire into the effect that the functionality of the disorder's correlation function $g(|x|/\lambda)$ (Sec. 1.3.3) may have on the transport and diffusion phenomena. To follow up this question, three very different types of disordered potentials $V(x)$, with correlation $\langle V(x)\ V(x')\rangle = g(|x-x'|/\lambda)$, are considered:

- The well known normal or Gaussian form,

$$g(|x-x'|/\lambda) = \frac{1}{2}e^{-\frac{(x-x')^2}{2\lambda^2}}\ , \tag{4.1}$$

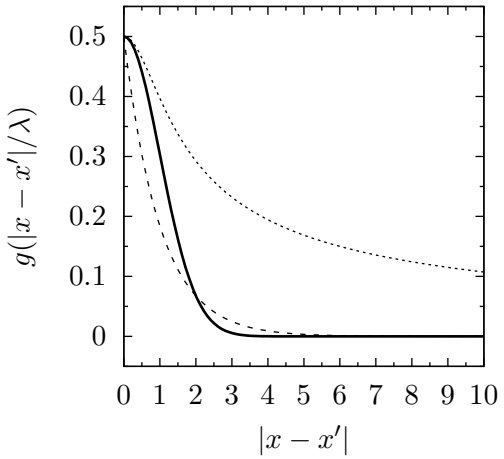

Figure 4.1 – Correlation functions. Gaussian (4.1) in continuous, double–sided exponential (4.2) in dashed, and power–law (4.4) in dotted lines ($\lambda = 1$, $\varepsilon = 2/3$).

which is used here as the reference scenario because it has a well defined characteristic short spatial length scale λ and no singularity in the entire domain (Fig. 4.1).

- The double–sided exponential correlation,

$$g(|x-x'|/\lambda) = \frac{1}{2} e^{-\frac{|x-x'|}{\lambda}} , \tag{4.2}$$

whose underlying force $F_r = -dV/dx$ exhibits a singularity at the origin in the form of a delta correlation $\delta(x - x\prime)$, much like spatial white noise, see Chapter 7 for further details,

$$\begin{aligned} \langle F_r(x)\ F_r(x')\rangle &= -\frac{d^2 g(|x-x'|)}{dx^2} = \frac{1}{\lambda^2} h(|x-x'|) \\ &= \frac{1}{\lambda^2}\left[\delta(x-x') - \frac{1}{2} e^{-\frac{|x-x'|}{\lambda}}\right] . \end{aligned} \tag{4.3}$$

Figure 4.2 plots the force correlation (4.3) to derive from a double–sided exponential correlation (4.2).

- A correlation function with a power–law tail,

$$g(|x-x'|/\lambda) = \frac{1}{2}\left(1 + \frac{(x-x')^2}{\lambda^2}\right)^{-\varepsilon/2} . \tag{4.4}$$

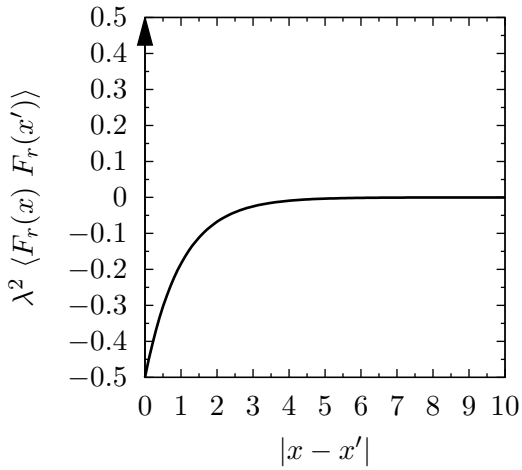

Figure 4.2 – Random force correlation function (4.3) of a random potential with double–sided exponential correlation (4.2). The arrow accounts for the Dirac-delta function.

The decay of the tail is determined by the exponent ε and by a short spatial length scale λ (Fig. 4.3).

4.1.2. Setting

The hereinafter outcome stems from the description of the Brownian motion through stochastic dynamics. Mathematical details concerning stochastic dynamics may be sought in Section 1.3.3. Langevin equations

$$\boldsymbol{v} = \boldsymbol{F} - \nabla V(\boldsymbol{r}, t) + \xi(t)\,, \tag{4.5}$$

with

$$\langle \xi_i(t)\, \xi_j(t')\rangle = 2T\, \delta_{ij}\, \delta(t - t')\,, \tag{4.6}$$

are numerically integrated following a second order Heun algorithm for ordinary stochastic differential equations [García-Ojalvo and Sancho, 1999; Toral and Colet, 2014], (Chap. 7). The random potential is generated following the explicit procedures described in [Suñé et al., 2012] and in Chapter 7.

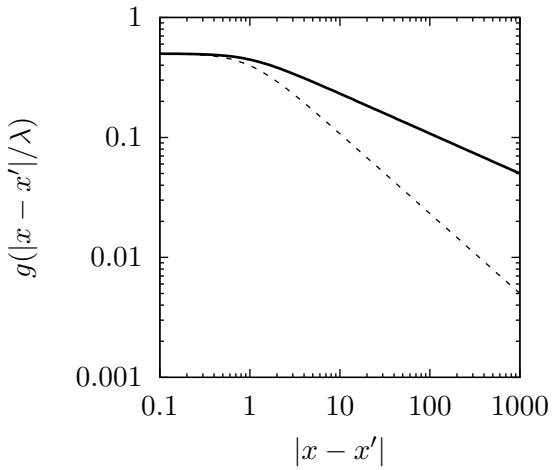

Figure 4.3 – Power–law correlation function (4.4) with different decay tails $\varepsilon = 1/3$—continuous—and $\varepsilon = 2/3$—dotted—; ($\lambda = 1$).

One hundred particles are used in each realization of 100 disordered potentials, so the statistical averages are over a 10000 event population. Particles are initially distributed uniformly along a large region of the potential landscape of size $20000\,\lambda$. Therefore each particle of the 100 in a given potential is likely to experience a different and independent portion of the potential. The potential landscape covers $N = 2^{23}$ lattice points with periodic boundary conditions and a lattice constant $\Delta = 0.1$. Other parameter values are $T = 0.1$ and disorder correlation length $\lambda = 1$. In order to explore different anomalous regimes, the force F is tuned as a control parameter.

Analogously to Section 3.2.4, the time integration step Δt should be chosen so that in each integration step particles do not move over a distance greater than that associated to the roughness of the potential. That is, $\Delta t \ll \lambda_{rgh}/\langle v \rangle$, where λ_{rgh} is the length scale of the disorder's roughness. In the overdamped approach, the asymptotic mean velocity for particles under large external forces obeys the relation $\langle v \rangle \propto F$, then Δt=0.1 may be settled for the Gaussian and the power–law correlated potentials. However, a shorter time step Δt=0.01 is required for the potential with a double–

sided exponential correlation because of the smaller roughness length scale associated with the singularity exhibited by its first derivative at the origin (4.3), plotted in Figure 4.2. Further in Section 4.1.5, this point will be retrieved to a deeper analysis.

In addition to this set of reference parameters, other values are explored as well: $T = 0.05$, $\Delta = 0.05$ (with $N = 2^{24}$), and Δt=0.005 and 0.001. No qualitative changes have been noted in the outcome, yet remarkable quantitative differences emerge, especially when changing Δ and Δt for the double–sided exponential correlation. This discussion will be addressed in detail further (Sec. 4.1.5).

4.1.3. Velocity and diffusion trajectories

Transport and diffusion anomalies are explored through the statistical averages, specifically through first moment and second cumulant of the trajectories $x(t)$—already described in Section 1.2.3—. From which it can be obtained respectively the mean velocity, and the diffusion coefficient.

To begin with, the time unfolding of the mean velocity exhibited by overdamped particles under thermal fluctuations and a Gaussian disorder (4.1) is shown in a log-log plot in Figure 4.4 for different values of the external force. Time independent curves, that is, normal behavior, are reached only at the limit of strong forces. Nonetheless, for weak forces straight decreasing trajectories unfold instead. This is a convincing evidence of the existence of anomalous subtransport.

Regarding the diffusion coefficient (Fig. 4.5), anomalous regimes are also displayed. Indeed, $D(t)$ decreases with a power of time lower than one either in the absence of a pulling force or being it weak; thus exhibiting subdiffusion. However, as the strength of the pulling force increases, the diffusion trajectories switch their trend; for the intermediate forces $D(t)$ increases in time with an exponent greater than one, leading to superdiffusion anomaly. Eventually, the normal diffusion regime is reached for high

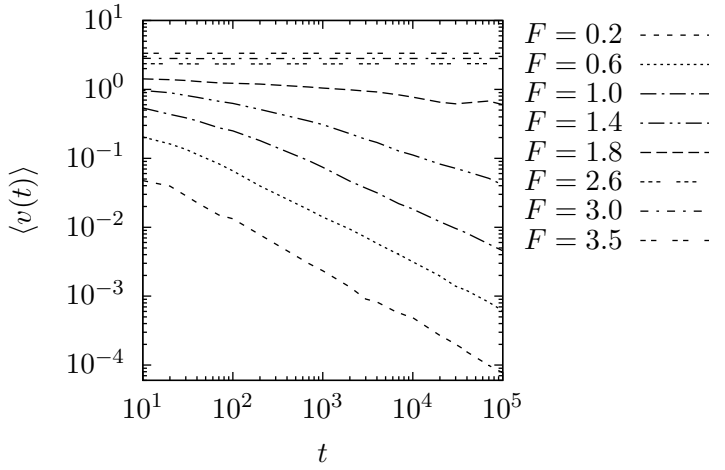

Figure 4.4 – Temporal evolution of the velocity. Simulation of the Langevin equation with a random potential with Gaussian correlation (4.1).

forces, in which the diffusion trajectories $D(t)$ remain constant. It ought to be noted the occurrence of a fourth special regime though. In this regime, detected for forces $F = 2.6$ and $F = 3.0$, diffusion does not reach a steady behavior, and thus it might be referred to as an uncertain regime, yet transport is normal. This discussion concerning the uncertain regime is to be continued later on (Sec. 4.1.6).

4.1.4. Transport and diffusion exponents

As it has already been stated, most trajectories in Figures 4.4 and 4.5 attain to a certain power of time. Therefore, differences among distinct trajectories may be accounted through their exponents, α (1.16) for the transport and β (1.17) for the diffusion, to be obtained by fitting a power–law function of time to the statistical moments $\langle x(t) \rangle$ and $\langle \Delta x^2(t) \rangle$. β can be also evaluated from the expression

$$\beta = log_{10} \left[\frac{\Delta x^2(10t)}{\Delta x^2(t)} \right], \tag{4.7}$$

which gives a series of β values that might converge to a limit. Table 4.1 includes the transport and diffusion coefficients exhibited by the trajectories

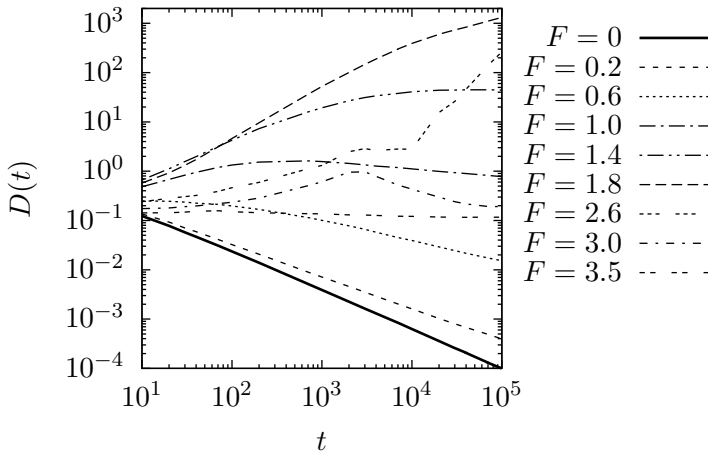

Figure 4.5 – Time trajectories of the diffusion coefficient. Simulation of the Langevin equation with a random potential with Gaussian correlation (4.1).

in Figures 4.4 and 4.5, as well as those to lead from simulations involving random potentials with different correlations. Besides, the outcome in Table 4.1 is depicted in Figure 4.6 for better analysis.

Overall, the data in Table 4.1 plotted in Figure 4.6 reveals the same transport and diffusion regimes to be reached despite the differences in the random potential correlations. That is, roughly speaking, subtransport ($\alpha < 1$) and subdiffusion ($\beta < 1$) at weak forces, and normal behavior at high forces ($\alpha = 1$, $\beta = 1$). Meanwhile, for intermediate forces, diffusion exhibits two different regimes, superdiffusion ($\beta > 1$) and uncertain diffusion, where β cannot be determined.

Figure 4.6 also shows the force interval associated with every dynamical regime—transport in the panel to the left, diffusion to the right—for each of the four types of potential correlations—color coded bars—. Indeed, subtransport—weakly colored filled bar—and normal transport—empty bar—appear from left to right on the α plot for every potential. Subdiffusion—weakly colored filled bar—, superdiffusion—vividly colored filled bar—, uncertain diffusion—patterned bar—and diffusion—empty bar—

	Ga		**Ex**		**Pw 1/3**		**Pw 2/3**	
F	α	β	α	β	α	β	α	β
0.0	-	0.20	-	0.24	-	0.33	-	0.33
0.2	0.29	0.36	0.27	0.36	0.47	0.88	0.36	0.60
0.4	0.28	0.48	0.34	0.53	0.64	1.29	0.42	0.84
0.6	0.32	0.58	0.34	0.63	0.89	1.56	0.54	1.11
0.8	0.33	0.67	0.32	0.74	1.00	1.45	0.64	1.32
1.0	0.40	0.84	0.46	0.84	1.00	+	0.91	1.54
1.2	0.41	0.96	0.53	0.93	1.00	+	1.00	1.51
1.4	0.58	1.07	0.46	1.03	1.00	0.94	1.00	1.72
1.6	0.64	1.23	0.54	1.12	1.00	0.98	1.00	+
1.8	0.90	1.51	0.66	1.21	1.00	0.99	1.00	+
2.0	0.99	1.60	0.72	1.31	1.00	0.99	1.00	+
2.5	1.00	+	0.84	1.40		n	1.00	0.99
3.0	1.00	+	0.96	1.58		n	1.00	1.00
3.5	1.00	0.98	0.99	1.44		n		n
4.0	1.00	0.99	1.01	+		n		n
4.5		n	1.00	+		n		n
5.0		n	1.00	+		n		n
5.5		n	1.00	+		n		n
6.0		n	1.00	1.00		n		n

Table 4.1 – α and β exponents of the velocity and the diffusion coefficient of a set of trajectories displayed by overdamped Brownian particles pulled by varying constant forces and undergoing different disorder types: Gaussian correlated (4.1) (Ga), double–sided exponential correlated (4.2) (Ex), and power–law correlated (4.4) with $\varepsilon = 1/3$ (Pw 1/3) and $\varepsilon = 2/3$ (Pw 2/3). "-" means there is no transport. "+" labels those cases in which the variance trajectories have uncertain time behavior. "n" means that simulations have been avoided since it is quite clear that the normal regime is expected.

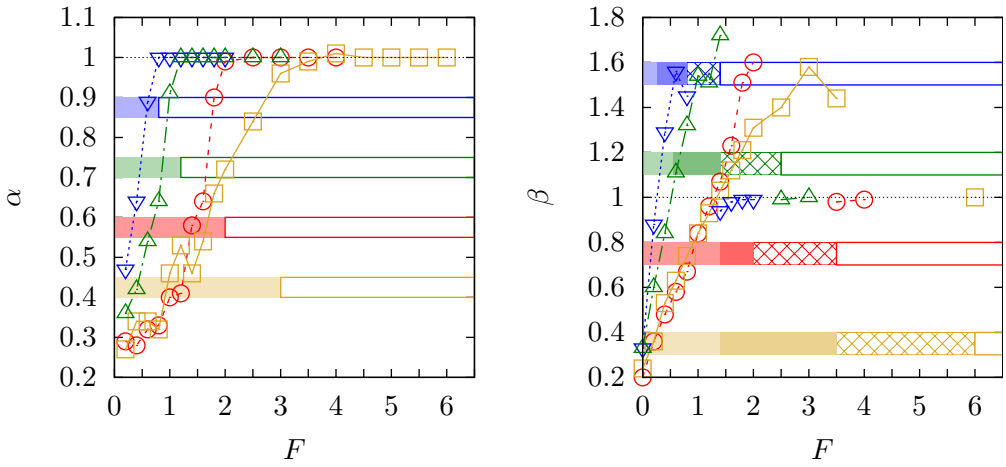

Figure 4.6 – Transport (left) and diffusion (right) exponents for different distributions of disorder; a Gaussian correlation in red, an exponential in gold, and two power-laws of different exponents; $\varepsilon = 1/3$ in green, and $\varepsilon = 2/3$ in blue. Wide horizontal colored bars indicate each dynamical regime, subtransport and subdiffusion in pale colors, superdiffusion in bright colors, uncertain diffusion in patterned bars, and normal transport and diffusion in empty bars.

are evident in the β curves for all the potentials considered.

4.1.5. Roughness' correlation length

It ought to be noted that the force's span of each dynamical regime (Fig. 4.6) is somehow linked to the correlation of the disorder; in particular, to its roughness. May an effective correlation length λ_{eff} be defined as $g(\lambda_{eff}/\lambda) = 0.25$, it reveals that a larger λ_{eff} leads to an earlier—in terms of force—recovery of the normal transport and diffusion regimes. Figure 4.7 displays the λ_{eff} values—right—of the disorders employed in the simulations—left—.

It might be noticed that landscapes with shallower wells exhibit larger λ_{eff}. It follows that the smoother a potential is, the weaker the forces that are needed to achieve normal transport and diffusion for Brownian motion in these potentials. This inference is in agreement with the inter-

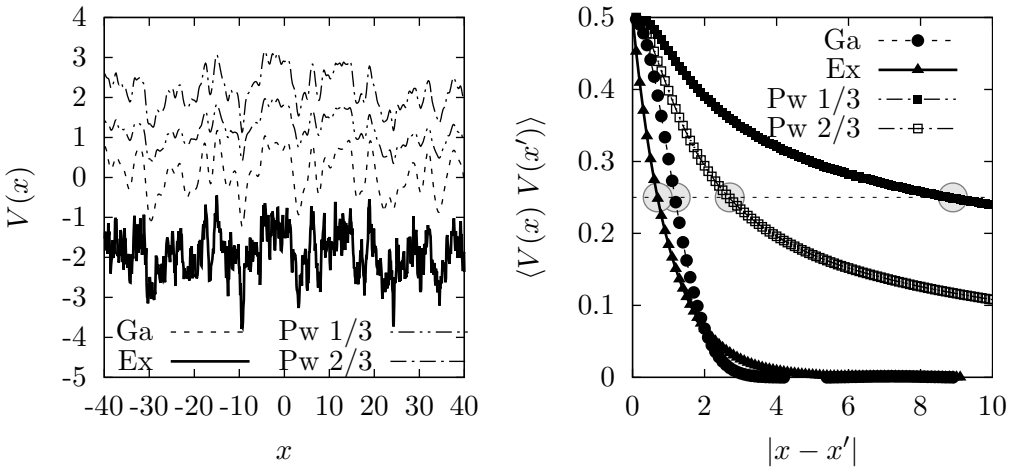

Figure 4.7 – Left: Potential landscapes for the Gaussian (Ga), double–sided exponential with discretization $\Delta = 0.1$ (Ex), and power–law with $\varepsilon = 1/3$ (Pw 1/3) and $\varepsilon = 2/3$ (Pw 2/3); $\lambda = 1$. A vertical shift is implemented for better visualization (2, 1 and -2 potential units respectively for Pw 2/3, Pw 1/3; and Ex). Right: Space correlations of the former landscapes. Grey circles at $\langle V(x)\ V(x')\rangle = 0.25$ provide a measure of the effective correlation lengths.

pretation of anomalous Brownian motion as a consequence of the interplay of "locked" and "running" states [Khoury et al., 2011]. Roughly speaking, in a smoother potential tilted by a force, thermal fluctuations are more likely to help the particles overcome its barriers, and thus normal behavior is recovered more easily.

Power–law correlated potentials not only are characterized by the length scale but also by the tail exponent ε, and thus they require a separate discussion. From Figure 4.7 it can be seen that λ_{eff} is inversely proportional to ε. Therefore the arguments involving ε might be expected to be antithetical to those invoked for λ_{eff}.

However, the λ_{eff} argument fails to explain the outcome of the simulations for a double–sided exponentially correlated disorder, which might be expected to be closer to those of the Gaussian disorder, for they have similar values of λ_{eff}. The reason is that the exponentially correlated potential

exhibits a second much finer structure of tiny wells due to the shorter spatial scale related to the discretization length Δ. This secondary structure is hardly affected by the action of the external force because of the large characteristic slope of the potential. Indeed, once the primary structure has almost been counterbalanced by F, these secondary tiny wells associated with the Δ length scale still remain. That is the reason why both the superdiffusive and the uncertain diffusive regimes for this disorder prevail up to higher forces compared to the Gaussian disorder. It may thus be asserted that, for the double–sided exponentially correlated potential, the λ_{eff} length scale controls the subdiffusive regime, whereas superdiffusion and uncertain diffusion are controlled by the Δ length scale.

Transport regimes associated with the Gaussian and double–sided exponential correlated disorders show the same trend up to a certain force. From that point, they diverge and the normal transport recovery is delayed for the exponential case. The force at which the two behaviors begin to diverge turns out to be precisely the force at which both systems become superdiffusive, and thus the former argumentation is reinforced. As to the transport behavior, the secondary scale Δ leads to a decrease of the velocity of the particles because of the presence of small obstacles and thus subtransport prevails longer.

These results lead to further consider the case of double–sided exponentially correlated disorder, now with a smaller discretization parameter than considered above, namely, $\Delta = 0.05$. Compared to the case with $\Delta = 0.1$, the smaller discretization parameter is associated with a higher degree of roughness in the secondary scale. The former reasoning then allows to conclude that the time step $\Delta t = 0.01$ might not be sufficiently small to accurately capture the behavior of the system. A smaller time step Δt=0.001 is hence picked. The behavior of transport and diffusion is analogous to the case of the exponential correlation with $\Delta = 0.1$, yet the subtransport, superdiffusive and uncertain diffusive regimes are extended in the case of $\Delta = 0.05$ (Fig. 4.8). This reinforces the idea that the secondary roughness associated with the Δ length scale regulates the persistence of

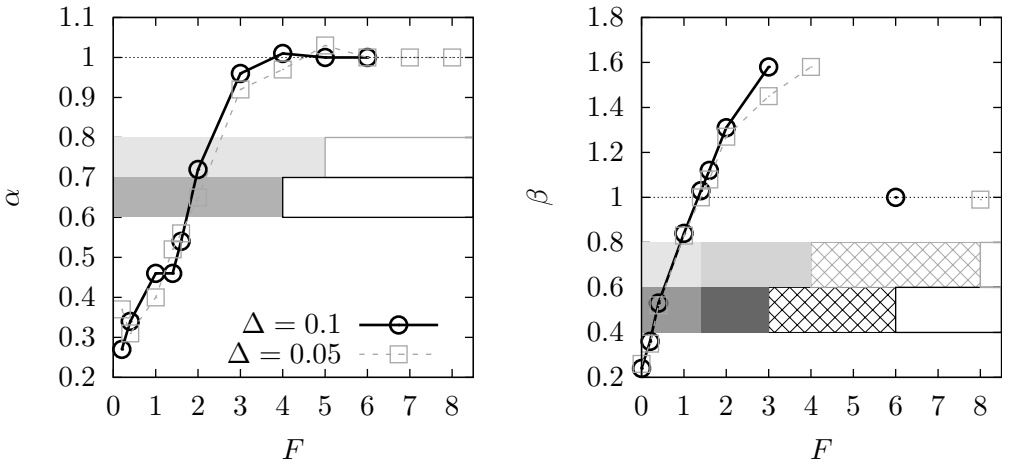

Figure 4.8 – Transport—left—and diffusion—right—exponents exhibited for Brownian motion under a disorder with double-sided exponential correlation and different roughness ($\Delta = 0.1$ and $\Delta = 0.05$). The time step is adjusted according to the discretization parameter, $\Delta t = 0.01$ for $\Delta = 0.1$ and Δt=0.001 for $\Delta = 0.05$. Wide horizontal colored bars label the dynamical regimes—as for in Figure 4.6—.

these anomalous regimes.

4.1.6. Final remarks

A qualitative similarity ought to be noted between behaviors observed here and in the case of underdamped Brownian particles in a periodic potential [Lindenberg et al., 2007]. In both cases there is a regime of forces where some particles are in a "running" state of essentially deterministic velocity $v \sim F$ while others are in a "locked" or trapped state of zero velocity. In the current random potentials there is thus a large variation of the particle distribution and of the motion of the particles for different realizations of the potentials, leading to anomalous dispersion, and thus to the uncertain diffusive regime, much as is observed in the underdamped problem.

Finally, the asymptotic temporal behavior of transport and diffusion

deserves a comment apart. The time t may compare to a characteristic time of the system to provide a sense of the temporal extent of the simulations. One can define the deterministic time t_0 that it takes to cover a distance λ under the action of a force F,

$$t_0 = \frac{\lambda}{F} \ , \tag{4.8}$$

which for the current systems lies in the domain $t_0 \sim\in (0.33, 2.0)$ (according to the choices for λ and F). Hence the alluded simulations run as far as five decades of this characteristic time. Several anomalies are observed over this full interval while others are shorter, with a duration two or three decades of this time. Recently this problem has been addressed in [Hanes and Egelhaaf, 2012], with similar qualitative results: the presence of a subdiffusive regime. However, it cannot be asserted that even with longer simulation times normal transport and diffusion will be achieved. While it is commonly accepted that at asymptotic times all behaviors will be normal and diffusive, from the experimental point of view time is finite, and it would be helpful to know if important anomalies appear in realistic observation time intervals. These interpretations of the current results are appropriate provided that the total simulation time is large enough without running into finite system size effects. The total length of the system is $\approx 8.39 \cdot 10^5$, but the system is periodic—in a statistical sense (Chap. 7)—, so it should be avoided covering more than half of this distance, $\approx 4.2 \cdot 10^5$. For a force of $F = 3.5$ and a maximum time of $t = 10^5$, particles would travel as far $\approx 3.34 \cdot 10^5$, that is, at most of the same order as half the length. For times much larger than this one can expect finite size effects and, accordingly, normal behavior.

4.2. Displacement distribution, a novel illustration of transport and diffusion anomalies

The current section is intended for the behavior of the particle density representative of the various combinations of behaviors discussed above. Figure 4.9 unveils the histogram of the relative displacements $x(t) - \langle x(t) \rangle$

of all the particles for various values of the external force and under a Gaussian disordered potential, where the brackets indicate an average over all the particles. From top to bottom, $F = 0.6, 1.8, 2.6$ and 4.0. These cases are chosen as representative of the variety of anomalies: subtransport and subdiffusion (A), subtransport and superdiffusion (B), uncertain diffusive regime (C) and finally, the case of both normal transport and diffusion (D).

When particles are pulled by weak forces ($F = 0.6$) they exhibit subtransport and subdiffusion (Fig. 4.9)–A. In such case, the displacement distribution is asymmetric; it displays a long forward exponential tail and as a consequence its maximum is shifted towards negative displacements. This shape is a trace of the particle's behavior, a few pull ahead but most are stuck.

When the force increases up to $F = 1.8$, there is subtransport as well, yet superdiffusive. In this case, the displacement distribution (Fig. 4.9)–B is also asymmetric, but now exhibits a backward tail and the maximum is shifted oppositely, that is, to displacements greater than zero. Hence it reveals that many particles are still stuck, yet a larger fraction of them now pull ahead. Note that the dispersion is much larger than in the previous case.

For a stronger force, $F = 2.6$, the transport is normal, $\langle v \rangle \sim F$—brackets label average over the ensemble of particles—, but the simulation data is not sufficient to obtain a reliable result to characterize the diffusion. The distribution in Figure 4.9–C also lacks of symmetry. It shows a very narrow maximum, which is the signature of the "running" state of most of the particles, even while there may still be a few particles in the "locked" state, $\langle v \rangle \sim 0$, which may become trapped in the few realizations of the potential that present the deepest wells. Figure 4.14 in the following section is helpful for a better understanding.

Finally, the figure with the strongest force, $F = 4.0$ (Fig. 4.9)–D, illustrates normal behavior, i.e. normal transport and normal diffusion, with a

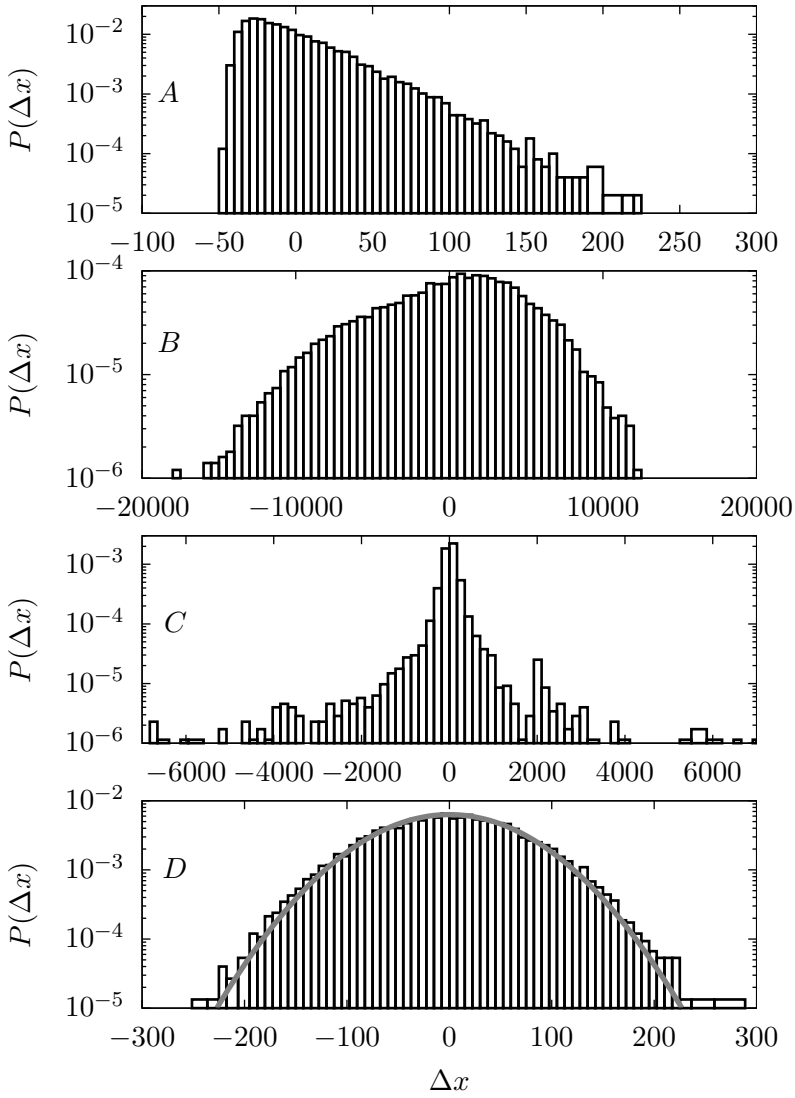

Figure 4.9 – Displacement distribution of the particles $P(\Delta x)$ for different combinations of displacements and diffusions. $F = 0.6$ (A), 1.8 (B), 2.6 (C) and 4.0 (D) at $t = 20000$. It is important to pay attention to the horizontal scale in each plot. Plot (D) includes the representation of a Gaussian function of zero mean ($\mu = 0$) and variance $\sigma^2 = 2D\,t$ ($D = T = 0.1$, $t = 20000$) in grey.

Gaussian–like distribution, as confirmed by the solid Gaussian curve ($\mu = 0$, $\sigma^2 = 2D\,t$, $D = T = 0.1$, $t = 20000$). Essentially perfect Gaussian behavior is expected for very large forces.

4.2.1. Transport and diffusion of particles on surfaces

Transport and diffusion in two dimensions exhibit new phenomena because one can study the orthogonal direction with respect to the force. In cartesian coordinates the force is written as,

$$\boldsymbol{F} = F\ \hat{\boldsymbol{u}}_{\parallel} = F\ (\cos\theta\,\hat{\boldsymbol{i}} + \sin\theta\,\hat{\boldsymbol{j}})\ , \tag{4.9}$$

which defines the parallel unit vector $\hat{\boldsymbol{u}}_{\parallel}$. The perpendicular unit vector is $\hat{\boldsymbol{u}}_{\perp} = -\sin\theta\,\hat{\boldsymbol{i}} + \cos\theta\,\hat{\boldsymbol{j}}$. The simulated trajectories yield the cartesian components of the average velocity $\langle \boldsymbol{v} \rangle = (\langle v_{\hat{i}} \rangle, \langle v_{\hat{j}} \rangle)$ and the cartesian diffusion tensor $\boldsymbol{D} = \{D_{\hat{i}\hat{j}}\}$. With this information, transport and diffusion in any direction $\hat{\boldsymbol{u}}$ can be computed,

$$\langle v_{\hat{\boldsymbol{u}}} \rangle = \langle \boldsymbol{v} \rangle \cdot \hat{\boldsymbol{u}}, \qquad D_{\hat{\boldsymbol{u}}} = \hat{\boldsymbol{u}} \cdot \boldsymbol{D} \cdot \hat{\boldsymbol{u}}\ . \tag{4.10}$$

The choices of the angles at which to perform the simulations can be made so as to provide the maximum amount of information. If $\theta = 0$, the cloud of particles might reach the system size quite fast without exploring the whole landscape. Periodic boundary conditions are not helpful in this case. This is clearly not a particularly informative choice. On the other hand, a finite θ along with periodic boundary conditions produces a spiraling motion along a torus. Therefore, helpful choices of θ are the ones that prevent intersection—or statistical correlation—between particle trajectories that coil the torus after each turn while allocating the maximum number of loops. For the hereinafter outcome, θ has been chosen according to these arguments.

It has been simulated the motion of overdamped Brownian particles in a $2-d$ Gaussian correlated disorder,

$$g(|\boldsymbol{r} - \boldsymbol{r'}|) = \frac{1}{2} e^{-\frac{(\boldsymbol{r}-\boldsymbol{r'})\cdot(\boldsymbol{r}-\boldsymbol{r'})}{2\lambda^2}}. \tag{4.11}$$

F	$\alpha_\parallel$	$\beta_\parallel$	$\beta_\perp$
0.6	0.11	0.43	0.20
1.0	0.18	0.59	0.38
1.2	0.32	1.00	0.42
1.3	0.57	1.36	0.47
1.5	0.80	2.01	0.82
2.0	1.00	+	0.99
3.0	1.00	1.01	1.02

Table 4.2 – Transport ($\alpha_\parallel$) and diffusion ($\beta_\parallel$, $\beta_\perp$) exponents corresponding to those trajectories in Figures 4.10 and 4.11. "+" denotes a case where the diffusion coefficient cannot be extracted from the simulation data.

This correlation is isotropic and does not introduce a bias in any direction. The simulations were run on a lattice of $N^2 = 4096^2$ sites with $\Delta x = \Delta y = 0.5$. The other simulation parameters were $\Delta t = 0.1$ and $T = 0.03$. The temperature is much lower than in the $1-d$ simulations because particles might avoid the highest potential barriers by changing their direction.

As in the one–dimensional scenario, the first moment and the second cumulant are computed on the ensemble of trajectories, now separately for the directions parallel and perpendicular to $\boldsymbol{F}$. This allows the fitting of the transport $(\alpha_\parallel, \alpha_\perp)$ and diffusion $(\beta_\parallel, \beta\perp)$ exponents. These results are included in Table 4.2. The corresponding time dependence of the velocity $(\langle v\rangle_\parallel, \langle v\rangle_\perp)$ and the diffusion coefficients $(D_\parallel, D_\perp)$ are shown in Figures 4.10 and 4.11.

Along the orthogonal direction (Fig. 4.10)–lower there is no transport ($\langle v_\perp\rangle \approx 0$), yet there is subdiffusive dispersion (Fig. 4.11)–right, as it should be expected since no force is present [Romero and Sancho, 1998]. The phenomenology in the parallel direction is the same as in the $1-d$ case. Nevertheless, there is a new remarkable situation: for intermediate forces the dispersion displays parallel superdiffusion with perpendicular subdiffusion.

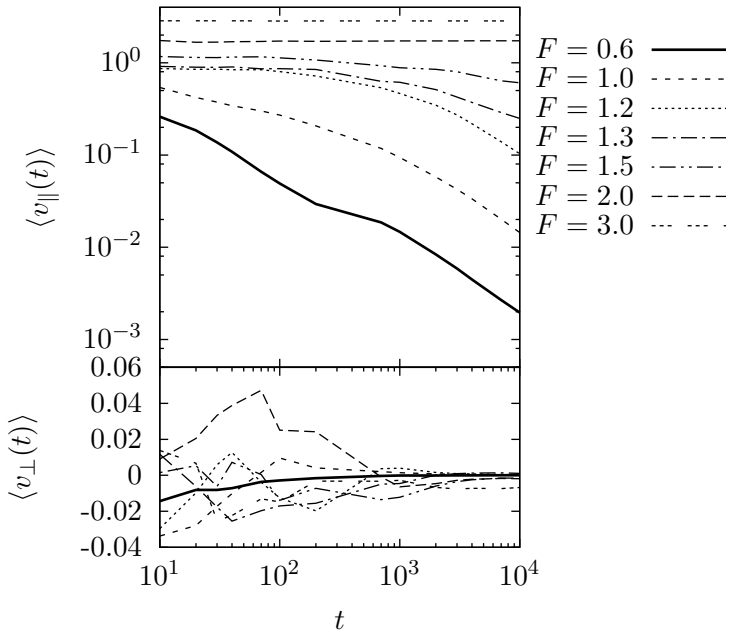

Figure 4.10 – Parallel (upper) and perpendicular (lower) mean velocities of 400 particles, averaged over 20 realizations of the random potential surface. $\theta = \arctan(100/N\Delta)$.

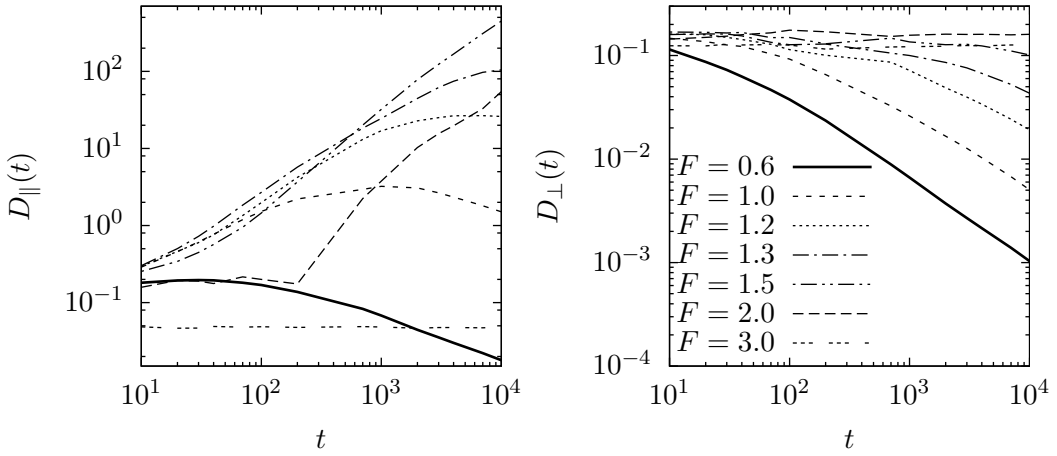

Figure 4.11 – Parallel (left) and perpendicular (right) diffusion coefficients. Same parameters as in Figure 4.10.

4.2.2. Clouds of particles

The $2-d$ scenario allows a novel representation of the simulations' outcome that sheds light on the underlying processes to bring about the already described transport and diffusion anomalous phenomena. Indeed, by plotting the particles' positions at different times it might be gathered some clues to understand their behavior. Figures 4.12 to 4.14 and 4.16 display the clouds of particle positions for some representative behaviors along the direction parallel to the external force: subdiffusion with subtransport (F=0.6) in Figure 4.12, superdiffusion and subtransport (F=1.5) in Figure 4.13, no well defined diffusion in Figure 4.14 (F=2.0), and both normal diffusion and transport (F=3.0) in Figure 4.16. The clouds are plotted on the same scales for the x and y directions to highlight the respective asymmetries.

A feeble force: subtransport and subdiffusion

For small forces, the majority of the particles are expected to be trapped most of the time. A few of them might undergo short random displacements with a bias toward the direction of the force. That is seen in Figure 4.12 for $F = 0.6$, in which the cloud spreads in the parallel direction showing some kind of a forward comet tail. Besides, particles in this tail are more likely to spread along the perpendicular direction as well, since they are the ones that have avoided the deepest wells along their trajectories. This information is complemented by the histograms of the particle positions in both directions (Fig. 4.12), where the asymmetry in the parallel direction contrasts with the symmetry in the perpendicular one. In what concerns the perpendicular way, it ought to be remarked that despite being symmetric, the distributions exhibit non–Gaussian shapes. Compare to the distributions in the following Figures 4.14 and 4.16, in which diffusive regimes are reached along the perpendicular direction. Indeed the actual histograms are narrower, thus revealing shorter particle perpendicular displacements, that might be imputed to the particle trapping to potential wells. It ought to be remarked that the outcome plotted in Figure 4.11 exhibited perpendicular subdiffusion for $F = 0.6$.

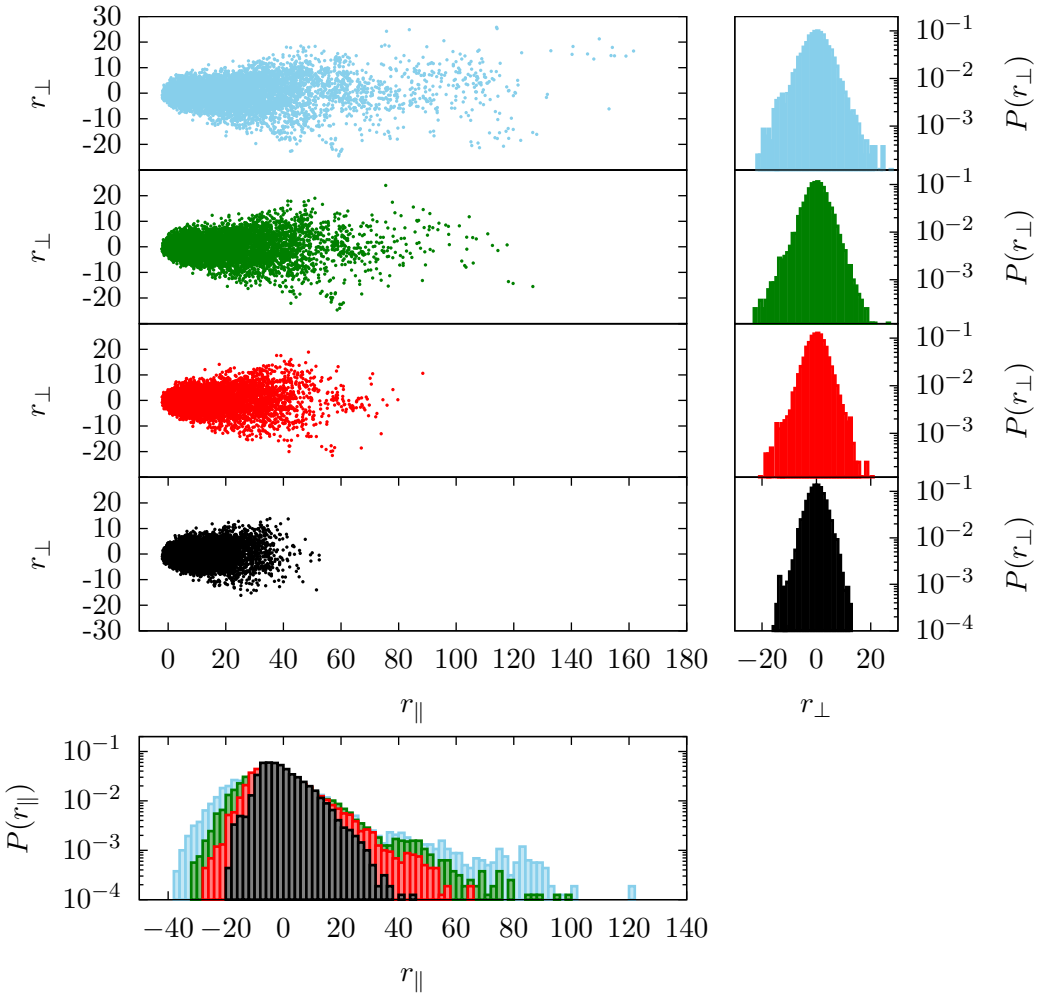

Figure 4.12 – $F = 0.6$. Top–left: Particle positions with respect to their initial conditions at different times. From lower to upper panel: $t = 250, 1000, 4000, 16000$. Top–right: Particle displacement distribution, after being subtracted the ensemble mean displacement, at the same times—the same color key is applied—along the perpendicular direction to the external applied force. Bottom: Particle displacement distribution along the external applied force's bearing.

A rather weak force: mixed anomaly

In the superdiffusive regime, along the force's direction ($F = 1.5$) the displacement distribution displays a comet-like shape with a larger density at its head. Compared to the $F = 0.6$ outcome, there is a large increase of the dispersion in the parallel direction and, in addition, its asymmetry is in the opposite direction, i.e., it has a backward long tail. This inference is corroborated by the histograms concerning the particle displacements along the force's bearing (Fig. 4.13)–bottom. Compared to Figure 4.12, the perpendicular displacement's distributions are wider, hence unveiling a decrease of particle trapping, yet Gaussian like distributions aren't reached. The histograms concerning the perpendicular bearing still exhibit a trace of particle confining, for they are more pointed than a Gaussian distribution.

Intermediate forces: undefined diffusion

The intermediate value of the force $F = 2.0$ corresponds to the regime in which it is not possible to define an anomalous exponent for the diffusion along the direction of the force. The cloud evolution under this condition (Fig. 4.14) exhibits a front of particles that travels at a deterministic velocity of about $v_{cloud} \approx F$. However, some particles remain stuck at a few points along the trajectory displayed by the front, revealing that the landscape hardly comprises unsurmountable obstacles. Indeed, the histogram of parallel displacements displays little frequencies at seldom locations smaller than the ensemble's mean position (Fig. 4.15). On the other hand, along the perpendicular direction, the displacements distribution exhibits a Gaussian shape, that is a trace that most of the particles freely diffuse (Fig. 4.14). Hence a Gaussian function with variance $\sigma^2 = 2D_\perp\, t$ fits the histogram, where $D_\perp$ is the asymptotic diffusion coefficient attained for the trajectory with $F = 2.0$ in Figure 4.11. This observations reinforce the argumentation developed earlier for $F = 2.6$ in the case of unidimensional Gaussian correlated disorder.

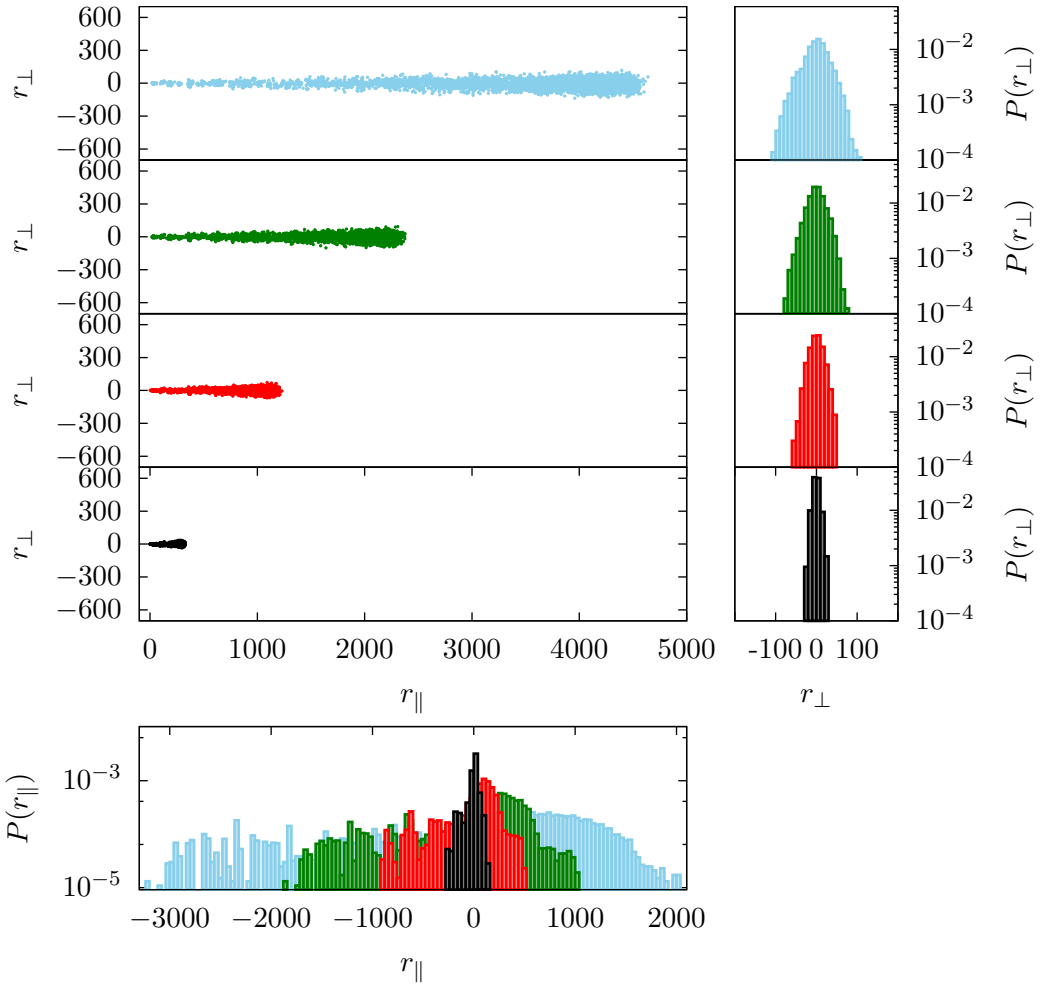

Figure 4.13 – $F = 1.5$. Top–left: Particle positions with respect to their initial conditions at different times. From lower to upper panel: $t = 250, 1000, 2000, 4000$. Top–right: Particle displacement distribution, after being subtracted the ensemble mean displacement, at the same times—the same color key is applied—along the perpendicular direction to the external applied force. Bottom: Particle displacement distribution along the external applied force's bearing.

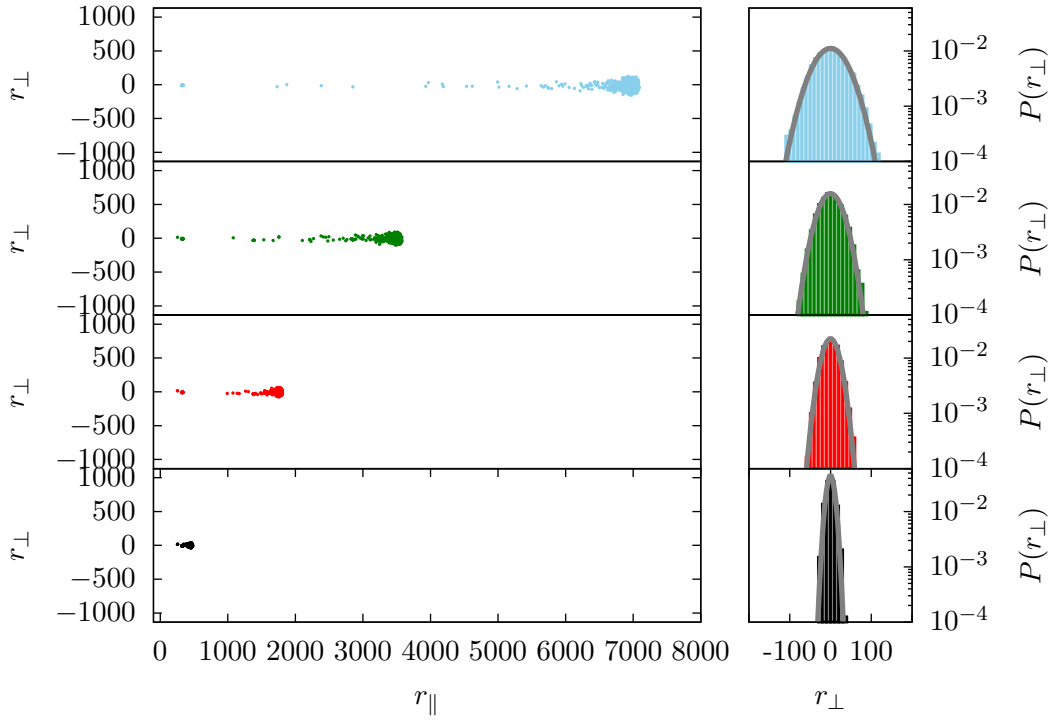

Figure 4.14 – $F = 2.0$. Left: Particle positions with respect to their initial conditions at different times. From lower to upper panel: $t = 250, 1000, 2000, 4000$. Right: Particle displacement distribution, after being subtracted the ensemble mean displacement, at the same times—the same color key is applied—along the perpendicular direction to the external applied force. A Gaussian with $\mu = 0$ and $\sigma^2 = 2D_\perp\, t$ ($D_\perp \approx 0.16$) is superimposed in every panel.

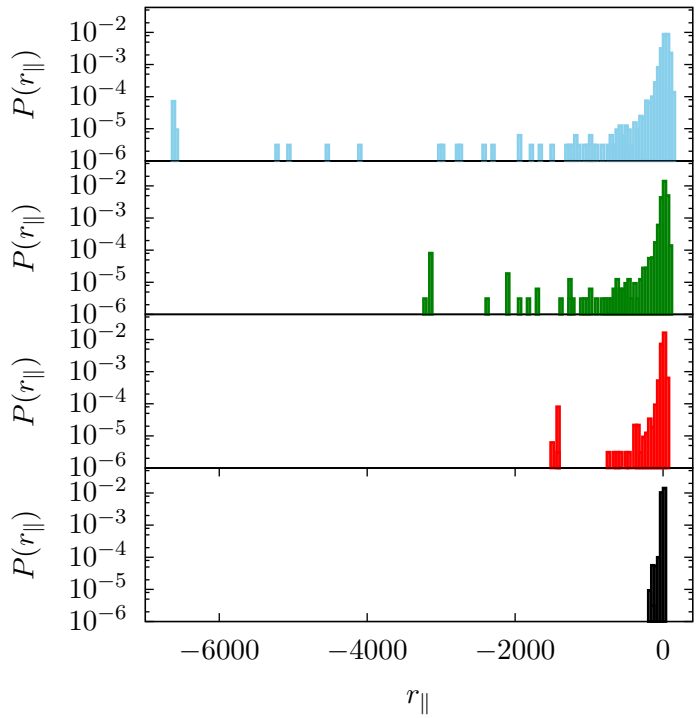

Figure 4.15 – $F = 2.0$. Particle displacement distribution along the external applied force's bearing, after being subtracted the ensemble mean displacement, at times $t = 250, 1000, 2000, 4000$ from lower to upper panel.

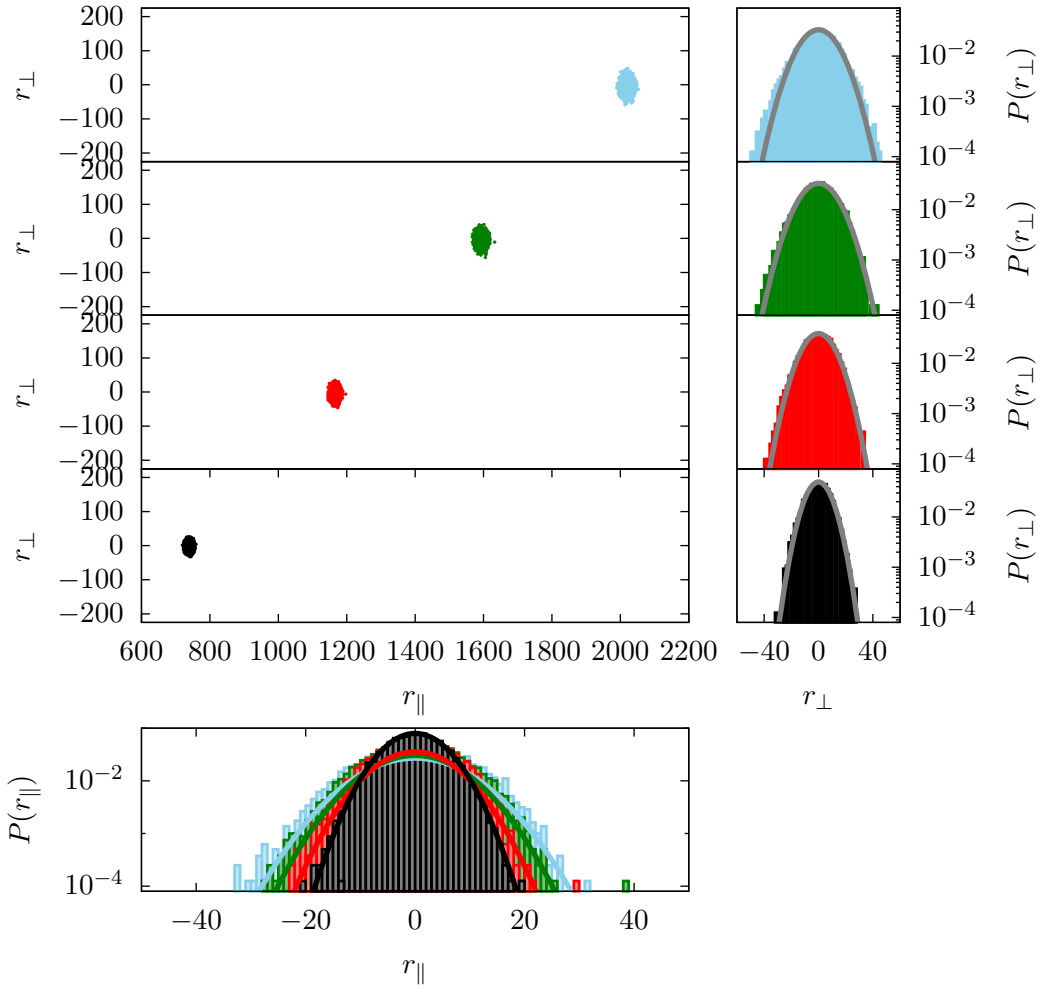

Figure 4.16 – $F = 3.0$. Top–left: Particle positions with respect to their initial conditions at different times. From lower to upper panel: $t = 250, 400, 550, 700$. Top–right: Particle displacement distribution, after being subtracted the ensemble mean displacement, at the same times—the same color key is applied—along the perpendicular direction to the external applied force. A Gaussian with $\mu = 0$ and $\sigma^2 = 2D_\perp t$ ($D_\perp \approx 0.13$) is superimposed in every panel. Bottom: Particle displacement distribution, after being subtracted the ensemble mean displacement, along the external applied force's bearing. A Gaussian with $\mu = 0$ and $\sigma^2 = 2D_\parallel t$ ($D_\parallel \approx 0.05$) is superimposed for each time.

Strong forces: normal transport and diffusion

Finally, for a large force, $F = 3.0$, normal transport and diffusion in both directions are recovered. These phenomena are featured in Figure 4.16, in which elliptical clouds travel along the parallel direction with a velocity $v_{cloud} \approx 3 \approx F$. Although there is normal diffusion along both directions, the elliptical shape reveals a different diffusion coefficient for each direction. This result is clearly confirmed by the corresponding histograms (Fig. 4.16), that display a wider Gaussian distribution in the direction perpendicular to the external force. This is not unexpected, since the external force breaks the symmetry of the system, that is, it smoothes the potential barriers along its direction. Indeed, Gaussian functions of different variances ($\sigma^2_{\parallel}$, $\sigma^2_{\perp}$) fit the parallel and perpendicular distributions of displacements; $\sigma^2_{\parallel} = 2D_{\parallel}\, t$ and $\sigma^2_{\perp} = 2D_{\perp}\, t$, where diffusion coefficients $D_{\parallel}$ and $D_{\perp}$ are those asymptotic limits for the $F = 3$ trajectories in Figure 4.11.

4.3. Conclusions

Transport and diffusion of unidimensional overdamped Brownian particles in totally disordered potentials show anomalous regimes whose strength and external force dependence in turn depend on the temperature T and on the statistical properties of the disorder. This dependence can be understood via the theoretical consideration of anomalous Brownian motion already developed in [Khoury et al., 2011]. In addition, the length scales of the roughness of the potentials have been shown to be essential parameters in the understanding of the effect of disorder in anomalous regimes.

The main practical difference between different kinds of disorder can be associated with an effective correlation length. Taking the Gaussian correlation as a reference, power–law correlations present a larger effective length and, accordingly, shallower wells, which implies that normal regimes are attained for lower tilting forces. On the other hand, the double–sided exponential correlation, despite having a similar effective length scale, it

exhibits a second much smaller length scale associated with the space discretization length Δ. This length scale causes the appearance of a secondary structure composed of tiny wells, yet with higher roughness—steep landscape slopes—. Once the external force is sufficiently strong to overcome the primary structure (associated with λ_{eff}) the secondary structure provided by Δ prevails, and so particles are still being hindered. In order to recover the standard diffusive regime this remaining structure should be overcome by increasing the applied force. Both super and uncertain diffusion thus continue to occur up to higher forces because of the continued simultaneous presence of "running" and "locked" states, the latter now due to the small wells associated with Δ. More generally, it may be inferred that when disorder exhibits two different length scales, subdiffusion is associated with the larger one, and both superdiffusion and and uncertain diffusion are associated with the shorter one.

The evolution of the particle density in Figures 4.9 and 4.12 to 4.15 reveals other interesting characteristics of the anomalies. Each different asymmetry of the histogram is related to subdiffusion and superdiffusion regimes for finite forces. The non Gaussian–like form of these distributions is thus an indicator that some anomaly is present.

For two dimensions, a completely different behavior of transport and diffusion is seen between the directions perpendicular and parallel to the force. It should be especially noted the coexistence of subdiffusion and superdiffusion along different spatial directions.

The uncertain diffusive regime is caused by the finite number of particles and of realizations of disordered potentials. A small number of locked particles have a great effect, leading to uncertain behavior of the statistical moments of the position of the particles.

Finally, concerning either $1-d$ or $2-d$ results, it should be noted that transport and diffusion anomalies have not been proved to be steady state regimes. However, simulation data show that anomalies span sev-

eral decades of time, which had already been predicted theoretically and observed experimentally [Hanes and Egelhaaf, 2012; Hanes et al., 2012; Evers et al., 2013]. Thus, even if the ultimate behavior might be simply diffusive—that is, "normal"—, the experimentally relevant behavior may be precisely the anomalous one. Furthermore, the finite time behavior has proved useful in the estimation of the properties of the system in the asymptotic limit [Schmiedeberg et al., 2007; Hanes et al., 2013].

Next Chapter deals with the same problem of Brownian motion under disordered landscapes, yet considering the underdamped approach.

CHAPTER 5

Transport and diffusion of underdamped Brownian particles in random potentials

Particles moving subject to thermal forces and the associated friction are said to be undergoing underdamped Brownian motion [Risken, 1989; Sancho et al., 2004; Lindenberg et al., 2007; Marchenko and Marchenko, 2012; Marchenko et al., 2014] when energy dissipation is feeble, so that they do have inertia. "Associated friction" means that the forces and friction satisfy the fluctuation–dissipation relation [Einstein, 1905; Von Smoluchowski, 1906; Langevin, 1908; Ornstein, 1919]. The underdamped Brownian movement is mostly found in solid state systems [Adelman and Doll, 1977; Goohpattader et al., 2009], such as organic molecules on a Cu(110) surface [Schunack et al., 2002], and benzene on graphite [De Wijn, 2011]. On top of that, experiments on hydroxide ions in amorphous solid water [Lee et al., 2014], embedded macromolecules on amorphous ice [McMullan et al., 2015], and colloids within porous polymer films [Skaug et al., 2015], among others, disclose the underdamped Brownian movement in disordered mediums to be worthy. Nonetheless, it might be worth studying the Brownian motion in the underdamped regime if nothing else to understand the parameter values at which acceleration can safely be ignored, so that the overdamped

approach already addressed in Chapter 4 may be thoroughly applied.

The present Chapter reports the numerical results for the transport and diffusion of underdamped Brownian particles in one–dimensional disordered and static potentials. The anomalies observed are compared with those found in Chapter 4 for the overdamped regime and with results for a periodic potential (Chap. 3). On the other hand, the probability distributions for the position and velocity of the particles are computed for they bring about novel clues to dig into the physical basis of the observed transport and diffusion phenomenology.

5.1. Preliminaries

5.1.1. The model

Likewise in Chapters 3 and 4, the stochastic dynamics description of Brownian movement is to be employed hereinafter,

$$\frac{dv}{dt} = -\gamma v + F - \frac{V(x)}{dx} + \xi(t)\,, \tag{5.1}$$

with the white noise's correlation

$$\langle \xi_i(t)\, \xi_j(t') \rangle = 2T\, \gamma\, \delta_{ij}\, \delta(t - t')\,. \tag{5.2}$$

Details upon the Langevin equation under the underdamped approach may be found in Section 1.4.1. For ease of computational effort and notation, the $1 - d$ scenario is considered; extension of the model to two and three dimensions is in principle straightforward but not within the present scope.

The model for underdamped Brownian movement reduces to four key parameters: the temperature T, the correlation length λ, the external force F, and the friction coefficient γ. All the physical quantities to appear all along this Chapter, such as the former ones, are scaled according to the procedure described in Section 1.4.1. Surveys of the overdamped Brownian movement in random static potentials [Khoury et al., 2011; Suñé et al.,

2013], (Chap. 4), have unveiled the potential's spatial length scale λ, a presumed constant force F, and the temperature T to have an impact on the transport and diffusion anomalies. May the temperature and the correlation length be fixed at $T = 0.2$ and $\lambda = 1$ for the present content, there remain only two free independent parameters, F, and γ, through which the underdamped Brownian motion is to be surveyed. This temperature choice entails that the thermal energy is lower than the mean square amplitude of the potential—which is appropriate for the particles to clearly perceive the potential landscape—, but not so low as to make typical potential barriers unsurmountable.

Concerning the functionality of the disorder's correlation function, it has been shown to affect quantitatively, yet not qualitatively, the transport and diffusion attributes [Suñé et al., 2013], (Sec. 4.1.4). Thus, for the present purpose, a disorder landscape of zero mean and Gaussian correlation function (4.1) is settled on.

In addition, the periodic potential,

$$V_p(x) = \cos\left(\frac{x}{\lambda}\right), \tag{5.3}$$

with the same length scale, is considered for comparison. Its spatial average over one period is $\langle V_p(x)\rangle = 0$ and its square value integrated over one period is $\langle V_p(x)\ V_p(x)\rangle = 1/2$—the angular brackets now indicate an integral over one spatial period—. These values are the same as the mean and the mean square of the random potential, and thus the two potentials are in this sense comparable. The correlation function for (5.3) is

$$\langle V_p(x)\ V_p(x')\rangle = \frac{1}{2}\cos\left(\frac{x-x'}{\lambda}\right). \tag{5.4}$$

A Taylor series expansion of the correlation functions (4.1) and (5.4) yield the same results up to second order in λ, further supporting the comparison of results for the two potentials.

The collected observables to inquire into the transport and diffusion properties of the Brownian movement are the long time behavior of the

displacement's first moment for the transport, and the long time behavior of the variance for the diffusion. Their mathematical description is carried out in Section 1.2.3.

Notwithstanding, the statistical moments of the instantaneous $1-d$ scaled velocity (v) and its variance might be further considered in the underdamped regime. Concerning the instantaneous velocity's variance, the theoretical Einstein's prediction for free Brownian motion states that,

$$\langle \Delta v^2(t) \rangle = T\,. \tag{5.5}$$

This relation is checked by the outcome to be covered further in the text.

5.1.2. Numerical setting

Random potentials with the assumed statistical properties can be generated using routine methods [Suñé et al., 2012], (Chap. 7). The space at which random potentials are defined should be isotropic and periodic boundary conditions apply. The positions and velocities of the particles are obtained by numerical simulation of the Langevin equation using a second order Heun algorithm for ordinary stochastic differential equations [García-Ojalvo and Sancho, 1999; Toral and Colet, 2014], (Sec. 7.5).

For the periodic potential, simulations are averaged over 1000 particles, whereas more runs are required for the random potential in order to obtain adequate statistics over distinct random landscapes. Therefore, simulations with random potentials run for 100 particles over 100 realizations of the potential with periodic boundary conditions in a space of $N = 2^{23}$ sites, with $\Delta = 0.1$ separation in–between. The particles are initially distributed uniformly along a spatial interval of length 20000λ centered at $N\Delta/10$, that is, distant from any boundaries. These particles thus experience different and independent portions of the random potential, avoiding statistical correlations. This is clearly not necessary for a periodic potential. For both potentials an initial Maxwellian distribution of velocities is implemented,

i.e.,

$$W(v, t=0) = \frac{1}{\sqrt{2\pi T}}\, e^{-v^2/2T}\,. \tag{5.6}$$

The time integration step must be chosen carefully, as must the maximum simulation time. The choice for the time integration step is settled on following the discussion in Section 3.2.4, thus according to the condition (3.15). With regard to the maximum time t_{max}, it is clearly advisable not to overtake the time needed for the particles to travel a distance greater than the half length of the space in which the potential is defined—such restriction does not apply for a periodic potential—, for the half of the potential is statistically constrained by the opposite; unwanted correlations would be injected into the process otherwise. Therefore, assuming the asymptotic velocity for free Brownian motion $v = F/\gamma$, the maximum time t_{max} ought not to exceed

$$t_{max} < \frac{N\,\Delta}{2}\frac{\gamma}{F}\,. \tag{5.7}$$

5.1.3. The high force regime and the overdamped limit

The hereinafter simulation results may compare to those obtained in well controlled limits. In the presence of a constant force, $F \neq 0$, particles exhibit a net velocity in the direction of the force. When the force is sufficiently high, it masks the nonlinear potential, and so the system should behave according the well known Einstein's results [Risken, 1989] for the mean velocity and diffusion,

$$\langle v\rangle = \frac{F}{\gamma}\,, \qquad D = \frac{T}{\gamma}\,. \tag{5.8}$$

In this limit and at long times, the steady state probability distributions should be the well known Maxwell–Boltzmann distributions,

$$P(x,t) = \frac{1}{\sqrt{2\pi D\,t}}\,\exp\left[-(x-\langle v\rangle t)^2/2D\,t\right], \tag{5.9}$$

$$W_{st}(v) = \frac{1}{\sqrt{2\pi T}}\,\exp\left[-(v-\langle v\rangle)^2/2T\right]. \tag{5.10}$$

The subindex *st* stands for "steady". The second limiting scenario is that of very high friction—overdamped limit—. It is instructive to compare the results concerning large but finite friction γ with those obtained by integration of the Langevin equation in the completely overdamped regime, where the acceleration is set to zero. However, comparison of underdamped and overdamped results is not straighforward, for that each regime has its own time scale, see Section 1.4 for further details. Using the transformations (1.33), large yet finite friction results to be obtained subsequently compare to those in Chapter 4, in the strictly overdamped limit.

5.2. Transport and diffusion: trajectories and exponents

Likewise the survey concerning the overdamped approach (Chap. 4), a systematic numerical study of underdamped Brownian motion for the disordered potential of correlation function (4.1) has been carried out. The outcome may compare to the overdamped results reported in Chapter 4 and in [Suñé et al., 2013], as well as to the results to be achieved with underdamped Brownian particles undergoing a periodic potential (5.4). Figures 5.1 and 5.2 display the transport and diffusion trajectories in logarithmic axes so as to find out putative deviations from normal transport and Fickian diffusion. Normal behavior is associated with constant asymptotic behavior—independent of time—. Only three forces are displayed, which nonetheless bring about an iconic overview of the anomalous regimes to be achieved.

There is a noticeably difference between those trajectories concerning simulations with periodic potentials, which attain a stationary quantity, and those with random potentials, that increase or decrease. Therefore, transport (1.16) and diffusion (1.17) exponents (Table 5.1) resulting from power–law fitting to the mean and the variance curves ought to exhibit contrastive values depending on the type of potential considered.

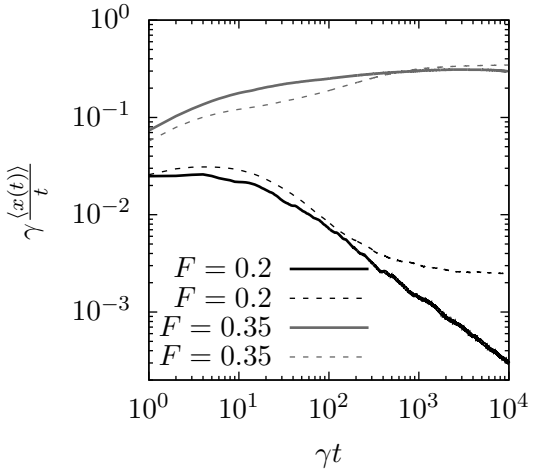

Figure 5.1 – Velocity curves. Solid lines are for the random potentials, dashed lines for the periodic potentials. The grey scale labels different forces, as indicated. In all cases $\gamma = 0.1$.

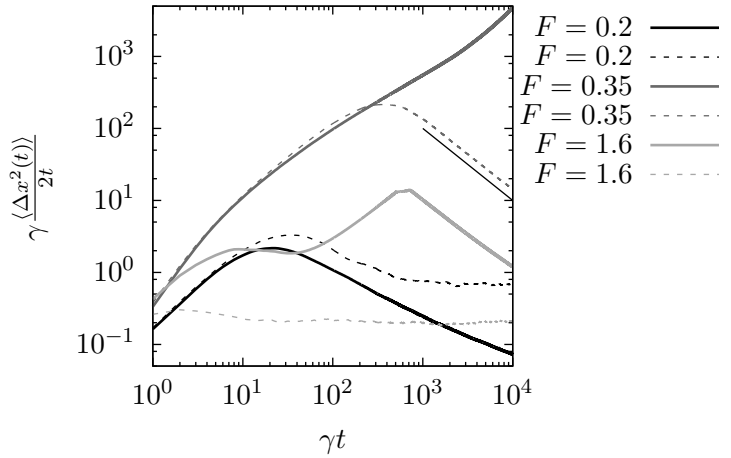

Figure 5.2 – Diffusion curves. Solid lines are for the random potentials, dashed lines for the periodic potentials. The grey scale labels different forces, as indicated. In all cases $\gamma = 0.1$. The black straight line under the dashed trajectory corresponding to the case with $F = 0.35$ and a periodic potential is a power–law with exponent -1.

	random						periodic	
	$\gamma = 0.1$		$\gamma = 1.0$		$\gamma = 4.0$		$\gamma = 0.1$	
F	α	β	α	β	α	β	α	β
0.2	**0.31**	**0.40**	0.50	0.84	0.56	0.80	**0.94**	**0.97**
0.25	0.26	0.42	0.56	0.88	0.44	0.88	1.02	1.09
0.3	0.42	0.69	0.54	0.91	0.47	0.89	1.03	*
0.35	**0.95**	**2.07**	0.52	0.98	0.57	0.96	**1.02**	*****
0.5	1.03	1.41	0.64	1.11	0.58	1.08	1.00	*
0.7	1.00	1.27	0.57	1.25	0.70	1.25	1.00	0.79
0.85	1.00	1.41	0.72	1.35	0.65	1.39	1.00	0.96
1.0	1.00	**	0.76	1.41	0.84	1.50	1.00	0.97
1.3	1.00	**	1.05	1.35	0.89	1.58	1.00	0.97
1.6	**1.00**	******	1.03	1.56	1.00	1.32	**1.00**	**1.02**
2.0	1.00	**	1.01	**	1.00	**	1.00	0.94
2.3	1.00	0.99	1.00	**	1.00	**	1.00	0.97
2.6	1.00	0.99	1.00	1.00	1.00	0.97	1.00	1.01

Table 5.1 – Transport (α) and diffusion (β) exponents. ** indicates that the diffusion curve does not exhibit a steady behavior as a function of time ("uncertain diffusion regime"). * indicates the so-called "dispersionless regime" [Lindenberg et al., 2007]. Bold rows are the ones graphed in Figures 5.1 and 5.2.

For a periodic potential—considering multiple forces and underdamping conditions—, α and β (Table 5.1) are those of normal transport and diffusion—those values in the two far right columns of Table 5.1 are nearly one—. There is but an exception for an intermediate range of forces $0.25 < F < 0.7$. In this range of forces, "dispersionless transport" arises [Lindenberg et al., 2007]. The behavior of the exponents (Table 5.1) concerning a random potential—considering multiple forces and Stokes friction values—involves nonetheless a rich variability that ought to be profoundly discussed.

At first glance, the behavior of α and β when increasing the external force—simulations with a random potential—is homologous for any friction considered—from underdamping to overdamping conditions—, Figure 5.3 compares fairly good to the pure overdamped outcome (Fig. 4.6) indeed. Notwithstanding, it should be pointed out that the course from subtransport to supertransport to normal transport, and from subdiffusion to superdiffusion to normal diffusion—as the force strength increases—is much

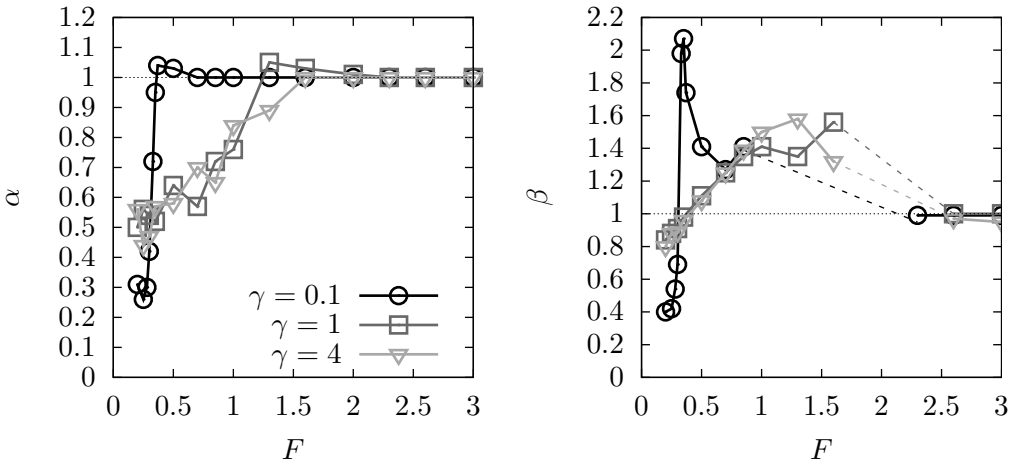

Figure 5.3 – Transport—left—and diffusion—right—exponents of underdamped Brownian particles in a random potential as listed in Table 5.1. Broken lines correspond to the uncertain diffusion regime.

more rapid or abrupt in underdamping conditions than in overdamping. This remark reveals the external force F to exert a more powerful influence on Brownian particles for feeble energy dissipation conditions. Such inference looks to be realistic, for particles in this regime hardly attach to the potential due to loss of energy [Risken, 1989], but because of the existence of particularly high barriers. Hence it means that underdamping conditions favor the transition from locked to running states and hinder the inverse.

Other features of the different dynamical regimes can be understood by inquiring into the distribution of the positions of the particles being pulled by different forces, displayed in Figure 5.4. These distributions confirm the interpretation argued in Chapter 4 and [Suñé et al., 2013], namely, that anomalous behavior is a consequence of the statistical coexistence of locked particles, that is, particles trapped in the potential, and running particles, particles whose dynamics is primarily dictated by the force. This is a behavior consistent with the notion that the random potential has regions of deep wells or high barriers as well as regions where the potential is relatively flat. These features are reflected in distributions that are far

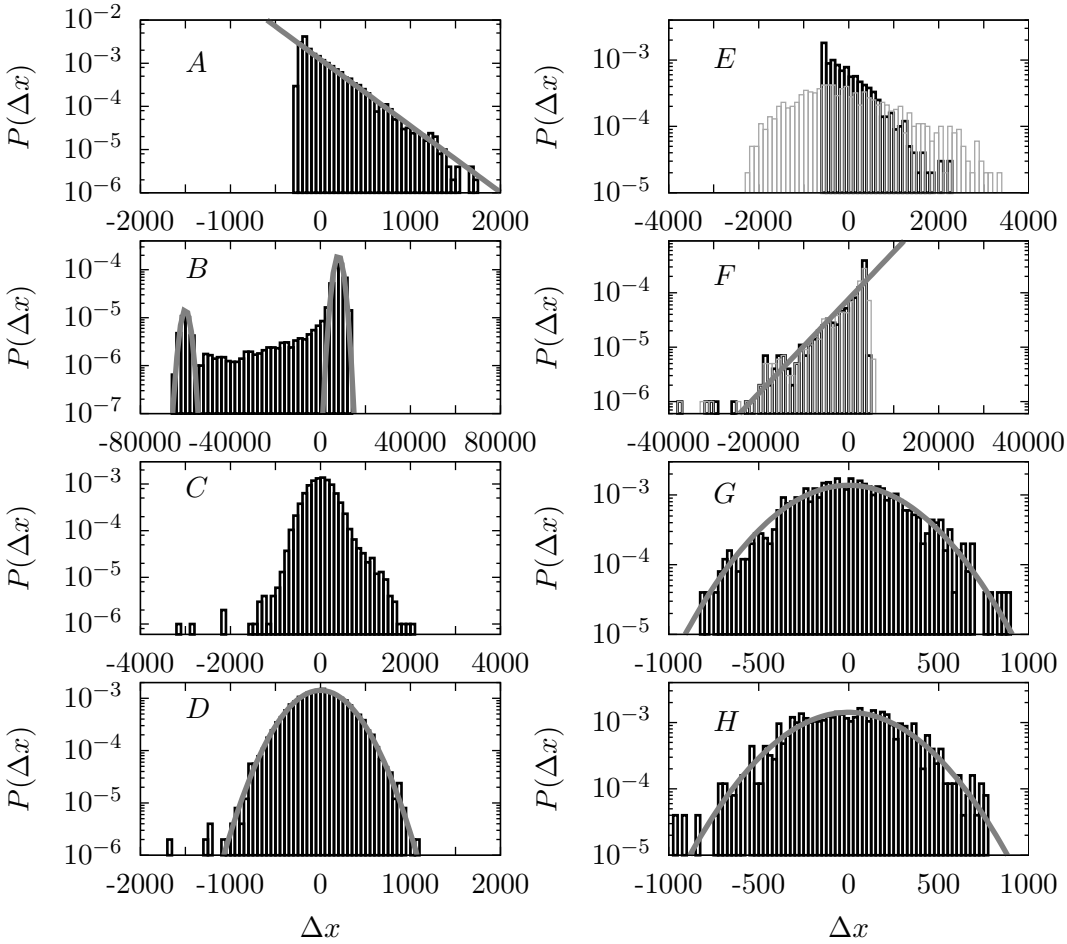

Figure 5.4 – Distribution of particle positions $P(\Delta x, t)$, where $\Delta x = x - \langle x(t) \rangle$, at time $t = 20000$ of underdamped ($\gamma = 0.1$) Brownian particles undergoing either a random potential with Gaussian correlation (4.1)—left—or a periodic one (5.3)—right—. The light grey histograms superimposed respectively in (E) and (F) correspond to $P(\Delta x, t)$ at $t = 100000$. Every plot corresponds to a characteristic regime controlled by the external force $F = 0.2$ (A–E), 0.35 (B–F), 1.6 (C–G), and 2.3 (D–H). Parabolic curves correspond to the Maxwell distribution (5.9). In panel (B) two parabolas are fitted around the two maxima. Exponential functions (5.11) and (5.14) are respectively fitted to the distributions in panels (A) and (F).

from Maxwellian—the logarithmic y–axis leads to a parabolic shape when the distribution is Maxwellian—. The left column of Figure 5.4 shows the distribution of particles in random potentials, with a constant force of increasing magnitude descending the column. From top to bottom, $F = 0.2$ (subtransport and subdiffusion), $F = 0.35$ (normal transport and superdiffusion), $F = 1.6$ (normal transport and uncertain diffusion), and $F = 2.3$ (the beginning of normal behavior). In the right column, it is shown the distributions for the same forces when the potential is periodic. The time at which the distributions in the figure have been computed is $t = 20000$ and the friction coefficient is $\gamma = 0.1$. It might be useful to inspect each regime apart.

5.2.1. Subtransport and subdiffusion regime

For weak forces (Fig. 5.4) $F = 0.2$, the distribution exhibits a pronounced asymmetry biased towards the force's direction, even in the case of the periodic potential, indicative of motion of particles in the direction of the force, just like its analogous in the overdamped (Fig. 4.9)–A. It is also included the distribution at larger times $t = 100000$ for the periodic potential, in the form of a paler histogram in panel (E). The distribution seems to tend towards the symmetric Maxwell distribution. That the particles in the random potential continue to exhibit anomalous behavior even beyond this long time, while those in the periodic potential approach Maxwellian behavior, is already manifested by the trajectories shown in Figures 5.1 and 5.2. The long time required to reach normal behavior may be due to the weakness of the force, which leads to long anomalous transients before normal behavior is reached.

A final observation about the very low force anomalous regime, exhibited in panel (A) of Figure 5.4, is in order. The shape of the displacements distribution might be argued to be a straight consequence of the motion of particles in the direction of the force, yet there is not a clear explanation for this rather unexpected asymmetry. The distribution presents a forward

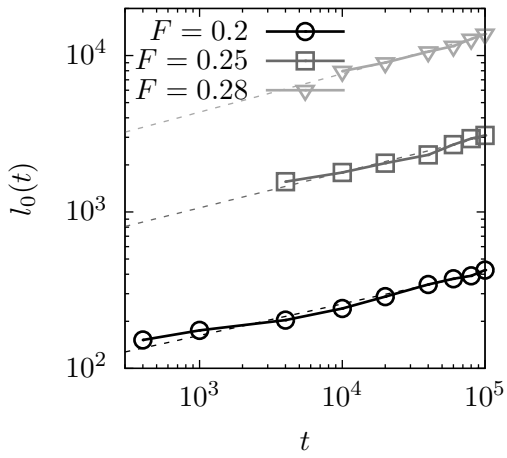

Figure 5.5 – Characteristic length $l_0(t)$ associated with the distribution $P(\Delta x, t)$ in (5.11) for a random potential, with forces $F = 0.2,\ 0.25,\ 0.28$—solid lines with symbols—. Fitting curves for these results as given in (5.12)—dashed lines—.

exponential decay that can be fitted by

$$P(x,t) \begin{cases} \sim A \exp(-x/l_0(t)), \text{ for } x \geq x_i \ , \\ \sim 0, \text{ for } x < x_i \ . \end{cases} \tag{5.11}$$

Here x_i is the coordinate at which the exponential decay begins; it may be set to zero by a simple translation. A time dependence of the distribution is included through the single force–dependent parameter $l_0(t)$. Evaluating it at different times and forces, cf. (Fig. 5.5), it follows a power–law,

$$l_0(t) = a\, t^b. \tag{5.12}$$

Table 5.2 summarizes the values of the fitted parameters a and b for various forces as well as the transport α and diffusion β exponents for these forces taken from Table 5.1.

Taking $x_i = 0$ as the position of the locked state $v(t) = 0$, the mean and variance of the—normalized—particle distribution of (5.11) can be computed,

$$\langle x(t) \rangle = l_0(t) = a\, t^b, \qquad \langle \Delta x^2 \rangle = l_0(t)^2 = a^2 t^{2b}. \tag{5.13}$$

F	a	b	α	β
0.2	40	0.20	0.31	0.40
0.25	220	0.23	0.26	0.42
0.28	800	0.25	0.30	0.54

Table 5.2 – Parameters of the power–law adjustment (5.12) to $l_0(t)$ for forces $F = 0.2$, 0.25, and 0.28 and its associated transport and diffusion exponents.

These results state that in this subtransport/subdiffusion regime, the transport and diffusion exponents are related by $\beta = 2\alpha$. This is an unexpected and surprising result which was also observed for Brownian motion in a periodic potential with very weak disorder [Khoury et al., 2011]. The data in Table 5.2 though manifests certain discrepancy with the former outcome; whereas it seems likely to infer that $\beta = 2b$, it is not so obvious for $\alpha = b$.

5.2.2. Normal transport and superdiffusion regime

Panels (B-F) in Figure 5.4 correspond to a force $F = 0.35$. In the random potential, the distribution of particles exhibits two peaks. May the velocities of the two peaks be computed at different times, it is noted that the left peak essentially does not move ($\langle v \rangle \approx 0$) while the right peak shifts at a velocity $\langle v \rangle = 3.55 \approx F/\gamma$. The stationary peak might thus be assigned to the particles locked to a position—by traps or barriers—and the moving peak to running particles pulled through the landscape by the external force. The increasing separation of the peaks with time leads to superdiffusive behavior. However, the average particle velocity is dominated by the second peak, and thus transport is essentially normal. There are some particles in the distribution between these two peaks, but the majority are in one or the other peak.

Particles in a periodic potential exhibit an entirely different behavior. The distribution of positions is a one–sided exponential that remains unaltered for different times; in panel (F) the distribution hardly changes from $t = 20000$ to $t = 100000$. This regime is the so–called dispersionless, and is a natural outcome of the underdamped Brownian motion in a washboard

potential [Lindenberg et al., 2007], (Sec. 3.2.1). The one–sided exponential distribution is a straight consequence of the well–known exponential distribution of the first exit times of particles emerging a potential well [Redner, 2007], (Sec. 1.3.1); which for underdamped particles, to escape at a velocity $v = F/\gamma$, transforms to an exponential spatial distribution [Lindenberg et al., 2007]. The persistence of this spatial distribution would last until $t \sim l_0^2/2D$ [Lindenberg et al., 2007], when thermal fluctuations arise, and so the Gaussian distribution is resumed. $l_0 = (F/\gamma)t_K$ is the width due to dispersion of emergence times of the potential well, where t_K is the mean exit time—given by the Kramers' escape rate (1.20)—that depends on the system's parameters, the temperature, and the external force. May an exponential function

$$P(x,t) \propto exp(x/l_0) \tag{5.14}$$

be adjusted to the distributions in Figure 5.4 (F), then $l_0 \approx 5 \cdot 10^3$, hence the persistence time for the distribution to be exponential like ought to be clearly greater than the times at which the distribution has been plotted. May $l_0 = (F/\gamma)t_K$ be computed, it is of the same order of magnitude ($l_0 \approx 2 \cdot 10^3$) than the result obtained from the fitting of (5.14) to the simulation outcome.

Back to Figures 5.1 and 5.2, for the present case, $F = 0.35$ and a periodic potential, it exhibits regular transport and a linear decrease of the diffusion coefficient. Thus, the ensemble of particles moves at a finite constant ensemble velocity and with a fixed dispersion even though the particles are persistently subject to thermal fluctuations. This features are just those of the dispersionless anomalous regime reported in [Lindenberg et al., 2007].

5.2.3. Normal transport and undefined diffusion regime

$F = 1.6$ leads to the normal transport and undefined diffusion regime. The time evolution of diffusion in Figure 5.2 exhibits different regimes: an accelerated initial regime is followed by a superdiffusive one, and finally, a kind of dispersionless regime. Thus the effective diffusion can not be

defined. In contrast, the periodic case converges to normal diffusion. The distribution of particles (Fig. 5.4) (C) exhibits a broader distribution for the random potential, probably composed of two parts: the quasi–Gaussian distribution corresponding to the locked states, and a dispersionless forward distribution corresponding to the finite velocity states. For the periodic potential, a perfect single Gaussian distribution is displayed instead (G).

5.2.4. Normal transport and diffusion regime

Finally, the normal regime for both potentials is recovered at $F = 2.3$. Here the distribution is Gaussian centered at the mean value $\langle x(t)\rangle \sim \langle v\rangle t$.

5.3. Distributions of velocities

As did the histograms of the positions of the Brownian particles, the distributions of velocities can also shed light on the observed transport and diffusion anomalies [Marchenko and Marchenko, 2012; Marchenko et al., 2014]. Since the instantaneous velocity is a dynamical stochastic variable, its statistical moments and its distribution can be understood according to the four regimes discussed for the distributions of positions.

5.3.1. Subtransport and subdiffusion regime

Velocity histograms concerning the subtransport and subdiffusion regime, $F = 0.2$, are shown in Figure 5.6. They display a bimodal structure; they seem to be composed of two Gaussian distributions centered respectively at $\langle v\rangle = 0$ and at $\langle v\rangle = F/\gamma = 2$ indeed. Therefore, these two distributions can be related to the population of particles trapped in potential wells ($\langle v\rangle = 0$), and of running particles ($\langle v\rangle = F/\gamma = 2$). Accordingly, the histograms may be fitted with a function made up of two Gaussian curves,

$$W(v,t) = \frac{a_1}{\sqrt{2\pi c_1}}\, e^{-(v-b_1)^2/2c_1} + \frac{a_2}{\sqrt{2\pi c_2}}\, e^{-(v-b_2)^2/2c_2} \ . \tag{5.15}$$

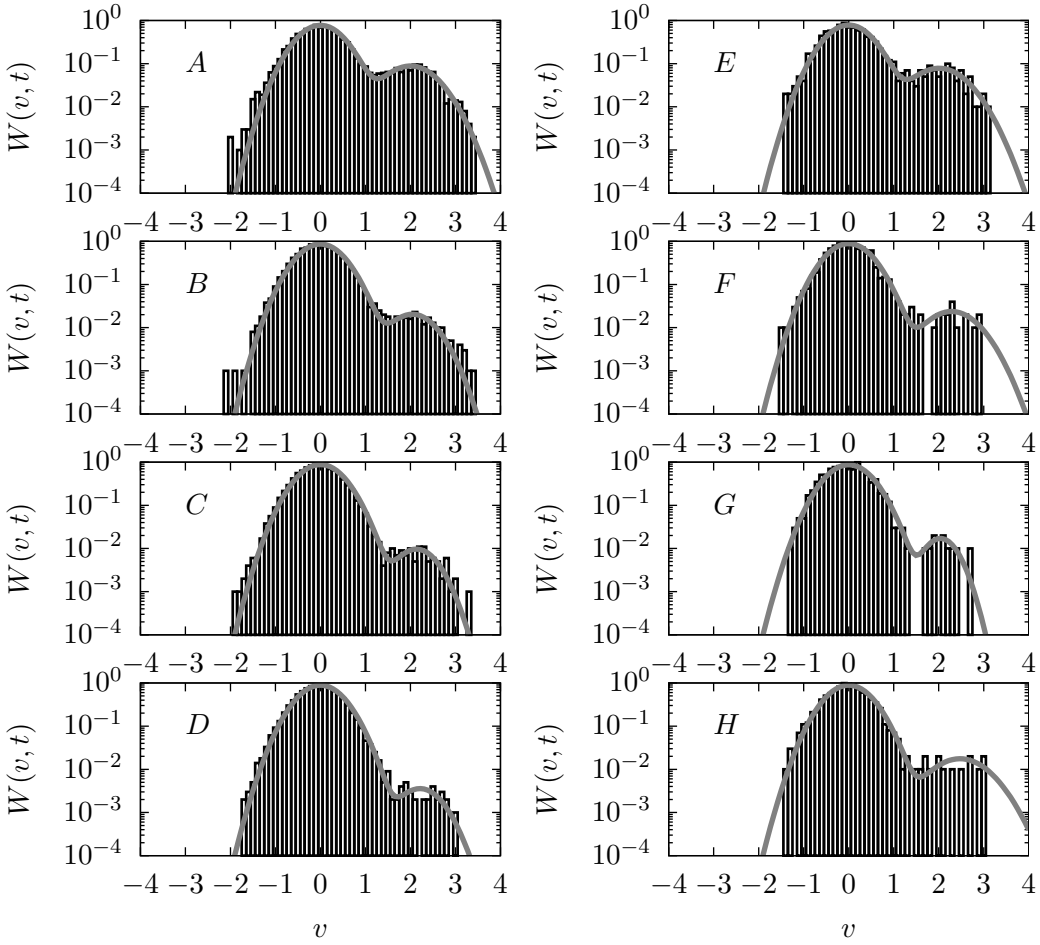

Figure 5.6 – Velocity histograms at times $t = 100$ (A-E), $t = 1000$ (B-F), $t = 10000$ (C-G), and $t = 100000$ (D-H) for underdamped Brownian particles ($\gamma = 0.1$) subject to an external force $F = 0.2$ in a random potential—left column—and in a periodic potential—right column—. A double Gaussian distribution (5.15) is also included in each plot, with the requirement that the left Gaussian in each case ought to correspond to the Maxwell's distribution (5.10) with $b_1 = 0$, and $c_1 = T = 0.2$.

random				
t	a_1	a_2	b_2	c_2
100	0.774 ± 0.009	0.09 ± 0.01	2.00 ± 0.07	0.26 ± 0.07
1000	0.86 ± 0.01	0.02 ± 0.01	2.1 ± 0.3	0.2 ± 0.3
10^4	0.88 ± 0.01	0.01 ± 0.01	2.1 ± 0.7	0.2 ± 0.5
10^5	0.89 ± 0.01	0.004 ± 0.015	2 ± 2	0 ± 2
periodic				
t	a_1	a_2	b_2	c_2
100	0.78 ± 0.02	0.08 ± 0.02	2.0 ± 0.16	0.28 ± 0.17
1000	0.88 ± 0.02	0.02 ± 0.03	2.3 ± 0.8	0.3 ± 0.7
10^4	0.87 ± 0.03	0.02 ± 0.05	2 ± 1	0.1 ± 0.9
10^5	0.88 ± 0.02	0.02 ± 0.02	2 ± 1	0 ± 1

Table 5.3 – Fitting parameters a_1, a_2, b_2, and c_2 upon adjusting (5.15) to the velocity histograms in Figure 5.6. Errors come from the numerical fitting process.

The constants b_1 and c_1 are settled on to $b_1 = 0$ and $c_1 = T$, for the first equilibrium Maxwell distribution in (5.15), so that they account for the distribution of particles trapped to a potential well. The remaining time–dependent parameters (a_1, a_2, b_2, and c_2) are fitted numerically and are listed for various times in Table 5.3. Since the population of particles in the second distribution—running particles—decreases with time, the relative uncertainty of the fitting parameters concerning this distribution increases for great times.

The numerical fitting of (5.15) brings about $b_2 \approx \langle v \rangle = F/\gamma = 2$ and $c_2 \approx 0.2 = T$ so it might be asserted that the second peak stands for a Maxwell's distribution of velocities for those particles that are pulled by the external force across the potential landscape indeed. The population of trapped particles is greater than that of running particles ($a_1 > a_2$). It ought to be enlightened that $a_1 + a_2 \neq 1$ as it might be expected, for the two Maxwellian distributions are entangled. Comparing the time unfolding of the distributions, it is gathered that the population of running particles undergoes a greater decrease for those underdamped particles in a random potential. The energy barriers of a periodic potential are all of the same height, thus, when a particle is able to escape from a potential well, it should remain in the running state until the friction, albeit weak,

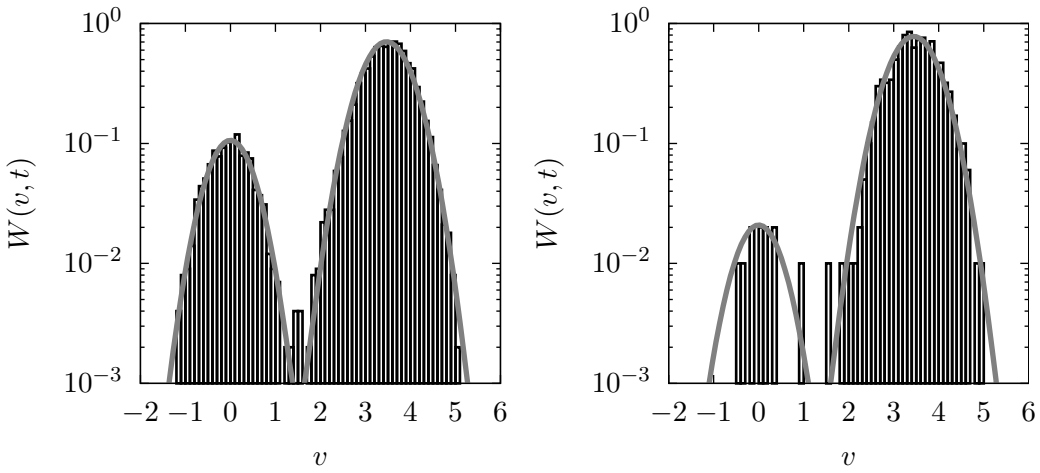

Figure 5.7 – Velocity histograms at time $t = 6000$ for underdamped Brownian particles ($\gamma = 0.1$) subject to an external force $F = 0.35$ in a random potential—left panel—and in a periodic potential—right panel—. A double Gaussian distribution (5.15) is also included in each plot, with the requirement that the left Gaussian in each case should correspond to the Maxwellian distribution with $b_1 = 0$, and $c_1 = T = 0.2$.

eventually dissipates enough kinetic energy and the particle resumes the locked state. Any particle in the running state under a random potential is otherwise likely to run into an unsurmountable barrier at any time; and so it might get trapped sooner. Besides, as the time goes on, the ensemble of particles in a random potential may attach to those deepest potential wells, therefore the releasing rate is expected to decrease; whereas in a periodic potential it should be invariable since the wells are all of the same depth.

The steady locked and the running state populations reached in a periodic potential lead to normal transport and Fickian diffusion (Fig. 5.1) and (Fig. 5.2). On the other hand, anomalous subtransport and subdiffusion is exhibited in a random potential (Fig. 5.1) and (Fig. 5.2) because of the unbalanced transition rate between states.

random				
t	a_1	a_2	b_2	c_2
100	0.377 ± 0.006	0.497 ± 0.007	3.449 ± 0.008	0.247 ± 0.008
400	0.237 ± 0.005	0.598 ± 0.006	3.461 ± 0.005	0.236 ± 0.005
1000	0.176 ± 0.005	0.650 ± 0.006	3.442 ± 0.005	0.238 ± 0.005
4000	0.117 ± 0.005	0.726 ± 0.006	3.450 ± 0.005	0.238 ± 0.005
10000	0.099 ± 0.005	0.90 ± 0.06	3.451 ± 0.004	0.235 ± 0.004
periodic				
t	a_1	a_2	b_2	c_2
100	0.531 ± 0.014	0.336 ± 0.017	3.443 ± 0.02	0.22 ± 0.03
400	0.454 ± 0.018	0.44 ± 0.02	3.45 ± 0.03	0.20 ± 0.02
1000	0.303 ± 0.015	0.516 ± 0.018	3.41 ± 0.02	0.26 ± 0.02
4000	0.044 ± 0.017	0.728 ± 0.018	3.437 ± 0.015	0.275 ± 0.015
10000	0.02 ± 0.03	0.84 ± 0.02	3.484 ± 0.014	0.22 ± 0.02

Table 5.4 – Fitting parameters a_1, a_2, b_2, and c_2 upon adjusting (5.15) to the histograms in Figure 5.7 and to the corresponding histograms for other times. Errors come from the numerical fitting process.

5.3.2. Normal transport and superdiffusion regime

$W(v,t)$ at $t = 6000$ is plotted in Figure 5.7 for the normal transport and superdiffusion regime ($F = 0.35$) displayed in a random potential. It clearly exhibits two peaks, again corresponding respectively to the locked and the running states of Brownian particles. The histogram is well fitted by a two Gaussian function (5.15)—results are included in Table 5.4 for different times—.

The parameter c_2 reveals a small systematic deviation from $T = 0.2$, yet b_2 fits very well with the deterministic velocity $\langle v \rangle \approx 3.5$. Therefore, the distribution of velocities is made of two Maxwellian distributions at $\langle v \rangle \approx 0$ (locked particles) and $\langle v \rangle \approx 3.5 = F/\gamma$ (running particles). The parameters a_1 and a_2 at all times satisfy the condition $a_1 + a_2 \simeq 1$ upon normalization of the histogram and because of the two distributions hardly merge.

It should be noted that, contrary to the behavior in the lower force regime discussed above, in this higher force regime the population in the

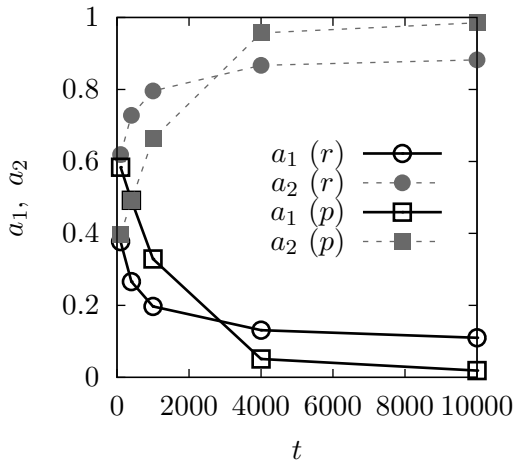

Figure 5.8 – Time evolution of the weight parameters a_1 and a_2 of the two Gaussian functions that parametrize the histogram of velocities for underdamped Brownian particles ($\gamma = 0.1$) under a random potential (r) and a periodic potential (p). The external force is $F = 0.35$ for both cases.

running state increases with time, whereas the locked state decreases, for both the random and the periodic potentials. This behavior is illustrated by a_1—decreasing with time—and a_2—increasing with time—in Table 5.4, and also plotted in Figure 5.8. For a periodic potential, there is a fast migration of locked particles into the running state, whereas this migration is slower in a random potential due to the presence of higher energy barriers. Considering a periodic potential, the fraction of particles in the running state attains $a_2 \approx 1$ within the time lasting the simulations, which is consistent with the already discussed dispersionless regime that comes to light under such setting. However, there is a steady, at least for the observational time, population of particles in the locked state when a random potential is otherwise employed, and hence superdiffusion might be observed endless in that case.

5.3.3. Normal transport and undefined diffusion regime

Normal transport and undefined diffusion is obtained for $F = 1.6$. The histogram of the velocities in this regime for both potentials is simply a steady Maxwell distribution centered at $\langle v \rangle = 16$,

$$W_{st}(v) = \frac{1}{\sqrt{2\pi\, T}}\, e^{-(v-\langle v \rangle)^2/2T}. \tag{5.16}$$

However, for a random potential at early times (Fig. 5.9), it is observed a small portion of the distribution centered at the origin, which is a tracer of the few particles that are still attached to the deepest wells of the random potential. This is reminiscent of the histogram at lower forces, in which there is an interplay between the running and the locked states, manifested by the presence of two Gaussians (Figures 5.6 and 5.7). This observation supports the description of undefined diffusion in Chapter 4, and [Suñé et al., 2013], as the interplay of a few locked particles while the majority of the particles are in the running state.

5.3.4. Normal transport and regime

Finally, the distribution of velocities in the normal transport and normal diffusion regime is Maxwellian (5.16), centered at $\langle v \rangle = F/\gamma = 23$. The force $F = 2.3$ completely overwhelms the effects of the nonlinear potential, leading to free Brownian motion.

5.4. Summary and conclusions

Transport and diffusion of underdamped Brownian particles in random potentials and driven by a constant external force exhibit anomalies similar to those seen in diffusion of overdamped Brownian particles (Chap. 4), [Suñé et al., 2013]. The present Chapter has been devoted to the effects of underdamping—as compared to the case of overdamped particles—and of disorder—as compared to the behavior in periodic potentials—. In general, no matter the damping or the potential, when the constant force is

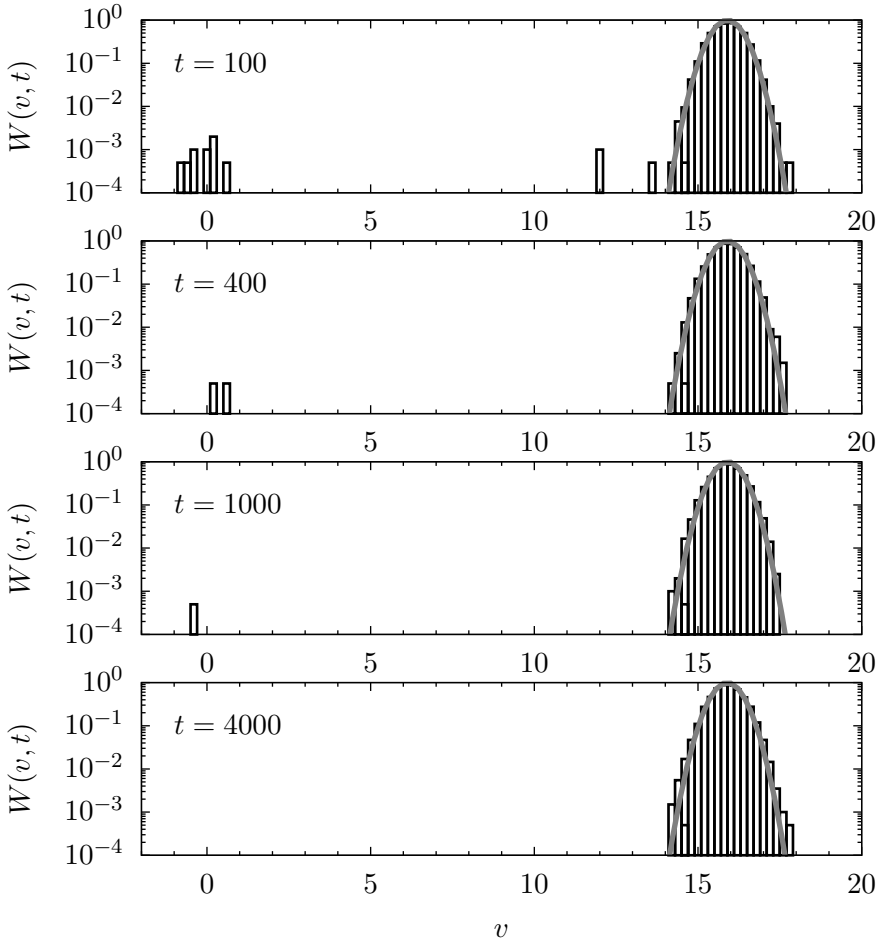

Figure 5.9 – Velocity histograms at different times for underdamped Brownian particles ($\gamma = 0.1$) subject to an external force $F = 1.6$ in a random potential. A Gaussian distribution (5.16) is depicted around the distribution centered at the mean velocity of free particles $\langle v \rangle = 16$.

sufficiently strong, the force masks all else and the particles simply move as pushed by the force, with a distribution due to the thermal noise. However, anomalous transport and diffusion regimes arise at rather weak forces both in periodic and random potentials.

Concerning random potentials, the observed anomalies are subtransport, supertransport—weak—, subdiffusion, superdiffusion, as well as undefined diffusion. They are arranged in the usual sequence: subtransport and subdiffusion for the weakest forces, increasing the force superdiffusion arises, normal transport is resumed subsequently; and eventually Fickian diffusion is recovered too, after a range of forces in which the dispersion of the particles' displacements does not reach a regular behavior, and so the diffusion coefficient cannot be computed.

Regarding supertransport, it ought to be enlightened its observation—albeit being it weak—just before normal transport is recovered. However, it might not be a conclusive proof—due to its weakness—to contradict the hypothesis that supertransport would not arise under static non-linear potentials (Chap. 3). Further investigations ought to be done in order to gather more convincing evidences of that scenario.

For the high–friction limit ($\gamma = 4$) transport exponents lie between subtransport ($\alpha < 1$) and normal transport ($\alpha = 1$), according to the overdamped outcome (Chap. 4).

The force span of the transport and diffusion features exhibits some dependence on the damping of the Brownian motion; the course of anomalies comes about at a weaker forces in the underdamped conditions indeed. Contrarily, when considering underdamped Brownian motion in a periodic potential, normal transport and Fickian diffusion are exhibited aside from some early transients and the well–known dispersionless regime [Lindenberg et al., 2007].

The histograms of the ensembles of particles' displacements shed light

on the physical mechanisms to bring about anomalous transport and diffusion regimes. On top of that, while in the overdamped approach the kinetic energy is assumed to be instantaneously dissipated by friction, and so particles come to a standstill, for underdamped Brownian motion the instantaneous velocity is but a non–zero random variate. Accordingly, the distribution of instantaneous velocities can be computed and might bring about additional information about the transport and diffusion clues. It is gathered that the velocity very rapidly reaches local equilibrium, displaying a Maxwell distribution either around the locked $\langle v \rangle = 0$ state or around the running $\langle v \rangle = F/\gamma$ state or both. This observation proves that the origin of the anomalies is the randomness of the barrier crossing process, as manifested in the distribution of particle positions. The specific features of the distribution, such as the weight of each Maxwell distribution and their time unfolding, are also correlated to the different anomalies.

The present results may help in the understanding of experimental results on diffusive motion of molecules on solid substrates where friction may be low [Schunack et al., 2002; De Wijn, 2011; Liu et al., 2012; Lee et al., 2014; McMullan et al., 2015; Skaug et al., 2015].

Next Chapter is devoted to the study of Brownian motion in disordered dynamic landscapes made of unsurmountable obstacles.

CHAPTER 6

Brownian motion on random dynamical landscapes

The previous Chapters deal with the transport and diffusion properties of mesoscopic particles suspended in a thermal environment and subject to a nonlinear potential [De Gennes, 1975; Bouchaud and Georges, 1990; Sancho and Lacasta, 2010]; attention is mainly concerned with static random potentials indeed [Sancho and Lacasta, 2010; Sancho et al., 2004; Khoury et al., 2011; Suñé et al., 2013; Suñé et al., 2014]. The reliability of the achieved outcome is thus hindered to the solid state scenario, in which potential configurations do not change with time [Schunack et al., 2002; Xu et al., 2011; De Wijn, 2011]. Nevertheless, Brownian motion is often employed to describe the motion of a solute immersed in soft matter mixtures, which may be better accounted by dynamic landscapes. Among many examples of Brownian motion in a soft matter solution, it could be mentioned the diffusion of regulatory proteins on DNA molecules [Goychuk and Kharchenko, 2014], the diffusion of small solutes and macromolecules, including green fluorescent protein GFP-S65T, fluorescently labelled dextrans, and DNAs, in cytoplasm [Dix and Verkman, 2008], the diffusivity of lipid and protein molecules in flat membranes [Khoshnood and Jalali, 2013], and the tracking of single particles immersed in artificial crowded fluids [Weiss, 2013]. A common property of these type of solutions—composed

of the Brownian solute, the aqueous solvent and other soft matter entities—is that they often undergo crowding effects [Ellis and Minton, 2003]; that is, the available volume for tracer particles to diffuse is drastically reduced by the presence of other solute particles, such as macromolecules, organelles, colloids and polymers. There are both experimental and computational evidences of anomalous transport and diffusion ascribed to the crowding phenomenon [Höfling and Franosch, 2013]: sublinear power–law increase of the mean–square displacement as function of the lag time, strongly reduced and time–dependent diffusion coefficients, persistent correlations in time, non–gaussian distributions of spatial displacements, heterogeneous diffusion, and a fraction of immobile particles.

The goal of the present Chapter is therefore to model Brownian motion of tracer particles in densely packed landscapes of moving deformable obstacles which interfere with the movement of the tracer particles. The model may extend, for example, to portray transport and diffusion in scenarios such as the cell cytoplasm [Dix and Verkman, 2008; Trovato and Tozzini, 2014], the cell membrane [Dix and Verkman, 2008; Khoshnood and Jalali, 2013], and monolayers of colonies of gliding bacteria [Peruani et al., 2012].

The former examples belong to the active matter realm, and so their dynamics may, for instance, be described by hydrodynamic equations for a macroscopic field [Basu et al., 2008; Sarkar and Basu, 2011; Marchetti et al., 2013]. Notwithstanding, here it is developed a reduced representation of the active matter media. The model consists in a static random potential [Suñé et al., 2012], which it is then transformed by a linear Langevin equation to generate a time–dependent random potential. The resulting random potential describes a medium (e.g., a surface) of moving wells and barriers. In order to account for big obstacles that may interfere with the motion of tracer particles, by the time they are deformed, they associate, and they stir, the random potential is nonlinearly transformed so that it brings about a new potential landscape of unsurmountable dynamic obstacles. Such obstacles disrupt the motion of Brownian particles, which would profoundly affect the velocity, diffusion coefficient [Vilaseca et al., 2011;

Gori et al., 2016], leading occasionally to the so–called "anomalous diffusion" [Höfling and Franosch, 2013], and chemical reaction rates [Pitulice et al., 2014; Klann et al., 2011].

Among the several approaches to the theoretical description of Brownian motion in various disordered settings [Stauffer et al., 2008; Jeon et al., 2014], the present method of choice is again the classical Langevin equation in the overdamped limit (Chap. 4). Friction is then much larger than inertial forces—Reynolds number is low, as it is in plenty of biological systems—. The landscape has no bias, but a constant force $\boldsymbol{F}$ is introduced so that transport can be studied along with diffusion. A variety of numerical results are submitted for the velocity and diffusion of the overdamped Brownian particles in this varying crowded landscape, for which it is assumed that the dynamics of the obstacles are slow compared to the time scales of the random motion of the tracer particles.

6.1. Spatio–temporal disorder

The dynamical landscape of impenetrable obstacles is described by a spatio–temporal potential $U(\boldsymbol{r}, t)$. The numerical algorithm to generate this potential is profoundly discussed in Chapter 7. It should be noted that the dimensionless variables and parameters defined in Section 1.4.2 will be employed throughout this Chapter.

The random potential $U(\boldsymbol{r}, t)$ will consist of obstacles of a fixed height in an otherwise flat landscape. The obstacles' width can vary with time and they move around on this landscape. The relevant parameters to characterize the obstacle landscape are the height V_H of the obstacles, the spatial disorder length scale λ, which translates to the average obstacle width, the time scale t_0^o of the obstacle dynamics, and the density of obstacles ρ.

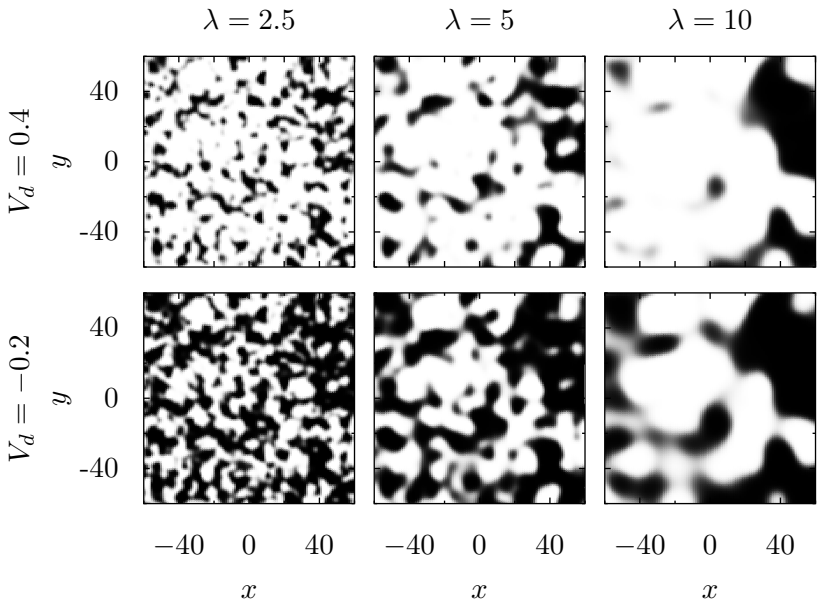

Figure 6.1 – $2-d$ random potentials $U(\boldsymbol{r},0)$ with $\lambda = 2.5$, 5, 10, a=0.1 (a controls the barrier stiffness, see Section 7.2), $V_H = 2$, and V_d= 0.4 (upper row) and -0.2 (bottom row) (V_d is the height at which $V(\boldsymbol{r},t)$ is cut to transform to $U(\boldsymbol{r},t)$, see Section 7.2). Other parameters: $\Delta = 0.5$, $N = 2^8$. White patches are the flat portions at null potential, black patches indicate the obstacles of height V_H.

6.1.1. Potential's settings

A discussion on the parameters that set up the potential's attributes is worth of consideration:

- The obstacles' height, V_H : Brownian particles undergo thermal fluctuations, whose intensity comes from the temperature T, and they may be as well pulled by an external force $\boldsymbol{F}$. Therefore, for the obstacles to be impassable, the following condition ought to rule,

$$V_H - |\boldsymbol{F}| \cdot \lambda \gg T\,. \tag{6.1}$$

- The characteristic length, λ: It is linked to the size of the potential's obstacles, hence it is necessary that

$$\lambda \ll N \cdot \Delta\,, \tag{6.2}$$

where $N\Delta$ is the size of the system, so as to preserve the statistical reliability. A characteristic length being not far smaller than the size of the system would reduce the number of obstacles, and so the collectivity's statistical reliability may decrease as well. Figure 6.1 includes realizations of the disordered field with different characteristic lengths. The shorter the characteristic length, the smaller the obstacles. The right panel in Figure 6.1 evidences that there may be few obstacles in a system with $\lambda = 10$ and size $N \cdot \Delta = 128$, hence it reinforces the assumption made (6.2).

- The time scale, t_0^o : The characteristic time to control the evolution of the disorder potential should be larger than the time for the particles to spread by diffusion a distance comparable to the potential's characteristic length, that is

$$t_0^o \gg \frac{\lambda^2}{2T}\,. \tag{6.3}$$

  Particles wouldn't explore the spatial features of the potential otherwise, and thus it might lead to a scenario far from the present proposal. Figure 6.2 displays the time series of a random potential with different time scales. It can be gathered that short time scales lead to rapid deforming and moving obstacles, since the time correlation of the landscape decreases fast. That is, the landscape with $t_0^o = 100$ hardly reshapes from $t = 0$ to $t = 2$; whereas for $t_0^o = 0.2$ the disorder exhibits no correlation, even concerning consecutive instants at times separated $t = 1$. Finally, it ought to be noticed that t_0^o is equivalent to τ_0, the relaxation time of the $\mathcal{V}_0$ mode of the random dynamic potential in Fourier space, from which is obtained the obstacle landscape (Chap. 7).

- The density of obstacles ρ: It is the ratio of sites at height $U(\boldsymbol{r}, t) = V_H$ to the total occupied system. Assuming that the parameter a is small so that barrier growth is fast enough to dismiss intermediate barrier heights, ρ is

$$\rho = \frac{1}{N^2 V_H} \sum_i U(\boldsymbol{r}_i\,, t)\,, \tag{6.4}$$

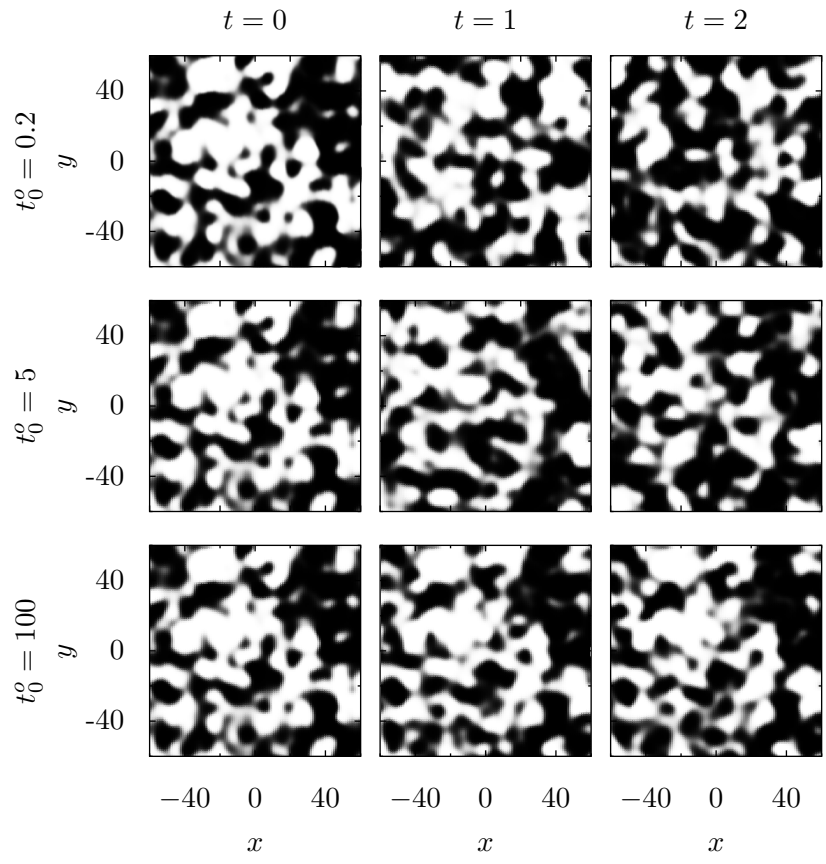

Figure 6.2 – $2-d$ random potentials $U(\boldsymbol{r}, t)$ at different times with $\lambda = 5$, $a = 0.1$, $V_H = 2$, and $V_d = -0.2$ of disordered fields with different time scales $t_0^o = 0.2,\ 5$, and 100. Other parameters: $\Delta = 0.5$, $N = 2^8$. White patches are the flat portions at null potential, black patches indicate the obstacles of height V_H.

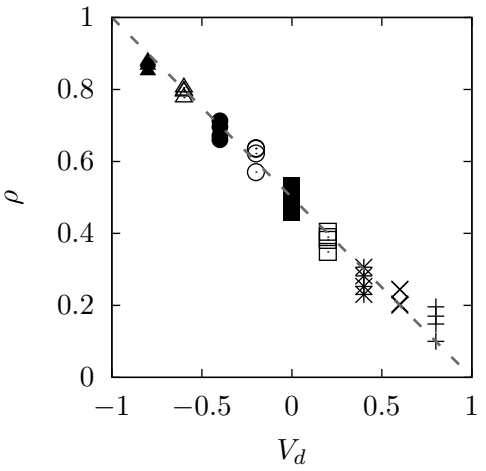

Figure 6.3 – Obstacle density ρ of the $2-d$ random potentials $U(\boldsymbol{r},t)$ as a function of V_d. Other parameters: $a=0.1$, $\lambda=5$, $\Delta=0.5$, and $N=2^8$.

where i labels all the mesh points of the real–space $2-d$ lattice. According to (6.4) the upper landscapes in Figure 6.1 have a density of obstacles $\rho\approx 0.3$, whereas for the lower panels $\rho\approx 0.6$. With other parameters fixed, V_d is thus the parameter that sets up the density of obstacles. The plot in Figure 6.3 reveals a linear relationship between ρ and V_d . The multiple symbols of a given shape denote repeated runs at that value of V_d , yet with different seeds for the random number generator.

6.2. Brownian motion in–between unsurmountable dynamic obstacles

Trajectories $\boldsymbol{r}(t)$ of tracer particles in the potential $U(\boldsymbol{r},t)$ with a constant biasing force $\boldsymbol{F}$ are generated through numerical simulations of Langevin dynamics. In particular, assuming the overdamped approach (Sec. 1.4.2), the stochastic differential equation describing the spatial w^{th} component $r_w(t)$ ($w=x$ and $w=y$) of $\boldsymbol{r}(t)$ is given by

$$\frac{dr_w(t)}{dt} = -\frac{\partial}{\partial r_w}U(\boldsymbol{r}/\lambda,t) + F_w + \xi_w(t). \tag{6.5}$$

The term $\boldsymbol{\xi}(\boldsymbol{r},t)$ is a zero–centered random Gaussian vector that satisfies the fluctuation–dissipation relation,

$$\langle \xi_w(t)\, \xi_{w'}(t')\rangle = 2\,\delta_{w,w'}\,T\,\delta(t-t'), \tag{6.6}$$

where T is the scaled temperature.

A second order Heun algorithm (Sec. 7.5.1) is employed for ordinary stochastic differential equations to simulate the trajectories predicted by the Langevin equation (6.5) [García-Ojalvo and Sancho, 1999; Toral and Colet, 2014]. The forces derived from the random potential $U(\boldsymbol{r},t)$ are computed by simple centered discrete derivatives [Suñé et al., 2012], (Sec. 7.3). At intermediate locations the random force is evaluated by standard linear interpolation of the forces at the lattice points [Suñé et al., 2012], (Sec. 7.4). As it is customary in the former Chapters, transport and diffusion properties of the Brownian motion of an ensemble of n particles are surveyed. The specific quantities that are computed with these trajectories are the mean velocity and diffusion coefficients,

$$\langle \boldsymbol{v}_{\parallel}(t)\rangle = \frac{\langle \boldsymbol{r}_{\parallel}(t)\rangle}{t}\,, \quad D_{\parallel,\perp}(t) = \frac{\langle \Delta \boldsymbol{r}^2_{\parallel,\perp}(t)\rangle}{2t}\,, \tag{6.7}$$

where the brackets indicate an ensemble average. The parallel and the perpendicular directions with respect to the external force $\boldsymbol{F}$ are explicitly distinguished. It should be noted that $\langle \boldsymbol{v}_{\perp}\rangle$ is always zero.

6.2.1. Numerical settings

The characteristic time t_0^o for the dynamical evolution of the potential must be greater than the time it typically takes the Brownian particles to spread over a distance comparable to the characteristic width of a potential obstacle (Sec. 6.1.1). Unless otherwise indicated, the scaled temperature is $T = 1$, and the scaled external force $|\boldsymbol{F}| = 0.6$. Simulations run up to a maximum time $t_{max} = 4000$. At the other end, the time step of integration Δt should be much shorter than the time it takes a Brownian particle to cover the distance λ when pulled by the force $\boldsymbol{F}$, that is, $\Delta t \ll \lambda/|\boldsymbol{F}|$. Thus, the choice for the integration time step is $\Delta t = 0.01$. The rest

n	N	Δ	t_{max}	Δt	$\lvert\boldsymbol{F}\rvert$	T	t_0^o	λ	ρ	V_H	a
4000	2^{11}	0.5	4000	0.01	0.6	1	400	2.5, 5	0.1-0.9	25	0.1

Table 6.1 – Settings for the further on outcome.

of parameters are settled on according to the discussion in Section 6.1.1: $\Delta = 0.5$, $N = 2^{11}$, $V_H = 25 \gg T + \lambda|\boldsymbol{F}|$, and $a = 0.1$. Hence there still remain three control parameters: V_d—or, equivalently, ρ—, λ, and t_0^o. Typically, the trajectories of 4000 particles are simulated in a single realization of the random potential of obstacles. Initially the particles are distributed uniformly in a square area of size $2\lambda \times 2\lambda$ centered at $(N/5, N/5)$ and placed on sites with $U(\boldsymbol{r}, 0) = 0$, thus avoiding locations on top of the obstacles. Table 6.1 summarizes the parameter choices for the simulation results to come.

6.2.2. General qualitative overview

In Figure 6.4 the force is directed at an angle $\arctan 0.5 \approx 26.57$ degrees with respect to the horizontal axis. Some interesting features of these simulations may be noticed. Blue patches indicate obstacles, and the light ones flat portions. In red there are the particles executing Brownian motion. The discrete x and y coordinates shown here extend from 0 to 120. Patterns in columns from left to right are for times $t = 0, 30, 60, 90$. Moving from top to bottom are four rows of different situations: parameter values $t_0^o = 400$, $\lambda = 2.5$, and $\rho = 0.6$ (first row); $t_0^o = 400$, $\lambda = 5$, $\rho = 0.3$ (second row); $t_0^o = 400$, $\lambda = 5$, $\rho = 0.6$ (third row), and $t_0^o = 10^5$, $\lambda = 5$, $\rho = 0.6$ (fourth row). The first and third rows differ only in the obstacle width, and so, since the density is the same in both cases—t_0^o as well—, there are more obstacles in the first row than in the third. Therefore, it reveals that Brownian particles are able to move around obstacles more readily when there are fewer—albeit wider—obstacles, in agreement with the results achieved by Monte Carlo simulations of particle diffusion in $3 - d$ obstructed lattices Vilaseca et al. [2011]. The second and third rows differ only in the density of obstacles, which are of the same width. It can be seen that Brownian particles spread more easily when the density is lower, that is, in the second row. The

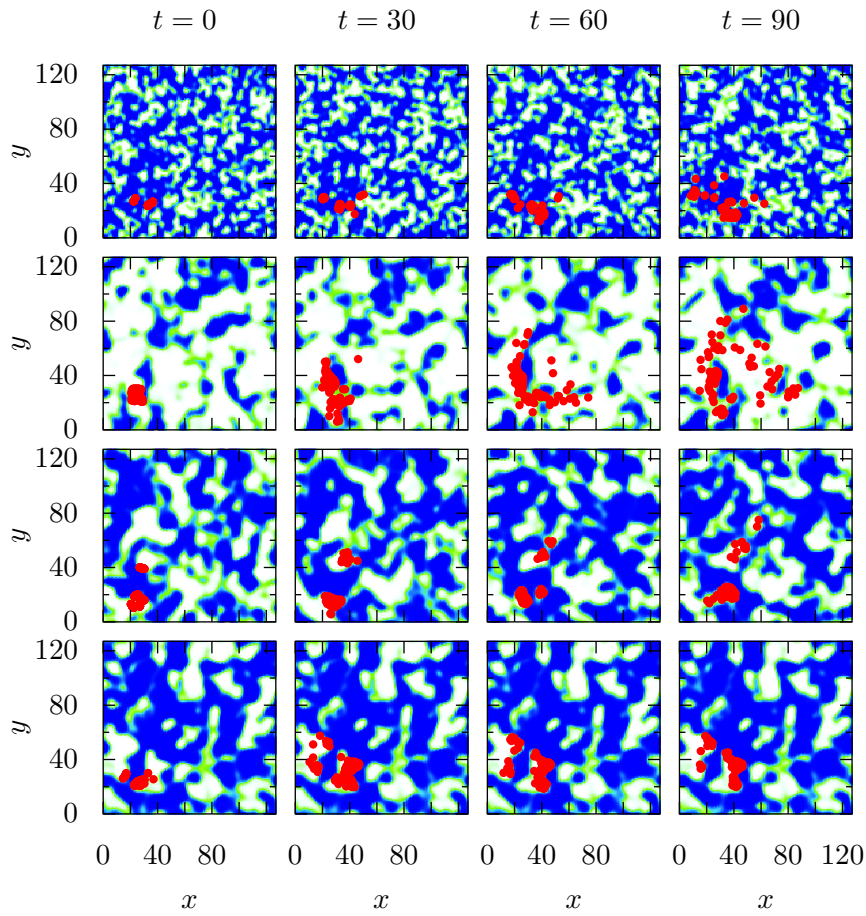

Figure 6.4 – The blue patches indicate the obstacles, and the light ones the flat portions. In red are the particles executing Brownian motion. Patterns from left to right in each row are for $t = 0$ (initial condition), $t = 30$, $t = 60$, and $t = 90$. Moving from top to bottom the panels are for the parameter values $t_0^o = 400$, $\lambda = 2.5$, and $\rho = 0.6$ (first row); $t_0^o = 400$, $\lambda = 5$, $\rho = 0.3$ (second row); $t_0^o = 400$, $\lambda = 5$, $\rho = 0.6$ (third row), and $t_0^o = 10^5$, $\lambda = 5$, $\rho = 0.6$ (fourth row). The force $|\boldsymbol{F}| = 0.6$ is directed at an angle $\arctan 0.5 \approx 26.57$ degrees with respect to the horizontal axis.

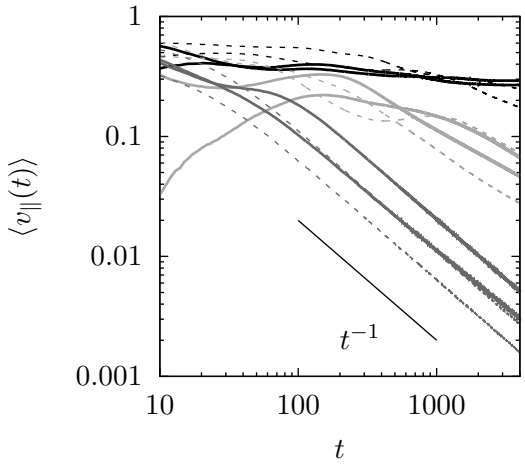

Figure 6.5 – Mean parallel velocity curves as a function of time for a set of particles on static surfaces of different obstacle densities: $\rho = 0.1$ black trajectories, $\rho = 0.3$ light gray trajectories, $\rho = 0.7$ dark gray trajectories; for $\lambda = 2.5$ solid lines, and $\lambda = 5.0$ dashed lines. The straight black line is a guide. There are two trajectories for each choice of parameters, that correspond each one to the 4000 particles average in a particular realization of the random potential and of the initial conditions—that is, they only differ from the seed taken for random number generator—.

third row most clearly shows the existence of two separate populations, one that is pretty much trapped and another that is pulled along by the constant force. The fourth row shows trapping of practically all of the Brownian particles that occurs when the obstacle dynamics is extremely slow, essentially one equivalent to a distribution of static obstacles over the time scale of this realization.

6.2.3. Static landscapes

As a first stage analysis, it is worthy of consideration the impact of the obstacle density and the obstacle width on the transport and diffusion displayed by Brownian particles undergoing a static obstacle landscape U, that is $t_0^o \to \infty$. The most iconic outcome in this scenario is plotted in Figures 6.5 and 6.6. For high obstacle densities ($\rho = 0.7$, dark gray curves), and disregarded the characteristic length, both the mean velocity and the diffusion coefficients decrease with time as t^{-1}, thus exhibiting particle

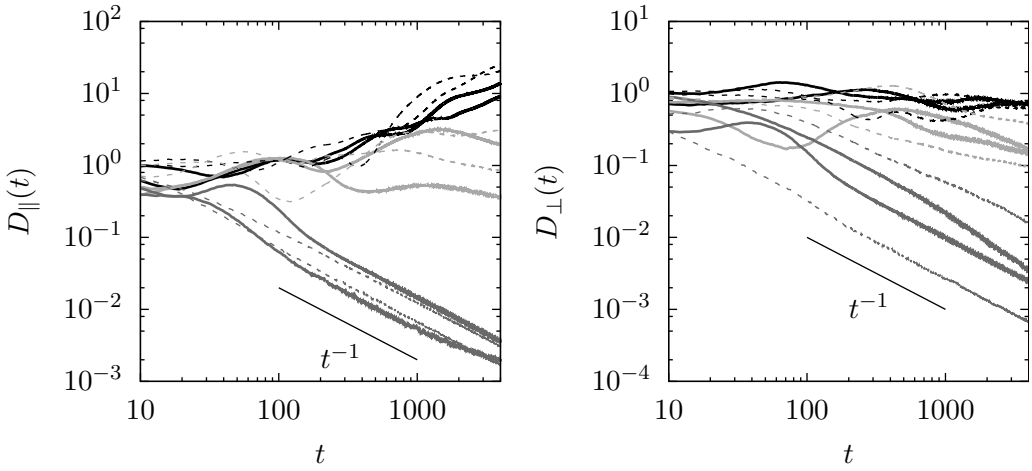

Figure 6.6 – Mean parallel and perpendicular diffusion curves corresponding to the simulation results already displayed in Figure 6.5. Grey scale legend is analogous. There are two trajectories for each choice of parameters, that correspond each one to the 4000 particles average in a particular realization of the random potential and of the initial conditions—that is, they only differ from the seed taken for random number generator—.

trapping in the potential obstacles. This case may be similar to the lowest row of Figure 6.4, in which the Brownian particles just can't spread indeed. Here there is no opportunity to develop two populations, one of trapped particles and another one running particles, as is seen with fewer obstacles and/or faster obstacle dynamics. Realizations of the potential, either with equal λ or not, exhibit differences which are a trace of the transient regime before all the particles become trapped. This transient regime may depend upon the landscape region where particles are initially allocated, and so the reported discrepancies are worthless.

The opposite limit, that is, particles undergoing a landscape with a very low density of obstacles ($\rho = 0.1$, black curves), displays a finite velocity, and a finite perpendicular diffusion coefficient as well. The parallel diffusion coefficient though grows with time—superdiffusion—mainly due to a reminiscence of the superdiffusive mechanism already described in [Sancho et al., 2004; Khoury et al., 2011; Suñé et al., 2013; Suñé et al., 2014], (Chapters 3

to 5), that is, particles are split among two populations, few are trapped by the potential obstacles, whereas the rest undergo ballistic motion pulled by the external force. Analogously to the high density scope, for low obstacle density landscapes the width of the obstacles does not affect the outcome significantly.

For what it concerns a rather low density ($\rho = 0.3$, trajectories in light gray), velocity exhibits an erratic transient, yet long lasting, regime that eventually leads to a decreasing steady trajectory with slope ≈ -1, indicating thus subtransport with nearly all the particles in the locked state. The results for the associated diffusion coefficients behave uncertain, yet exhibiting an undoubtably decreasing tendency with time—subdiffusion—for the perpendicular diffusion coefficient in all cases.

In summary, when obstacles are immobile there may be particles trapped by the obstacles during the entire simulation, at a rate—trapped to free particles—that depends on the density of obstacles. The entire ensemble of particles remains attached to the landscape at high obstacles densities, while an increasing number of particles are able to move on as the density of obstacles decreases. Therefore, anomalous transport and diffusion regimes are observed as the density of obstacles decreases, similar to the results for static corrugated random potentials when increasing the tilting force [Suñé et al., 2013], (Chap. 4).

No pulling force

Consider now a zero external force ($\boldsymbol{F} = \mathbf{0}$). It should be noted that there is no transport ($\langle v_{\parallel}(t) \rangle = 0$ as well). Some differences arise when comparing diffusion trajectories in Figure 6.7 to those in Figure 6.6. Firstly, superdiffusion no longer appears because there's no force. For particles undergoing low density potentials, constant diffusion coefficients are reached instead. As the density increases, subdiffusion regimes arise. Finally, within potentials exhibiting a high concentration of obstacles, diffusion coefficients display t^{-1} behavior, revealing thus particle caging.

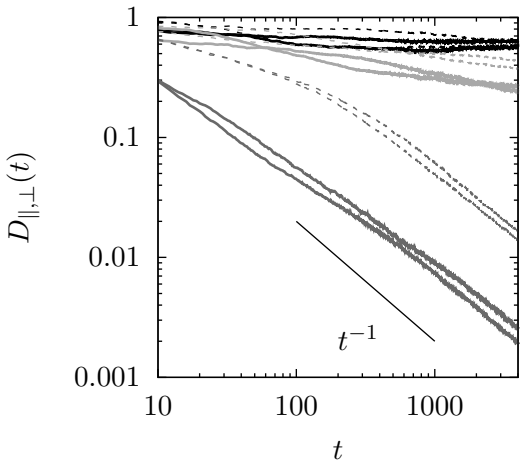

Figure 6.7 – Mean parallel and perpendicular diffusion curves as a function of time for the same conditions as in Figure 6.5, but with zero external force ($\boldsymbol{F} = \mathbf{0}$). Black trajectories label the results to arise from $\rho = 0.1$, light grey those from $\rho = 0.3$, and dark grey the ones with $\rho = 0.7$. As usual, dashed lines refer to $\lambda = 5$, whereas $\lambda = 2.5$ are displayed in solid. There are two trajectories for each choice of parameters, that correspond each one to the 4000 particles average in a particular realization of the random potential and of the initial conditions—that is, they only differ from the seed taken for random number generator—.

Figure 6.7 also uncovers the obstacle size to play a remarkable role in the results. For an ensemble of particles running potentials with a fixed density of obstacles, diffusion trajectories reach the asymptotic limit t^{-1} earlier when the length scale is shorter, that is, when the landscape is made of a great number of narrow obstacles. Therefore, it seems that particle caging is faster under such circumstances than when there are a few yet wider obstacles.

It ought to be enlightened that the former inferences concerning static potentials do apply unchanged for landscapes of extremely slow dynamics. There is agreement between those results to come from simulations with a large, yet finite, t_0^o and the depicted features in Figures 6.5 to 6.7.

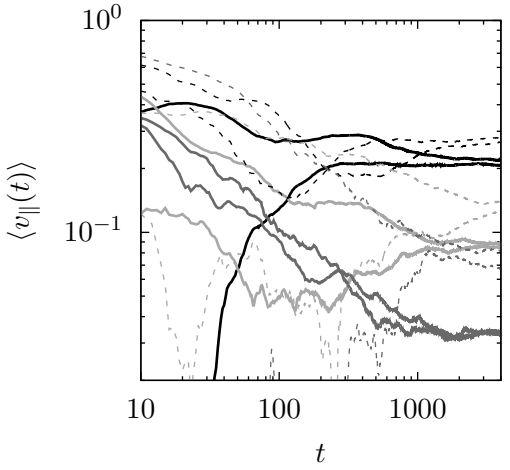

Figure 6.8 – Mean parallel velocity curves as a function of time for a set of particles on dynamic surfaces of different obstacle densities: $\rho = 0.1$ black trajectories, $\rho = 0.3$ light gray trajectories, $\rho = 0.7$ dark gray trajectories; and widths $\lambda = 2.5$ solid lines, and $\lambda = 5.0$ dashed lines. There are two trajectories for each choice of parameters, that correspond each one to the 4000 particles average in a particular realization of the random potential and of the initial conditions—that is, they only differ from the seed taken for random number generator—.

6.2.4. Dynamic landscapes

In the opposite limit of small values of t_0^o—rapid rearrangement of the obstacles—normal transport and diffusion arise, as it would be expected. The most revealing scenario might thus be the intermediate case of the motion of Brownian particles in–between dynamic obstacles, yet moving slowly compared to the Brownian movement—settings enlisted in Table 6.1—. In this milieu, transport and diffusion exhibit two different regimes: anomalous for $t \leq t_0^o$, and asymptotically ($t \gg t_0^o$) settling to a constant value (Figures 6.8 and 6.9). This behavior is also reported for both Monte Carlo simulations [Vilaseca et al., 2011] and experimental measurements [Dix and Verkman, 2008] of diffusing particles undergoing molecular crowding. It is worth noting that those results concerning a landscape of wider obstacles—dashed trajectories—seem to exhibit longer transient regimes as well as a greater discrepancy between repetitions of the simulations. This might be a consequence of the decrease of statistical population, for that increasing

the obstacles' size reduces the amount of obstacles of the landscape.

This asymptotic behavior differs strikingly from the outcome brought about by a static potential (Sec. 6.2.3). Within such a scenario the asymptotic mean velocity as well as the diffusion coefficient can be computed, hence it can be studied the effect of the remaining control parameters—the size and density of obstacles—on them. On the one hand, the asymptotic mean velocity decreases nonlinearly with increasing obstacle density; starting at the free Brownian motion result $v_{\parallel} = |\boldsymbol{F}| = 0.6$ when there are no obstacles (Fig. 6.10). On top of that, greater velocities are attained for the wider obstacles; therefore it means that narrower obstacles better hinder particles' progress.

On the other, the asymptotic diffusion coefficient along the perpendicular direction to the force (Fig. 6.11) decreases with increasing obstacle density, as expected from both random walk models [Vilaseca et al., 2011; Gori et al., 2016] and from experimental evidences [Dix and Verkman, 2008], and is lower for narrower obstacles [Vilaseca et al., 2011]. However, along the direction of the pulling force, the diffusion coefficient reaches a maximum value greater than that of the free particle diffusion coefficient $D = T$. This behavior is indicative of the transient anomalous superdiffusive behavior for times $t \leq t_0^o$ when Brownian motion of some particles is hindered by a small number of obstacles while other particles move along. This is in agreement with the steady superdiffusive regime displayed by Brownian particles on a static landscape of a rather low concentration of obstacles (Fig. 6.6). Now obstacles do move, which renders this trapping transient. Following this maximum, when the obstacle density increases, particles undergo mostly hindered dispersion, and the diffusion coefficient resumes its decrease to a value beneath that of free Brownian motion.

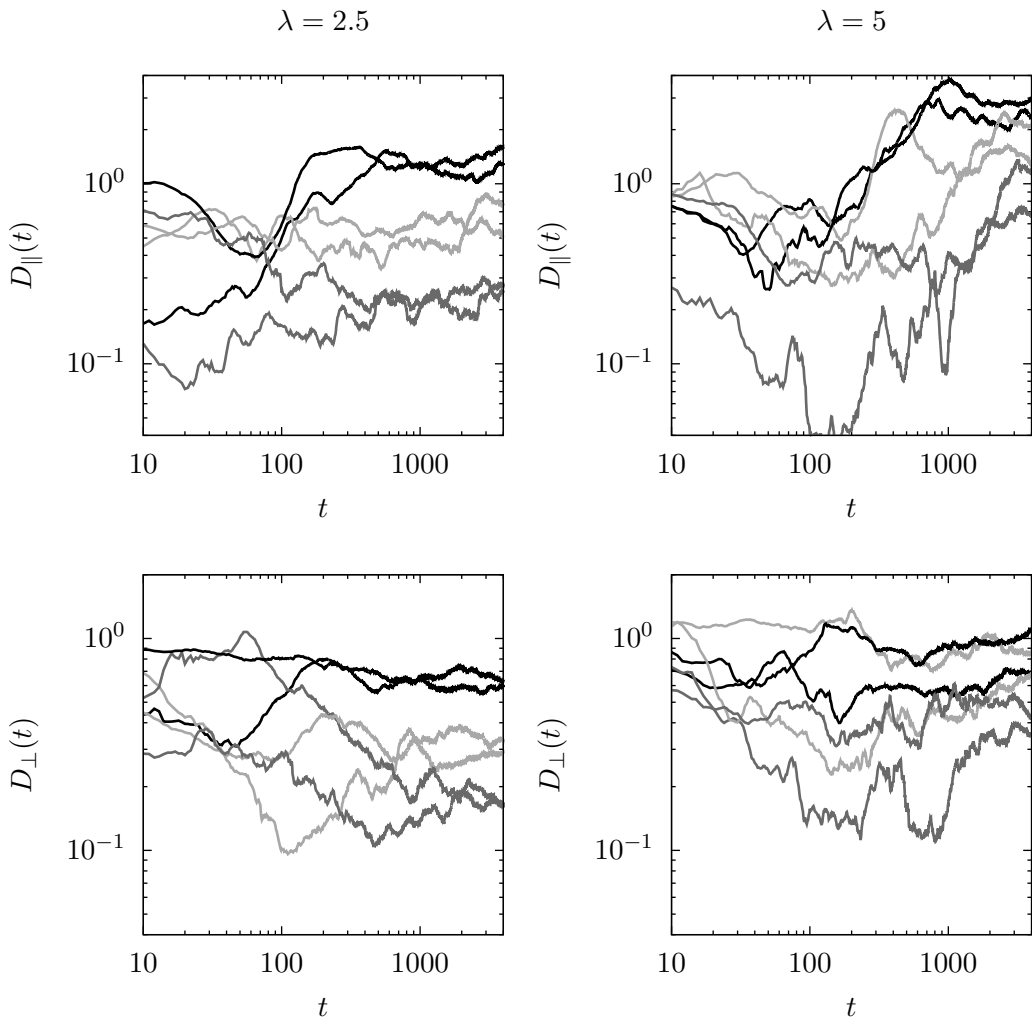

Figure 6.9 – Parallel—top—and perpendicular—bottom—diffusion coefficients as a function of time for a set of particles on dynamic surfaces of different obstacle densities: $\rho = 0.1$ black trajectories, $\rho = 0.3$ light gray trajectories, $\rho = 0.7$ dark gray trajectories; and widths $\lambda = 2.5$—left—, and $\lambda = 5.0$—right—. There are two trajectories for each choice of parameters, that correspond each one to the 4000 particles average in a particular realization of the random potential and of the initial conditions—that is, they only differ from the seed taken for random number generator—.

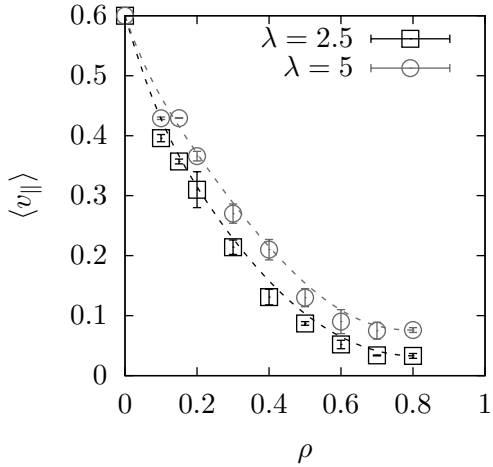

Figure 6.10 – Asymptotic values of the parallel mean velocity as a function of obstacle density computed over the last 1000 units of time. Error bars indicate the variations among realizations as well as the fluctuations in each realization. The smooth curves are best fits to clarify the trends. The time scale of the obstacle dynamics is $t_0^0 = 400$.

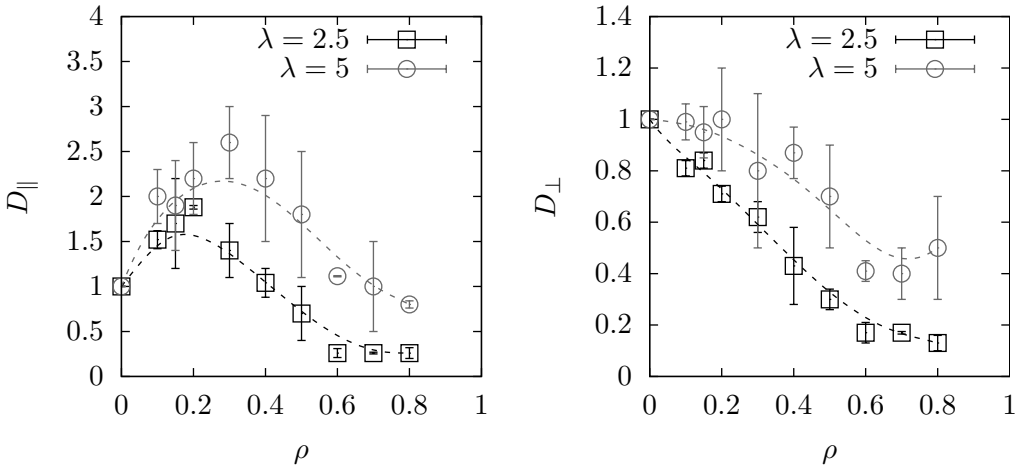

Figure 6.11 – Parallel—left—and perpendicular—right—diffusion coefficients computed over the last 1000 units of time. Error bars are again computed from the fluctuations and the differences between realizations. Smoothed curves are best fits to clarify the trends. The obstacle dynamic time scale is $t_0^o = 400$.

6.3. Summary and conclusions

The present Chapter addresses the problem of transport and diffusion of tracer particles suspended in a thermal environment and subject to a random potential made of unsurmountable stirring obstacles. Obstacles are of equal heights—height variations do not matter in this scenario—and move on a characteristic time scale t_0^o. The average obstacle width and time scales are well controlled quantities, and the density of obstacles is constant in time. The density is the fraction of sites at height V_H—the remaining sites are at height 0—. Density's steadiness is a realistic feature for most systems, even for a monolayer of colonies of gliding bacteria that are likely to divide, since the relaxation dynamics of the nonequilibrium cluster–size distribution is much faster than the proliferation time of the bacteria [Peruani et al., 2012].

The motion of Brownian particles in the dynamical obstacle landscape has been numerically simulated through Langevin overdamped equations for various settings; the control parameters being the obstacle density ρ, the correlation length—mean obstacle width—λ, and the correlation time t_0^o. The main inferences of the investigations focus on the intermediate scenarios of landscapes of rather low densities of obstacles moving on a time scale between that of Brownian motion and the total observation time. In this scenario, the transient behavior of transport and diffusion over time scales shorter than t_0^o mimics that of a static landscape. On the basis of the previous work in [Suñé et al., 2013] and in Chapter 4, which deals with static random potential landscapes subject to a constant external force, it may be concluded that a—dynamical—fraction of the particles are prevented from moving by the obstacles, whereas the rest of the particles freely diffuse. This leads to anomalous behavior of both the average velocity along the direction of the force—it is reduced by the stationary trapped particles—and of the diffusion coefficients, parallel and perpendicular to the direction of the force. After time t_0^o these anomalies disappear because the motion of the obstacles allows previously trapped particles to become loose. Therefore, transport and diffusion coefficients reach asymptotic constant values,

which nonetheless depend on the anomalous transient regimes. Indeed, the parallel diffusion coefficient may increase well above the free diffusion value because of the greater spread of particles brought about by transient superdiffusion. Furthermore, at a given obstacle density, wider—and therefore fewer—obstacles favor transport and diffusion when compared to the behavior for narrower—and therefore a greater number—of obstacles, as it had already been seen for random walk models [Vilaseca et al., 2011].

The outcome discussed throughout this Chapter endorses some of the phenomena already reviewed in [Höfling and Franosch, 2013]. For example, diffusion of endogenous lipid granules at short time scales—so that static landscape simulations should apply—within the fission yeast *Schizosaccharomyces Pombe* [Selhuber-Unkel et al., 2009] undergoes subdiffusive motion with an exponent that is significantly smaller during interphase than during any stage of the mitotic cell division, when there is less abundantly presence of elastic cytoskeletal elements; that is, sublinear power–law increase of the mean–square displacement tends to exhibit a lower exponent as the density increases; a behavior that is exhibited in Figures 6.6 and 6.7. On the other hand, experiments in a broad time range, such as tracking the motion of telomeres in the nucleus of human osterosarcoma cells [Bronstein et al., 2009] display a crossover from subdiffusive motion at short time scales to normal diffusion for longer times, which is also displayed in Figures 6.8 and 6.9. Finally, translational diffusion of DNAs in solutions made crowded with Ficoll-70 and in *in vitro* experiments in the cytosol—prepared from mouse liver—[Dauty and Verkman, 2005], reveals a reduced diffusion coefficient compared to its free diffusion in saline. It means thus that molecular crowding by mobile obstacles is likely to lower the diffusion coefficient, as it happens for certain concentrations in Figure 6.11 indeed.

It ought to be remarked that the most suggestive transport and diffusion phenomena occur at rather low densities $0.1 \lessapprox \rho \lessapprox 0.5$, which is precisely the usual volume occupation exhibited by the cell cytoplasm ($5\% - 40\%$) [Ellis and Minton, 2003].

Furthermore, it may be inferred from the present study that an effective set of quantities to portray transport and diffusion in fluid systems with large obstacles compared to the size of Brownian particles are the characteristic time scale of the dynamics of the obstacles, their width, and their concentration. This may constitute a different approach to active matter media [Basu et al., 2008; Sarkar and Basu, 2011; Marchetti et al., 2013]. Examples of such systems include a number of those presented in the introduction to the present Chapter.

The following Chapter aims at reviewing the numerical techniques employed throughout the investigations. Notwithstanding that the procedures employed are well established, some refinements and improvements have been done. The Chapter hence also includes some novel and original material.

CHAPTER 7

Methodology

The present Chapter is an overview of the various numerical techniques, algorithms, and mathematics employed to carry out the numerical simulations reported in the former chapters. With regard to the potential landscape, it is of particular interest when it includes some amount of disorder with prescribed statistical properties, since it brings about anomalies in both transport and diffusion [Suñé et al., 2013; Suñé et al., 2014], (Chapters 4 and 5). Therefore, a numerical technique to generate random potentials with any desired spatial isotropic correlation is built up (Sec. 7.1.1). Further, other physical scenarios of interest are those in which the disorder reshapes in time and when it is not made of a distribution of barriers, but of impassable obstacles [Suñé et al., 2016], (Chap. 6). Mathematical transformations to bring about such landscapes are also detailed (Sections 7.1.2 and 7.2). Force correlations to be derived from random potentials are analyzed in Section 7.3. In Section 7.4 it is outlined a guide to implement these forces to the simulations of Brownian movement through Langevin dynamics. Finally, Section 7.5 is devoted to sum up the mathematical methods to handle stochastic differential equations, such as the Langevin equation.

7.1. Generation of random potentials

Random potentials with well prescribed statistical properties are ubiquitous in the study of transport and diffusion of Brownian particles in disorder media. The following sections settle down to the methods to build random processes with controlled space and time attributes that are employed throughout this thesis.

7.1.1. Static spatial disorder

A static spatial disorder is a stochastic process that exhibits spatial correlation. That is to say, every random variable concerns a space location and is subject to aleatory variations, yet it exhibits some sort of statistical dependence on the remaining variates. However, with respect to time, a static disorder is independent.

In this section it is conceived a procedure to generate a Gaussian potential landscape with an arbitrary spatial correlation with the only requirement of isotropy. The method has the particularity that, although it uses the Fourier space as other techniques do, all its constraints and information are in real space. Mathematical details of the entire process will be explained subsequently. Afterwards, the method is applied to three different types of disordered potentials with correlations: normal, double–sided exponential and power–law long tail, which cover illustrative scenarios from the physical point of view.

Backdrop

The Fourier filtering method (*FFM*) is a well established procedure to generate a sequence of random numbers with a prescribed correlation in real space [García-Ojalvo et al., 1992; Pang et al., 1995; Makse et al., 1996]. However, it has some practical disadvantages because it needs the analytical Fourier transform of the correlation function and presents a finite cutoff in the range of correlation. This second limitation makes it a low

efficient method, specially in the limit of large systems, and thus for the study of long range correlations, since only small fraction of the sequence of generated numbers is actually correlated. Different versions of the *FFM*, such as those in [Pang et al., 1995; Makse et al., 1996], remove its cutoff in the range of correlations by imposing isotropy and periodic boundary conditions to the correlation function in real space. However, they still require an expression for the Fourier transform of the desired correlation function, which sometimes may lead to cumbersome expressions, like for the power–law correlation [Pang et al., 1995; Makse et al., 1996]. Following these previous methods, the current procedure goes one step beyond by simplifying the calculations in the Fourier space.

To start with, the $1-d$ scaled space will be considered; extension to higher dimensions will be illustrated further. Hence, for the meantime it is intended for building a Gaussian random potential landscape $V(x)$ with zero mean and correlation function $g(|x|)$,

$$\langle V(x)\, V(x')\rangle = g(|x-x'|)\,, \tag{7.1}$$

where brackets indicate space average. May the correlation $g(|x|)$ be a finite, isotropic and decaying function, the correlation in the Fourier space is, the brackets now indicating an average over the Fourier modes,

$$\langle \mathcal{V}(k)\, \mathcal{V}(k')\rangle = 2\pi\ \mathcal{G}(k)\ \delta(k+k')\,, \tag{7.2}$$

where $\mathcal{G}(k)$ is the Fourier transform of the spatial correlation function $g(x)$,

$$\mathcal{G}(k) = \int_{-\infty}^{+\infty} g(x)\ e^{-ikx}\ dx\,. \tag{7.3}$$

It should be enlightened that, to obtain (7.2), the expression for the Dirac delta function has been applied,

$$\delta(k+k') = \frac{1}{2\pi}\int_{-\infty}^{+\infty} e^{i(k+k')x}\ dx\,. \tag{7.4}$$

A Gaussian random variate $\zeta(k)$ with null mean and anticorrelation,

$$\langle \zeta(k)\ \zeta(k') \rangle = \delta(k+k')\,, \tag{7.5}$$

may be straightforwardly obtained by already proved numerical techniques [García-Ojalvo et al., 1992; García-Ojalvo and Sancho, 1999]. Therefore, from expression (7.2) it can be gathered that the random process in the Fourier space may be generated by means of such a Gaussian aleatory variable $\zeta(k)$,

$$\mathcal{V}(k) = \sqrt{2\pi\ \mathcal{G}(k)}\ \zeta(k)\,. \tag{7.6}$$

Eventually, the Gaussian random potential $V(x)$ is achieved by making use of the inverse Fourier transform of the aleatory variable in the k–space,

$$V(x) = \frac{1}{2\pi} \int_{-\infty}^{+\infty} \mathcal{V}(k)\ e^{ikx}\ dk\,. \tag{7.7}$$

Numerical algorithm

In order to implement the former discussion to set up a numerical algorithm, discrete space ought to be employed. Indeed, the procedure works in a finite lattice of N cells and total length $L = N\Delta$, where Δ is the cell size. Therefore x_i denotes the position in the discrete $1-d$ space, $x_i = i \cdot \Delta \to x$ as $\Delta \to 0$. With regard to the Fourier space, the cell size is

$$\Delta k = \frac{2\pi}{L}\,, \tag{7.8}$$

hence, the Dirac delta function relates to the Kronecker delta,

$$\delta(k+k') = \lim_{\Delta k \to 0} \frac{\delta_{\mu,-\mu'}}{\Delta k}\,, \tag{7.9}$$

where μ labels any mode in the discrete Fourier space,

$$k_\mu = \frac{2\pi\mu}{L}\,. \tag{7.10}$$

According to (7.8), (7.9) and (7.2), the correlation for the random potential in the discrete Fourier space is

$$\langle \mathcal{V}(k_\mu)\ \mathcal{V}(k_{\mu'}) \rangle = \mathcal{G}(k_\mu)\, N\Delta\ \delta_{\mu,-\mu'}\,, \tag{7.11}$$

where $\mathcal{G}(k_\mu) = \Delta \cdot FFTW(-1, g(x_j))$. $FFTW(-1, g(x_j))$ labels the discrete *Fast Fourier Transform* (*FFT*) of the $FFTW$ C subroutine library [Frigo and Johnson, 2005]; $g(x_j)$ is an array comprising the correlation function images $g(x)$ at the N mesh points in which real space is been discretized. For one dimensional systems,

$$c_\mu = \Delta \sum_{j=0}^{N-1} c_j e^{-i2\pi\mu j/N} = \Delta \cdot FFTW(-1, c_j)\,, \tag{7.12}$$

is the direct discrete Fourier transform[1], where $FFTW(-1, c_j)$ [2] is the numerical algorithm forward FFT of complex numbers c_j ; and

$$c_j = \frac{1}{N\Delta} \sum_{\mu=0}^{N-1} c_\mu e^{i2\pi\mu j/N} = \frac{1}{N\Delta} \cdot FFTW(+1, c_\mu)\,, \tag{7.13}$$

is the inverse discrete Fourier transform of c_μ .

Analogously to the reasoning applied to the continuous space, the correlation (7.11) may be built by means of the potential $\mathcal{V}(k_\mu)$ in the k_μ–space,

$$\mathcal{V}(k_\mu) = \sqrt{\mathcal{G}(k_\mu)}\ \zeta_\mu\,, \tag{7.14}$$

where ζ_μ are complex Gaussian random numbers anti–correlated [García-Ojalvo et al., 1992],

$$\langle \zeta_\mu\ \zeta_{\mu'} \rangle = N\Delta\ \delta_{\mu,-\mu'}\,. \tag{7.15}$$

Therefore, the main steps that configure the numerical algorithm to get the potential $V(x)$ are:

1. Given the choice of an analytical correlation $g(|x|)$ with the mentioned properties, the table of $(j,\ g(x_j))$, $j\ \in\ (0, N-1)$, is built.

[1] The relations between continuous and discrete variables are: $x_j = j\Delta$ and $k_\mu = 2\pi\mu/N$. Subindex j is employed instead of the usual i in the expressions concerning the Fourier Transforms in order to avoid confusion with the imaginary unit $i^2 = -1$.

[2] The first argument, -1, indicates the direction of the transform. It can be either -1 for forward transform or $+1$ for backward. Technically, it is the sign of the exponent in the transform.

Although $g(x_j)$ are purely real numbers in real space, to compute the discrete Fourier transforms, the imaginary parts ought to be settled to $Im(g(x_j)) = 0$ [3].

2. The random numbers ζ_μ have special requirements of symmetry to fulfill the anticorrelation statistics [García-Ojalvo et al., 1992; García-Ojalvo and Sancho, 1999]. A better option is to use N random numbers $a_j = b_j/\sqrt{\Delta}$, where b_j are Gaussian random numbers with zero mean an variance 1, obtained from the *Marsenne Twister* generator and using the alternative *Marsaglia-Tsang ziggurat* and *Kinderman-Monahan-Leva* ratio methods [Galassi et al., 2009]. One can show that Fourier transform (7.12) of a_j with $Im(a_j) = 0$ gives the desired random numbers ζ_μ.

3. After this two steps, one can build $\mathcal{V}(k_\mu)$ by (7.14) ($\mathcal{G}(k_\mu)$ is obtained applying the *FFT* (7.12) to $g(x_j)$). The desired random values of the potential $V(x_j)$ are obtained by the inverse discrete Fourier transform (7.13) of $\mathcal{V}(k_\mu)$.

Proofs

To check the process' success, the correlation of the generated potential may be compared to the proposed analytical correlation (7.1). In order to dig into some illustrative scenarios, yet with contrasting mathematical properties, the method is applied to obtain disordered potentials with correlations normal, double–sided exponential, and power–law long tail; see Figure 7.1. It may be gathered that the larger is N, the better is the agreement between theory and simulations. Nonetheless, for optimizing statistics and time computing, the parameter choice for the simulation outcome presented in Figure 7.1 is $\Delta = 0.1$ and $N = 2^{20}$.

The normal or so–called Gaussian disordered potential has the following

[3] *FFTW* library includes facilities to compute real and half–complex sequences by generating itself those necessary symmetries. It might be useful to apply these options once the method has been proved to succeed.

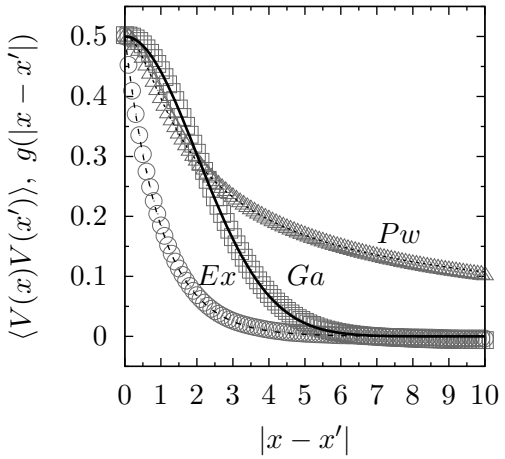

Figure 7.1 – Simulation results for three types of potential correlation; Gaussian (Ga) (7.16)($\lambda = 2$), in blank squares; double–sided exponential (Ex) (7.17)($\lambda = 1$), grey circles; and power–law (Pw) (7.19)($\lambda = 1, \varepsilon = 2/3$) in black triangles. Analytical functions are also plotted in continuous (7.16), dashed (7.17) and dotted (7.19) lines.

correlation,

$$g(|x-x'|) = \frac{1}{2}\, e^{-\frac{(x-x')^2}{2\lambda^2}}, \tag{7.16}$$

which is well behaved in all spatial domain with a finite characteristic length λ. This potential has been used in plenty of different situations [García-Ojalvo et al., 1992; García-Ojalvo and Sancho, 1999; Khoury et al., 2009] and it is reviewed here to bring the standard reference.

The exponential correlated random potential has a statistical correlation,

$$g(|x-x'|) = \frac{1}{2}\, e^{-\frac{|x-x'|}{\lambda}}, \tag{7.17}$$

with a correlation length λ. This is a double–sided exponential which shows a discontinuity in the first derivative at the origin ($x = 0$), and so its second derivative diverges there. Therefore, it leads to a force whose correlation diverges at the origin as a Dirac delta, and so it may be regarded as the analogous force to a Gaussian white noise in space (Sec. 7.3.1).

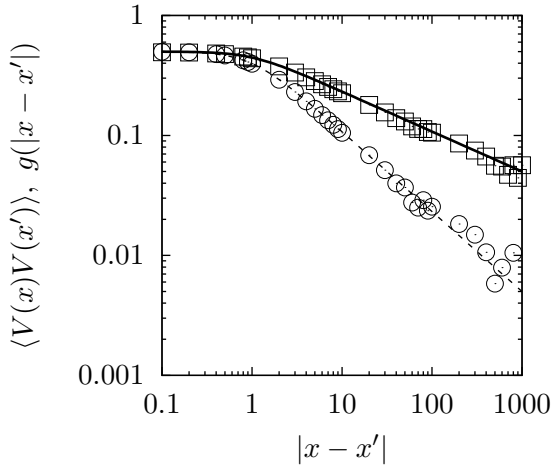

Figure 7.2 – Log–log plot of the power–law correlation (7.19) for $\varepsilon = 1/3$ (squares, continuous curve) and $\varepsilon = 2/3$ (circles, dashed curve). Numerical results are represented by symbols and analytical functions by lines. $\lambda = 1$.

Finally, the power–law correlation decays without any characteristic length at its tail, and it can be used to explore the role of long ranged disorder. It is defined as,

$$\langle V(x)\ V(0)\rangle \propto x^{-\varepsilon},\ (\varepsilon > 0)\,. \tag{7.18}$$

However, expression (7.18) has a singularity at he origin ($x = 0$) that may induce to incongruences when computing its discrete version. To avoid this scenario, the following correlation function, inspired in [Makse et al., 1996], may be proposed instead,

$$g(|x-x'|) = \frac{1}{2}\left(1 + \frac{(x-x')^2}{\lambda^2}\right)^{-\varepsilon/2}, \tag{7.19}$$

which is defined for any real value, including $x = x'$. ε is the exponent that regulates the decay process, and λ is here a short length to avoid discontinuities at the origin. It should be noted that for $x \gg \lambda$ the power–law behavior is recovered. In order to enlighten the power–law tail that a correlation of type (7.18) must exhibit, Figure 7.2 displays the outcome for two random potentials with power–law correlation with exponents $\varepsilon = 1/3$ and $\varepsilon = 2/3$ in a logarithmic scale. It ought to be noted that the correlation's

slope is indeed controlled by the exponent ε.

Figures 7.1 and 7.2 prove that the numerical algorithm outcome is in agreement with the theoretical predictions. Besides, the numerical algorithm is also tested with differing settings. One one hand, different cell sizes Δ =0.05, Δ =0.1 and Δ =0.4 have been employed. Thus, in order to keep the system's length constant ($L = N\Delta$), $N = 2^{18}$, $N = 2^{20}$ and $N = 2^{21}$ for Δ =0.4, Δ =0.1 and Δ =0.05 respectively. On the other, three different correlation lengths have been chosen for the normal and exponential cases: λ =0.5, λ =1 and λ =4. Since the power–law correlation has no characteristic length, two different long tail exponent values have been inquired instead, ε =1/3 and ε =2/3 (Fig. 7.2). It has been proven that the procedure runs for those settings as well.

Potential landscape

It is worth to show here how the potential landscapes of the former three examples look like (Fig. 7.3). The first observation is that the general trend of the three cases match because the same seed to generate the random numbers has been employed. A second observation is that normal and power–law cases look very similar, but this is because a short scale is displayed. Finally, strong differences are clearly seen between them and the exponential case, where the signature of the delta–like correlation of the force is manifested (Sec. 7.3.1).

Two dimensional space

Generalization to the two dimensional space is straightforward but involves larger computer facilities. Actually, a two dimensional system with a suitable system size to observe time dependent anomalies will require a large amount of computational memory. The procedure to generate a disordered surface with an isotropic space correlation function is analogous to the $1 - d$ algorithm (Sec. 7.1.2), yet now the two dimensional Fourier

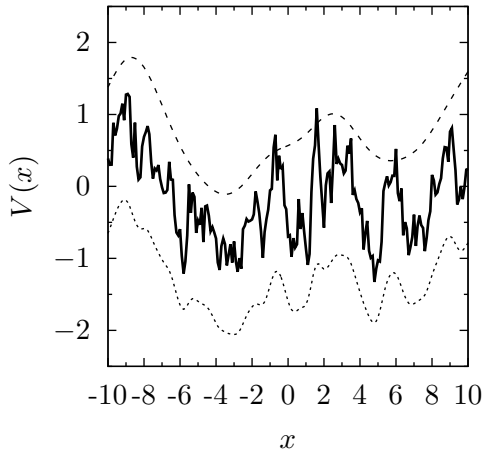

Figure 7.3 – Potential landscape for each of the three correlation types: normal correlated potential (7.16)($\lambda = 2$) (dashed line) has been shifted one unit along vertical axes; while the one with power–law correlation (7.19)($\lambda = 1$, $\varepsilon = 2/3$) (dotted line) has been shifted the same amount but opposite, and the double–sided exponential (7.17)($\lambda = 1$) (solid line) is left in the middle.

transforms to be carried out in a torus geometry. With regard to the notation, $\boldsymbol{r}_i$[4] is the vector that denotes the position of a cell in the $2-d$ lattice space, $\boldsymbol{r}_i = \Delta(i_1 \cdot \hat{\boldsymbol{e}}_1 + i_2 \cdot \hat{\boldsymbol{e}}_2) \to \boldsymbol{r}$ as $\Delta \to 0$, $\hat{\boldsymbol{e}}_1$ and $\hat{\boldsymbol{e}}_2$ are unit vectors of an orthonormal cartesian basis, and i is the set of indices required to label this cell (i_1, i_2). Nevertheless, the following plots employ x, y to label the continuous length axes along $\hat{\boldsymbol{e}}_1$ and $\hat{\boldsymbol{e}}_2$.

A correlation

$$\langle V(\boldsymbol{r})\ V(\boldsymbol{r}')\rangle = g(|\boldsymbol{r} - \boldsymbol{r}'|/\lambda)\,, \tag{7.20}$$

is now proposed with the same symmetries already discussed in both axis. Its discrete version is,

$$\langle V_i\ V_j\rangle = g_{ij}\,. \tag{7.21}$$

Transforming g_{ij} to the Fourier space $\mathcal{G}(\boldsymbol{k}_\mu) = \mathcal{G}_\mu$, the corresponding two

[4]The bold face notation refers to a vector in a d–dimensional space.

dimensional potential (7.6) is,

$$\mathcal{V}(\boldsymbol{k}_\mu) = \sqrt{\mathcal{G}_\mu}\,\zeta_\mu\,. \tag{7.22}$$

The cell location in Fourier space is given by $\boldsymbol{k}_\mu = 2\pi(\mu_1\hat{\boldsymbol{u}}_1 + \mu_2\hat{\boldsymbol{u}}_2)/N\Delta$. The vectors $\hat{\boldsymbol{u}}_1$ and $\hat{\boldsymbol{u}}_2$ are unit vectors of an orthonormal basis in Fourier space, and the cells are labeled by the cell indices (μ_1, μ_2). In the continuum limit $\boldsymbol{k}_\mu \to \boldsymbol{k}$. ζ_μ are Gaussian anti-correlated random numbers of zero mean and correlation

$$\langle \zeta_\mu\ \zeta_{\mu'} \rangle = (N\Delta)^2\ \delta_{\mu_1,\mu_2;-\mu_1',-\mu_2'}\,, \tag{7.23}$$

that are obtained by the two–dimensional discrete Fourier transforms of[5]

$$a_i = \frac{b_i}{\Delta}\,, \tag{7.24}$$

where b_i are Gaussian random numbers $N(0,1)$ with $Im(b_i) = 0$. Analogously to the one–dimensional case, a real field is recovered when anti–transforming $\mathcal{V}(\boldsymbol{k}_\mu)$. Again, Δ is the segment length in both directions of discretization in real space, and N is the number of discretization points in any of the two perpendicular directions in space.

The procedure described throughout this section is employed to generate a corrugated surface with Gaussian correlation (7.25),

$$\langle V(\boldsymbol{r})\ V(\boldsymbol{r}')\rangle = g(|\boldsymbol{r}-\boldsymbol{r}'|/\lambda) = \frac{1}{2}\ e^{-(\boldsymbol{r}-\boldsymbol{r}')^2/2\lambda^2}\,. \tag{7.25}$$

The brackets indicate a spatial average over a system of size $L \times L$, $L = N\,\Delta$. The lattice version of this correlation function is

$$\langle V_i\ V_j\rangle = g_{ij} = \frac{1}{2}\ e^{-(\boldsymbol{r}_i-\boldsymbol{r}_j)^2/2\lambda^2}\,. \tag{7.26}$$

The Fourier transform of the spatial correlation function g_{ij} is

$$\mathcal{G}_\mu = \pi\lambda^2 e^{-\lambda^2\boldsymbol{k}_\mu^2/2}\,. \tag{7.27}$$

Being the choice for the parameters $\lambda = 5$, $N = 2^8$, and $\Delta = 0.5$; the outcome of the process is displayed in Figure 7.4. A check of the correlation leading from the simulation is further carried out in Section 7.1.2.

[5]The *FFTW* library is also applied to compute two dimensional discrete Fourier transforms.

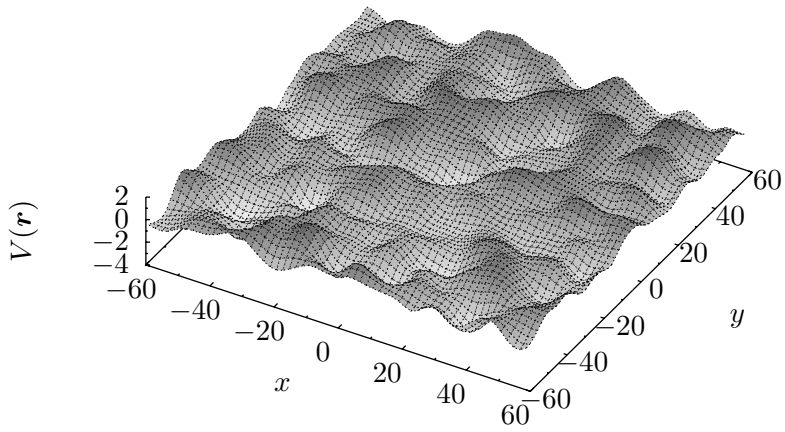

Figure 7.4 – $2-d$ Gaussian random potential $V(\boldsymbol{r})$ with spatial correlation (7.25).

7.1.2. Dynamic disorder

A dynamic disorder is a stochastic process exhibiting not only spatial correlation but also temporal. Hence, every random variable concerns both a space location and a time moment. Statistical dependence is exhibited among variates concerning different locations at a precise instant, yet also among variates regarding a precise location at different times.

Formalism

As it has been already shown, it is particularly useful for Gaussian random processes with symmetric spatial correlation functions to transfer the discussion to Fourier space [Makse et al., 1996; Suñé et al., 2012]. The algorithm to simulate the random process takes advantage of properties of Fourier variables [García-Ojalvo and Sancho, 1999; Suñé et al., 2012]. The Fourier transform $\mathcal{V}(\boldsymbol{k}_\mu)$ of $V(\boldsymbol{r}_i)$ is conveniently also a Gaussian random process. In discrete space, may it be paralleled the notation of real space,

the correlation function in the Fourier space reads

$$\langle \mathcal{V}_\mu \; \mathcal{V}_{\mu'} \rangle = \mathcal{G}_\mu \, (N\Delta)^d \, \delta_{\mu,-\mu'} \, , \tag{7.28}$$

where d refers to the space's dimension. It is next designed a random dynamical process that at any time preserves the spatial correlation function (7.20), but whose configuration changes in time as an Ornstein–Uhlenbeck process for each Fourier mode. The simplest way to accomplish this is to generate a Gaussian process in Fourier space, with temporal correlation function

$$\langle \mathcal{V}_\mu(t) \; \mathcal{V}_{\mu'}(t') \rangle = \langle \mathcal{V}_\mu(t) \; \mathcal{V}_{\mu'}(t) \rangle e^{-\frac{|t-t'|}{\tau_\mu}} \, . \tag{7.29}$$

Brackets now denote a double average, one over $\boldsymbol{k}_\mu$ modes and the other over time. The parameter τ_μ is the relaxation time of the $\mathcal{V}_\mu$ mode, and the coefficient $\langle \mathcal{V}_\mu(t) \; \mathcal{V}_{\mu'}(t) \rangle$ is exactly as given in (7.28).

The procedure presented in [García-Ojalvo and Sancho, 1999] is followed to generate this noise, hence it is assumed that each $\mathcal{V}_\mu$ evolves according to the linear Langevin equation

$$\frac{d\mathcal{V}_\mu}{dt} = -\frac{1}{\tau_0}\frac{\mathcal{G}_0}{\mathcal{G}_\mu} \; \mathcal{V}_\mu + \frac{1}{\sqrt{\tau_0}} \; \xi_\mu(t) \, , \tag{7.30}$$

$$\langle \xi_\mu(t) \; \xi_{\mu'}(t') \rangle = 2\mathcal{G}_0 \; (N\Delta)^d \; \delta_{\mu,-\mu'} \; \delta(t-t') \, , \tag{7.31}$$

where τ_0 is the characteristic time of the $\mu = 0$ mode $\mathcal{V}_0$. (7.30) is a set of decoupled ordinary stochastic differential equations for each Fourier mode in Fourier space. It can be straightforwardly integrated because of its linearity, leading to the algorithm

$$\begin{aligned} \mathcal{V}_\mu(t+\Delta t) = \mathcal{V}_\mu(t) \exp\left[-\frac{\mathcal{G}_0}{\mathcal{G}_\mu \tau_0} \; \Delta t\right] \\ + \sqrt{(N\Delta)^d \; \mathcal{G}_\mu \left(1 - \exp\left[-2\frac{\mathcal{G}_0}{\mathcal{G}_\mu \tau_0}\Delta t\right]\right)} \; \zeta_\mu \, , \end{aligned} \tag{7.32}$$

where ζ_μ is a Gaussian random variate anticorrelated (7.15), that is simulated as already has been described in Section 7.1.1[6]. Thus, the algorithm (7.32) generates a stochastic process at time $t + \Delta t$ from its values

[6] See the point number 2 in the enumeration (Sec. 7.1.1). The expression for a_j in a d-dimensional space is $a_j = b_j/\sqrt{\Delta^d}$.

at time t, preserving the spatial correlation $g(|\mathbf{r} - \mathbf{r}'|)$. (7.29) is indeed recovered, since the stationary time correlation of each mode is given by

$$\langle \mathcal{V}_\mu(t)\ \mathcal{V}_{\mu'}(t')\rangle_{st} = G(\boldsymbol{k}_\mu, |t-t'|)\ (N\Delta)^2\ \delta_{\mu,-\mu'}\ . \tag{7.33}$$

For the mode μ,

$$G(\boldsymbol{k}_\mu, |t-t'|) = \mathcal{G}_\mu \exp\left(-\frac{\mathcal{G}_0}{\mathcal{G}_\mu \tau_0}|t-t'|\right)\ , \tag{7.34}$$

decays on a time scale $\tau_\mu = \frac{\mathcal{G}_\mu}{\mathcal{G}_0}\tau_0$. In particular, the decay time of mode $\mu = 0$ then has the desired value τ_0 . Furthermore, this random process is stationary from the onset since (7.28) is retrieved at any time by setting $t' = t$.

A final brief comment on the convenience of Fourier space rather than coordinate space in the construction of the spatiotemporal colored noise is appropriate. There is a straightforward connection between the spatial correlation function (7.25) or (7.26) and the simple Langevin dynamics (7.30). This greatly helps the computational effort; a direct calculation in real space might involve complex operators that could seriously slow down the simulations.

Usage

Starting from the static corrugated surface with Gaussian correlation, that is to say, the $2-d$ random potential displayed in Figure 7.4 ($\lambda = 5$, $N = 2^8$, and $\Delta = 0.5$), the method just described brings about a time evolution of the field preserving its spatial correlation. The outcome of the process, setting $\tau_0 = 10$ and $\Delta t = 0.01$, is displayed in Figure 7.5, that exhibits the section portrait between $\boldsymbol{r} = (-100, 0)$ and $\boldsymbol{r} = (100, 0)$ of the random potential at different times.

In order to check the accuracy of the method, spatial correlation of the potential at different times may be computed and compared to (7.25). As Figure 7.6—left—shows, there is agreement between prediction (7.25)

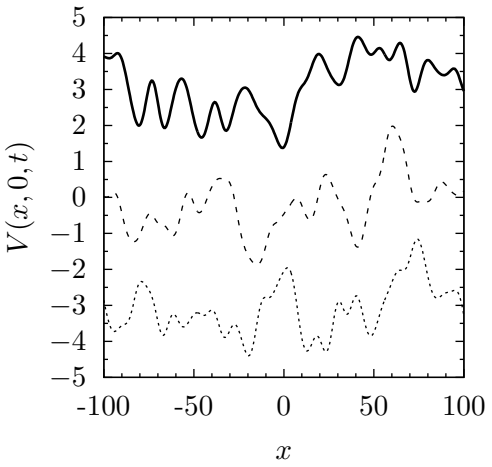

Figure 7.5 – Random potential $V(x,0,t)$ with isotropic Gaussian spatial correlation (7.25) at $t = 400$ (solid line) shifted one unit along vertical axes, at $t = 800$ (dashed line) in the middle, and at $t = 1200$ (dotted line) shifted the same amount but opposite. $\lambda = 5$, $\tau_0 = 10$, and $\Delta t = 0.01$.

and the computational results. On the other hand, the time correlation of the potential at the Fourier space concerning some wave–vectors may be computed as well. They ought to compare with the theoretical predictions to arise from (7.29). Both panels of Figure 7.6 unveil agreement between the simulations and theoretical predictions to come from the model. Therefore, the method is proved to work.

7.2. Barrier landscapes

A random process simulated by means of the methods discussed in Section 7.1 exhibits a random distribution of barrier heights, either static or dynamic. To model some physical scenarios may require a landscape made of impassable obstacles instead (Chap. 6). It turns out to be most convenient to construct a landscape of obstacles of equal height. The following transformation of the field $V(\boldsymbol{r},t)$ to a new potential landscape $U(\boldsymbol{r},t)$ is

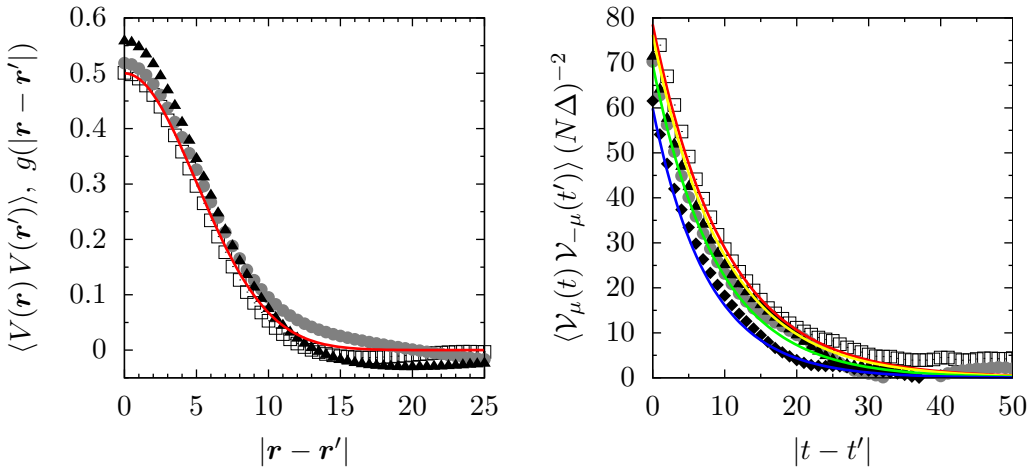

Figure 7.6 – Left: space correlations of the random potential $V(\boldsymbol{r}, t)$ at different times: $t = 400$ (blank squares), $\tau = 800$ (grey circles), and $t = 1200$ (black triangles). The Gaussian (7.25) spatial correlation imposed is also displayed in red. Right: time correlation of the random potential $\mathcal{V}_\mu(t)$ at the Fourier space for different wave–vectors; $\boldsymbol{k} = (0, 0)$ in blank squares, $\boldsymbol{k} = (0, 2)$ in grey circles, $\boldsymbol{k} = (0, 4)$ in black triangles, and $\boldsymbol{k} = (0, 6)$ in black rhombi. Theoretical prediction (7.29) has been included as well for comparison in red for $\boldsymbol{k} = (0, 0)$, yellow for $\boldsymbol{k} = (0, 2)$, green for $\boldsymbol{k} = (0, 4)$, and blue for $\boldsymbol{k} = (0, 6)$.

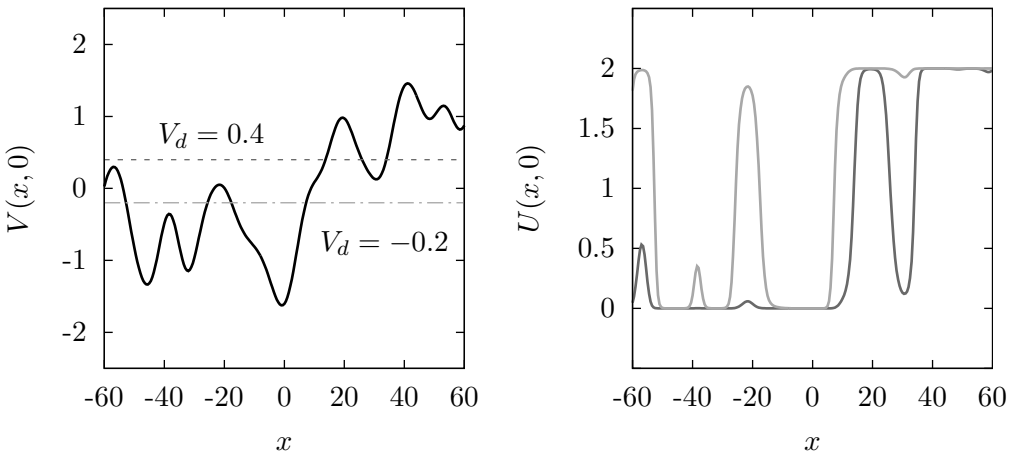

Figure 7.7 – Random potential ($\lambda = 5$, $N = 2^8$, and $\Delta = 0.5$) $V(x,0)$ with spatial correlation (7.25)—left panel—. Horizontal lines label the potential height at which V is cut by (7.35) to transform to U; $V_d = 0.4$ (dashed dark grey) and $V_d = -0.2$ (dot–dashed light grey). To the right, there are the cut potentials $U(x,0)$ from the transformation (7.35) with $V_d = 0.4$ (dark grey) and $V_d = -0.2$ (light grey). In both cases $a = 0.1$, $V_H = 2$.

hence implemented,

$$U(\boldsymbol{r},t) = \frac{V_H}{1+\exp\left[-(V(\boldsymbol{r},t)-V_d)/a\right]}\,. \tag{7.35}$$

When $(V(\boldsymbol{r},t)-V_d)/a$ is positive (say, larger than 1), the new field in the region around $\boldsymbol{r}$ is an obstacle whose maximum height is V_H. In the opposite case, $(V(\boldsymbol{r},t)-V_d)/a$ negative (say, smaller than -1), the new potential is essentially zero, see Figure 7.7. It is said "around $\boldsymbol{r}$" because the original potential is assumed smooth and slowly varying. Parameter a controls the barrier stiffness, that is, the sharpness of the boundary between a flat region and an obstacle. Figure 7.8 shows the $2-d$ landscapes that lead to the $1-d$ cross sections in Figure 7.7.

In "designing" the potential $U(\boldsymbol{r},t)$ from $V(\boldsymbol{r},t)$, it is set out to preserve the spatial and temporal correlation properties of the original potential. The left panel of Figure 7.9 captures a plot in logarithmic–normal coordinates showing the spatial correlation function of the original potential—

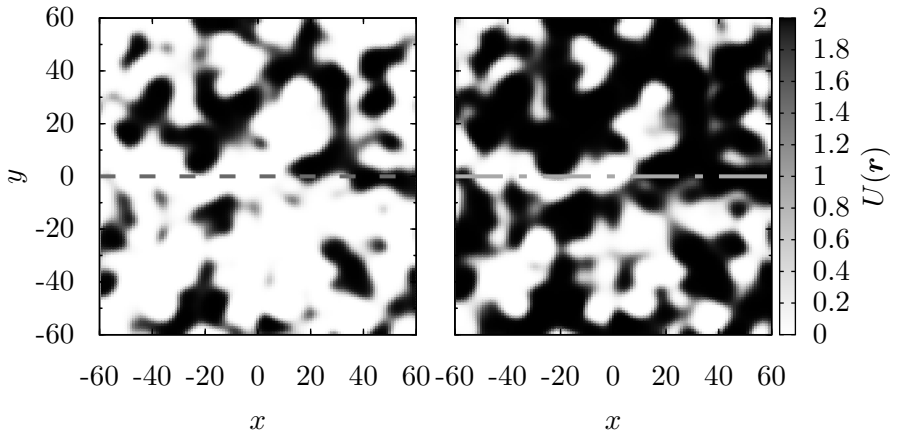

Figure 7.8 – $2-d$ random potentials $U(\boldsymbol{r})$ after the transformation (7.35) is applied to $V(\boldsymbol{r})$ ($\lambda = 5$, $N = 2^8$, and $\Delta = 0.5$) with $a = 0.1$, $V_H = 2$, and $V_d = 0.4$ (left panel), and -0.2 (right panel). Grey scale lines enlighten the sections at which the portraits in Figure 7.7 are plotted.

solid line—, and the two cases of the new potential displayed in Figure 7.8. Indeed, the slope of the potential with $V_d = 0.4$ is essentially identical to that of the original potential, whereas that of the potential with $V_d = -0.2$, while not the same, is close. The difference in the absolute values of the three lines is due to the fact that the average value of the new potential is no longer zero and, in fact, it depends on V_d. A comparison of the decay of temporal correlations of the original and modified potentials also shows that the new potential captures the behavior of the original one (Fig. 7.9)–right. The absolute values of the three curves again differ because the mean value of U being nonzero.

The configuration of obstacles of height $U(\boldsymbol{r}, t) = V_H$ separated by flat regions $U(\boldsymbol{r}, t) = 0$ at each time allows to define a convenient quantity, the relative density of obstacles $\rho(t)$, as the ratio of sites at height $U(\boldsymbol{r}, t) = V_H$ to the total occupied system (6.4):

$$\rho(t) = \frac{1}{N^2 V_H} \sum_i U(\boldsymbol{r}_i, t)\,. \tag{7.36}$$

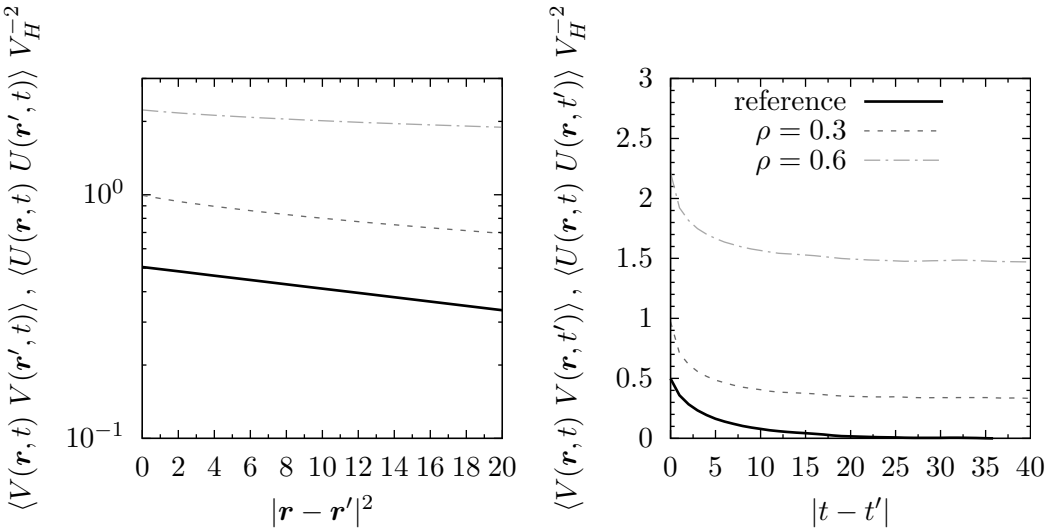

Figure 7.9 – Spatial—left—and temporal—right—numerical correlations of the potentials. The solid curve corresponds to the potential $V(\boldsymbol{r},t)$ with Gaussian correlation (7.25) and $\lambda = 5$ and $\tau_0 = 10$. The dashed curves are for the potential $U(\boldsymbol{r},t)$ with parameter values $a = 0.1$, $V_H = 2$, and $V_d = 0.4$ (dark gray) and -0.2 (light gray).

Here i again labels all the mesh points of the real–space $2-d$ lattice. According to (7.36), the landscape in the left panel in Figure 7.8 has a density of obstacles $\rho = 0.3$, and the one to the right, $\rho = 0.6$. With other parameters fixed, V_d is the parameter employed to modify the density of obstacles. The plot in Figure 7.10 reveals a linear relationship between ρ and V_d. The multiple symbols of a given shape denote repeated runs at that value of V_d, yet with different seeds for the random number generator. Furthermore, the fact that V_d determines ρ—other parameters being the same—, and that V_d is independent of time, establishes that the density ρ is also statistically independent of time. Obstacles can thus move and deform over the slow time scale τ_0, with ρ oscillating around a steady value. Finally, it should be noted that the potential's characteristic correlation length λ is a measure of the obstacles' size for the transformed potential $U(\boldsymbol{r},t)$.

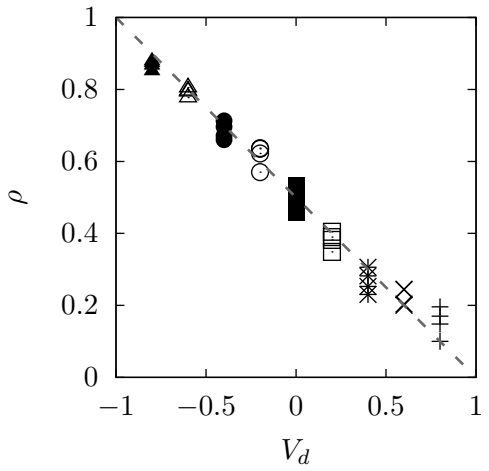

Figure 7.10 – Obstacle density ρ of the $2-d$ random potentials $U(\boldsymbol{r},t)$ as a function of V_d. Other parameters: $a=0.1$, $\lambda=5$, $\Delta=0.5$, and $N=2^8$.

7.3. From potentials to forces, simple centered discrete derivatives

Once the random field $V(x)$ is generated in $1-d$ space, the force at any point i may be derived employing, for example, the simple centered derivative formula

$$F_i = -\frac{dV(x)}{dx} = -\frac{V(x_{i+1}) - V(x_{i-1})}{2\Delta} \ . \tag{7.37}$$

On the other hand, from the analytical expression for the correlation function (7.1) one can obtain the statistical properties of the corresponding forces $F(x) = -V'(x)$ as well,

$$\langle F(x)\, F(x')\rangle = -\frac{\partial^2 g(|x-x'|)}{\partial x^2} = \frac{1}{\lambda^2}\ h(|x-x'|) \ , \tag{7.38}$$

which defines the dimensionless correlation function of the force $h(|x|)$. This relation is also useful to check the correct properties of the numerically generated force (Fig. 7.11).

Applying (7.38) to the already studied correlation types (7.16), and (7.19)—

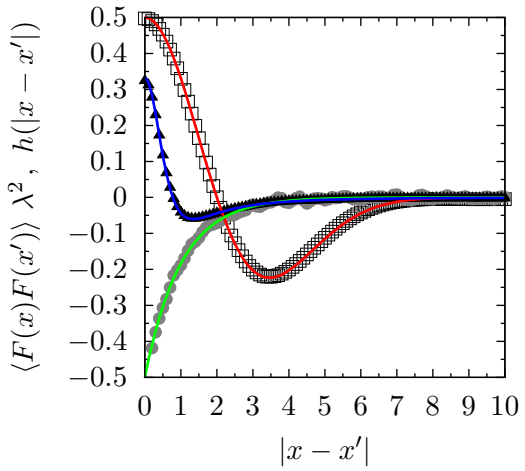

Figure 7.11 – Simulation results for the forces to derive from three types of potential correlation; Gaussian (7.16)($\lambda = 2$), in blank squares; double–sided exponential (4.2)($\lambda = 1$), grey circles; and power–law (4.4)($\lambda = 1, \varepsilon = 2/3$) in black triangles. Analytical functions are also plotted in red (7.39), green (7.41) and blue (7.40) lines.

the double–sided exponential correlation is postponed—, it leads to

$$h(|x|) = \frac{1}{2}\left(1 - \frac{x^2}{\lambda^2}\right) e^{-\frac{x^2}{2\lambda^2}}\,, \tag{7.39}$$

for the normal correlation (7.16), and

$$h(|x|) = \frac{\varepsilon}{2}\left[1 - \frac{x^2}{\lambda^2}(1+\varepsilon)\right]\left(1 + \frac{x^2}{\lambda^2}\right)^{-\varepsilon/2-2}\,, \tag{7.40}$$

for the power–law (7.19). It should be noticed that x' is fixed to $x' = 0$ for both cases.

7.3.1. The double–sided exponential correlation

The double–sided exponential correlation function (7.17) deserves a comment apart. It exhibits a cusp at the origin, and thus its first derivative at $x = 0$ has a finite jump—Heaviside function—. Since the derivative of a Heaviside function is a Dirac–δ function, the associated force correlation function includes a Dirac–δ function at the origin. Applying (7.38)

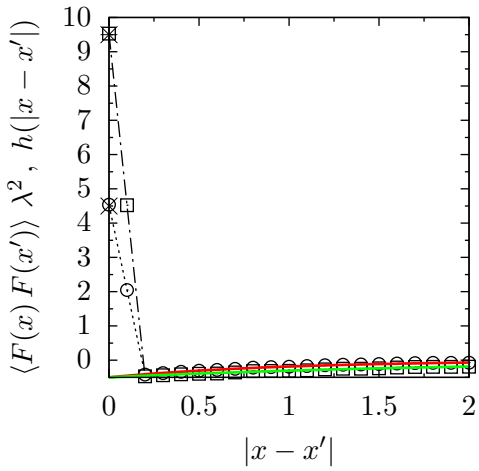

Figure 7.12 – Magnification of the force correlation (7.17) for the exponential correlated potential. Blank circles and dotted line label the $\lambda = 1$ case. The $\lambda = 2$ case is labeled by blank squares and dot dashed line. Theoretical predictions are drawn in solid lines; red for $\lambda = 1$, green for $\lambda = 2$. Points at the origin are the spatial discrete contribution of the continuous Dirac–δ distributions. Analytical values (7.42)—a cross for $\lambda = 1$, a star for $\lambda = 2$—coincide with simulation's results.

to (7.17), and taking $x' = 0$,

$$h(|x|) = \delta\left(\frac{x}{\lambda}\right) - \frac{1}{2}e^{-\frac{|x|}{\lambda}} \ . \tag{7.41}$$

Particularly, at the origin, in the discrete space, it behaves as

$$h(0) \simeq \frac{\lambda}{2\Delta} - \frac{1}{2} \ . \tag{7.42}$$

Figure 7.12 displays the theoretical prediction, based on (7.41) and (7.42), and the simulation outcome for the force correlation to lead from a random potential with a double–sided exponential correlation (7.17).

Due to the Dirac–δ distribution at the origin in (7.41), which is $\sim \lambda/2\Delta$ because of normalization and isotropy, the first simulation points are enhanced respect to the rest. Theoretically, only the point for $x = 0$ might be enhanced because of the Dirac–δ distribution at the origin. However, since the simulations run in a discrete space, when computing the derivatives of

the potential, also at $x = \Delta$ the force correlation shows an enhancement respect to the exponential curve (7.41) that is expected for $x \neq 0$. Figure 7.12 shows a magnification of these features for a λ =1, and $\lambda = 2$.

7.3.2. Bidimensional space

For a $2-d$ space, the components of the force $\boldsymbol{F}_i = F_{i,1} \cdot \hat{\boldsymbol{e}}_1 + F_{i,2} \cdot \hat{\boldsymbol{e}}_2$ [7] are obtained as,

$$\begin{aligned} 8\Delta\ F_{i,1} &= V(r_{i_1+1,i_2+1}) + 2 \cdot V(r_{i_1+1,i_2}) + V(r_{i_1+1,i_2-1}) \\ &\quad - V(r_{i_1-1,i_2+1}) - 2 \cdot V(r_{i_1-1,i_2}) - V(r_{i_1-1,i_2-1})\,, \\ 8\Delta\ F_{i,2} &= V(r_{i_1-1,i_2+1}) + 2 \cdot V(r_{i_1,i_2+1}) + V(r_{i_1+1,i_2+1}) \\ &\quad - V(r_{i_1+1,i_2-1}) - 2 \cdot V(r_{i_1,i_2-1}) - V(r_{i_1-1,i_2-1})\,. \end{aligned} \tag{7.43}$$

The notation employed r_{i_1,i_2} accounts for $\Delta(i_1, i_2)$. It ought to be reminded that $\boldsymbol{r}_i = \Delta(i_1 \cdot \hat{\boldsymbol{e}}_1 + i_2 \cdot \hat{\boldsymbol{e}}_2) \to \boldsymbol{r}$ as $\Delta \to 0$, $\hat{\boldsymbol{e}}_1$ and $\hat{\boldsymbol{e}}_2$ are unit vectors of an orthonormal cartesian basis, and i is the set of indices required to label this cell (i_1, i_2).

7.4. Forces at intermediate locations, linear interpolation

Given now the discrete $1-d$ potential $V(x_i)$, one can generate the ensemble of discrete forces according to (7.37). However, the Brownian particle trajectory is defined in a continuous domain of the variable position x, and thus the discrete forces defined in the array of mesh points ought to be interpolated in order to get the force at any point of the domain,

$$F(x) = F(x_n) + R[x_n, x_{n+1}](x - x_n)\,, \tag{7.44}$$

[7] $i = (i_1, i_2)$ labels any point in a $2-d$ grid with discretization length Δ, hence $F_{i,1}$ and $F_{i,2}$ are the force components along the $\hat{\boldsymbol{e}}_1$ and $\hat{\boldsymbol{e}}_2$ directions respectively in the space location (i_1, i_2).

where $R[x_n, x_{n+1}]$ is the first order Newton Divided Difference Formula,

$$R[x_n, x_{n+1}] = \frac{F(x_{n+1}) - F(x_n)}{x_{n+1} - x_n}\,, \tag{7.45}$$

and $x \in (x_n, x_{n+1})$.

In $2-d$, the forces at any point $\boldsymbol{r} = (r_1\,,\, r_2)$ in the continuous domain are obtained by the interpolation formula [Kunz, 1957],

$$\begin{aligned}
F_1(\boldsymbol{r}) = &\frac{F_1(Q_{n,m})}{(r_{1,n+1} - r_{1,n})(r_{2,m+1} - r_{2,m})}\ (r_{1,n+1} - r_1)\ (r_{2,m+1} - r_2) \\
&+ \frac{F_1(Q_{n+1,m})}{(r_{1,n+1} - r_{1,n})(r_{2,m+1} - r_{2,m})}\ (r_1 - r_{1,n})\ (r_{2,m+1} - r_2) \\
&+ \frac{F_1(Q_{n,m+1})}{(r_{1,n+1} - r_{1,n})(r_{2,m+1} - r_{2,m})}\ (r_{1,n+1} - r_1)\ (r_2 - r_{2,m}) \\
&+ \frac{F_1(Q_{n+1,m+1})}{(r_{1,n+1} - r_{1,n})(r_{2,m+1} - r_{2,m})}\ (r_1 - r_{1,n})\ (r_2 - r_{2,m})\,, \\
F_2(\boldsymbol{r}) = &\frac{F_2(Q_{n,m})}{(r_{1,n+1} - r_{1,n})(r_{2,m+1} - r_{2,m})}\ (r_{n+1} - r_1)\ (r_{2,m+1} - r_2) \\
&+ \frac{F_2(Q_{n+1,m})}{(r_{1,n+1} - r_{1,n})(r_{2,m+1} - r_{2,m})}\ (r_1 - r_{1,n})\ (r_{2,m+1} - r_2) \\
&+ \frac{F_2(Q_{n,m+1})}{(r_{1,n+1} - r_{1,n})(r_{2,m+1} - r_{2,m})}\ (r_{1,n+1} - r_1)\ (r_2 - r_{2,m}) \\
&+ \frac{F_2(Q_{n+1,m+1})}{(r_{1,n+1} - r_{1,n})(r_{2,m+1} - r_{2,m})}\ (r_1 - r_{1,n})\ (r_2 - r_{2,m})\,,
\end{aligned} \tag{7.46}$$

where $Q_{i,j} = (r_{1,i}\,,\, r_{2,j})$ with $i = n, n+1;\ j = m, m+1$, and $(r_1\,,\, r_2) \in (r_{1,n}\,,\, r_{2,m}\,;\, r_{1,n+1}\,,\, r_{2,m+1})$. For ease of notation, it has been assumed $r_{1,n} = \Delta \cdot (i_1 = n)$.

7.5. Stochastic partial differential equations

Stochastic partial differential equations (*SPDEs*) of a field ϕ may be written in the general form for a Euclidean $d-$space,

$$\frac{\partial \phi(\boldsymbol{r}, t)}{\partial t} = f(\phi(\boldsymbol{r}, t), \nabla, \alpha) + g(\phi(\boldsymbol{r}, t), \nabla)\ \eta(\boldsymbol{r}, t)\,, \tag{7.47}$$

where the bold–face notation tags a vector in the multidimensional space. $\eta(\boldsymbol{r}, t)$ is the noise term that has a correlation

$$\langle \eta(\boldsymbol{r}, t)\ \eta(\boldsymbol{r'}, t') \rangle = \epsilon\ C\left(\frac{\boldsymbol{r} - \boldsymbol{r'}}{\lambda}\,,\ \frac{|t - t'|}{\tau_0} \right)\,, \tag{7.48}$$

where ϵ is the noise's intensity, and λ and τ_0 are respectively the correlation length and time. The brackets indicate a space and time averages. For the Gaussian white–noise case, the function C is the product of two Dirac delta functions. f designates the deterministic force, that depends on the field variable ϕ, its spatial derivatives, and a likely set of control parameters α. Thus, this force comprises the diffusion term and a reaction term, that may represent any interaction in the system, such as those concerning chemical kinetics. g is the random force coupling term; despite employing the same notation (g) it has nothing to do with the correlation function of a static spatial disorder.

The numerical analysis of the stochastic partial differential equation onsets from the discretization of space, that leads to a set of coupled ordinary stochastic differential equations on a lattice

$$\frac{\partial \phi_i}{\partial t} = f_i(\phi(t)) + \sum_j g_{ij}(\phi(t))\ \eta_j(t)\,, \tag{7.49}$$

where indexes i and j label a point in the hypercubic $d-$space. It should be remarked that f_i and g_{ij} depend on ϕ_i.

May the spatiotemporal Gaussian noise be additive, it is presumed that it has no interpretation problem in any dimension. That is to say, the size of the lattice cells is assumed to be small compared to other spatial length scales of the system, yet it is large enough to prevent the spatially extended noise from producing large fluctuations of the coarse–grained field between adjacent cells. Hence, the field is assumed to behave smoothly. Further details on this discussion are addressed in [García-Ojalvo and Sancho, 1999; Toral and Colet, 2014].

Were the noise terms of a stochastic differential equation multiplicative instead, they must be interpreted. Gaussian white noise might be

considered, for physical reasons, the limit of a real noise when its correlation time decreases to zero. Therefore, it has to be interpreted in the Stratonovich sense, instead of the Itô sense, commonly employed in mathematics. These interpretations involve two main differences. On one hand, in the Stratonovich sense, the multiplicative noise term, as well as the noise itself, have non–zero mean values, whereas they do have null mean values in the Itô sense. On the other, within the Stratonovich interpretation, the stochastic terms follow the general rules of calculus concerning integration and derivation, yet not within the Itô sense.

From now on, when considering the discrete version of the *SPDEs*, it will be assumed that they state in a $d-$dimensional lattice of N^d cells of size Δ^d, and so space isotropy is presumed as well. Therefore, the total size of the system is $(N\Delta)^d$.

7.5.1. The Heun method for the Langevin equation

Considering a white noise term in both space and time, its correlation in discrete space reads

$$\langle \eta_i(t)\ \eta_j(t')\rangle = 2\epsilon\ \frac{\delta_{ij}}{\Delta^d}\ \delta(t-t')\,, \tag{7.50}$$

indexes i, j label each of them a point in the hypercubic $d-$space.

Integration of the stochastic partial differential equation (7.47) between t and $t+\Delta t$, after choosing the time step Δt, leads to

$$\phi_i(t+\Delta t) - \phi_i(t) = \int_t^{t+\Delta t} f_i(\phi(t'))\ dt'\ + \sum_j \int_t^{t+\Delta t} g_{ij}(\phi(t'))\ \eta_j(t')\ dt'\,. \tag{7.51}$$

That after some transformations, see [García-Ojalvo and Sancho, 1999] for

further details, becomes

$$\begin{aligned}\phi_i(t+\Delta t) = \phi_i(t) + f_i(\phi(t))\ \Delta t + \sum_j g_{ij}(\phi(t))\ X_j \\ + \sum_{jkl} \frac{\partial g_{ij}}{\partial \phi_k}\ g_{kl}(\phi(t))\ Y_{jl} + \mathcal{O}\left(\Delta t^{3/2}\right)\,,\end{aligned} \tag{7.52}$$

where

$$X_i \equiv \int_t^{t+\Delta t} \eta_i(t')\ dt'\,, \tag{7.53}$$

$$Y_{ij} \equiv \int_t^{t+\Delta t} \eta_i(t')\ dt' \int_t^{t'} \eta_j(t'')\ dt''\,. \tag{7.54}$$

Since $\eta_i(t)$ is a Gaussian random variable with zero mean and integration is a linear operation, X_i is also Gaussian with null mean and a correlation like (7.50), that is,

$$\langle X_i\ X_j \rangle = 2\epsilon\ \frac{\delta_{ij}}{\Delta^d}\ \Delta t\,. \tag{7.55}$$

The brackets indicate a spatial average. From which it is straightforwardly achieved the expression

$$X_i = \sqrt{\frac{2\epsilon \Delta t}{\Delta^d}}\ \gamma_i\,, \tag{7.56}$$

to generate the random variable X_i. γ_i are Gaussian random numbers with null mean and variance equal to 1. They may be generated by means of pseudorandom algorithms [García-Ojalvo and Sancho, 1999; Galassi et al., 2009].

Notwithstanding, the random process Y_{ij} is not so easily computed. On paper, it is a non–Gaussian random variable which cannot be simulated exactly, even though its statistical properties are well established [Mannella, 1989]. May it be considered the particular scenario in which g_{ij} is a constant coupling function, the last term in (7.52) vanishes, and thus there is no need to compute Y_{ij}. This case corresponds to an additive noise, like

the white noise usually employed in the inquiries of this theses. Therefore, from now on, the assumption g_{ij} being a constant is made.

The algorithm to generate a random variable ϕ that obeys the *SPDE* (7.49), considering a constant coupling function g_{ij}, is hence,

$$\phi_i(t+\Delta t) = \phi_i(t) + f_i(\phi(t))\ \Delta t + \sum_j g_{ij}(\phi(t))\ X_j\,, \tag{7.57}$$

and constitutes an algorithm of Euler type, which are the lowest–order algorithms. The following order of approximation is the Heun algorithm, or also called improved Euler method. For the white noise in time it reads

$$\begin{aligned}\phi_i(t+\Delta t) = \phi_i(t) &+ \frac{1}{2}\left[f_i(\phi(t)) + f_i\left(\tilde{\phi}(t)\right)\right]\Delta t \\ &+ \frac{1}{2}\sum_j \left[g_{ij}(\phi(t)) + g_{ij}\left(\tilde{\phi}(t)\right)\right] X_j\,,\end{aligned} \tag{7.58}$$

where $\tilde{\phi}(t)$ is given by the Euler algorithm

$$\tilde{\phi}_i(t) = \phi_i(t) + f_i(\phi(t))\ \Delta t + g_{ij}(\phi(t))\ X_j\,. \tag{7.59}$$

The Heun algorithm is a second–order Runge–Kutta method [García-Ojalvo and Sancho, 1999].

One last comment on the numerical simulations of *SPDE*s ought to be done. Since Δt needs to be the smallest time scale of the system, it has to be chosen small enough. A proper choice for the integration time step thus makes higher–order algorithms unnecessary, because most of the systematic deviations originate in the deterministic part of the algorithm. And that is why the Heun method improves the accuracy compared to the simple Euler algorithm. Nevertheless, improvement might be achieved by increasing the number of realizations and the quality of the random number generator, since trajectories are stochastic.

7.6. Summary

The numerical procedure to generate disorder potentials applies to any statistical correlation, which must be isotropic and periodic in the finite simulation domain; notwithstanding, it is worth to remark that $V(\boldsymbol{r})$ is a non–symmetric random function. The method relies on two Fourier transforms and one antitransform, yet all the constraints can be inferred to real space, and thus Fourier space is left as a mere stage in the process, theoretically fundamental but numerically practical.

It is also reported the numerical recipe based on [García-Ojalvo and Sancho, 1999; Suñé et al., 2012] that brings about time unfolding to the disorder. The algorithm relies on the Fourier space as well and works out to preserve the disorder's spatial correlation at any time. Furthermore, time properties of the outcome are set up by a time scale parameter. On the other hand, it is implemented a transformation so as to reshape the disorder into a landscape of obstacles of equal height. The proposed procedure conserves the space and time features of the original potential. The average obstacle width and time scales are thus well controlled quantities; besides, the density of obstacles is constant in time. The fixed density is ubiquitous in nature, even for those nonequilibrium systems exhibiting birth and death processes—such as a monolayer of colonies of gliding bacteria [Peruani et al., 2012]—, since the relaxation dynamics of the nonequilibrium cluster–size distribution may be much faster that the proliferation time of the population.

With regard to the forces to be derived from the random potentials, it is overviewed the numerical algorithm to carry out the discrete derivative both in one and in two dimensions. Further, the force correlations are also inquired. Linear interpolation is required in order to implement this discrete force field to the continuous Langevin equation.

Finally, discretization of stochastic differential equations is reported, as well as the second–order Heun method to integrate them.

CHAPTER 8

Spare investigations

The present Chapter reports two cases of study that can be addressed employing those skills and proceedings acquired along the former chapters. State of the art in both scenarios is the early stage, in which a description of the problem is attained by stochastic Langevin dynamics. Besides, numerical simulations have been carried out for those reference scenarios that entail a low degree of complexity. The outcome reveals some interesting insights, from which new hypotheses might be made to go on with further investigations.

8.1. Brownian motion at interfaces

This section deals the physics of particles undergoing thermal fluctuations, different viscosities, and a confining field, in a finite volume. The potential displays a minimum at a thin—quasi $2-d$—interface to which particles are attracted, and from which they are promoted by thermal fluctuations. Similarly, it is considered a different viscosity in the interface respect to the rest of the $3-d$ space. Both theoretical analysis and stochastic simulations are employed to check the equilibrium and non–equilibrium properties of the system.

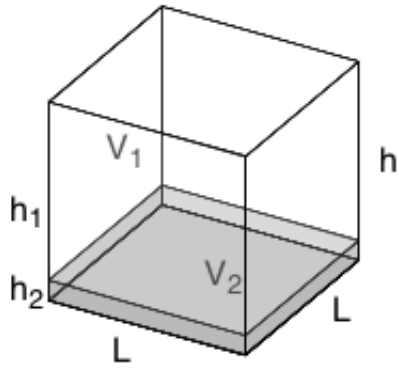

Figure 8.1 – Pictorial scheme of the system.

8.1.1. Interface attraction

Equilibrium thermodynamics

A thermodynamic system of n particles, occupying a total enclosed volume $\hat{V}$, at temperature $\hat{T}$, is considered. At a fixed height $\hat{h}_2$, there is an attractive potential, such that particles undergo a force that confines them at $\hat{z} \leq \hat{h}_2$. Hence, this potential displays two energy states, $\hat{V}(\hat{z} > \hat{h}_2) = 0$, and $\hat{V}(\hat{z} \leq \hat{h}_2) = -V_0$. V_0 is employed as a energy reference to scale the potential and the temperature. From now on, scaled quantities are assumed according to this energy scale; space is also scaled by any characteristic length scale λ_0.

h_2 splits the volume V into two volumes V_1—height h_1—, and V_2—height h_2—, with a population of particles n_1 and n_2 respectively, see Figure 8.1. Therefore, $V = V_1 + V_2$, $n = n_1 + n_2$.

Thermal equilibrium is assumed in the whole system, so that T is con-

stant; hence the thermodynamic equilibrium is given by the the equality of the chemical potentials concerning each of the two subsystems, μ_1, μ_2,

$$\mu_1(T, n_1, V_1) = \mu_2(T, n_2, V_2)\,. \tag{8.1}$$

Applying this thermodynamic equilibrium condition, assuming the ideal gas approximation, and using the macrocanonical partition function, it is obtained the population of particles in each fraction of volume,

$$\frac{n_2}{n_1} = \frac{V_2}{V_1}\, e^{\beta}\ ,\ (\beta \equiv T^{-1})\,. \tag{8.2}$$

In the high temperature limit $\beta \to 0$,

$$\rho_2 = \rho_1\ ,\ (\rho_i \equiv n_i/V_i)\,, \tag{8.3}$$

where ρ_1 is the density of particles in volume V_1, and ρ_2 in V_2. Notwithstanding, the opposite limit $\beta \to \infty$ ($T \to 0$) is *a priori* undetermined. May (8.2) be rewritten in terms of the total number of particles, n,

$$\frac{n_2}{n} = \frac{1}{1 + \frac{V_1}{V_2}\, e^{-\beta}}\,, \tag{8.4}$$

then the limit $\beta \to \infty$ exists,

$$\frac{n_2}{n} = 1\,. \tag{8.5}$$

Hence all the particles are in the volume V_2. The physical interpretation of this limit is straightforward: when $T \to 0$ particles can't overcome the potential barrier to escape from the volume V_2 to V_1.

The Boltzmann distribution

Further, this scenario may be addressed employing the Boltzmann distribution, that accounts for the probability measure of a system to be in any of the various possible energy states. Concerning the current system, in which there is but one energy profile along the vertical direction (z), the distribution is

$$P(z) = \frac{1}{C_1}\, e^{-V(z)/T}\,, \tag{8.6}$$

where $V(z)$ is any potential to bring about the two energy states at V_1, $V(z > h_2) = 0$, and V_2, $V(z < h_2) = -1$. A plausible choice for the potential would be—$h_2 = 1$ without loss of generality—,

$$V(z) = \frac{1}{2}\left[\tanh\left(\frac{z-1}{a_0}\right) - 1\right], \tag{8.7}$$

for it is a continuous and derivable function; a_0 states for the steepness of the potential increase from $V(z < 1) = -1$ to $V(z > 1) = 0$. z is the vertical coordinate, and C_1 is the normalizing factor,

$$C_1 = \int_0^h dz\; e^{-V(z)/T}\,, \tag{8.8}$$

the system to be defined from $z = 0$ to $z = h$.

Stochastic Dynamics

Trajectories of an ensemble of n particles in an enclosed system of volume V, at a temperature T, and undergoing a potential (8.7), are simulated by Langevin equations for each particle $i = 1, \ldots, n$—assuming the overdamped approach in its scaled version (Sec. 1.4.2)—

$$\begin{aligned} \frac{dx_i}{dt} &= \xi_x(t)\,, \\ \frac{dy_i}{dt} &= \xi_y(t)\,, \\ \frac{dz_i}{dt} &= -\frac{dV(z)}{dz} + \xi_z(t)\,. \end{aligned} \tag{8.9}$$

The fluctuation–dissipation theorem for each component reads

$$\langle \xi_w(t)\; \xi_w(t')\rangle = 2\,T\,\delta(t-t')\,,\ (w = x, y, z)\,. \tag{8.10}$$

The scaling length parameter has been chosen to be z_0, the coordinate—the height—such that $\hat{V}(z_0) = -V_0/2$. As usual, a second order Heun algorithm for ordinary stochastic differential equations (Sec. 7.5.1) is employed to simulate the trajectories predicted by (8.9).

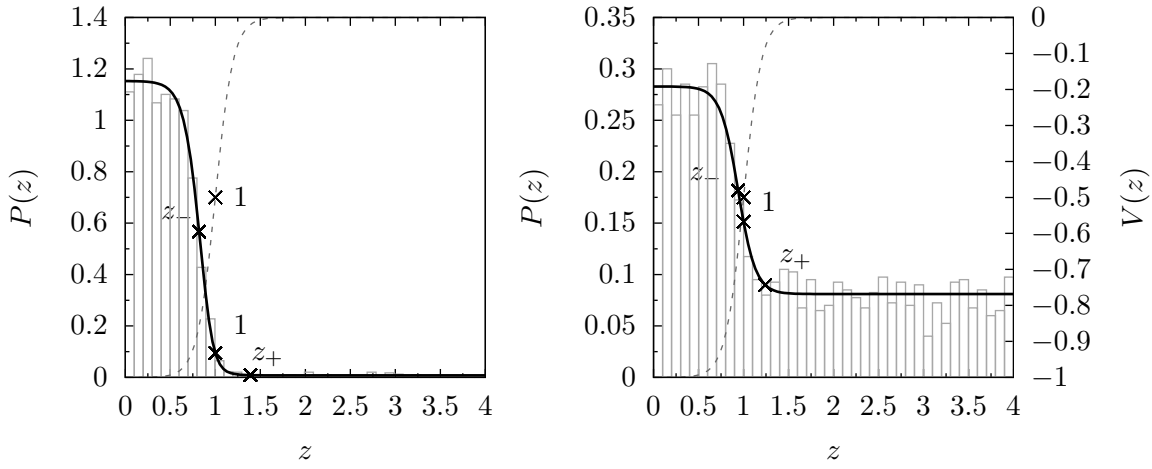

Figure 8.2 – Normalized particle position histogram for temperatures $T = 0.2$ (left) and $T = 0.8$ (right). Superimposed are the Boltzmann distribution (8.6) in black, and the potential $V(z)$ (8.7) in grey dashed lines—the right hand scale for the potential applies to the left panel as well—.

Results

Simulations run up to $t = 2000$ with an integration step $\Delta t = 0.01$, for $n = 4000$ particles in a volume $V = L \times L \times h$, $L = 40$, $h = 10$, at different temperatures $T = 0.2, 0.4, 0.6, 0.8, 1$; and $a_0 = 0.2$. At grater times than the diffusive scale $\sim \frac{h^2}{2T}$, the system is expected to attain the thermodynamic equilibrium, for the whole vertical space is explored. The histogram of particle's locations along vertical direction (z) at the end of simulations $t = 2000$, when equilibrium is expected to be reached, is plotted in Figure 8.2 for $T = 0.2$ and 0.8.

Results in Figure 8.2 display a fairly good agreement with the Boltzmann distribution (8.6). The concordance is better at low temperatures because in this scenario there are less fluctuations. Similarly to the function of the potential, $P(z)$ displays a soft profile between the concentrations in V_2 and V_1. The effect of this transition region may be measured computing the ratio of particles at V_2, n_2, over the total n. The outcome should then compare to the theoretical prediction (8.4), that in the current

T	n_2/n	$z_{2\to1} = z_-$	n_2/n	$z_{2\to1} = 1$	n_2/n	$z_{2\to1} = z_+$
0.2	0.87	0.82	0.92	1.0	0.93	1.39
0.4	0.51	0.89	0.53	1.0	0.56	1.32
0.6	0.33	0.92	0.34	1.0	0.37	1.28
0.8	0.25	0.94	0.26	1.0	0.29	1.24
1.0	0.21	0.95	0.22	1.0	0.24	1.22

Table 8.1 – Ratio of particles in volume V_2 to the total. Results are obtained by integration of (8.6) with various temperatures and upper limits for the integral $z_{2\to1}$.

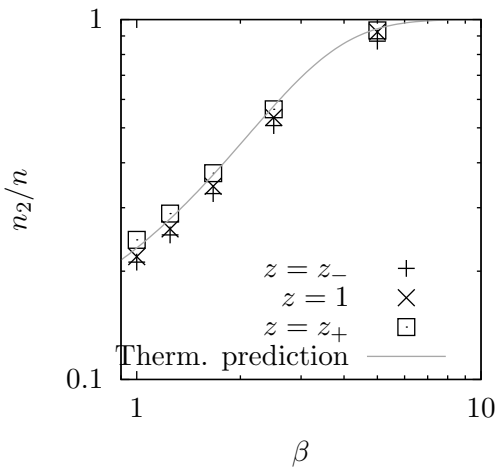

Figure 8.3 – Comparison between the data in Table 8.1 and the thermodynamic prediction (8.11).

scenario reads—assuming $h_2 = 1$—,

$$\frac{n_2}{n} = \frac{1}{1 + \frac{V_1}{V_2}\, e^{-\beta}} \;=\; \frac{1}{1 + (h-1)\, e^{-\beta}}\,. \tag{8.11}$$

n_2/n is computed by integration of (8.6) with (8.7) up to a coordinate $z_{2\to1}$. A first choice for $z_{2\to1}$ might be 1, the abscissa where the confining potential has drop one half $V(1) = -1/2$. Further, other values would be; $z_{2\to1} = z_-$, that corresponds to the abscissa where the transition between the two plateaus is half done ($P(z_-) = [e^{1/T} - 1]/(2\, C_1)$), and $z_{2\to1} = z_+$, that corresponds to the shortest abscissa such that $[P(z_+)\, C_1 - 1] < 0.1$. Figure 8.2 displays $z_{2\to1} = z_-$, 1, and z_+ for the corresponding settings. Results for the ratio n_2/n, for the three $z_{2\to1}$ choices, and various temperatures, are enlisted in Table 8.1.

Figure 8.3 reveals that the current results exhibit a fairly good accord with the thermodynamic prediction (8.11). In particular, the best criteria to compute the ratio of particles at V_2 n_2/n is to integrate the Boltzmann distribution (8.6) up to z_+.

8.1.2. Brownian movement at two viscosities with interface attraction

Considering again the scheme in Figure 8.1, it is assumed that particles undergo a different viscosity (γ_2 , γ_1) depending on whether they are in V_2, or in V_1; in addition to the potential (8.7). Analogously to the function employed to characterize the attracting potential (8.7), the scaled friction along the vertical coordinate might be,

$$\gamma(z) = \frac{1}{2}\left[1 + \gamma_0 - (1-\gamma_0)\;\tanh\left(\frac{z-1}{a_0}\right)\right]\,, \tag{8.12}$$

where $\gamma_0 = \gamma_1/\gamma_2$ (γ_2 is been employed as the scaling viscosity); see Figure 8.4.

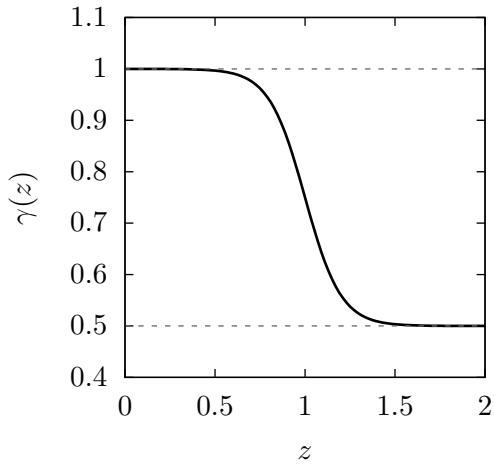

Figure 8.4 – Viscosity portrait along the vertical direction. $\gamma_0 = 0.5$.

The set of adimensional stochastic differential equations that describe this scenario in the overdamped approach (Sec. 1.4.2) is,

$$\begin{aligned} \frac{dx_i}{dt} &= \frac{1}{\gamma(z)}\,\xi_x(t)\,, \\ \frac{dy_i}{dt} &= \frac{1}{\gamma(z)}\,\xi_y(t)\,, \\ \frac{dz_i}{dt} &= \frac{-1}{\gamma(z)}\,\frac{dV(z)}{dz} + T\,\frac{d}{dz}\left(\frac{1}{\gamma(z)}\right) + \frac{1}{\gamma(z)}\,\xi_z(t)\,, \end{aligned} \tag{8.13}$$

where $\xi_w(t)$ $(w = x, y, z)$ are independent Gaussian random variates of zero mean, variance 1, and correlation according to the fluctuation–dissipation theorem,

$$\langle \xi_w(t)\ \xi_w(t')\rangle = 2\ \gamma(z)\,T\,\delta(t-t')\ . \tag{8.14}$$

Now the scaling characteristic time is $\tau_0 = (z_0^2\ \gamma_2)/V_0$ (Sec. 1.4.2). The term with the space derivative of the viscosity in (8.13) arises from the Itô interpretation of the overdamped Langevin equation compatible with the Fokker–Planck equation for a multiplicative noise. This term provides a steady friction independent result of the integration of the Langevin equation (8.13), even though γ does depend on the position z; in agreement with the steady non equilibrium distribution obtained from the corresponding

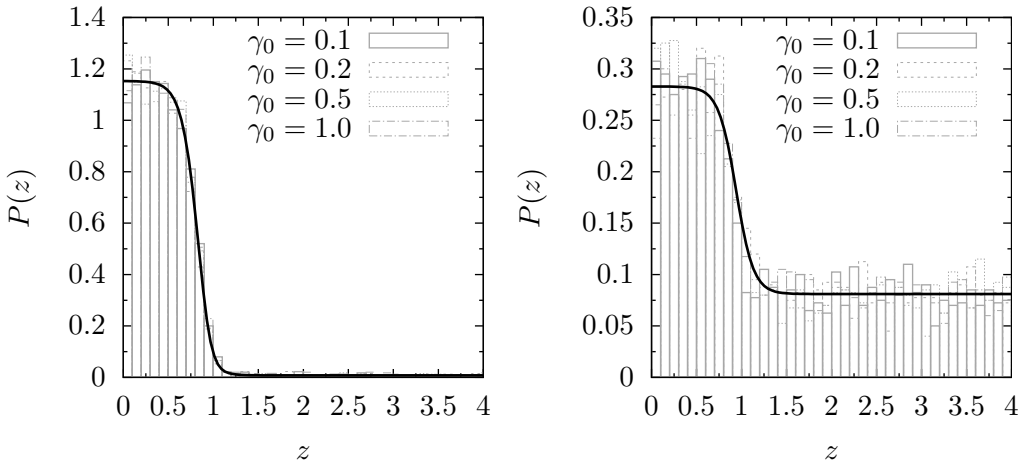

Figure 8.5 – Normalized particle position histogram for temperatures $T = 0.2$ (left) and $T = 0.8$ (right). Superimposed is the Boltzmann distribution (8.6) in black.

Fokker–Planck equation [Sagués et al., 2007; Sancho, 2015].

Results

Simulations of (8.13) by a Heun algorithm (Chap. 7.5.1) run for the same settings than in the former scenario ($V = L \times L \times h$, $L = 40$, $h = 10$, $n = 4000$, $a_0 = 0.2$), up to $t = 1000$. Now, the control parameters are T and γ_0. The term $T \frac{d}{dz}\left(\frac{1}{\gamma(z)}\right)$ in (8.13) exhibits a strong dependence on the parameter γ_0. Therefore, Δt should be shorter the lower is the quotient between frictions γ_0. In particular, for the current simulations, $\Delta t = 0.0025$ for $\gamma_0 < 0.5$; $\Delta t = 0.01$ otherwise.

From Figure 8.5 it is gathered that the ensemble's distribution is preserved, despite the friction does change along the vertical direction, as it is foreseen through the discussion of the viscosity's derivative term added to the Langevin equation (8.13). The Boltzmann distribution (8.6) is displayed indeed. Accordingly, from this data, it may be computed the fraction of particles in the volume V_2 over the total, n_2/n, employing z_+, as stated in Section 8.1.1. Figure 8.6 compares the attained values to (8.11), and they

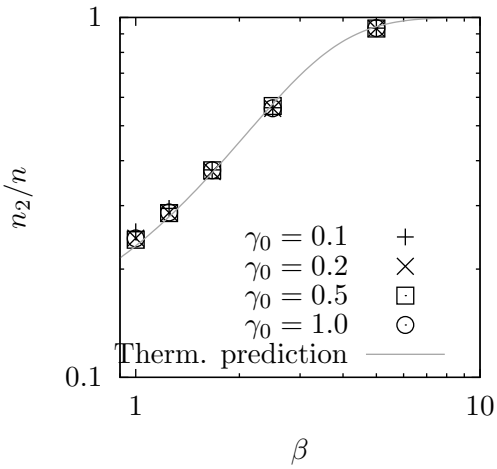

Figure 8.6 – Comparison between the simulation data and the thermodynamic prediction (8.11).

display almost a perfect alignment.

Particle displacements

The distribution of particle displacements accounts for the probability that a particle has moved a certain distance during a time lag. This distribution is quantified in terms of the self part of the van Hove correlation function,

$$G_s(\Delta w, \Delta t) = \frac{1}{n}\left\langle \sum_{i=1}^{n} \delta(w + w_i(\tau) - w_i(t + \Delta t)) \right\rangle, \tag{8.15}$$

where $\langle\cdot\rangle$ labels ensemble averaging; $w = x, y, z$. The distribution of particle displacements is a ubiquitous interpretation of experimental findings [Skaug et al., 2013]. From the simulation data in the former section, $G_s(\Delta w, \Delta\tau)$ is computed separately for $w = x, y, z$.

When $\gamma_0 = 1$, and so the friction is constant for the whole system, the distribution exhibits the expected Gaussian functionality in the plane xy

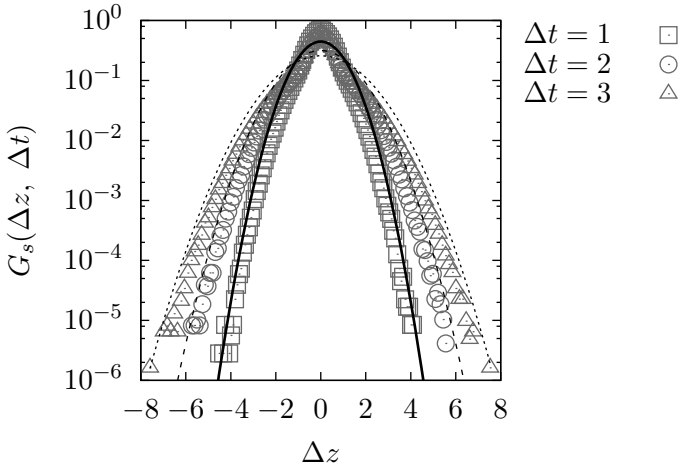

Figure 8.7 – Distribution of particle displacements along the vertical direction z for time lags $\Delta t = 1, 2, 3$; $\gamma_0 = 1$. Superimposed functions are the Gaussian distributions (8.16). $T = 0.4$.

where particles must undergo free Brownian motion,

$$G_s(\Delta w, \Delta t) = \frac{1}{\sqrt{2\pi\ \sigma^2}} e^{-\Delta w^2/(2\sigma^2)}, \tag{8.16}$$

where $\sigma^2 = 2T\Delta t$, and $w = x, y$. However, may the particles' displacements be computed along the vertical axis, along which particles are attracted according to (8.7), the outcome exhibits a more peaked cusp at the mean value than the Gaussian function does (Fig. 8.7). The probability for the particles to undergo displacements $\Delta z \leq 1$ is thus enhanced. It should be noted that 1 is indeed the range of the potential, that exerts a force to the particles that tends to confine them at $z \leq 1$. Displacements $\Delta z > 1$ attain nonetheless to the Gaussian distribution.

Concerning the scenario in which particles undergo two different viscosities, the distribution of displacements are no longer Gaussian–like in any direction. The distribution of particle displacements along x, y is now accounted by a combination of weighed Gaussian distributions ($w = x, y$),

$$G_s(\Delta w, \Delta t) = \frac{n_2}{n}\ f_2(\Delta w, \sigma_2) + \left(1 - \frac{n_2}{n}\right)\ f_1(\Delta w, \sigma_1), \tag{8.17}$$

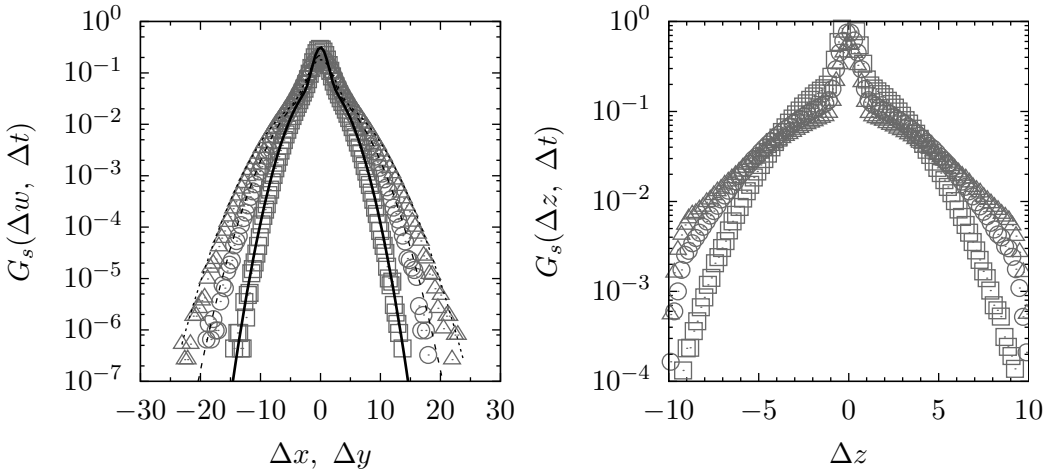

Figure 8.8 – Distribution of particle displacements along the horizontal directions $w = x, y$—left panel—and along the vertical—right panel—; for time lags $\Delta t = 1$ (squares), 2 (circles), and 3 (triangles); $\gamma_0 = 0.1$. Superimposed are the weighed Gaussian distributions (8.17) in the left plot. $T = 0.4$.

where $f_{2(1)}(\Delta w, \sigma_{2(1)})$ are Gaussian functions (8.16), with $\sigma_2^2 = 2T\Delta t$, and $\sigma_1^2 = 2\frac{T}{\gamma_0}\Delta t$. The fraction of particles in V_2 employed in Figure 8.8—left—comes from the results already plotted in Figure 8.6.

However, the distribution of displacements along the vertical direction z does not exhibit any well known functionality. Besides, for the time lags considered, the distributions are altered by the finite size of the system; the data in Figure 8.8—right—is constrained between $z = -10$ to $z = 10$, for the length of the system in z is $h = 10$.

Finally, comparing the particle displacements concerning cases with the same viscosity (Fig. 8.7) to those with a viscosity gradient (Fig. 8.8), it ought to be noted that the viscosity does affect the distribution. In contrast, it has been shown in Figures 8.5 and 8.6 that the population of particles in each state remains constant despite different viscosities being considered.

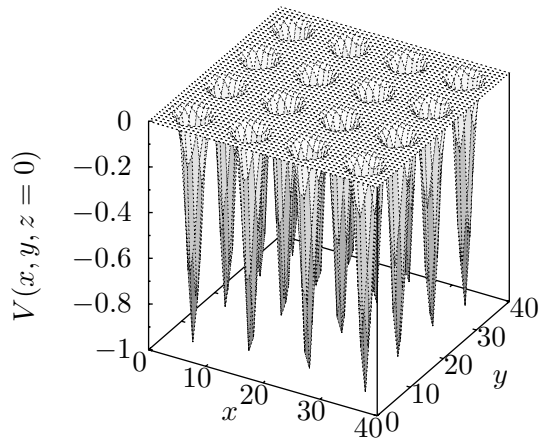

Figure 8.9 – Potential landscape (8.18) at $z = 0$. Parameters choice: $a_0 = 0.2$, $b_0 = 10$, $A = 4$, $B = 1$, and $\phi = 5$.

8.1.3. Intermittent molecular hopping

Studies on the mobility of molecules on a solid–fluid interface reveal desorption–mediated displacements to be universal to portray the diffusion in these physical milieus [Skaug et al., 2013]. Applying Langevin dynamics, as in Section 8.1.2, attention is now committed to modeling the solid–fluid interface diffusion. A $3-d$ periodic attracting potential may be considered as a first approximation,

$$V(x, y, z) = \frac{1}{2}\left[\tanh\left(\frac{z-1}{a_0}\right)\right]\frac{1+e^{-2A(1-B)}}{1+e^{-f(x,y)}}\,, \tag{8.18}$$

$$f(x, y) = A\left[\cos\left(\frac{2\pi}{b_0}(x+\phi)\right) + \cos\left(\frac{2\pi}{b_0}(y+\phi)\right) - 2B\right]. \tag{8.19}$$

a_0 is the steepness of the potential along z, b_0 is the period of the potential wells in the xy plane, A constrains the slope of the wells, B their width, and ϕ is a phase to shift the potential along the xy surface. Figure 8.9 plots a realization of the potential.

It might be nonetheless useful to define an effective radius of the potential wells; for such purpose, the following constraint about the field

component in the xy plane is assumed,

$$\frac{1+e^{-2A(1-B)}}{1+e^{-f(x,y)}} = 0.9\,. \tag{8.20}$$

Hence the radius of the potential wells is,

$$r_{pw} = \frac{b_0}{2\pi}\arccos\left\{\frac{-1}{A}\ln\left[\frac{1}{0.9}\left(1+e^{-2A(1-B)}\right)-1\right]-1+2B\right\}. \tag{8.21}$$

The space derivative of (8.18) brings about the force to which particles are subjected,

$$F_w = -\frac{\partial V}{\partial w} = \frac{\pi A}{b_0}\left[\tanh\left(\frac{z-1}{a_0}\right)-1\right]\frac{\left[1+e^{-2A(1-B)}\right]\sin\left[\frac{2\pi}{b_0}(w+\phi)\right]}{e^{f(x,y)}\left[1+e^{-f(x,y)}\right]^2}, \tag{8.22}$$

$$F_z = -\frac{\partial V}{\partial z} = \frac{-1}{2}\left[a_0\cosh^2\left(\frac{z-1}{a_0}\right)\right]^{-1}\frac{\left[1+e^{-2A(1-B)}\right]}{\left[1+e^{-f(x,y)}\right]}, \tag{8.23}$$

where $w = x, y$, and $f(x,y)$ is defined in (8.19).

With regard to the viscosity, it is assumed to exhibit the same $3-d$ dependence than $V(x,y,z)$, so that,

$$\gamma(x,y,z) = \gamma(z)\,\frac{1+e^{-2A(1-B)}}{1+e^{-f(x,y)}}, \tag{8.24}$$

$\gamma(z)$ being defined in (8.12), and $f(x,y)$ in (8.19).

Results

Experimental results on tracking individual molecules, such as fatty acid molecules [Honciuc et al., 2008], and different polymers [Skaug et al., 2013], at a planar interface between a liquid and a solid—fused silica for example—are employed as a reference for the choice of the simulation parameters. According to the mean–square displacement results at short times, molecules undergo Fickian–like diffusion within a square compartment with reflective boundaries of size $\mathcal{L} = (2.4 \pm 0.9)\,\mu$m [Honciuc et al.,

2008], so the characteristic length scale is set to $z_0 = 2.4\,\mu$m. The flow cell of the experiments used to be of height ≈ 0.12 mm [Honciuc et al., 2008], for that $h = 50$ is employed. "Jumping" is inferred to undergo activation barriers of ≈ 50 kJ/mol [Honciuc et al., 2008]—and so the energy scale is $V_0 = 50\,(N_A)^{-1}$ kJ, N_A is the Avogadro number—, which corresponds to a temperature choice $T = 0.05$. However, other temperatures will also be explored. A standard diffusion coefficient for these type of molecules in bulk solution may be $\hat{D} \approx 10^3\,\mu\text{m}^2/\text{s}$ [White, 1955]. The characteristic time scale $\tau_0 = (z_0^2\ \gamma_2)/V_0$, already defined in Section 8.1.2, may be rewritten in terms of the temperature, the scaling diffusion coefficient ($\hat{D} = k_B\ \hat{T}/\gamma_1$; γ_1 is the dimensioned viscosity in the bulk), the scaled viscosity, and the dimensioned length scale,

$$\tau_0 = \frac{T\ z_0^2}{\gamma_0\ \hat{D}} = \frac{T}{\gamma_0}\,5.76\cdot 10^{-3}\,\text{s}\,. \tag{8.25}$$

The scaled viscosity, as well as the temperature, will be the tuning parameters of the simulations. According to Section 8.1.2, the integration step Δt ought to be $\Delta t = 0.0025$ for $\gamma_0 < 0.5$, and $\Delta t = 0.01$ otherwise. The lasting parameters are: $n = 400$ particles, $t = 4000$, $a_0 = 0.2$, $\gamma_0 = 0.2$, $L = 40$, $b_0 = 2$, $A = 8$, $B = 0.5$, and $\phi = 1$. With this choice, the effective radius of the potential wells (8.21) is $r_{pw} = 0.41$, so that the effective area of a well is $\approx 3.04\,\mu\text{m}^2$, of the same order of magnitude than $\mathcal{L}^2 \approx 5.76\,\mu\text{m}^2$—the area of the square compartment in which molecules undergo Fickian diffusion—.

Considering the population of particles trapped in the potential wells n_2 respect to the total n for different temperatures and scaled viscosities (Fig. 8.10)[1], it should be gathered that, at $T = 0.05$ and $T = 0.1$, particles cannot surmount the potential barriers once they are trapped in a well, $n_2/n \to 1$. The hereunder analysis focuses on temperatures $T = 0.1$ and $T = 0.2$; the latter exhibits a steady fraction of particles at the interface $n_2/n \neq 1$,

[1]It ought to be enlightened that, until the end of Section 8.1, figures might display dimensioned quantities, and so axes would allude to dimensional scales. However, the "hat" notation—employed in the thesis to label dimensioned quantities—is not applied to the axis labels to appear until the end of the present Section. Anyway, physical units will be displayed in–between brackets when axes are dimensional.

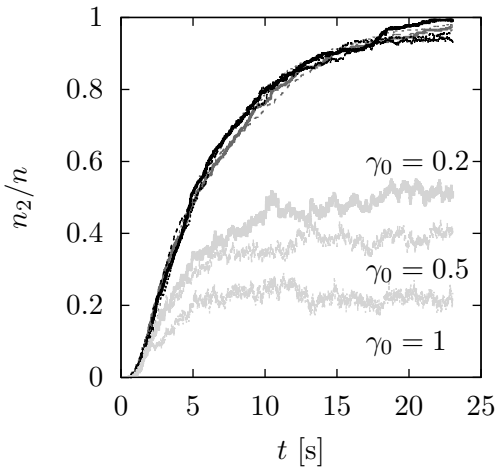

Figure 8.10 – Fraction of trapped particles in the potential wells for different temperatures $T = 0.05$ (dark grey), 0.1 (black), and 0.2 (light grey); and friction quotients $\gamma_0 = 0.2$ (solid), 0.5 (dashed), and 1 (dotted). In order to compute n_2, it is employed z_+, see Section 8.1.2.

a [s^{-1}]	$\gamma_0 = 0.2$	$\gamma_0 = 0.5$	$\gamma_0 = 1$
T =0.1	0.14 ± 0.01	0.20 ± 0.01	0.44 ± 0.01
T =0.2	6.66 ± 0.07	13.36 ± 0.08	31.7 ± 0.6

Table 8.2 – Exponential decay of the confinement time (t_c) distributions.

and splitting of the trajectories concerning different viscosities. Indeed, the steady fraction of particles attached to the interface n_2/n increases according to the difference of friction between the two phases.

Trajectories in the plane $z = 0$ ($T = 0.2$, $\gamma_0 = 0.2$) display confinement into the potential wells punctuated by rare hops (Fig. 8.11). The confinement time distributions for different temperatures and frictions are plotted in Figure 8.12. Disregarding those points at $t = 0$ s, they may be fitted by a an exponential function, whose slope is the inverse of the characteristic confinement time. The outcome for the confinement time is summarized in Table 8.2.

The distribution of displacements (8.15) at the xy plane for adsorbed–

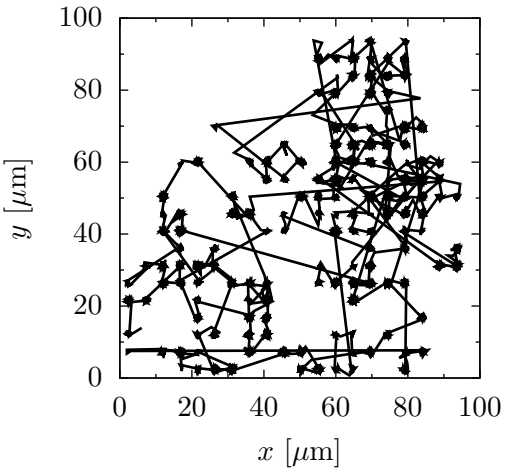

Figure 8.11 – Few of the 400 trajectories at the $z = 0$ plane simulated according to the parameters choice detailed in the beginning of this section.

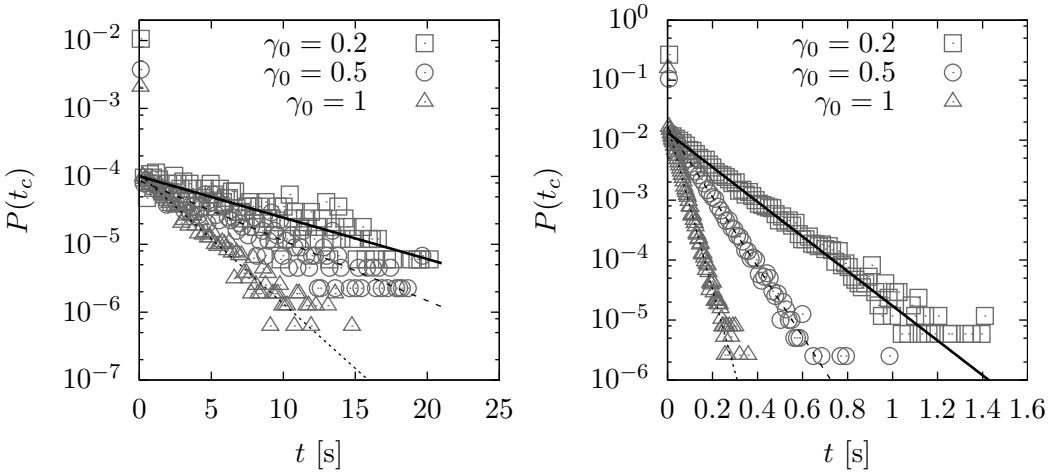

Figure 8.12 – Distribution of confinement times in the potential wells for $T = 0.1$ (left) and $T = 0.2$ (right). Straight lines correspond to fitting an exponential function $f(t) = b\exp(-at)$ excluding the points at $t = 0$ s.

$\hat{D}_{xy}$ [μm^2/s]	$\gamma_0 = 0.2$	$\gamma_0 = 0.5$	$\gamma_0 = 1$
$T = 0.1$	2.1 ± 0.6	4.3 ± 0.5	8.8 ± 0.4
$T = 0.2$	178 ± 8	360 ± 10	470 ± 30

Table 8.3 – $1 - d$ diffusion coefficient in the plane xy for the interface.

desorbed molecules at an interface, that undergo Fickian diffusion along the bulk excursions, has been showed to possess long algebraic tails [Bychuk and O'Shaughnessy, 1995],

$$G_s(\Delta w) \approx r^{*-2} \left(\frac{r^*}{\Delta w} \right)^3 \ , \ (\Delta w > r^*) \ , \ (w = x, y) \, , \tag{8.26}$$

where $r^* = (\hat{D}t^*)^{1/2}$ is the diffusion length, corresponding to the re–adsorbing time t^*; $\hat{D}$ is the bulk diffusivity. The distributions of molecular displacements at different time intervals for the simulation with $T = 0.1$ (Fig. 8.13)—left—reveals a rather good agreement with the theoretical prediction (8.26). In particular, fitting (8.26) to the $\Delta t = 0.4$ s points leads to $r^* = (0.114 \pm 0.002)\,\mu$m for $\gamma_0 = 0.2$, and $r^* = (0.177 \pm 0.007)\,\mu$m for $\gamma_0 = 1$. Notwithstanding, the $T = 0.2$ distributions of molecular displacements do not exhibit a well known functionality. From the diffusion length r^*, it can be calculated the corresponding re–adsorbing time t^*—applying the bulk diffusion coefficient $\hat{D} = 10^3\,\mu$m^2/s—, $t^* = (1.30 \pm 0.05) \cdot 10^{-5}$ s for $\gamma_0 = 0.2$, and $t^* = (3.1 \pm 0.3) \cdot 10^{-5}$ s for $\gamma_0 = 1$.

The mean square displacement of the trajectories in the xy plane scales linearly with time after an initial transient regime. Hence, the ubiquitous Einstein–Smoluchowski expression (1.3), brings about the diffusion coefficient $\hat{D}_w$, that should be equivalent regardless of the direction because of space isotropy in the xy plane; the $1 - d$ diffusion coefficients in the interface are summarized in Table 8.3.

8.1.4. Random confinement

Instead of considering a set of periodically distributed wells that adsorb particles (Sec. 8.1.3), now the potential barriers may be stochastic. Bearing

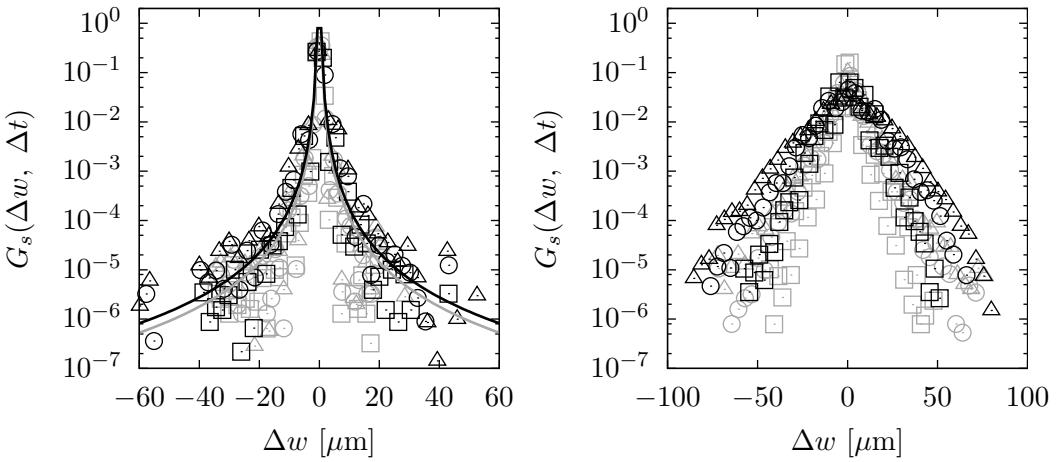

Figure 8.13 – Distributions of displacements (8.15) at the xy plane ($w = x, y$) for different time steps $\Delta t = 0.2$ s (squares), $\Delta t = 0.4$ s (circles), and $\Delta t = 0.6$ s (triangles). Grey symbols label simulation results for $\gamma_0 = 0.2$, whereas those for $\gamma_0 = 1$ are in black. To the left, $T = 0.1$, and $T = 0.2$ to the right. The curves in the left panel are the fitting of (8.26) to the $\Delta t = 0.4$ s data.

in mind the pictorial scheme in Figure 8.1, the potential to adsorb the particles at the interface V_2 is the one already defined in (8.7), yet its amplitude ought to be a random variate. Hence,

$$\bar{V}(x, y, z) = V_0(x, y)\ V(z)\,, \tag{8.27}$$

where $V(z)$ is equivalent to (8.7), and $V_0(x, y)$ is the random potential height at any point (x, y). $V_0(x, y)$ is a Gaussian random process with a spatial Gaussian correlation—assuming space isotropy—,

$$V_0(x, y) \propto g(|\boldsymbol{r} - \boldsymbol{r}'|/\lambda) = e^{-(\boldsymbol{r}-\boldsymbol{r}')^2/2\lambda^2}\,. \tag{8.28}$$

$\boldsymbol{r}$ and $\boldsymbol{r}'$ are vectors in the xy plane, and λ is the correlation length. It can be numerically simulated by the algorithms developed in [Suñé et al., 2012], (Sec. 7.1); being generated in $N = 1024$ lattice sites, with a discretization length $\Delta = 0.05$, and $\lambda = 1$, $V_0(x, y)$ is plotted in Figure 8.14. From the random attractive potential $\bar{V}(x, y, z)$, the forces on the xy plane are obtained by simple centered discrete derivatives [Suñé et al.,

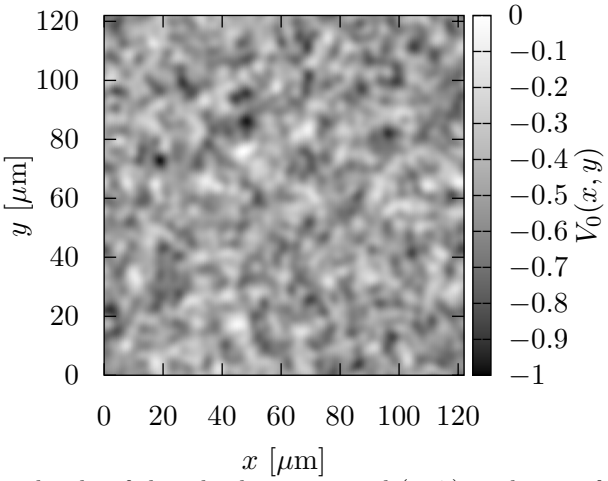

Figure 8.14 – Barrier height of the adsorbing potential (8.27) to the interface with spatial Gaussian correlation (8.28). Simulation runs for $N = 1024$ lattice sites, with a discretization length $\Delta = 0.05$, and $\lambda = 1$.

2012], (Sec. 7.3). Then standard linear interpolation of the force at the lattice points is employed to assess the force at intermediate locations [Suñé et al., 2012], (Sec. 7.4).

Results

Simulations of the set of Langevin equations (8.13), with the viscosity functionality (8.12) along the vertical axis, and the random adsorbing potential (8.27), are run for 400 particles. $V_0(x, y)$ is defined in a $2-d$ lattice space with $N = 1024$ squared cells of side $\Delta = 0.05$. Other parameters are $t = 4000$, $a_0 = 0.2$, and $h = 50$, as in Section 8.1.3. Several temperatures and friction quotients are considered, for the integration time step Δt ought to be adapted according to Section 8.1.2. The heat map in Figure 8.15 displays the particle density in the interface ($z \leq 3.5\,\mu$m, according to the criteria adopted in Section 8.1.1; $z_+ = 1.46 \cdot 2.4\,\mu$m for $T = 0.1$) for $T = 0.1$ and $\gamma_0 = 0.2$. It ought to be enlightened that there is a strong correlation (Fig. 8.16) between the particle density heat map (Fig. 8.15)

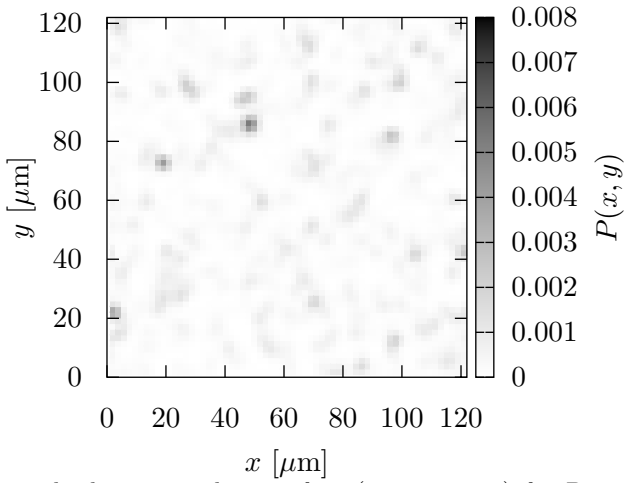

Figure 8.15 – Particle density in the interface ($z \leq 3.5$ μm) for Brownian particles adsorbed by a random potential (8.27) at a high viscosity interface (8.12). $T = 0.1$ and $\gamma_0 = 0.2$.

and the barrier height landscape (Fig. 8.14).

The rate of attached particles to the interface motivates the choice for the temperature $T = 0.1$, since it exhibits a rather high fraction of attached particles, yet there is still some population of free particles diffusing in the bulk (Fig. 8.17). Unlike the intermittent molecular hopping (Fig. 8.10), now the steady n_2/n does not split for different values of the quotient between viscosities.

Notwithstanding, the behavior of particles is expected to attain that of intermittent molecular hopping (Sec. 8.1.3), that is, the trajectories at the interface to exhibit confinement at certain regions—the most probable are the darkest ones in Figure 8.15—interspersed by rare hops through the bulk. Therefore, the confinement time distributions might be computed so as to reach the characteristic confinement time (Fig. 8.18).

The confinement time distributions for $T = 0.1$ exhibit an exponential decay that depends on the quotient of viscisities $a(\gamma_0 = 0.2) = (1.68 \pm$

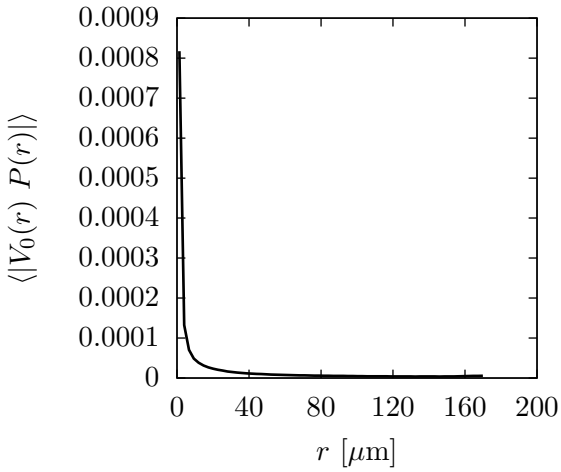

Figure 8.16 – Absolute value of the correlation between the barrier height of the adsorbing potential (8.27) (Fig. 8.14) and the particle density in the interface (Fig. 8.15).

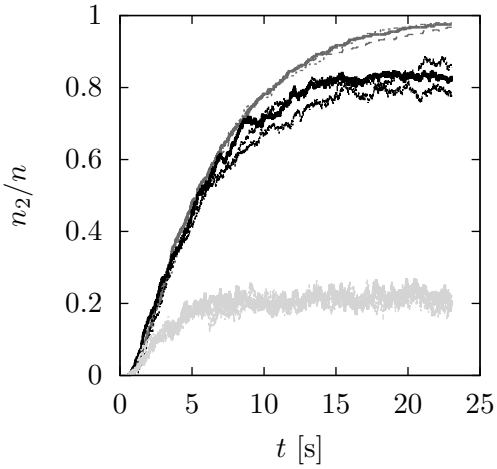

Figure 8.17 – Fraction of trapped particles at the interface for different temperatures $T = 0.05$ (dark grey), 0.1 (black), and 0.2 (light grey) and friction quotients $\gamma_0 = 0.2$ (solid), 0.5 (dashed), and 1 (dotted). In order to compute n_2 it is employed z_+ (Sec. 8.1.2).

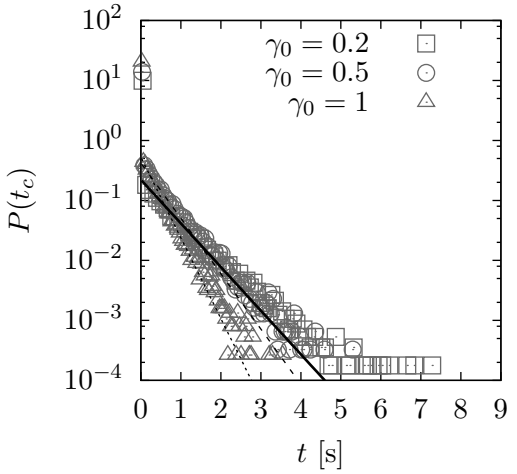

Figure 8.18 – Distribution of confinement times at the interface for $T = 0.1$. Straight lines correspond to fitting an exponential function $f(t) = b\exp(-at)$ excluding the points at $t = 0$ s.

$0.02)\,\mathrm{s}^{-1}$, $a(\gamma_0 = 0.5) = (2.13 \pm 0.03)\,\mathrm{s}^{-1}$, and $a(\gamma_0 = 1) = (3.10 \pm 0.03)\,\mathrm{s}^{-1}$. Additionally, the particle detach mediated displacements (8.15) at the interface might be also computed (Fig. 8.19). They do not seem to fulfill any regular functionality.

The mean square displacement of the trajectories at the interface scale linearly with time, after a likely transient regime, hence the diffusion coefficient can be worked out by fitting the Einstein–Smoluchowski equation (1.3). The diffusion coefficient to come out from the data of the simulations is $\hat{D}_{xy} = (150 \pm 20)\,\mu\mathrm{m}^2/\mathrm{s}$.

8.1.5. Summary and conclusions

Although being it at an early stage, some conclusions can be gathered from the study of Brownian motion with $2 - d$ confinement and changes of viscosity; wouldn't they bring about astonishing disclosures, they might serve as a foundation to further hypotheses if nothing else.

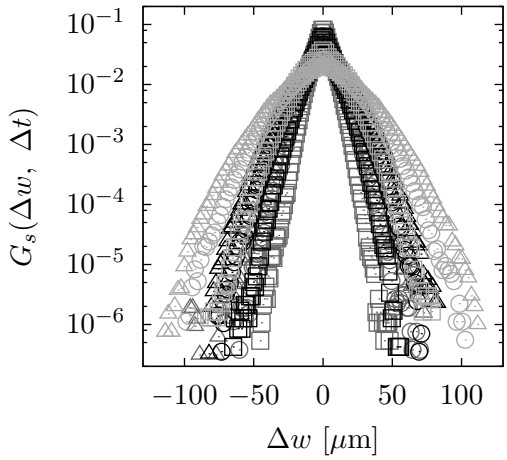

Figure 8.19 – Distributions of displacements (8.15) at the xy plane ($w = x, y$) for $T = 0.1$ and different time steps $\Delta t = 0.2$ s (squares), $\Delta t = 0.4$ s (circles), and $\Delta = 0.6$ s (triangles). Dark–grey symbols label simulation results for $\gamma_0 = 0.2$, black symbols are employed for $\gamma_0 = 0.5$, and light–grey symbols for $\gamma_0 = 1$.

The population of confined particles can be computed by equilibrium thermodynamics arguments, as well as by integration of the Boltzmann distribution, that adjusts to the histogram of particles' positions. It has been developed a criteria to settle on the coordinate up to which integration of the Boltzmann distribution should be carried out in order to attain the theoretical prediction.

Numerical simulations of stochastic dynamics have been run for three different scenarios. All of them consider two different potential energy states and viscosities along the vertical direction, yet they differ from each other concerning space's functionality of these quantities. In the first scenario, there is only vertical dependence, whereas horizontal dependency is considered for the others, either periodic or random. It has been inquired into the population of particles at each state and its dependency on γ_0—the quotient of viscosities—, the particles' displacements distributions—both in vertical and horizontal directions—, the confinement times distribution,

and the mean square displacement in the xy plane—those last two only for the second and third scenarios—.

It ought to be enlightened that several experimental and theoretical previous works have been employed to substantiate the design of these different scenarios, the parameters choices, and the analyses of the results [White, 1955; Bychuk and O'Shaughnessy, 1995; Honciuc et al., 2008; Skaug et al., 2013].

8.2. Two–dimensional ratchet model for KIF1A

Kinesines are molecular motors that move along microtubules, hollow cylindrical tubes of 12 nm radius—R_{MT}—and several micrometers long. In addition to the polarity brought about by the $\alpha\beta$ dimers, that associate forming linear protofilaments, microtubules also exhibit a left–handed helix of pitch 12 nm due to the dislocation from one linear protofilament to another [Chrétien and Wade, 1991]. Hence, the motion of a motor would display a twisty trajectory around the microtubule [Yajima and Cross, 2005]. The aim of this section is to study the motion of kinesin motors through simulations of Langevin stochastic dynamics in $2-d$ spaces.

8.2.1. The model

Consider a KIF1A motor that can move in a two–dimensional surface; its position in the plane is $\boldsymbol{r} = x\ \hat{\boldsymbol{e}}_x + y\ \hat{\boldsymbol{e}}_y$. In order to mimic the KIF1A–microtubule binding energy, the surface over which the motor travels will be modeled as an oblique Bravais lattice with primitive vectors $\boldsymbol{a}_i$, $i = 1, 2$, forming an angle $\theta > 0$ (Fig. 8.20). Latin indices will be employed to label the primitive directions of the lattice, and greek indices to the cartesian directions. The nodes of the lattice,

$$\boldsymbol{R}(n_1, n_2) = n_1\ \boldsymbol{a}_1 + n_2\ \boldsymbol{a}_2\,, \tag{8.29}$$

where $n_1,\ n_2$ are integer numbers, correspond to the binding sites of the motor. The set (n_1, n_2) indicates a given primitive cell in the lattice, de-

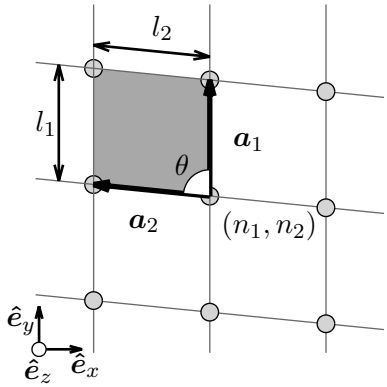

Figure 8.20 – Oblique Bravais lattice with primitive vectors $\boldsymbol{a}_1$ and $\boldsymbol{a}_2$ of size l_1 and l_2 respectively, forming an angle θ. Gray parallelogram—the primitive cell of the lattice. Gray circles—nodes of the cell.

limited by the nodes $\{(n_1, n_2), (n_1 + 1, n_2), (n_1, n_2 + 1), (n_1 + 1, n_2 + 1)\}$. The two primitive vectors are:

$$\begin{aligned} \boldsymbol{a}_1 &= l_1 \ \hat{\boldsymbol{e}}_y \,, \\ \boldsymbol{a}_2 &= l_2(-\sin\theta \ \hat{\boldsymbol{e}}_x + \cos\theta \ \hat{\boldsymbol{e}}_y) \,, \end{aligned} \tag{8.30}$$

where l_i, $i = 1, 2$ are the periodicities for each primitive direction. The reciprocal basis $\boldsymbol{q}_i$ reads:

$$\begin{aligned} \boldsymbol{q}_1 &= 2\pi \ \frac{\boldsymbol{a}_2 \times \hat{\boldsymbol{e}}_z}{|\boldsymbol{a}_1 \times \boldsymbol{a}_2|} = \frac{2\pi}{l_1} \ (\cot\theta \ \hat{\boldsymbol{e}}_x + \hat{\boldsymbol{e}}_y) \,, \\ \boldsymbol{q}_2 &= 2\pi \ \frac{\boldsymbol{e}_z \times \boldsymbol{a}_1}{|\boldsymbol{a}_1 \times \boldsymbol{a}_2|} = -\frac{2\pi}{l_2} \ \csc\theta \ \hat{\boldsymbol{e}}_x \,. \end{aligned} \tag{8.31}$$

The motor can be in two possible states $k = 1, 2$; $k = 1$ labels the strongly–bound state, in which the motor attaches to a potential landscape $U_1(x, y)$ that exhibits minima at the Bravais lattice's nodes, and $k = 2$ the weakly–bound state, meaning that the motor diffuses through a flat potential $U_2(x, y)$—and against a constant force if so—. The motor is assumed to decay from state $k = 2$ to the state $k = 1$ with exponentially distributed decay times of mean τ. Decay processes are delocalized in space. Antithetically, excitations from state $k = 1$ to the state $k = 2$ occur only when the

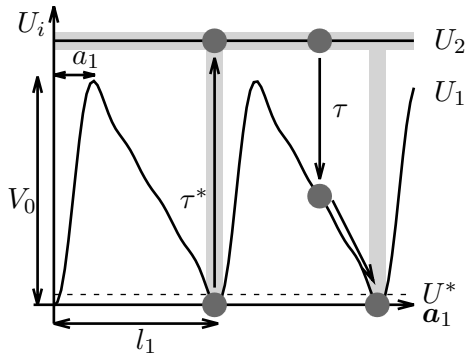

Figure 8.21 – Sawtooth linear potential (8.32) ($i = 1,\ j = 4,\ \mu_{11} = 1,\ \mu_{12} = 0.9,\ \mu_{13} = 0.65,\ \mu_{14} = 0.35$) for the motor–track interaction. Gray—the zone where transitions are allowed: excitation is localized with exponentially distributed excitation times of mean τ^* from U_1 to U_2, and decay is delocalized with exponentially distributed decay times of mean τ from U_2 to U_1. Dashed line—excitation time starts when the particle's potential energy is lower than U^*. See more details in the text.

motor approaches a node in the lattice; that is, motors can be prompted to the weakly–bound state $k = 2$ only if their potential energy is below U^*, a smaller energy than V_0—the potential's $U_1(x, y)$ height—. Again, an exponential distribution of exciting times is assumed, with mean time τ^*.

It is well established that the potential $U_1(x, y)$ ought to be asymmetric, so as to enable a biased advance of the motor prompted by thermal fluctuations and ATP consumption; microtubules, the substrates along which motors are propelled, do have a polar configuration indeed. A common choice to mimic such structure is a sawtooth wave landscape. The oblique Bravais lattice of primitive vectors defined in (8.30) is employed in order to build up a two dimensional oblique sawtooth landscape. Indeed, the potential is assumed to be periodic in the $\boldsymbol{a}_1$ and $\boldsymbol{a}_2$ directions, with periodicities l_1 and l_2 respectively. A possible choice would be $U = V_1 + V_2$, with V_i, $i = 1, 2$ being a sawtooth $1-d$ function in each primitive direction of the Bravais lattice. Each $1-d$ sawtooth may be constructed by a Fourier

series,

$$V_i(x,y) = V_0 \sum_{j=1} \frac{\mu_{ij}}{j} \ \sin(j \cdot \boldsymbol{q}_i \cdot \boldsymbol{r}) \ ; \ i = 1,2 \ , \tag{8.32}$$

that leads to a continuous smooth landscape (Fig. 8.21) with analytic derivatives at each point.

Langevin dynamics is employed to simulate the motion of the motor, for which it is assumed the overdamped approach[2],

$$\eta \, \dot{\boldsymbol{r}} = -\delta_{k1} \, \nabla U - \boldsymbol{F} + \xi(t) \ . \tag{8.33}$$

η is the friction coefficient fulfilling the Einstein's relation $D = k_B T/\eta$ (D is the diffusion coefficient), the nabla operator is $\nabla \equiv (\partial_x, \partial_y)$, $\boldsymbol{F}$ is a constant external force, and ξ is a random force vector with zero mean satisfying $\langle \xi_\alpha(t) \, \xi_\beta(t') \rangle = 2 k_B T \, \eta \, \delta_{\alpha\beta} \, \delta(t - t')$, $\alpha, \beta = x, y$. δ_{k1} and $\delta_{\alpha\beta}$ are Kronecker's deltas.

The motion of unidimensional KIF1A motor uses to be remarkably diffusive, $D \approx 20 - 40 \, \mathrm{nm^2 \, ms^{-1}}$ [Okada and Hirokawa, 1999; Okada et al., 2003]. In bidimensional space, the diffusion tensor should be isotropic, so that diffusion on and off–axis is the same.

Experimental results on KIF1A [Okada et al., 2003] also reveal a stall force $F_s \approx 0.1 \, \mathrm{pN}$, and a rotational pitch P_1 of a few hundreds of nanometers [Yajima and Cross, 2005]. In order to fit these quantities, the shape of the potential landscape is critical. Considering the unidimensional scenario as the reference, numerical results for a single monomeric KIF1A motor in $1 - d$ exhibit a stall force of $\approx 0.1 \, \mathrm{pN}$ when the ratchet potential has an asymmetry $\bar{a} = 0.2$ [Oriola and Casademunt, 2013]. In the present model, the asymmetry $\bar{a}_i = a_i / l_i$ is not a parameter itself, but it is determined by the choice of the coefficients μ_{ij}. Two harmonics may be enough to generate an asymmetric landscape; however, $\bar{a}_i$ is limited because, for $\mu_{i2} \geq 1$,

[2] Unlike the rest of the thesis, in this Section it is employed quantities that do have dimensions, yet the "hat" notation to distinguish from scaled quantities is avoided for ease of notation.

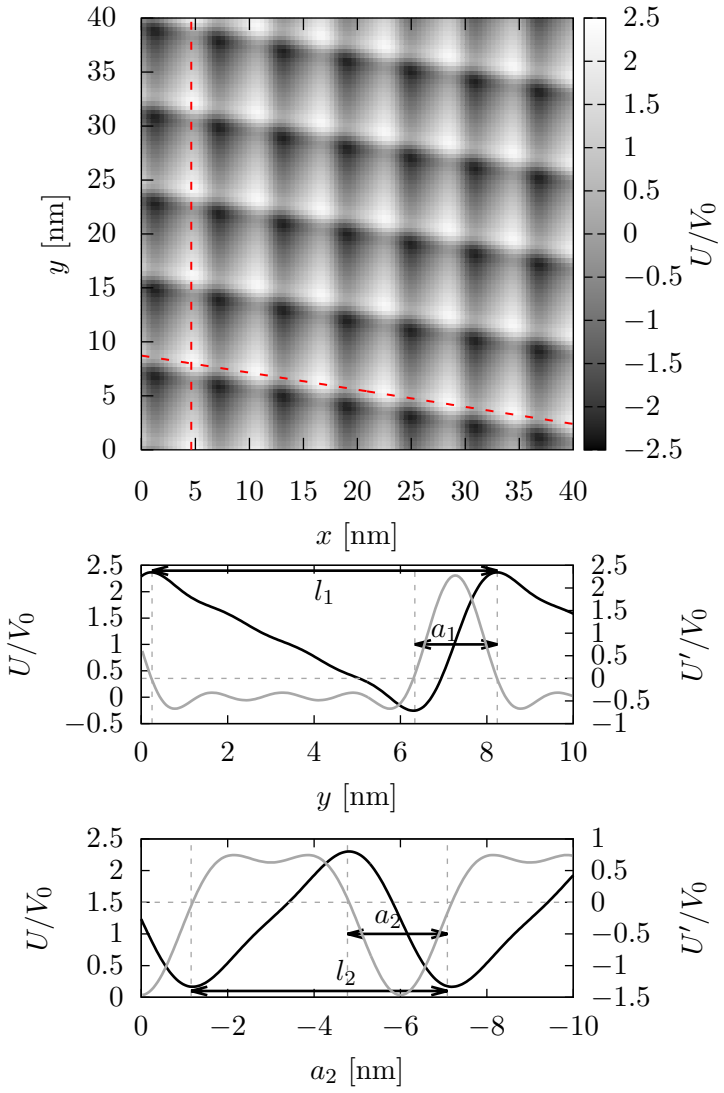

Figure 8.22 – Top: $2-d$ potential built in a Bravais lattice by (8.32) with $\mu_{11} = 1$, $\mu_{12} = 0.9$, $\mu_{13} = 0.65$, $\mu_{14} = 0.35$, $\mu_{21} = 1$, and $\mu_{22} = 0.4$. Red dashed—directions along which $1-d$ sections of the potential are plotted in the lower panels. Center: Potential section along $\hat{\boldsymbol{e}}_y$, $\boldsymbol{a}_1$. Gray—partial derivative of the potential, its roots (intersections of the gray dashed lines) label the maxima and minima of the potential. $l_1 = 7.9$ nm, $a_1 = 1.9$ nm. Bottom: Potential section along $\boldsymbol{a}_2$. Gray—partial derivative of the potential. $l_2 = 6.0$ nm, $a_1 = 2.6$ nm.

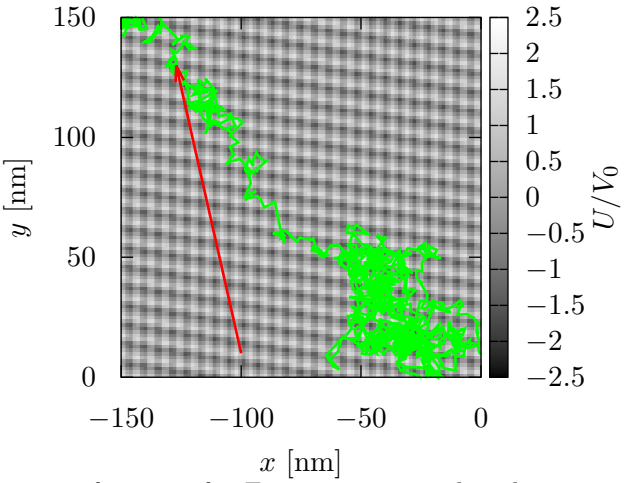

Figure 8.23 – Tajectory of a motor for $\boldsymbol{F} = 0$ superimposed to the potential landscape. The arrow points at the mean velocity's direction.

the potential displays a second local minimum in each period that would bring about a worthless outcome. This restriction is overcome by the employment of higher order harmonics. For example, may it be considered a landscape built by (8.32) up to the fourth harmonic along $\boldsymbol{a}_1$, with $\mu_{11} = 1$, $\mu_{12} = 0.9$, $\mu_{13} = 0.65$, $\mu_{14} = 0.35$, and up to the second along $\boldsymbol{a}_2$, with $\mu_{21} = 1$, $\mu_{22} = 0.4$, asymmetries are $\bar{a}_1 = 0.24$ and $\bar{a}_2 = 0.39$, see Figure 8.22.

In vitro experiments [Okada and Hirokawa, 1999; Okada et al., 2003; Nishinari et al., 2005] reveal a proper choice for the rest of parameters to be: $\tau = \tau^* = 4\,\mathrm{ms}$, $\theta = 0.45\pi$, and $V_0 = 20\,k_B T$.

8.2.2. Simulations

May a Heun algorithm (Sec. 7.5.1) be applied to simulate the Langevin equation (8.33), including a potential landscape (8.32), with parameters as in Figure 8.22, it is obtained an ensemble of trajectories like the one displayed in Figure 8.23.

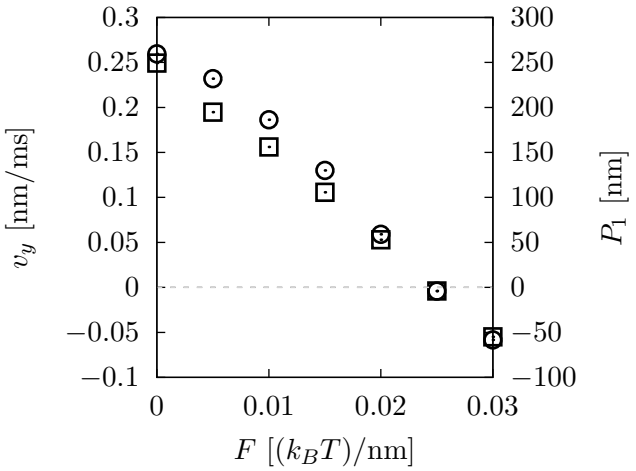

Figure 8.24 – Simulations with 1000 motors in a landscape generated by (8.32) with $\mu_{11} = 1$, $\mu_{12} = 0.9$, $\mu_{13} = 0.65$, $\mu_{14} = 0.35$, $\mu_{21} = 1$, and $\mu_{22} = 0.4$. Squares—velocity–force curve—, circles—rotational pitch—.

In such case, it may be computed the rotational pitch,

$$P_1 = v_y\, t = 2\pi\, R_{MT}\, \frac{v_y}{v_x} = 2\pi\, R_{MT}\, (\bar{v}\, \csc\theta + \cot\theta)\,, \tag{8.34}$$

$\bar{v} \equiv v_1/v_2$, that ought to compare with the experimental findings [Yajima and Cross, 2005]. Simulation results for the stationary velocity and the rotational pitch against the external force are included in (Fig. 8.24). It is gathered that experimental and computational outcome for the velocity at zero load [Okada et al., 2003; Oriola and Casademunt, 2013], the stall force [Okada et al., 2003] and the rotational pitch [Yajima and Cross, 2005] are attained.

8.2.3. Perspectives

Now that the two–dimensional ratchet model for KIF1A has been demonstrated to account for the properties that have been checked by *in vitro* experiments of the motor, the next step on the investigation would be to introduce some amount of disorder into the potential. That is to say, in the periodic ratchet (Fig. 8.22), there may be certain potential wells to which the motor would not be able to attach, meaning that it should change its

trajectory to avoid them. This scenario would mimic the presence of defects in microtubules, and is expected to alter the kinesin's velocity, and so its functionality, just like as it has been observed experimentally *in vitro* employing crowding agents to increase the effective viscosity of the solution [Sozański et al., 2015].

Catalan résumé of the thesis – Resum en català de la tesi

Introducció

El moviment Brownià

El moviment Brownià és el bellugueig aleatori que efectuen les partícules de tamany micromètric quan estan suspeses en un dissolvent. Des de la seva descoberta a finals del segle *XVIII*, ha esdevingut un element central en la formulació probabilística de la mecànica estadística i ha estat objecte permanent d'investigacions fins a l'actualitat.

La formulació en termes matemàtics del moviment Brownià fou originalment desenvolupada per Albert Einstein [Einstein, 1905] i Marian von Smoluchowski [Von Smoluchowski, 1906], i constituí una evidència definitiva de la composició atomística de la matèria. No obstant, Paul Langevin feu una adaptació de les idees d'Einstein i von Smoluchowski; fent ús la dinàmica de Newton, permeté l'obtenció de la trajectòria descrita per una partícula sotmesa al moviment Brownià [Langevin, 1908; Lemons and Gythiel, 1997]. La formulació de Langevin a través de les anomenades equacions diferencials estocàstiques consisteix en separar el balanç de forces en una part determinista i una altra aleatòria, la caracterització de la qual es deu a l'aportació feta per Leonard Ornstein [Ornstein, 1919], que establí les bases del soroll blanc—un procés aleatori generat per mitjà de nombres aleatoris distribuïts de forma Gaussiana i no correlacionats—.

Transport i difusió

Quan el moviment Brownià té lloc en un solvent simple, és a dir, en absència de forces externes, els desplaçaments que efectuen les partícules exhibeixen una distribució Gaussiana de mitjana nul·la i variança proporcional al temps. Aquest resultat fou raonat per Einstein [Einstein, 1905], que al mateix temps fou capaç de determinar que la constant que relaciona la dispersió del conjunt de desplaçaments i el temps és el coeficient de difusió—el mateix que Adolf Eugen Fick havia establert per a la difusió d'espècies químiques en solucions aquoses [Fick, 1855]—, i que aquest depèn de la constant de Boltzmann, la temperatura, i el coeficient de fricció.

Per altra banda, si les partícules estan sotmeses a una força externa en una determinada direcció, la velocitat mitjana del conjunt serà no nul·la—la mitjana de la distribució de desplaçaments ja no serà zero—i, per tant, hi haurà transport. En aquestes condicions, el primer moment—el valor mig—de la distribució de desplaçaments presenta un creixement lineal amb el temps.

Tanmateix, l'aparició de tècniques experimentals—marcatge mitjançant proteïnes fluorescents, pinces òptiques i magnètiques, microscopia de força atòmica, entre d'altres [Greenleaf et al., 2007]—que permeten el seguiment de partícules sotmeses al moviment Brownià en ambients complexos, tals com el citoplasme cel·lular [Golding and Cox, 2006; Dix and Verkman, 2008], membranes [Khoshnood and Jalali, 2013], solucions artificials complexes [Weiss, 2013], o superfícies sòlides desordenades [Xu et al., 2011; De Wijn, 2011], ha permès observar desviacions—anomalies—en els resultats clàssics del transport i la difusió, és a dir, dependències no lineals de la mitjana i la dispersió respecte el temps. Els ambients en els quals s'oberven aquestes anomalies es poden caracteritzar per mitjà de potencials no–lineals, ja siguin periòdics—existeix una unitat que es repeteix de forma recursiva—, o bé aleatoris—l'estructura del potencial no segueix un ordre determinat, si bé pot presentar propietats estadístiques concretes—. La

característica comuna en els potencials no–lineals és la presència de barreres que les partícules superen per fluctuacions tèrmiques [Kramers, 1940]. Aquestes barreres modifiquen la distribució dels desplaçaments, donant lloc a les desviacions del transport i la difusió.

La tesi

L'objecte de la present tesi és explorar les anomalies del transport i la difusió de partícules Brownianes independents—en absència d'interacció mútua—sotmeses a una força externa constant i a un potencial desordenat. El mètode emprat és la simulació numèrica de les equacions de Langevin clàssiques en els règims de sobreesmorteïment—alta fricció, partícules idealment sense inèrcia, règim sovint manifestat en contextos biològics i de matèria tova—i d'infraesmorteïment—baixa dissipació de l'energia cinètica, aproximació vàlida típicament en sòlids—.

En concret, la tesi indaga en les causes que motiven l'aparició de les esmentades anomalies i la influència que hi tenen les propietats del potencial desordenat, la força externa, la temperatura, el coeficient de fregament—únicament en l'aproximació d'infraesmorteïment—, etc. En paral·lel, s'han desenvolupat noves tècniques numèriques—reformulant tècniques existents—per tal de simular les equacions dinàmiques estocàstiques en cadascun dels escenaris contemplats, així com per optimitzar la generació de desordres en l'espai i el temps.

Resultats

El primer cas tractat és l'estudi del moviment Brownià en un potencial periòdic. Aquesta avinentesa constitueix un punt de partida sobre el qual edificar les hipòtesis que articularan la resta d'exploracions, les quals són: el transport anòmal és sublineal per un desordre estàtic; en un medi desordenat els fenòmens de difusió gegant i superdifusió són afavorits; el transport i la difusió anòmals requereixen l'atrapament estacionari d'una certa fracció de la població de partícules Brownianes.

Pel que fa als contextos amb presència de desordre, el primer cas d'estudi és el moviment Brownià sobreesmorteït en un potencial aleatori estàtic inclinat. Les simulacions numèriques en aquest escenari inclouen casos unidimensionals i bidimensionals. Els règims de transport i difusió anòmals es caracteritzen a través dels exponents de les funcions temporals de la mitjana i la variança de la distribució de desplaçaments; però també dels histogrames dels desplaçaments i—en el cas bidimensional—de la forma del núvol de punts que representa els desplaçaments efectuats per cada partícula en diferents instants de temps. En una dimensió, l'estudi contempla potencials desordenats amb diverses propietats estadístiques. Existeix un paràmetre, la longitud efectiva característica de la rugositat del potencial, que afecta els resultats. Si bé en tots els casos estudiats s'observa la mateixa seqüència d'anomalies—subtransport i subdifusió, superdifusió, i difusió indefinida—a mesura que s'incrementa la força externa—finalment s'obté transport i difusió normals—, el rang de forces pel qual esdevé cada fenòmen varia en funció de la longitud efectiva característica de la rugositat del potencial. En efecte, com més gran és aquest paràmetre, el potencial presenta una forma més suau i això fa que la seqüència d'anomalies i, per tant, el reestabliment del transport i la difusió normals, es produeixi per una força menor. Aquesta constatació, juntament amb les formes que s'observen en els histogrames dels desplaçaments i en els núvols de punts, reforcen la interpretació que relaciona les anomalies amb la divisió de la població de partícules entre aquelles que estan atrapades en els pous més profunds del

potencial, i les que són propulsades lliurement per la força externa [Khoury et al., 2011]. Resulta destacable, en el cas bidimensional, la coexistència d'anomalies de caràcter oposat en la direcció de la força—superdifusió—i la seva perpendicular—subdifusió—.

El cas anàleg a l'anterior, però considerant el règim d'infraesmorteïment, ofereix la possibilitat d'estudiar la distribució de velocitats instantànies del conjunt de partícules. Aquesta mostra clarament la separació de la població de partícules en l'estat de velocitat zero—partícules atrapades—i en el de velocitat no nul·la, corresponent a partícules lliures propulsades per la força externa. En aquest règim, s'observen les mateixes anomalies en el transport i la difusió independentment del coeficient de fricció. S'aprecia també un tímid fenòmen de supertransport, si bé els resultats no són prou concloents per contravenir una de les hipòtesis fetes.

Tornant al règim d'alta dissipació, el tercer estudi contempla l'escenari en que el medi bidimensional on difonen les partícules presenta una alta concentració d'obstacles mòbils i deformables—de dinàmica sensiblement més lenta que la del moviment Brownià de les partícules—que les partícules no poden superar. El transport i la difusió en aquest escenari presenta dos règims clarament diferenciats. Per una banda, per temps inferiors a l'escala de temps característica del moviment dels obstacles, es poden produir anomalies; per l'altra, es recupera el transport i la difusió normals quan el temps de simulació sobrepassa aquest valor. Aquest fet provoca que, malgrat la presència d'obstacles que interfereixen en el moviment Brownià, el coeficient de difusió pugui ser més gran que el corresponent a la difusió de partícules lliures. Finalment, l'estudi fixa el conjunt de paràmetres efectius que determinen el comportament del sistema: el temps característic dels obstacles, que estableix la durada dels règims transitoris anòmals i, per tant, els coeficients estacionaris del transport i la difusió; la densitat d'obstacles, a major densitat, menor transport i difusió; i el tamany dels obstacles, obstacles de tamany més gran—per una mateixa concentració—afavoreixen el transport i la difusió.

Pel que fa als aspectes metodològics, s'ha refinat el mètode per generar desordres Gaussians amb una correlació espacial arbitrària amb l'únic requeriment d'isotropia per a la funció de correlació. El nou algorisme fa ús de l'espai de Fourier de forma transitòria en el procés, però totes les condicions són imposades en l'espai real. Per altra banda, també s'ha dissenyat una transformació adient per transformar un desordre—conformat per pous i barreres—en un conjunt d'obstacles de la mateixa alçària. La transformació permet controlar el tamany característic dels obstacles i preserva la densitat d'obstacles quan el potencial d'origen és un desordre espaciotemporal.

Per últim, la tesi inclou dos casos inacabats d'aplicació del moviment Brownià en contextos físics concrets i propers a treballs experimentals.

Per una banda, s'estudia les propietats de patícules Brownianes sotmeses a un potencial que les confina en una interfície on la viscositat és més elevada que a la resta del volum. L'estudi s'efectua a través de simulacions de l'equació de Langevin, que incorpora un terme addicional quan la viscositat no és constant en tot el sistema. A partir dels resultats, es determinen diverses magnituds, com la població de partícules atrapades a la interfície, la distribució dels desplaçaments de les partícules i dels temps de confinament, o la variança dels desplaçaments—per determinar el coeficient de difusió en el cas que la dispersió sigui lineal amb el temps—. L'estudi contempla tres escenaris diferents—tots ells tenen en comú l'existència de dos estats energètics i dues viscositats en la direcció vertical—en funció de la dependència espacial del potencial i la viscositat: en el primer cas només depenen de l'alçada, mentre que en els altres dos també presenten una dependència en les coordenades del pla xy, periòdica en l'un, aleatòria en l'altre.

Per l'altra, el segon cas presenta un model bidimensional en forma de dent de serra pel motor molecular Brownià KIF1A. En la fase vigent de l'estudi, s'ha dissenyat el potencial i s'han escollit els paràmetres de forma que els resultats de les simulacions de l'equació de Langevin en el règim

sobreesmorteït reprodueixin els valors experimentals de certes magnituds físiques conegudes, com la velocitat en l'eix del microtúbol i l'avanç de les trajectòries helicoïdals descrites pels motors. L'objectiu final de la investigació és, no obstant, introduir desordre en el sistema en forma d'obstacles immòbils distribuïts aleatòriament que interfereixin en el moviment dels motors.

Els resultats d'aquesta tesi han estat publicats en diversos articles, la referència dels quals es troba en la secció següent.

List of publications

This thesis is based on the following articles:

- M. Suñé, J. M. Sancho, and A. M. Lacasta. On generating random potentials. *Fluctuation and Noise Letters*, **11**(04):1250026, 2012. (Chap. 7).
- M. Suñé, J. M. Sancho, and K. Lindenberg. Transport and diffusion of overdamped Brownian particles in random potentials. *Phys. Rev. E*, **88**:062105, 2013. (Chap. 4).
- M. Suñé, J. M. Sancho, and K. Lindenberg. Transport and diffusion of underdamped Brownian particles in random potentials. *The European Physical Journal B*, **87**(9):1–10, 2014. (Chap. 5).
- M. Suñé, J. M. Sancho, and K. Lindenberg. Brownian motion on random dynamical landscapes. *The European Physical Journal B*, **89**(3):1–7, 2016. (Chap. 6).

Nomenclature

α	Transport power–law exponent. Set of control parameters (Chap. 7)
β	Diffusion power–law exponent. Inverse of the temperature (Chap. 8)
$\delta()$	Dirac–delta function
δ_{ij}	Kronecker delta
Δ	Distance between lattice points of the discretized space
Δt	Time integration step
$\Delta\hat{V}$	Height of a potential barrier (Chap. 1)
$\Delta\hat{\boldsymbol{r}}(\hat{t})$	Increments of the position of a Brownian particle concerning a time scale where the particle moves significantly
ϵ	Noise intensity
ε	Exponent of a power–law correlation function
η	Phenomenological friction coefficient
$\eta(\boldsymbol{r}, t)$	Noise term in the generalized stochastic partial differential equation formulation (Chap. 7)
$\eta_j(t)$	Noise term in the generalized stochastic partial differential equation formulation in a discrete space (Chap. 7)
γ	Scaled dimensionless phenomenological friction coefficient

$\gamma()$ Scaled friction with spatial dependence (Chap. 8)

γ_0 Quotient between two viscosities γ_1, γ_2 (Chap. 8)

γ_1, γ_2 Viscosity at each volume V_1, V_2 (Chap. 8)

γ_i Gaussian random numbers with null mean and variance equal to 1 (Chap. 7)

λ Scaled characteristic length scale

λ_0 Length scale

λ_p Length scale of a periodic potential

λ_r Correlation length of a random potential

λ_{rgh} Scaled length scale of the disorder's roughness

μ Expected value of a Gaussian distribution (Chap. 4). Index for any mode in the discrete Fourier space (Chap. 7)

μ_1, μ_2 Chemical potential of a thermodynamic system (Sec. 8.1)

μ_i Coefficients of the Fourier series that are employed to build up the $1-d$ sawtooth potentials in Section 8.2

∇ Vector differential operator,

$$\nabla \equiv \sum_{i=1}^{n} \hat{\boldsymbol{e}}_i \frac{\partial}{\partial x_i}$$

in the Cartesian coordinate system $\mathbb{R}^n$ with coordinates $(x_1, \ldots, x_n)$ and orthonormal basis $\{\hat{\boldsymbol{e}}_1, \ldots, \hat{\boldsymbol{e}}_n\}$

ν Kinematic viscosity

ϕ A phase to shift a potential along the xy surface (Chap. 8)

$\phi(\boldsymbol{r}, t)$ A field that follows a stochastic partial differential equation in an Euclidean $d-$space (Chap. 7)

ϕ_i A discrete field that follows a stochastic partial differential equation in an Euclidean discrete $d-$space (Chap. 7)

$\tilde{\phi}(t)$ Intermediate step of the Heun method; field to be obtained by employing the Euler algorithm to integrate a stochastic partial differential equation (Chap. 7)

ρ	Density of a fluid. Density of obstacles of a random landscape made of obstacles
ρ_1, ρ_2	Density of particles
σ^2	Variance of a Gaussian distribution
σ_1^2, σ_2^2	Variance of each Gaussian distribution concerning each volume (Sec. 8.1)
τ	Mean of a exponential distribution of decay times (Sec. 8.2)
τ_0	Time scale (Chap. 1). Relaxation time of the $\mathcal{V}_0$ mode of a random dynamic potential in Fourier space (Chap. 7)
τ_μ	Relaxation time of the $\mathcal{V}_\mu$ mode of a random dynamic potential in Fourier space
τ^*	Mean of a exponential distribution of exciting times (Sec. 8.2)
$\xi(t)$	Scaled dimensionless Gaussian white noise
$\xi_i(t)$	Cartesian components of scaled Gaussian white noise
ξ_μ	μ mode of the Gaussian white noise in Fourier space
$\hat{\xi}(\hat{t})$	Random force. Gaussian white noise
$\hat{\xi}_i$	Cartesian components of Gaussian white noise
$\zeta(k)$	Anticorrelated Gaussian random variate in Fourier space
ζ_μ	Complex Gaussian random numbers anti–correlated ascribed to the discrete Fourier modes
θ	Angle
A	Auxiliary constant in mathematical formulation
a	It may refer to any auxiliary parameter or fitting constant throughout the thesis. However, in Chapters 6 and 7 it is the parameter that controls barrier stiffness of obstacles when a random distribution of barriers transforms into a random distribution of obstacles of the same height
a_0	Steepness of the hyperbolic tangent function for the potential in Chapter 8
a_1, a_2	Weight of each Gaussian curve that fits the distribution of velocities
a_i	Horizontal distance of the shortest side of a sawtooth potential (Chap. 8.2)

a_j	Random numbers obtained by transforming b_j
$\boldsymbol{a}_i$	Bravais lattice primitive vectors (Chap. 8)
$\bar{a}$	Asymmetry of a ratchet potential (Chap. 8.2)
B	Auxiliary constant in mathematical formulation
b	It may refer to any auxiliary parameter or fitting constant throughout the thesis
b_0	Period in the xy plane of a $3-d$ periodic potential potential
b_1, b_2	Mean velocity for each Gaussian curve that fits the distribution of velocities
b_j	Gaussian random numbers with zero mean and variance 1
$C()$	Spatiotemporal noise correlation function
C_1	Normalizing factor of a Boltzmann distribution
c_1, c_2	Width—variance—of each Gaussian curve that fits the distribution of velocities
c_j	Array of complex numbers in discrete real space
c_μ	Discrete Fourier transform of any sequence of complex numbers ascribed to real space
D_0	Scaled diffusion coefficient for free Brownian particles
D_u	Scaled diffusion coefficient employing the underdamped characteristic time scale
$D_\parallel$	Diffusion coefficient along the external force's direction
$D_\perp$	Diffusion coefficient along the direction perpendicular to the external force
$\hat{D}$	Diffusion coefficient
$\hat{D}_0$	Diffusion coefficient for free Brownian particles
$\hat{D}_{i_1,\ldots,i_d}$	Tensor components in an Euclidean d–space
$\hat{D}_{xy}$	Diffusion coefficient at an interface (Sec. 8.1)
$\hat{D}_{\hat{\boldsymbol{u}}}$	Component along $\hat{\boldsymbol{u}}$ of the Cartesian diffusion tensor
$\boldsymbol{D}$	Scaled diffusion tensor

$\hat{\boldsymbol{D}}$ Diffusion tensor

d Dimension of an Euclidean space

E Energy

$\hat{\boldsymbol{e}}_i$ Unit vectors of an orthonormal cartesian basis, also labelled $\hat{\boldsymbol{e}}_w$

F Scaled scalar force

F_c Scaled critical force

F_r Scaled force derived from a random potential

F_s Stall force for a molecular motor (Chap. 8.2)

$\hat{F}$ $1-d$ scalar force

$\hat{F}_c$ Critical force

$\boldsymbol{F}$ Scaled dimensionless force vector in Euclidean d-space

$\hat{\boldsymbol{F}}$ Force vector in Euclidean d-space

$f()$ Deterministic force term in the generalized stochastic partial differential equation formulation (Chap. 7). Any presumed function in mathematical formulation

$f_{2(1)}(\Delta w, \sigma_{2(1)})$ Gaussian functions (Chap. 8.1.2)

f_i Deterministic force term in the generalized stochastic partial differential equation formulation in a discrete space

$G(\boldsymbol{k}_\mu, \mid t - t' \mid)$ Stationary time correlation function of a dynamic random potential in Fourier space

$G_s(\Delta w, \Delta t)$ Self part of the van Hove correlation function

$\mathcal{G}(k)$ Fourier transform of the spatial correlation function $g(\mid x - x' \mid)$

$\mathcal{G}_\mu$ Fourier transform of the discrete spatial correlation function g_{ij}

$g()$ Correlation function. Random force coupling term in the generalized stochastic partial differential equation formulation (Chap. 7)

g_{ij} Discrete spatial correlation function. Random force coupling term in the generalized stochastic partial differential equation formulation in a discrete space

h Total height of a thermodynamic system of volume V, $h = h_1 + h_2$ (Sec. 8.1)

$h(x)$ Force correlation function

h_i Scaled height (Sec. 8.1)

$\hat{h}_2$ Height at which there is an attractive potential (Sec. 8.1)

i Imaginary unit, $i^2 = 2$. Counter variable. Label of any point in a $2-d$ grid

i_1 , i_2 Set of indices to label a cell in the $2-d$ real discrete space

$\hat{\boldsymbol{i}}$ Unit vector in the direction of the x axis of a Cartesian coordinate system

j Counter variable

$\hat{\boldsymbol{j}}$ Unit vector in the direction of the y axis of a Cartesian coordinate system

k Escape rate of a thermally driven particle over an energy barrier (Chap. 1). Fourier mode of a unidimensional space (Chap. 7). Counter variable

k_B Boltzmann's constant

k_K Kramers' escape rate

k_μ Fourier mode in a discrete $1-d$ space

$\boldsymbol{k}$ Fourier mode in a d–dimensional Fourier space

$\boldsymbol{k}_\mu$ Fourier mode in a discrete d–dimensional Fourier space

L Period of a periodic potential (Chap. 3). Length of the sides in the xy plane of a volume V (Chap. 8)

$\mathcal{L}$ Characteristic length of the compartment in which particles attached to an interface undergo Fickian diffusion (Sec. 8.1.3), taken from [Honciuc et al., 2008]

l_0 Characteristic length of an exponential distribution of particle displacements (Chap. 5)

l_e Distance travelled at the free-particle velocity $v = F/\gamma$ during the actual exit time t_e

l_i Periodicities for each primitive direction of a Bravais lattice (Chap. 8)

l_K Distance travelled at the free-particle velocity $v = F/\gamma$ during the mean exit time t_K

l_t Distance travelled at the free-particle velocity $v = F/\gamma$ during time t

m Mass. Counter variable (Chap. 7)

N Number of lattice points in which space is discretized to define a random potential

N_A Avogadro number

n Number of identical particles of an ensemble. Counter variable (Chap. 7)

n_1, n_2 Number of particles in a volume V_1, V_2 (Chap. 8.1). Integer numbers that correspond to the binding site of a KIF1A motor in a $2-d$ lattice (Chap. 8.2)

$P()$ Distribution of displacements

P_1 Rotational pitch (Chap. 8.2)

$Q_{n,m}$ Notation employed for the interpolation of the force at any point from the grid of forces derived from a $2-d$ potential

$\boldsymbol{q}_i$ Primitive vectors of the reciprocal basis of a Bravais lattice (Chap. 8)

R_{MT} Radius of a microtubule (Chap. 8.2)

$R[x_n, x_{n+1}]$ First order Newton Divided Difference Formula

$\boldsymbol{R}(n_1, n_2)$ Vector that points to a node of a $2-d$ lattice (Chap. 8)

r Scaled modulus of the position vector

r_h Hydrodynamic radius of a sphere immersed in a solvent

r_{pw} Effective radius of the $3-d$ periodic potential wells (Chap. 8)

r_w Components of the scaled vector position along the $w = x, y, z$ cartesian axes

$r_{\parallel}$ Component of the position vector along the external force's direction

$r_{\perp}$ Component of the position vector along the direction perpendicular to the external force

r^* Diffusion length corresponding to the re–adsorbing time t^* (Chap. 8)

$\boldsymbol{r}$	Scaled dimensionless position vector in Euclidean d-space
$\boldsymbol{r}_i$	Vector that denotes the position of any cell in the real $2-d$ lattice space
$\hat{r}$	Modulus of the position vector
$\hat{\boldsymbol{r}}$	Position vector in Euclidean d-space
$\hat{\boldsymbol{r}}'$	Vector position
T	Scaled dimensionless absolute temperature
$\hat{T}$	Absolute temperature
t	Scaled dimensionless time
t_0	Scaled deterministic time that it takes to cover a distance λ under the action of a force F within the overdamped regime
t_c	Confinement time of a particle in a potential well (Chap. 8)
t_e	Scaled escape time from a potential well
t_K	Scaled Kramers characteristic escape time
t_{max}	Maximum time, that corresponds to the time needed for free Brownian particles to travel a distance greater than the half length of the space in which a random potential is defined
t_u	Scaled time employing the underdamped characteristic time scale
t'	Scaled dimensionless time
t^*	Re–adsorbing time, time spent in a bulk excursion for a Brownian particle under interface attraction (Chap. 8)
t_0^o	Dimensionless obstacle dynamics time scale
$\hat{t}$	Time
$\hat{t}_K$	Kramers characteristic escape time. Inverse of the Kramers' escape rate
$\hat{t}'$	Time
$U(\boldsymbol{r},t)$	Scaled dimensionless random potential of equal height obstacles
$U_i(x,y)$	$2-d$ potential landscapes that a KIF1A motor undergoes (Chap. 8.2)
U^*	Energy level (Sec. 8.2)

$\hat{\boldsymbol{u}}$ Unit vector in any Euclidean d-space

V Scaled volume

$V()$ Scaled dimensionless potential

V_0 Energy scale

$V_0(x, y)$ Random potential height at any point xy (Chap. 8)

V_1, V_2 Volumes in which the total volume V splits

V_d Scaled height at which $V(\boldsymbol{r}, t)$ is cut to transform to $U(\boldsymbol{r}, t)$

V_H Scaled obstacles' height of a dynamic random potential made of obstacles

V_i Potential in discrete real space

$V_p()$ Scaled periodic potential

$\mathcal{V}(k)$ Fourier transform of the field $V(x)$

$\mathcal{V}_\mu$ Fourier transform of the potential in discrete real space

$\hat{V}$ Volume

$\hat{V}()$ Potential energy

$\bar{V}(x, y, z)$ $3-d$ random attracting potential to an interface (Chap. 8)

v Scaled modulus of the velocity vector

v_u Scaled $1-d$ velocity employing the underdamped characteristic time scale

v_w Components of the scaled vector velocity along the $w = x, y, z$ cartesian axes

$v_\parallel$ Component of the velocity vector along the external force's direction

$v_\perp$ Component of the velocity vector along the direction perpendicular to the external force

$\boldsymbol{v}$ Scaled dimensionless velocity vector in Euclidean d-space

$\boldsymbol{v}_u$ Scaled velocity vector employing the underdamped characteristic time scale

$\hat{v}$ $1-d$ velocity

$\hat{v}_{\hat{\boldsymbol{u}}}$ Velocity component along direction $\hat{\boldsymbol{u}}$

$\hat{\boldsymbol{v}}$ Velocity vector in Euclidean d-space

$\bar{v}$ Quotient of velocities (Chap. 8.2)

$W()$ Distribution of velocities

$W_{st}()$ Steady velocity distribution

w Dummy variable that accounts for any of the $3-d$ Euclidean coordinates x, y, z

X_i Random process in the time integration of the Langevin equation (Chap. 7)

x Scaled $1-d$ position

x_i Auxiliary coordinates for the unidimensional integral of the Boltzmann's factor to obtain the Krammers' escape rate

x_{min}, x_{max} Coordinates of the potential's minimum (maximum) when it displays a barrier over which thermally driven particles escape (Chap. 1)

$\hat{x}$ $1-d$ position

Y_{ij} Random process in the time integration of the Langevin equation (Chap. 7)

y Scaled $1-d$ position

$\hat{y}$ $1-d$ position

z Scaled $1-d$ position

z_0 Coordinate such that $\hat{V}(z_0) = -V_0/2$, that is employed to scale the length variables in Chapter 8

$z_{2\to1}$ Upper limit for the integral of the Boltzmann distribution to obtain the ratio n_2/n (Chap. 8)

z_+ Particular choice for the upper limit for the integral of the Boltzmann distribution to obtain the ratio n_2/n (Chap. 8)

z_- Particular choice for the upper limit for the integral of the Boltzmann distribution to obtain the ratio n_2/n (Chap. 8)

Bibliography

S. A. Adelman and J. D. Doll. Brownian motion and chemical dynamics on solid surfaces. *Accounts of Chemical Research*, **10**(10):378–384, 1977.

H. P. Babcock, C. Chen, and X. Zhuang. Using single-particle tracking to study nuclear trafficking of viral genes. *Biophysical Journal*, **87**(4):2749 – 2758, 2004.

L. Bachelier. *Théorie de la spéculation*. Gauthier-Villars, 1900a.

L. Bachelier. Théorie de la spéculation. *Annales Scientifiques de l'École Normale Supérieure*, 1900b.

V. Balakrishnan. Anomalous diffusion in one dimension. *Physica A: Statistical Mechanics and its applications*, **132**(2-3):569–580, 1985.

E. Barkai, Y. Garini, and R. Metzler. Strange kinetics of single molecules in living cells. *Physics today*, **65**(8):29, 2012.

A. Baskaran and M. C. Marchetti. Statistical mechanics and hydrodynamics of bacterial suspensions. *Proceedings of the National Academy of Sciences USA*, **106**(37):15567–15572, 2009.

H. Bässler. Viscous flow in supercooled liquids analyzed in terms of transport theory for random media with energetic disorder. *Phys. Rev. Lett.*, **58**:767–770, 1987.

A. Basu, J. F. Joanny, F. Jülicher, and J. Prost. Thermal and non-thermal fluctuations in active polar gels. *The European Physical Journal E*, **27**:149–160, 2008.

T. Bickel. Brownian motion near a liquid-like membrane. *The European Physical Journal E*, **20**:379–385, 2006.

P. Bitlloch, X. Ruiz, L. Ramírez-Piscina, and J. Casademunt. Turbulent bubble jets in microgravity. Spatial dispersion and velocity fluctuations. *Microgravity Science and Technology*, **27**(3):207–220, 2015.

V. Blickle, T. Speck, C. Lutz, U. Seifert, and C. Bechinger. Einstein relation generalized to nonequilibrium. *Phys. Rev. Lett.*, **98**:210601, 2007.

J.-P. Bouchaud and A. Georges. Anomalous diffusion in disordered media: Statistical mechanisms, models and physical applications. *Physics Reports*, **195**: 127–293, 1990.

I. Bronstein, Y. Israel, E. Kepten, S. Mai, Y. Shav-Tal, E. Barkai, and Y. Garini. Transient anomalous diffusion of telomeres in the nucleus of mammalian cells. *Phys. Rev. Lett.*, **103**:018102, 2009.

R. Brown. A brief account of microscopical observations made in the months of june, july, and august, 1827, on the particles contained in the pollen of plants; and on the general existence of active molecules in organic and inorganic bodies. *The Edinburgh New Philosophical Journal*, **5**:358–371, 1828.

L. Bruno, V. Levi, M. Brunstein, and M. A. Despósito. Transition to superdiffusive behavior in intracellular actin-based transport mediated by molecular motors. *Phys. Rev. E*, **80**:011912, 2009.

P. Bursac, G. Lenormand, B. Fabry, M. Oliver, D. A. Weitz, V. Viasnoff, J. P. Butler, and J. J. Fredberg. Cytoskeletal remodelling and slow dynamics in the living cell. *Nature Materials*, **4**(7):557–561, 2005.

O. V. Bychuk and B. O'Shaughnessy. Anomalous diffusion at liquid surfaces. *Phys. Rev. Lett.*, **74**:1795–1798, 1995.

H. B. Callen and T. A. Welton. Irreversibility and generalized noise. *Phys. Rev.*, **83**:34–40, 1951.

A. Caspi, R. Granek, and M. Elbaum. Enhanced diffusion in active intracellular transport. *Phys. Rev. Lett.*, **85**:5655–5658, 2000.

S. Chandrasekhar. Brownian motion, dynamical friction, and stellar dynamics. *Rev. Mod. Phys.*, **21**:383–388, 1949.

D. Chrétien and R. H. Wade. New data on the microtubule surface lattice. *Biology of the Cell*, **71**(1-2):161–174, 1991.

P. Colet, M. San Miguel, J. Casademunt, and J. M. Sancho. Relaxation from a marginal state in optical bistability. *Phys. Rev. A*, **39**:149–156, 1989.

S. Condamin, V. Tejedor, R. Voituriez, O. Bénichou, and J. Klafter. Probing microscopic origins of confined subdiffusion by first-passage observables. *Proceedings of the National Academy of Sciences USA*, **105**(15):5675–5680, 2008.

J.-M. Courtault, Y. Kabanov, B. Bru, P. Crépel, I. Lebon, and A. Le Marchand. Louis Bachelier on the centenary of *Théorie de la Spéculation*. *Mathematical Finance*, **10**(3):341–353, 2000.

J. Crane and A. S. Verkman. Long–range nonanomalous diffusion of quantum dot–labeled Aquaporin–1 water channels in the cell plasma membrane. *Biophysical Journal*, **94**:702–713, 2008.

E. Dauty and A. S. Verkman. Actin cytoskeleton as the principal determinant of size-dependent DNA mobility in cytoplasm: A new barrier for non-viral gene delivery. *The Journal of Biological Chemistry*, **280**(9):7823–7828, 2005.

V. Démery, O. Bénichou, and H. Jacquin. Generalized Langevin equations for a driven tracer in dense soft colloids: construction and applications. *New Journal of Physics*, **16**(5):053032, 2014.

S. I. Denisov, E. S. Denisova, and H. Kantz. Biased diffusion in a piecewise linear random potential. *The European Physical Journal B*, **76**(1):1–11, 2010.

R. M. Dickson, D. J. Norris, Y.-L. Tzeng, and W. E. Moerner. Three–dimensional imaging of single molecules solvated in pores of poly(acrylamide) gels. *Science*, **274**:966, 1996.

J. A. Dix and A.S. Verkman. Crowding effects on diffusion in solutions and cells. *Annual Review of Biophysics*, **37**(1):247–263, 2008.

K. M. Douglass, S. Sukhov, and A. Dogariu. Superdiffusion in optically controlled active media. *Nature Photonics*, **6**:834–837, 2012.

D. H. Dunlap, P. E. Parris, and V. M. Kenkre. Charge-dipole model for the universal field dependence of mobilities in molecularly doped polymers. *Phys. Rev. Lett.*, **77**:542–545, 1996.

W. Ebeling and I. M. Sokolov. *Statistical thermodynamics and stochastic theory of nonequilibrium systems*. World Scientific, 2005.

A. Einstein. Über die von der molekularkinetischen Theorie der Wärme geforderte Bewegung von in ruhenden Flüssigkeiten suspendierten Teilchen. *Annalen der Physik*, **17**:549–560, 1905.

R. J. Ellis and A. P. Minton. Join the crowd. *Nature*, **425**:27–28, 2003.

F. Evers, C. Zunke, R. D. L. Hanes, J. Bewerunge, I. Ladadwa, A. Heuer, and S. U. Egelhaaf. Particle dynamics in two-dimensional random-energy landscapes: Experiments and simulations. *Phys. Rev. E*, **88**:022125, 2013.

A. E. Fick. Über Diffusion. *Poggendorff's Annalen der Physik und Chemie*, **94**: 59–86, 1855.

A. D. Fokker. Die mittlere Energie rotierender elektrischer Dipole im Strahlungsfeld. *Annalen der Physik*, **43**:810–820, 1914.

B. J. Ford. Brownian movement in clarkia pollen: A reprise of the first observations. *The Microscope*, **40**(4):235–241, 1992.

M. Frigo and S. G. Johnson. The design and implementation of FFTW3. *Proceedings of the IEEE*, **93**(2):216–231, 2005.

P. Fulde, L. Pietronero, W. R. Schneider, and S. Strässler. Problem of Brownian motion in a periodic potential. *Phys. Rev. Lett.*, **35**:1776–1779, 1975.

M. Galassi, J. Davies, J. Theiler, B. Gough, G. Jungman, P. Alken, M. Booth, and F. Rossi. *GNU Scientific Library Reference Manual*. Network Theory Ltd, 2009.

J. García-Ojalvo and J. M. Sancho. *Noise in Spatially Extended Systems*. Springer, 1999.

J. García-Ojalvo, J. M. Sancho, and L. Ramírez-Piscina. Generation of spatiotemporal colored noise. *Phys. Rev. A*, **46**:4670–4675, 1992.

C. W. Gardiner. *Handbook of Stochastic Methods*. Springer, 1985.

P. G. de Gennes. Brownian motion of a classical particle through potential barriers. Application to the helix-coil transitions of heteropolymers. *Journal of Statistical Physics*, **12**(6):463–481, 1975.

J. P. Gleeson, J. M. Sancho, A. M. Lacasta, and K. Lindenberg. Analytical approach to sorting in periodic and random potentials. *Phys. Rev. E*, **73**:041102, 2006.

I. Golding and E. C. Cox. Physical nature of bacterial cytoplasm. *Phys. Rev. Lett.*, **96**:098102, 2006.

P. S. Goohpattader, S. Mettu, and M. K. Chaudhury. Experimental investigation of the drift and diffusion of small objects on a surface subjected to a bias and an external white noise: Roles of Coulombic friction and hysteresis. *Langmuir*, **25**(17):9969–9979, 2009.

M. Gori, I. Donato, E. Floriani, I. Nardecchia, and M. Pettini. Random walk of passive tracers among randomly moving obstacles. *Theoretical Biology & Medical Modelling*, **13**:13, 2016.

L. G. Gouy. Sur le mouvement Brownien. *Comptes Rendus*, **109**:102, 1889.

I. Goychuk and V. O. Kharchenko. Anomalous features of diffusion in corrugated potentials with spatial correlations: Faster than normal, and other surprises. *Phys. Rev. Lett.*, **113**:100601, 2014.

W. J. Greenleaf, M. T. Woodside, and S. M. Block. High–resolution, single–molecule measurements of biomolecular motion. *The Annual Review of Biophysics and Biomolecular Structure*, **36**:171–190, 2007.

D. G. Grier. A revolution in optical manipulation. *Nature*, **424**:810–816, 2003.

R. D. L. Hanes and S. U. Egelhaaf. Dynamics of individual colloidal particles in one-dimensional random potentials: a simulation study. *Journal of Physics: Condensed Matter*, **24**(46):464116, 2012.

R. D. L. Hanes, C. Dalle-Ferrier, M. Schmiedeberg, M. C. Jenkins, and S. U. Egelhaaf. Colloids in one dimensional random energy landscapes. *Soft Matter*, **8**:2714–2723, 2012.

R. D. L. Hanes, M. Schmiedeberg, and S. U. Egelhaaf. Brownian particles on rough substrates: Relation between intermediate subdiffusion and asymptotic long-time diffusion. *Phys. Rev. E*, **88**:062133, 2013.

P. Hänggi and F. Marchesoni. 100 years of brownian motion. *Chaos*, **15**:026101, 2005.

J. W. Haus and K. W. Kehr. Diffusion in regular and disordered lattices. *Physics Reports*, **150**:263–406, 1987.

W. Ho. Single-molecule chemistry. *The Journal of Chemical Physics*, **117**:11033, 2002.

F. Höfling and T. Franosch. Anomalous transport in the crowded world of biological cells. *Reports on Progress in Physics*, **76**(4):046602, 2013.

A. Honciuc, A. W. Harant, and D. K. Schwartz. Single-molecule observations of surfactant diffusion at the solution-solid interface. *Langmuir*, **24**(13):6562–6566, 2008.

M. R. Horton, F. Höfling, J. O. Rädler, and T. Franosch. Development of anomalous diffusion among crowding proteins. *Soft Matter*, **6**:2648–2656, 2010.

L. R. Huang, E. C. Cox, R. H. Austin, and J. C. Sturm. Continuous particle separation through deterministic lateral displacement. *Science*, **304**:987–990, 2004.

J. Ingen-Housz. *Bemerkungen über den Gebrauch des Vergrösserungsglases. Vermischte Schriften physisch–medicinischen Inhalts.* Wappler, Vienna, 1784.

J. Ingen-Housz. *Nouvelles expériences et observations sur divers objets de physique.* Théophile Barrois le jeune, 1789.

M. B. Isichenko. Percolation, statistical topography, and transport in random media. *Rev. Mod. Phys.*, **64**:961–1043, 1992.

J.-H. Jeon, V. Tejedor, S. Burov, E. Barkai, C. Selhuber-Unkel, K. Berg-Sørensen, L. Oddershede, and R. Metzler. *In Vivo* anomalous diffusion and weak ergodicity breaking of lipid granules. *Phys. Rev. Lett.*, **106**:048103, 2011.

J.-H. Jeon, A. V. Chechkin, and R. Metzler. Scaled Brownian motion: a paradoxical process with a time dependent diffusivity for the description of anomalous diffusion. *Phys. Chem. Chem. Phys.*, **16**:15811–15817, 2014.

A. Katsumi, C. Nakada, K. Ritchie, K. Murase, K. Suzuki, H. Murakoshi, R. S. Kasai, J. Kondo, and T. Fujiwara. Paradigm shift of the plasma membrane concept from the two–dimensional continuum fluid to the partitioned fluid: High–speed single–molecule tracking of membrane molecules. *Annual Review of Biophysics and Biomolecular Structure*, **34**:351–378, 2005.

A. Khoshnood and M. A. Jalali. Anomalous diffusion of proteins in sheared lipid membranes. *Phys. Rev. E*, **88**:032705, 2013.

M. Khoury, J. P. Gleeson, J. M. Sancho, A. M. Lacasta, and K. Lindenberg. Diffusion coefficient in periodic and random potentials. *Phys. Rev. E*, **80**:021123, 2009.

M. Khoury, A. M. Lacasta, J. M. Sancho, and K. Lindenberg. Weak disorder: Anomalous transport and diffusion are normal yet again. *Phys. Rev. Lett.*, **106**: 090602, 2011.

M. T. Klann, A. Lapin, and M. Reuss. Agent-based simulation of reactions in the crowded and structured intracellular environment: Influence of mobility and location of the reactants. *BMC Systems Biology*, **5**:71, 2011.

S. Köhler, V. Schaller, and A. R. Bausch. Structure formation in active networks. *Nature Materials*, **10**:462–468, 2011.

P. T. Korda, M. B. Taylor, and D. G. Grier. Kinetically locked-in colloidal transport in an array of optical tweezers. *Phys. Rev. Lett.*, **89**:128301, 2002.

A. S. Kozlov, D. Andor-Ardó, and A. J. Hudspeth. Anomalous Brownian motion discloses viscoelasticity in the ear's mechanoelectrical-transduction apparatus. *Proceedings of the National Academy of Sciences USA*, **109**(8):2896–2901, 2012.

H. A. Kramers. Brownian motion in a field of force and the diffusion model of chemical reactions. *Physica*, **7**:284, 1940.

R. Kubo. Statistical–mechanical theory of irreversible processes. I. General theory and simple applications to magnetic and conduction problems. *Journal of the Physical Society of Japan*, **12**(6):570–586, 1957.

R. Kubo, M. Toda, and N. Hashitsume. *Statistical Physics II: Nonequilibrium Statistical Mechanics*. Springer–Verlag Berlin Heidelberg, 1991.

K. S. Kunz. *Numerical Analysis*. McGraw-Hill, 1957.

P. I. Kuznetsov, V. I. Tikhonov, and R. L. Stratonovich. *Non-linear transformations of stochastic processes*. Oxford, Pergamon Press, 1965.

A. M. Lacasta, J. M. Sancho, A. H. Romero, and K. Lindenberg. Sorting on periodic surfaces. *Phys. Rev. Lett.*, **94**:160601, 2005.

A. M. Lacasta, M. Khoury, J. M. Sancho, and K. Lindenberg. Sorting of mesoscopic particles driven through periodic potential landscapes. *Mod. Phys. Lett. B*, **20**: 1427–1442, 2006.

P. Langevin. Sur la théorie du mouvement Brownien. *Comptes Rendus Hebdomadaires des Seances de l'Academie des Sciences. D, Sciences Naturelles (Paris)*, **146**:530–533, 1908.

A. W. C. Lau, B. D. Hoffman, A. Davies, J. C. Crocker, and T. C. Lubensky. Microrheology, stress fluctuations, and active behavior of living cells. *Phys. Rev. Lett.*, **91**:198101, 2003.

D. H. Lee, C. H. Choi, T. H. Choi, B. J. Sung, and H. Kang. Asymmetric transport mechanisms of hydronium and hydroxide ions in amorphous solid water: Hydroxide goes Brownian while hydronium hops. *The Journal of Physical Chemistry Letters*, **5**(15):2568–2572, 2014.

S.-H. Lee and D. G. Grier. Giant colloidal diffusivity on corrugated optical vortices. *Phys. Rev. Lett.*, **96**:190601, 2006.

D. S. Lemons and A. Gythiel. Paul Langevin's 1908 paper "On the theory of Brownian motion" ["Sur la théorie du mouvement Brownien," C. R. Acad. Sci. (Paris) 146, 530-533 (1908)]. *American Journal of Physics*, **65**(11):1079–1081, 1997.

K. Lindenberg, A. M. Lacasta, J. M. Sancho, and A. H. Romero. Transport and diffusion on crystalline surfaces under external forces. *New Journal of Physics*, **7**(1):29, 2005.

K. Lindenberg, J. M. Sancho, A. M. Lacasta, and I. M. Sokolov. Dispersionless transport in a washboard potential. *Phys. Rev. Lett.*, **98**:020602, 2007.

K. Lindenberg, J. M. Sancho, M. Khoury, and A. M. Lacasta. Weak disorder in periodic potentials: anomalous transport and diffusion. *Fluctuation and Noise Letters*, **11**(01):1240004, 2012.

B. Lindner and I. M. Sokolov. Giant diffusion of underdamped particles in a biased periodic potential. *Phys. Rev. E*, **93**:042106, 2016.

B. Lindner, M. Kostur, and L. Schimansky-Geier. Optimal diffusive transport in a tilted periodic potential. *Fluctuation and Noise Letters*, **01**(01):R25–R39, 2001.

S. Liu, X. F. Xu, R. G. Xie, G. Zhang, and B. W. Li. Anomalous heat conduction and anomalous diffusion in low dimensional nanoscale systems. *The European Physical Journal B*, **85**(10):337, 2012.

L. Longobardi, D. Massarotti, G. Rotoli, D. Stornaiuolo, G. Papari, A. Kawakami, G. P. Pepe, A. Barone, and F. Tafuri. Thermal hopping and retrapping of a Brownian particle in the tilted periodic potential of a NbN/MgO/NbN Josephson junction. *Phys. Rev. B*, **84**:184504, 2011.

W. D. Luedtke and U. Landman. Slip diffusion and Lévy flights of an adsorbed gold nanocluster. *Phys. Rev. Lett.*, **82**:3835–3838, 1999.

M. P. MacDonald, G. C. Spalding, and K. Dholakia. Microfluidic sorting in an optical lattice. *Nature*, **426**:421–424, 2003.

H. A. Makse, S. Havlin, M. Schwartz, and H. E. Stanley. Method for generating long-range correlations for large systems. *Phys. Rev. E*, **53**:5445–5449, 1996.

R. Mannella. *Noise in nonlinear dynamical systems*, volume 3. Experiments and simulations, chapter Computer experiments in non–linear stochastic physics, pages 189–221. Cambridge University Press, 1989.

I. G. Marchenko and I. I. Marchenko. Diffusion in the systems with low dissipation: Exponential growth with temperature drop. *EPL (Europhysics Letters)*, **100** (5):50005, 2012.

I. G. Marchenko, I. I. Marchenko, and A. V. Zhiglo. Particle transport in space-periodic potentials in underdamped systems. *The European Physical Journal B*, **87**:10, 2014.

M. C. Marchetti, J. F. Joanny, S. Ramaswamy, T. B. Liverpool, J. Prost, M. Rao, and R. A. Simha. Hydrodynamics of soft active matter. *Rev. Mod. Phys.*, **85**: 1143–1189, 2013.

G. McMullan, K. R. Vinothkumar, and R. Henderson. Thon rings from amorphous ice and implications of beam-induced Brownian motion in single particle electron cryo-microscopy. *Ultramicroscopy*, **158**:26 – 32, 2015.

O. Medalia, I. Weber, A. S. Frangakis, D. Nicastro, G. Gerisch, and W. Baumeister. Macromolecular architecture in eukaryotic cells visualized by cryoelectron tomography. *Science*, **298**:1209–1213, 2002.

R. Metzler and J. Klafter. The random walk's guide to anomalous diffusion: a fractional dynamics approach. *Physics Reports*, **339**(1):1 – 77, 2000.

E. W. Montroll. Random walks on lattices. III. Calculation of first-passage time with application to exciton trapping on photosynthetic units. *Journal of Mathematical Physics*, **10**:753, 1969.

E. W. Montroll and G. H. Weiss. Random walks on lattices. II. *Journal of Mathematical Physics*, **6**:167, 1965.

K. J. Morton, K. Loutherback, D. W. Inglis, O. K. Tsui, J. C. Sturm, S. Y. Chou, and R. H. Austin. Hydrodynamic metamaterials: Microfabricated arrays to steer, refract, and focus streams of biomaterials. *Proceedings of the National Academy of Sciences USA*, **105**:7434–7438, 2008.

K. Nishinari, Y. Okada, A. Schadschneider, and D. Chowdhury. Intracellular transport of single-headed molecular motors KIF1A. *Phys. Rev. Lett.*, **95**:118101, 2005.

I. Nordlund. *Zeitschrift für Physikalische Chemie*, **87**:40, 1914.

S.-M. Oh, S. J. Koh, K. Kyuno, and G. Ehrlich. Non–nearest–neighbor jumps in 2D diffusion: Pd on W(110). *Phys. Rev. Lett.*, **88**:236102, 2002.

Y. Okada and N. Hirokawa. A processive single–headed motor: Kinesin superfamily protein KIF1A. *Science*, **283**(5405):1152–7, 1999.

Y. Okada, H. Higuchi, and N. Hirokawa. Processivity of the single–headed kinesin KIF1A through biased binding to tubulin. *Nature*, **424**:574–577, 2003.

D. Oriola and J. Casademunt. Cooperative force generation of KIF1A Brownian motors. *Phys. Rev. Lett.*, **111**:048103, 2013.

L. S. Ornstein. On the Brownian motion. *Proceedings Royal Netherlands Academy of Arts and Science*, **21**:96–108, 1919.

N.-N. Pang, Y.-K. Yu, and T. Halpin-Healy. Interfacial kinetic roughening with correlated noise. *Phys. Rev. E*, **52**:3224–3227, 1995.

P. E. Parris, M. Kuś, D. H. Dunlap, and V. M. Kenkre. Nonlinear response theory: Transport coefficients for driving fields of arbitrary magnitude. *Phys. Rev. E*, **56**:5295–5305, 1997.

K. Pearson. The problem of the random walk. *Nature*, **72**:294, 1905.

J. B. Perrin. L'agitation moléculaire et le mouvement Brownien. *Comptes Rendus Hebdomadaires des Séances de l'Academie des Sciences. D, Sciences Naturelles (Paris)*, **146**:967–970, 1908.

J. B. Perrin. Mouvement Brownien et réalité moléculaire. *Annuaire de Chimie et de Physique (VIII)*, **18**:5–114, 1909.

F. Peruani, J. Starruß, V. Jakovljevic, L. Søgaard-Andersen, A. Deutsch, and M. Bär. Collective motion and nonequilibrium cluster formation in colonies of gliding bacteria. *Phys. Rev. Lett.*, **108**:098102, 2012.

L. Pitulice, E. Vilaseca, I. Pastor, S. Madurga, J. Ll. Garcés, A. Isvoran, and F. Mas. Monte Carlo simulations of enzymatic reactions in crowded media. Effect of the enzyme-obstacle relative size. *Mathematical Biosciences*, **251**:72 – 82, 2014.

M. Planck. Über einen Satz der statistischen Dynamik und seine Erweiterung in der Quantentheorie. *Sitzung der physikalisch–mathematischen Klasse vom 10*, pages 324–341, 1917.

G. E. Poirier and E. D. Plyant. The self–assembly mechanism of alkanethiols on Au(111). *Science*, **272**:1145, 1996.

E. M. Purcell. Life at low Reynolds number. *American Journal of Physics*, **45** (5265):3–11, 1977.

S. Redner. *A Guide to First–Passage Processes*. Cambridge University Press, Cambridge UK, 2007.

P. Reimann and R. Eichhorn. Weak disorder strongly improves the selective enhancement of diffusion in a tilted periodic potential. *Phys. Rev. Lett.*, **101**: 180601, 2008.

P. Reimann, C. Van den Broeck, H. Linke, P. Hänggi, J. M. Rubi, and A. Pérez-Madrid. Giant acceleration of free diffusion by use of tilted periodic potentials. *Phys. Rev. Lett.*, **87**:010602, 2001.

P. Reimann, C. Van den Broeck, H. Linke, P. Hänggi, J. M. Rubi, and A. Pérez-Madrid. Diffusion in tilted periodic potentials: Enhancement, universality, and scaling. *Phys. Rev. E*, **65**:031104, 2002.

H. Risken. *The Fokker–Planck Equation*. Springer–Verlag, second edition, 1989.

A. H. Romero and J. M. Sancho. Brownian motion in short range random potentials. *Phys. Rev. E*, **58**:2833–2837, 1998.

F. Sagués, J. M. Sancho, and J. García-Ojalvo. Spatiotemporal order out of noise. *Rev. Mod. Phys.*, **79**:829–882, 2007.

J. M. Sancho. Brownian colloids in underdamped and overdamped regimes with nonhomogeneous temperature. *Phys. Rev. E*, **92**:062110, 2015.

J. M. Sancho and A. M. Lacasta. The rich phenomenology of Brownian particles in nonlinear potential landscapes. *The European Physical Journal Special Topics*, **187**(1):49–62, 2010.

J. M. Sancho, A. M. Lacasta, K. Lindenberg, I. M. Sokolov, and A. H. Romero. Diffusion on a solid surface: Anomalous is normal. *Phys. Rev. Lett.*, **92**:250601, 2004.

J. M. Sancho, M. Khoury, K. Lindenberg, and A. M. Lacasta. Particle separation by external fields on periodic surfaces. *Journal of Physics: Condensed Matter*, **17**(49):S4151–S4163, 2005.

N. Sarkar and A. Basu. Fluctuations and symmetries in two-dimensional active gels. *The European Physical Journal E*, **34**:44, 2011.

H. Scher and E. W. Montroll. Anomalous transit-time dispersion in amorphous solids. *Physical Review B: Condensed Matter and Materials Physics*, **12**:2455, 1975.

M. Schmiedeberg, J. Roth, and H. Stark. Brownian particles in random and quasicrystalline potentials: How they approach the equilibrium. *The European Physical Journal E*, **24**(4):367–377, 2007.

W. R. Schneider and W. Wyss. Fractional diffusion equation. *Helvetica Physica Acta*, **60**:358, 1987.

W. R. Schneider and W. Wyss. Fractional diffusion and wave-equations. *Journal of Mathematical Physics*, **30**:134, 1989.

M. Schunack, T. R. Linderoth, F. Rosei, E. Lægsgaard, I. Stensgaard, and F. Besenbacher. Long jumps in the surface diffusion of large molecules. *Phys. Rev. Lett.*, **88**:156102, 2002.

Z. Schuss. *Theory and Applications of Stochastic Differential Equations*. Wiley, 1980.

C. Selhuber-Unkel, P. Yde, K. Berg-Sørensen, and L. B. Oddershede. Variety in intracellular diffusion during the cell cycle. *Physical Biology*, **6**(2):025015, 2009.

D. C. Senft and G. Ehrlich. Long jumps in surface diffusion: One-dimensional migration of isolated adatoms. *Phys. Rev. Lett.*, **74**:294–297, 1995.

M. F. Shlesinger, B. J. West, and J. Klafter. Lévy dynamics of enhanced diffusion: Application to turbulence. *Phys. Rev. Lett.*, **58**:1100–1103, 1987.

M. F. Shlesinger, G. M. Zaslavsky, and J. Klafter. Strange kinetics. *Nature*, **363**: 31–37, 1993.

M. J. Skaug, J. Mabry, and D. K. Schwartz. Intermittent molecular hopping at the solid-liquid interface. *Phys. Rev. Lett.*, **110**:256101, 2013.

M. J. Skaug, L. Wang, Y. Ding, and D. K. Schwartz. Hindered nanoparticle diffusion and void accessibility in a three-dimensional porous medium. *ACS Nano*, **9**(2):2148–2156, 2015.

M. Slutsky, M. Kardar, and L. A. Mirny. Diffusion in correlated random potentials, with applications to DNA. *Phys. Rev. E*, **69**:061903, 2004.

M. von Smoluchowski. Zur kinetischen Theorie der Brownschen Molekularbewegung und der Suspensionen. *Annalen der Physik*, **21**:757–779, 1906.

I. M. Sokolov and R. Metzler. Towards deterministic equations for Lévy walks: The fractional material derivative. *Phys. Rev. E*, **67**:010101, 2003.

I. M Sokolov, J. Klafter, and A. Blumen. Fractional kinetics. *Physics Today*, **55** (11):48–54, 2002.

K. Sozański, F. Ruhnow, A. Wiśniewska, M. Tabaka, S. Diez, and R. Hołyst. Small crowders slow down kinesin-1 stepping by hindering motor domain diffusion. *Phys. Rev. Lett.*, **115**:218102, 2015.

D. Stauffer, C. Schulze, and D. W. Heermann. Superdiffusion in a model for diffusion in a molecularly crowded environment. *Journal of Biological Physics*, **33**(4):305–312, 2008.

R. L. Stratonovich. *Radiotekh. Elektron. (Moscow)*, **3**:497, 1958.

M. Suñé, J. M. Sancho, and A. M. Lacasta. On generating random potentials. *Fluctuation and Noise Letters*, **11**(04):1250026, 2012.

M. Suñé, J. M. Sancho, and K. Lindenberg. Transport and diffusion of overdamped Brownian particles in random potentials. *Phys. Rev. E*, **88**:062105, 2013.

M. Suñé, J. M. Sancho, and K. Lindenberg. Transport and diffusion of underdamped Brownian particles in random potentials. *The European Physical Journal B*, **87**(9):1–10, 2014.

M. Suñé, J. M. Sancho, and K. Lindenberg. Brownian motion on random dynamical landscapes. *The European Physical Journal B*, **89**(3):1–7, 2016.

S. M. A. Tabei, S. Burov, H. Y. Kim, A. Kuznetsov, T. Huynh, J. Jureller, L. H. Philipson, A. R. Dinner, and N. F. Scherer. Intracellular transport of insulin granules is a subordinated random walk. *Proceedings of the National Academy of Sciences USA*, **110**(13):4911–4916, 2013.

P. Tierno, P. Reimann, T. H. Johansen, and F. Sagués. Giant transversal particle diffusion in a longitudinal magnetic ratchet. *Phys. Rev. Lett.*, **105**:230602, 2010.

I. M. Tolić-Nørrelykke, E.-L. Munteanu, G. Thon, L. Oddershede, and K. Berg-Sørensen. Anomalous diffusion in living yeast cells. *Phys. Rev. Lett.*, **93**:078102, 2004.

R. Toral and P. Colet. *Stochastic Numerical Methods*. Wiley-VCH, 2014.

F. Trovato and V. Tozzini. Diffusion within the cytoplasm: A mesoscale model of interacting macromolecules. *Biophysical Journal*, **107**:2579–2591, 2014.

C. S. Tucker. Reaction rates in condensed phases. Perspective on "Brownian motion in a field of force and the diffusion model of chemical reactions". *Theoretical Chemistry Accounts*, **103**(3):209–211, 2000.

E. Vilaseca, A. Isvoran, S. Madurga, I. Pastor, J. Ll. Garcés, and F. Mas. New insights into diffusion in 3D crowded media by Monte Carlo simulations: effect of size, mobility and spatial distribution of obstacles. *Phys. Chem. Chem. Phys.*, **13**:7396–7407, 2011.

M. Wachsmuth, W. Waldeck, and J. Langowski. Anomalous diffusion of fluorescent probes inside living cell nuclei investigated by spatially–resolved fluorescence correlation spectroscopy. *Journal of Molecular Biology*, **298**(4):677–689, 2000.

M. C. Wang and G. E. Uhlenbeck. On the theory of the Brownian motion II. *Rev. Mod. Phys.*, **17**:323–342, 1945.

S. C. Weber, A. J. Spakowitz, and J. A. Theriot. Bacterial chromosomal loci move subdiffusively through a viscoelastic cytoplasm. *Phys. Rev. Lett.*, **104**:238102, 2010.

A. V. Weigel, B. Simon, M. M. Tamkun, and D. Krapf. Ergodic and nonergodic processes coexist in the plasma membrane as observed by single-molecule tracking. *Proceedings of the National Academy of Sciences USA*, **108**(16):6438–6443, 2011.

M. Weiss. Single-particle tracking data reveal anticorrelated fractional Brownian motion in crowded fluids. *Phys. Rev. E*, **88**:010101, 2013.

M. Weiss, M. Elsner, F. Kartberg, and T. Nilsson. Anomalous subdiffusion is a measure for cytoplasmic crowding in living cells. *Biophysical Journal*, **87**: 3518–3524, 2004.

J. R. White. Diffusion coefficients of fatty acids and monobasic phosphoric acids in *n*-decane. *The Journal of Chemical Physics*, **23**:2247–2251, 1955.

A. S. de Wijn. Internal degrees of freedom and transport of benzene on graphite. *Phys. Rev. E*, **84**:011610, 2011.

Q. Xu, L. Feng, R. Sha, N. C. Seeman, and P. M. Chaikin. Subdiffusion of a sticky particle on a surface. *Phys. Rev. Lett.*, **106**:228102, 2011.

J. Yajima and R. A. Cross. A torque component in the kinesin-1 power stroke. *Nature Chemical Biology*, **1**(6):338–341, 2005.

T. Yokoyama, S. Yokoyama, T. Kamikado, Y. Okuno, and S. Mashiko. Selective assembly on a surface of supramolecular aggregates with controlled size and shape. *Nature*, **413**:619–621, 2001.

R Zwanzig. Diffusion in a rough potential. *Proceedings of the National Academy of Sciences USA*, **85**(7):2029–2030, 1988.